Direct numerical simulation of a spatially developing turbulent boundary layer separating over a curved wall

Abhiram B. Aithal

A dissertation
submitted in partial fulfillment of the
requirements for the degree of

Doctor of Philosophy

University of Washington

2022

Reading Committee:

Antonino Ferrante, Chair

James Riley, Member

Marco Salviato, Member

Owen Williams, Member

Program Authorized to Offer Degree:
Aeronautics & Astronautics

University of Washington

Abstract

Direct numerical simulation of a spatially developing
turbulent boundary layer separating over a curved wall

Abhiram B. Aithal

Chair of the Supervisory Committee:
Associate Professor Antonino Ferrante
Aeronautics & Astronautics

Flow separation is encountered in many engineering devices, e.g., turbines, diffusers, wings and aftbodies of aircrafts. The physical mechanisms of separated turbulent boundary layers over curved walls are not yet well understood. The main objectives of the present study are to: (i) develop an efficient numerical methodology to perform direct numerical simulations (DNS) of spatially-developing turbulent boundary layers (SDTBLs) over curved walls, and (ii) enhance our knowledge on the dynamics of turbulence in SDTBLs separating over curved walls.

To achieve these objectives, we have developed a new pressure-correction method, called FastRK3, for simulating incompressible flows over curved walls. FastRK3 solves the incompressible Navier-Stokes (NS) equations written in orthogonal curvilinear coordinates. The orthogonal formulation of the NS equations substantially reduces the computational cost of the flow solver and the numerical stencils of its second-order finite difference discretization mirror that of the Cartesian formulation. This property allows us to develop an FFT-based Poisson solver for pressure, called FastPoc, for those cases where the components of the metric tensor are independent of one spatial direction: surfaces of linear translation (e.g., curved ramps and bumps) and surfaces of revolution (e.g., axisymmetric shapes). Our results show that the new FFT-based Poisson solver, FastPoc, is thirty to sixty times faster

than the multigrid-based linear solver, and the new flow solver, FastRK3, is overall four to seven times faster when using FastPoc rather than multigrid. FastRK3 is an explicit, three-stage, third-order Runge-Kutta based projection-method which requires solving the Poisson equation for pressure only once per time step. We show theoretically and numerically that (i) FastRK3 has the same temporal order of accuracy for pressure and velocity as the standard RK3 method for both free-shear and wall-bounded flows when the RK3 coefficients and the pressure extrapolation scheme satisfy specific conditions herein theoretically derived, (ii) FastRK3 is third-order accurate in time for velocity and second-order accurate in time for pressure for free-shear flows, and (iii) FastRK3 is second-order accurate in time for velocity and pressure for 'stiff' wall-bounded flows. In summary, given that the computational mesh satisfies the property of orthogonality, FastRK3 simulates flows over curved walls with second-order accuracy in both space and time.

Using FastRK3, we perform DNS of a SDTBL separating over a curved wall. We validate FastRK3 by comparing our numerical results with published experiments. For the first time, we derive the budget equations of the turbulence kinetic energy and of the Reynolds stresses in orthogonal coordinates, and report the results from our DNS. We study the dynamics of turbulence of the separated flow over the curved wall by analyzing these budget equations. Our analysis shows that, in the separated region over the curved ramp, the TKE production occurs through the production of $\langle u^2 \rangle$ as well as $\langle v^2 \rangle$, in contrast to a ZPG SDTBL where the TKE production is mostly through the production of $\langle u^2 \rangle$. In the curved ramp region, the viscous diffusion and dissipation of $\langle v^2 \rangle$ and $-\langle uv \rangle$ are not zero at the wall, unlike that for both a ZPG SDTBL over a flat-plate as well as a pressure-gradient induced turbulent flow separation over a flat plate. And, the curved ramp region of the flow is characterized by enhanced transport of the Reynolds stresses compared to those of the upstream ZPG SDTBL due to the mixing layer created in the flow by the flow separation. Finally, our results have shown, for the first time, that the Reynolds stress profiles and budgets in the orthogonal curvilinear coordinates are very similar to those in the APG region of the ‘pressure-gradient induced flow separation’ in a flat-plate turbulent boundary layer. Such a comparison is only possible because (i) we employ a structured orthogonal grid over the curved ramp in our simulations, and (ii) FastRK3 solves the governing equations written in orthogonal curvilinear coordinates.

DEDICATION

to my dear nephew, Pranav

आ नो भद्राः क्रतवो यन्तु विश्वतः|

ā no bhadrāḥ kratavo yantu viśvataḥ

Let noble thoughts come to us from every side

-Rigveda, I-89-i

ACKNOWLEDGMENTS

I would like to begin by thanking my doctoral advisor, Prof. Antonino Ferrante for his constant guidance, which was instrumental in the successful completion of my Ph.D. I am grateful for the intellectual freedom I received from him as well as for his belief in my abilities to see through to the end, whatever new derivations and algorithms I wanted to develop. I also appreciate his advice and high standards for scientific research. This made my research experience truly rewarding. I would also like to thank my Ph.D. committee members, Prof. James Riley, Prof. Marco Salviato, Prof. Owen Williams and Prof. Randall LeVeque, for valuable comments and suggestions on my research. I would also like to acknowledge Darren Adams, of the National Center for Supercomputing Applications (NCSA) at the University of Illinois at Urbana-Champaign.

I would also like to thank the many friends I have met during my time at the University of Washington. I appreciate all the help and support I received from you. I have learnt a lot from you, and I will always cherish the time we spent together. Special thanks to the special folks from GUG307. You are like my family. I also thank all the staff members of Aeronautics and Astronautics, especially Ed Connery, for their support.

It is such a privilege to receive the inagural Condit Dissertation Year Fellowship. This fellowship to give me the resources I needed to finish my dissertation. I am immensely grateful to Geda and Phil Condit for their generosity.

Finally, I would like to thank my brother, Anirudh Aithal, and my sister-in-law, Radhika Agumbe, for their kindness and invaluable support throughout my studies. I will forever be grateful to them. Finally, I thank my parents for their unceasing support and care, and for making me the person I am today.

The academic year 2016-17 for this project was funded by the Joint Center for Aerospace Technology Innovation (JCATI) and by the Boeing Co. This work was partly facilitated though the use of advanced computational, storage, and networking infrastructure provided by the Hyak supercomputer and the e-Science Institute at the University of Washington, Seattle. This work used the Extreme Science and Engineering Discovery Environment (XSEDE) Comet at the San Diego Supercomputer Center (SDSC) through allocation TG-CTS100024. XSEDE is supported by National Science Foundation grant number ACI-1548562. We thank Darren Adams of the National Center for Supercomputing Applications (NCSA) for his assistance which was made possible through the XSEDE Extended Collaborative Support Service (ECSS) program.

TABLE OF CONTENTS

Page

LIST OF FIGURES

LIST OF TABLES

Table Number Page

Chapter 1

INTRODUCTION

1.1 Background and Motivation

The Paris Agreement, signed in 2016 and built upon the United Nations Framework Convention on Climate Change (UNFCCC, 2015), urges us to pursue efforts to limit the increase in global average temperature to a maximum of 1.5°C above pre-industrial levels. The special report by the Intergovernmental Panel on Climate Change (IPCC, 2018) recognizes that the pathways to achieving this target will require 'rapid and far-reaching transitions in energy, land, urban and infrastructure (including transport and buildings), and industrial systems'. The global aviation is predicted to account for 1.4% to 2% of the total anthropogenic warming associated to fossil fuel emissions by 2050, and if no significant emission mitigation is implemented, the warming from the aviation sector could further increase to 5.2% by 2100 (Terrenoire *et al.*, 2019). The growing aviation sector has been contributing to increased air traffic and CO2 emissions, therefore further research is needed to improve the commercial airplane design. For instance, improved design of rear-end of the aft-body of a commercial airplane has the potential to reduce the airplane fuel consumption by as much as 1% (Lorang & Carr, 2017). Peak performance of such devices among others, namely, turbines, diffusers, wings and aftbodies of aircrafts, is often obtained close to flow separation, i.e., at incipient separation (Ohlsson *et al.*, 2010). Flow separation is referred to the flow reversal that occurs when the wall shear stress vanishes due to the adverse pressure gradient (APG) over curved bodies, and is accompanied by thickening of the boundary layer, a vortex filled wake and increased values of wall-normal component of velocity. At the same time, separation of turbulent boundary layers leads to degradation of performance such as increase of form drag and lack of maneuverability. Flow separation is also significant in physiological flows, for e.g., the occurrence of boundary layer separation in blood flow is indicative of a normal angiogram (Nicholls *et al.*, 1989). The prediction and control of separated flows are complicated due to their unsteadiness, three-dimensionality, and vortex-filled wakes. Wilcox (2006) regards these flows around curved objects with APG as one of the most challenging fluid dynamics problems to predict using turbulence models. Reynolds averaged Navier-Stokes (RANS) models fail in this regime of full separation, making RANS prediction of separated turbulent flows unreliable (Fröhlich *et al.*, 2005; Wang *et al.*, 2004). There is a need to develop a deeper understanding of the physical mechanisms of separated turbulent flows to improve the RANS models, which are also employed in wall-modeled large-eddy simulations (WMLES) (Piomelli *et al.*, 1989) and hybrid RANS/LES methods (Balaras & Benocci, 1994; Balaras *et al.*, 1996; Spalart *et al.*, 1997).

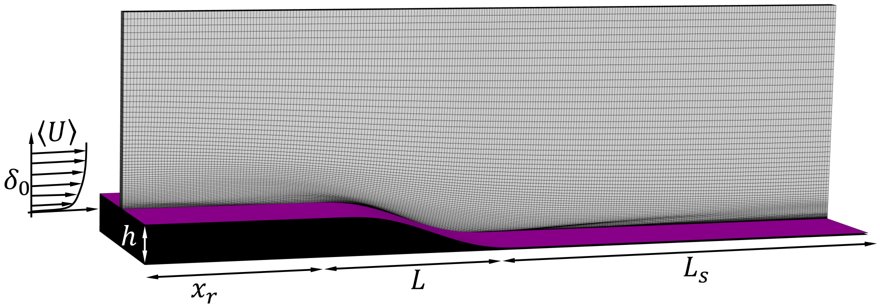

Figure 1.1: Schematic of flow over curved wall. L is the length of the curved surface in the streamwise direction, δ_0 is the inflow boundary layer thickness, and $\langle U \rangle (y)$ the inflow mean velocity profile.

Numerical methods In order to simulate turbulent flows over curved walls, the incompressible Navier-Stokes (NS) equations can be transformed to a more general formulation that allows them to be discretized in curved domains (Aris, 1962). Thus far, the incompressible NS equations in curved domains have been solved using one of the following five techniques: (i) complete transformation of the governing equations (Ge & Sotiropoulos, 2007); (ii) partial transformation of the governing equations (Ge & Sotiropoulos, 2007; Choi *et al.*, 1993; Jang *et al.*, 2011); (iii) finite volume method (Rosenfeld *et al.*, 1991); (iv) finite/spectral element methods (Fischer *et al.*, 2008) and (v) orthogonal formulation of the governing equations (Nikitin, 2006*a*). In all these techniques, the underlying numerical approach is always the projection-method (Chorin, 1967) which requires solving a Poisson equation for pressure at every time step for advancing the numerical solution in time. In general, the Poisson solver is the computational bottleneck of the projection-method. The Poisson equation for pressure is usually solved using either fast Poisson solvers, which can involve a combination of fast Fourier transforms (FFT) and Gaussian elimination (e.g., Dodd & Ferrante (2014)), or iterative methods such as multigrid methods (e.g., Jang *et al.* (2011)) or Krylov methods (e.g., Ge & Sotiropoulos (2007); Fischer *et al.* (2008); Nikitin (2006*a*)). The Poisson equation for pressure that arises in a general curvilinear domain consists of variable coefficients and cross derivatives. As a result, the use of fast Poisson solvers is not feasible for the techniques (i)-(iii) mentioned above. In method (iv), finite-element or higher-order spectral basis functions are used to solve the governing equations. However, the usage of unstructured grids in this case requires iterative solutions to the pressure Poisson equation at every time step which leads to high computational costs (Kooij *et al.*, 2018). Further, the computational cost of the iterative methods depends on problem parameters (e.g., grid stretching) and convergence tolerance, while the FFT-based methods have the advantage of fixed operation count (Dodd & Ferrante, 2014; Aithal & Ferrante, 2018). An alternative way to methods (i)-(iv) is method (v) in which the incompressible NS equations are expressed in the orthogonal formulation and discretized with finite-difference (Nikitin, 2006*a*). However, Nikitin (2006*a*) solves the NS equations in the vorticity-formulation for specific orthogonal coordinates such as cylindrical, spherical, cylindrical-elliptic and bipolar. Therefore, there is a need to develop numerically efficient and accurate methods to simulate turbulent flows over curved walls.

Flow physics Numerical studies of flow separation in the literature fall into two categories: (i) geometry induced flow separation and (ii) ‘pressure-gradient induced flow separation’ in a flat plate boundary layer. Due to the significant computational challenges of simulating turbulent flows over curved walls discussed above, the latter method is usually preferred to study turbulent flow separation. Some examples of geometry induced turbulent flow separation are Wu & Squires (1998); Wasistho & Squires (2005); Fröhlich *et al.* (2005); Ohlsson *et al.* (2010); Marquillie *et al.* (2011); Omidyeganeh & Piomelli (2013); Balakumar *et al.* (2014). Mollicone *et al.* (2017) conducted direct numerical simulation (DNS) to study the effects of geometry and Reynolds number on a turbulent flow over a bulge in a channel. Recently, Balin & Jansen (2021) conducted DNS of a turbulent boundary layer separating over a Gaussian-shaped bump and studied the relaminarization of the flow over the bump.

The seminal study of the 'pressure-gradient induced flow separation' in a flat plate boundary layer were conducted by Spalart & Coleman (1997) and Na & Moin (1998). Lee & Sung (2008) studied the budgets of turbulence kinetic energy (TKE) and the Reynolds stresses for a 'pressure-gradient induced flow separation' in a flat plate boundary layer. Abe *et al.* (2012) performed DNS of such flows at $\mathrm{Re}_\theta = 300, 600$ and 985 and reported positive values of $\langle uv \rangle$ near the top of the separation bubble where the streamline curvature is convex. Kitsios *et al.* (2017) studied a flat plate boundary layer on the verge of separation due to the imposed pressure-gradient and compared the results from (a) zero pressure-gradient, (b) mild adverse pressure gradient and (c) strong adverse pressure gradient. They study the balance of mean momentum as well as that of the TKE. Recent DNS studies of these flows include Abe (2017); Coleman *et al.* (2018). Abe (2019) used the DNS data of Abe (2017) to study in detail the role of $-\langle uv \rangle$. More recently, Wu *et al.* (2020) performed DNS of a flat plate turbulent boundary layer with induced separation and compared the characteristics of the separation bubble for two cases with imposed suction/blowing velocity at the boundary away from the wall: (a) with suction followed by blowing and (b) with suction only. They found that the suction-only case exhibits the pressure gradient and Reynolds stress distribution that are in much better qualitative agreement with separated flows over airfoils and in diffusers with respect to that produced by the suction followed by blowing case. However, a detailed study of the budgets of the Reynolds stress tensor, and TKE in separated flows over curved surfaces are yet to be conducted. Thus, the main goal of our proposed research is to conduct a numerical study aimed to explain the dynamics of turbulence in a separated turbulent flow over a curved ramp as shown in Fig. 1.1.

1.2 Objectives

The primary goals of his Ph. D. thesis are to

1. advance the state-of the-art for the simulation of turbulent flows over curved walls, and

2. enhance the understanding of the flow physics of turbulent flows separating over curved walls.

Specifically, the objectives of the present work are

1. develop an efficient, accurate and scalable numerical methodology to perform direct numerical simulations (DNS) of turbulent flows over curved walls,

2. develop new analytical tools such as the momentum integral equation and Reynolds stress budget equations developed in curvilinear coordinates to study turbulent flows over curved walls,

3. explain the physical mechanisms of a spatially-developing turbulent boundary layer (SDTBL) over curved ramps using the budgets of turbulence kinetic energy and Reynolds stresses.

Chapter 2

MATHEMATICAL FORMULATION

2.1 Governing equations in orthogonal curvilinear coordinates

In the present work, we choose to discretize the incompressible NS equations written in the orthogonal coordinates rather than the general formulation in curvilinear coordinates. In the orthogonal formulation of the NS equations, there are no cross derivatives in the advection, diffusion, Laplacian, and gradient operators. To begin with, the absence of the cross derivatives results in a significant reduction in the number of terms to be resolved in the transformed NS equations. Further, the absence of the cross derivatives allows us to develop an FFT-based Poisson solver for pressure.

The NS equations for an incompressible flow in conservative form are

$$\nabla \cdot \mathbf{U} = 0, \tag{2.1}$$

$$\frac{\partial \mathbf{U}}{\partial t} + \nabla \cdot (\mathbf{U}\mathbf{U}) = -\frac{1}{\rho}\nabla p + \nu \nabla^2 \mathbf{U}. \tag{2.2}$$

In Cartesian coordinates ($\mathbf{x} = x^i \mathbf{e}_i = (x, y, z)$), $\nabla = \mathbf{e}_x\ \partial/\partial x + \mathbf{e}_y\ \partial/\partial y + \mathbf{e}_z\ \partial/\partial z$ is the gradient operator, $\mathbf{U}(\mathbf{x}, t) = U\mathbf{e}_x + V\mathbf{e}_y + W\mathbf{e}_z$ is the fluid velocity, $p(\mathbf{x}, t)$ is the pressure. ν is the fluid kinematic viscosity, and ρ is the fluid density. It is convenient for our discussion here to define the following:

$$\begin{aligned} (\mathbf{conv}) &\equiv \nabla \cdot (\mathbf{U}\mathbf{U}), \\ (\mathbf{pres}) &\equiv \nabla p, \\ (\mathbf{visc}) &\equiv \nu \nabla^2 \mathbf{U}. \end{aligned} \tag{2.3}$$

We define a generalized curvilinear coordinate frame $\boldsymbol{\xi} = \xi^i \mathbf{g}_i = (\xi, \eta, \zeta)$, which correspond to streamwise, wall-normal and spanwise directions respectively. Consider a point whose Cartesian position vector is $\mathbf{r}$ as shown in Fig. 2.1. A covariant base vector corresponding to the direction ξ^i is given by

$$\mathbf{g}_i = \frac{\partial \mathbf{r}}{\partial \xi^i}. \tag{2.4}$$

The covariant basis vector defined in Eq. (2.4) is tangential to the corresponding coordinate line ξ^i (Hung, 2002). In Fig. 2.1, the fluid velocity $\mathbf{U}$ can be expressed as

$$\mathbf{U} = U^i \mathbf{e}_i = \hat{U}^i \mathbf{g}_i, \tag{2.5}$$

where U^i and $\hat{U}^i$ are the Cartesian and contravariant components of velocity respectively, and are related to each other as

$$U^i = \hat{U}^j \frac{\partial x^i}{\partial \xi^j}, \tag{2.6}$$

and inversely as

$$\hat{U}^i = U^j \frac{\partial \xi^i}{\partial x^j}. \tag{2.7}$$

In the generalized curvilinear coordinate frame, the governing equations (2.1) and (2.2) take the following form (Aris, 1962):

$$\nabla_i \, \hat{U}^i = 0, \tag{2.8}$$

$$\frac{\partial \hat{U}^i}{\partial t} + \nabla_j \hat{U}^i \hat{U}^j = -\frac{1}{\rho} g^{ij} \nabla_j p + \nu g^{jk} \nabla^2_{jk} \hat{U}^i. \tag{2.9}$$

Here, ∇_k is the covariant derivative operator, g^{ij} is the inverse of the metric tensor g_{ij} ($g_{ij} g^{ik} = \delta^k_j$, the Kronecker symbol), and $\hat{U}^i = (\hat{U}, \hat{V}, \hat{W})$ are the contravariant components of the velocity vector in the curvilinear coordinate frame. The covariant derivative operator ∇_k is defined as

$$\nabla_k \hat{U}^j = \frac{\partial \hat{U}^j}{\partial \xi^k} + \mathit{\Gamma}^j_{ik} \hat{U}^i, \tag{2.10}$$

where $\mathit{\Gamma}^i_{jk}$, the Christoffel symbols of second kind are given by

$$\mathit{\Gamma}^i_{jk} = \frac{1}{2} g^{ip} \left[\frac{\partial g_{pj}}{\partial x^k} + \frac{\partial g_{pk}}{\partial x^j} - \frac{\partial g_{jk}}{\partial x^p} \right]. \tag{2.11}$$

The metric tensor, g_{ij} which relates distance to the infinitesimal coordinate increments (Aris, 1962) is defined as

$$g_{ij} = \sum_{k=1}^{3} \frac{\partial x^k}{\partial \xi^i} \frac{\partial x^k}{\partial \xi^j}. \tag{2.12}$$

It is numerically expensive to solve the fully generalized incompressible NS equations in general curvilinear coordinates (Eqs. (2.8) and (2.9)). The eighteen unique Chrisoffel symbols of second kind are computationally expensive to be computed and stored for each grid point (Ge & Sotiropoulos, 2007). Furthermore, as noted by Rosenfeld *et al.* (1991), the discrete form of the Poisson equation for pressure using a second-order central difference scheme depends on nineteen points. Thus, computing fast solutions of the Poisson equation is extremely challenging. However, the fully generalized incompressible NS equations in curvilinear coordinates can be greatly simplified if the axes of the coordinate system satisfy the property of orthogonality.

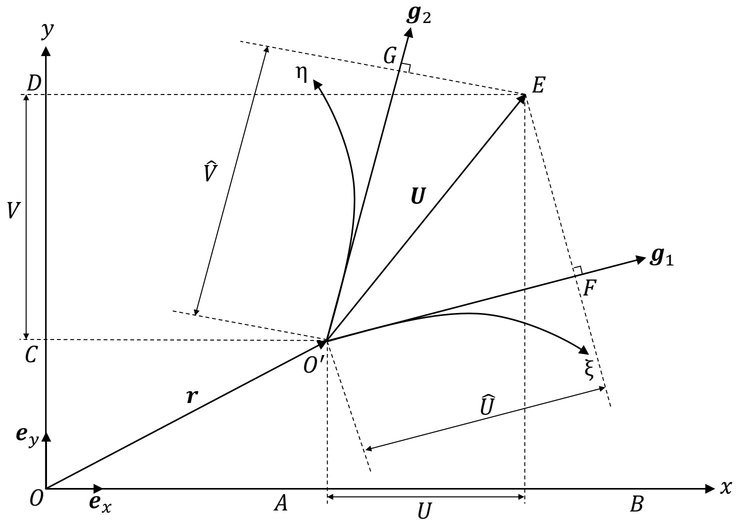

Figure 2.1: Cartesian and curvilinear coordinates. In Cartesian coordinates, the vector $\mathbf{U} = \overrightarrow{AB} + \overrightarrow{CD} = U\mathbf{e_x} + V\mathbf{e_y}$ where $\mathbf{e_x}$ and $\mathbf{e_y}$ are Cartesian basis vectors. In curvilinear coordinates, $\mathbf{U} = \overrightarrow{O'F} + \overrightarrow{O'G} = \hat{U}\mathbf{g_1} + \hat{V}\mathbf{g_2}$, where $\mathbf{g_1}$ and $\mathbf{g_2}$ are covariant basis vectors.

In orthogonal coordinates the off-diagonal terms of the metric tensor are identically zero: $g_{ij} = 0, \forall i \neq j$. This results in the absence of cross derivatives in the advection, diffusion, Laplacian, and gradient operators of the NS equations in orthogonal computational domains. Consequently, the discrete form of the Poisson equation for pressure using a second-order central difference scheme depends on seven points, just as in the Cartesian formulation. This compact stencil allows us to develop an FFT-based Poisson solver, that we call FastPoc (see Sec. 2.3). It is convenient to define scale factors (h_ξ, h_η, h_ζ):

$$\begin{aligned} h_\xi &\equiv \sqrt{g_{11}}, \\ h_\eta &\equiv \sqrt{g_{22}}, \\ h_\zeta &\equiv \sqrt{g_{33}}. \end{aligned} \tag{2.13}$$

The determinant of the metric tensor in orthogonal coordinates is given by:

$$g = g_{11} g_{22} g_{33} = h_\xi^2 h_\eta^2 h_\zeta^2. \tag{2.14}$$

Using the property of orthogonality, the governing equations (Eqs. (2.8) and (2.9)) are simplified to the following:

$$\frac{1}{\sqrt{g}} \left[\frac{\partial}{\partial \xi} \left(\sqrt{g} \hat{U} \right) + \frac{\partial}{\partial \eta} \left(\sqrt{g} \hat{V} \right) + \frac{\partial}{\partial \zeta} \left(\sqrt{g} \hat{W} \right) \right] = 0. \tag{2.15}$$

$$\frac{\partial \hat{U}^i}{\partial t} + (\mathrm{conv})^i = -\frac{1}{\rho} (\mathrm{pres})^i + (\mathrm{visc})^i \tag{2.16}$$

where $(\mathrm{conv})^\xi$, $(\mathrm{pres})^\xi$, and $(\mathrm{visc})^\xi$ denote the ξ^{th} contravariant component of the corresponding vectors in orthogonal coordinates and are given in Eqs. (2.17), (2.18), and (2.20). The convective terms are given by

$$\begin{aligned}
(\mathrm{conv})^{\xi} = {} & \frac{1}{\sqrt{g}h_{\xi}}\left[\frac{\partial}{\partial\xi}\left(\sqrt{g}h_{\xi}\hat{U}^{2}\right)+\frac{\partial}{\partial\eta}\left(\sqrt{g}h_{\xi}\hat{U}\hat{V}\right)+\frac{\partial}{\partial\zeta}\left(\sqrt{g}h_{\xi}\hat{U}\hat{W}\right)\right] \\
& +\frac{\hat{U}\hat{V}}{h_{\xi}}\frac{\partial h_{\xi}}{\partial\eta}+\frac{\hat{U}\hat{W}}{h_{\xi}}\frac{\partial h_{\xi}}{\partial\zeta}-\frac{\hat{V}^{2}h_{\eta}}{h_{\xi}^{2}}\frac{\partial h_{\eta}}{\partial\xi}-\frac{\hat{W}^{2}h_{\zeta}}{h_{\xi}^{2}}\frac{\partial h_{\zeta}}{\partial\xi}, \\
(\mathrm{conv})^{\eta} = {} & \frac{1}{\sqrt{g}h_{\eta}}\left[\frac{\partial}{\partial\xi}\left(\sqrt{g}h_{\eta}\hat{U}\hat{V}\right)+\frac{\partial}{\partial\eta}\left(\sqrt{g}h_{\eta}\hat{V}^{2}\right)+\frac{\partial}{\partial\zeta}\left(\sqrt{g}h_{\eta}\hat{V}\hat{W}\right)\right] \\
& +\frac{\hat{V}\hat{W}}{h_{\eta}}\frac{\partial h_{\eta}}{\partial\zeta}+\frac{\hat{U}\hat{V}}{h_{\eta}}\frac{\partial h_{\eta}}{\partial\xi}-\frac{\hat{W}^{2}h_{\zeta}}{h_{\eta}^{2}}\frac{\partial h_{\zeta}}{\partial\eta}-\frac{\hat{U}^{2}h_{\xi}}{h_{\eta}^{2}}\frac{\partial h_{\xi}}{\partial\eta}, \\
(\mathrm{conv})^{\zeta} = {} & \frac{1}{\sqrt{g}h_{\zeta}}\left[\frac{\partial}{\partial\xi}\left(\sqrt{g}h_{\zeta}\hat{U}\hat{W}\right)+\frac{\partial}{\partial\eta}\left(\sqrt{g}h_{\zeta}\hat{V}\hat{W}\right)+\frac{\partial}{\partial\zeta}\left(\sqrt{g}h_{\zeta}\hat{W}^{2}\right)\right] \\
& +\frac{\hat{W}\hat{U}}{h_{\zeta}}\frac{\partial h_{\zeta}}{\partial\xi}+\frac{\hat{V}\hat{W}}{h_{\zeta}}\frac{\partial h_{\zeta}}{\partial\eta}-\frac{\hat{U}^{2}h_{\xi}}{h_{\zeta}^{2}}\frac{\partial h_{\xi}}{\partial\zeta}-\frac{\hat{V}^{2}h_{\eta}}{h_{\zeta}^{2}}\frac{\partial h_{\eta}}{\partial\zeta}.
\end{aligned} \tag{2.17}$$

The components of the pressure gradient are

$$\begin{aligned}
(\mathrm{pres})^{\xi} &= \frac{1}{h_{\xi}^{2}}\frac{\partial p}{\partial\xi}, \\
(\mathrm{pres})^{\eta} &= \frac{1}{h_{\eta}^{2}}\frac{\partial p}{\partial\eta}, \\
(\mathrm{pres})^{\zeta} &= \frac{1}{h_{\zeta}^{2}}\frac{\partial p}{\partial\zeta}.
\end{aligned} \tag{2.18}$$

The viscous terms are given by taking the Laplacian of velocity which can be expressed as

$$\nabla^{2}\mathbf{U} = \nabla\left(\nabla\cdot\mathbf{U}\right)-\nabla\times\left(\nabla\times\mathbf{U}\right) = -\nabla\times\left(\nabla\times\mathbf{U}\right), \tag{2.19}$$

where we have used the incompressibility condition, $\nabla\cdot\mathbf{U}=0$. The motivation for using this formulation Eq. (2.19), of the viscous terms is discussed in Appendix A. Using Eq. (2.19), the components of the viscous term are

$$
\begin{aligned}
(\mathrm{visc})^{\xi} &= \frac{\nu}{\sqrt{g}}\left\{\frac{\partial}{\partial\zeta}\left[\frac{h_{\eta}}{h_{\xi}h_{\zeta}}\left(\frac{\partial(h_{\xi}^{2}\hat{U})}{\partial\zeta}-\frac{\partial(h_{\zeta}^{2}\hat{W})}{\partial\xi}\right)\right]-\frac{\partial}{\partial\eta}\left[\frac{h_{\zeta}}{h_{\xi}h_{\eta}}\left(\frac{\partial(h_{\eta}^{2}\hat{V})}{\partial\xi}-\frac{\partial(h_{\xi}^{2}\hat{U})}{\partial\eta}\right)\right]\right\},\\
(\mathrm{visc})^{\eta} &= \frac{\nu}{\sqrt{g}}\left\{\frac{\partial}{\partial\xi}\left[\frac{h_{\zeta}}{h_{\xi}h_{\eta}}\left(\frac{\partial(h_{\eta}^{2}\hat{V})}{\partial\xi}-\frac{\partial(h_{\xi}^{2}\hat{U})}{\partial\eta}\right)\right]-\frac{\partial}{\partial\zeta}\left[\frac{h_{\xi}}{h_{\eta}h_{\zeta}}\left(\frac{\partial(h_{\zeta}^{2}\hat{W})}{\partial\eta}-\frac{\partial(h_{\eta}^{2}\hat{V})}{\partial\zeta}\right)\right]\right\},\\
(\mathrm{visc})^{\zeta} &= \frac{\nu}{\sqrt{g}}\left\{\frac{\partial}{\partial\eta}\left[\frac{h_{\xi}}{h_{\eta}h_{\zeta}}\left(\frac{\partial(h_{\zeta}^{2}\hat{W})}{\partial\eta}-\frac{\partial(h_{\eta}^{2}\hat{V})}{\partial\zeta}\right)\right]-\frac{\partial}{\partial\xi}\left[\frac{h_{\eta}}{h_{\zeta}h_{\xi}}\left(\frac{\partial(h_{\xi}^{2}\hat{U})}{\partial\zeta}-\frac{\partial(h_{\zeta}^{2}\hat{W})}{\partial\xi}\right)\right]\right\}.
\end{aligned}
\tag{2.20}
$$

2.2 *Pressure correction method: FastRK3*

The governing equations in orthogonal formulation, Eqs. (2.16) and (2.15), are discretized in space on a staggered Cartesian unigrid ($\varDelta\xi = \varDelta\eta = \varDelta\zeta = 1$) of the computational domain (see Fig. 12.2 of (Fletcher, 1988)), using second-order central difference scheme Harlow & Welch (1965):

$$
\begin{aligned}
DU + b(t) &= 0,\\
\frac{dU}{dt} &= F(U) - Gp,
\end{aligned}
\tag{2.21}
$$

where, $U(t)$ and $p(t)$ are the arrays of the discretized three-dimensional contravariant components of velocity and pressure, respectively, D is the discretized divergence operator, $b(t)$ is a smooth function that accounts for unsteady boundary conditions, F is the combined array of discretized terms of convection $C = C(U)$ and diffusion VU of momentum, where $C(U)$ is the discrete form of $\nabla \cdot \mathbf{uu}$ and VU is the discrete form of $\mathrm{Re}^{-1}\nabla^2\mathbf{u}$,

$$
F(U) = C(U) + VU, \tag{2.22}
$$

and G is the discretized gradient operator. It should be noted that C and by extension F are non-linear functions of U, i.e., $F(U)$ and $C(U)$, whereas V is a linear operator ($\mathrm{Re}^{-1}\nabla^2$) applied to U, i.e., VU. Note that independently of the formulation of the incompressible NS equations used (e.g., written in Cartesian, orthogonal or generalized coordinates) and independently from the spatial discretization used (e.g., finite difference and finite volume), the numerical method, FastRK3, to integrate Eq. (2.21) in time, remains the same. In the interest of minimizing computational costs, we use an explicit scheme to integrate the governing equations in time. The stability regions of three explicit schemes: second-order Adams-Bashforth (AB2), second-order Runge-Kutta (RK2), and third-order Runge-Kutta (RK3) are shown in Fig. 2.2. From numerical tests of the Stokes' first problem (Warsi, 1993), we observed that the second-order Adams-Bashforth scheme exhibits loss of accuracy and the resulting solution of velocity is only first-order accurate in time. Also, second-order explicit schemes are unconditionally unstable for pure convection systems when spatial discretization is performed using the second-order central difference scheme. The stability regions of the second-order schemes, AB2 and RK2 shown in Fig. 2.2, do not include any segment of the imaginary axis (Hirsch, 1990). As noted by Le & Moin (1991) (LM), the stability of such schemes depends on the viscous term and the Reynolds number. In contrast, the RK3 scheme is conditionally stable for pure convection since the stability region intersects the imaginary axis at $\mathrm{Im}(\lambda \Delta t) = \pm\sqrt{3}$ as shown in Fig. 2.2. Further, the RK3 scheme has a higher stability limit for pure diffusion since the point of intersection of its stability region with the real axis lies to the left of the other two schemes. Therefore, we propose and use a three-stage RK3 scheme for time integration in this work. Runge-Kutta schemes usually require the solution to the Poisson equation for pressure at each stage (Sanderse & Koren, 2012). The LM method (Le & Moin, 1991) is a semi-implicit, three-stage Runge-Kutta based method, in which the Poisson equation for pressure is solved only at the final stage, and which is claimed to be second-order accurate in time for velocity. We start from the idea of the LM method (Le & Moin, 1991) of solving the Poisson equation for pressure only once per time step to develop an *explicit*, *third-order* accurate in time, Runge-Kutta based pressure-correction method.

For an explicit RK3 scheme, the Butcher tableau (Butcher, 2016) is given by

$$\begin{array}{c|ccc} 0 & 0 & & \\ c_2 & a_{21} & 0 & \\ c_3 & a_{31} & a_{32} & 0 \\ \hline & b_1 & b_2 & b_3 \end{array} \tag{2.23}$$

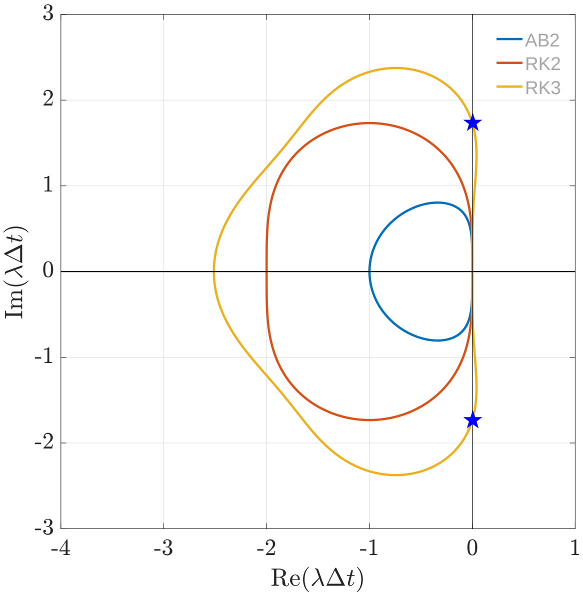

Figure 2.2: Stability regions for the explicit schemes: second-order Adams-Bashforth (AB2), second-order Runge-Kutta (RK2), and third-order Runge-Kutta (RK3)

Note that $i = 1, 2, 3$ corresponds to the three stages of the RK3 scheme where the numerical solution is advanced in time from t_n to t_{n+1} with the time of each i-stage as $t_i = t_n + \check{c}_i \mathit{\Delta} t$, where $\mathit{\Delta} t = t_{n+1} - t_n$. We define a shifted coefficient matrix $\check{\mathbf{a}}$ and a shifted vector $\check{\mathbf{c}}$ similarly to SK (Sanderse & Koren, 2012):

$$\check{\mathbf{a}} = \begin{bmatrix} a_{21} & 0 & 0 \\ a_{31} & a_{32} & 0 \\ b_1 & b_2 & b_3 \end{bmatrix}; \qquad \check{\mathbf{c}} = \begin{bmatrix} c_2 \\ c_3 \\ 1 \end{bmatrix}. \tag{2.24}$$

For the pressure-correction method (Harlow & Welch, 1965), the solution algorithm begins with the computation of the approximate velocity field U^*, which is not divergence free. U_n and U_{n+1} denote the divergence-free velocity fields at t_n and t_{n+1}, respectively. At each stage i of the RK3 scheme, U_i^* denotes the approximate velocity field, U_i the divergence-free velocity field, and ϕ_i the pressure-like scalar field. Sanderse & Koren (2012) note that ϕ is a first-order approximation of the pressure p, therefore, ϕ_i is a second-order approximation of the pressure p at $t_n + \check{c}_i \Delta t/2$:

$$\phi_i = p\left(t_n + \frac{\check{c}_i \Delta t}{2}\right) + \mathcal{O}\left(\Delta t^2\right). \tag{2.25}$$

Standard RK3 $\tilde{U}_i$, $\tilde{U}_i^*$, $\tilde{F}_i$ and $\tilde{\phi}_i$ are the arrays of discretized velocity fields, approximate velocity fields, flux terms and the pressure-like scalar fields, respectively, computed using the standard RK3 scheme of SK (Sanderse & Koren, 2012) for which the governing equations (2.21) are integrated in time as

$$\tilde{U}_i^* = \tilde{U}_n + \Delta t \sum_{j=1}^{i} \check{a}_{ij} \tilde{F}(\tilde{U}_{j-1}) \quad \text{for } i = 1, 2, 3, \tag{2.26}$$

where i denotes the stage of RK3, and

$$U_0 \equiv U_n; \quad U_0^* \equiv U_n; \quad c_0 \equiv 0; \quad U_3 \equiv U_{n+1}; \quad U_3^* \equiv U_{n+1}^*. \tag{2.27}$$

The approximate velocity fields are then projected onto a divergence free space to satisfy Eq. (2.21), by applying the pressure-correction as

$$\tilde{U}_i = \tilde{U}_i^* - \check{c}_i \Delta t \frac{G\tilde{\phi}_i}{\rho} \qquad \text{for} \;\; i = 1, 2, 3, \tag{2.28}$$

where $\tilde{\phi}_i$ is obtained by solving the following Poisson equation:

$$DG\tilde{\phi}_i = \frac{\rho}{\check{c}_i \Delta t}\left(D\tilde{U}_i^* + b_i\right) \quad \text{for } i = 1, 2, 3, \tag{2.29}$$

and, thus, three times per time step.

FastRK3 In FastRK3, in order to solve the Poisson equation for ϕ only once per time step in FastRK3, instead of three times as in standard RK3, we compute ϕ_1 and ϕ_2 by performing a linear extrapolation of ϕ in time, using the known values of $\phi_{n-\beta}$ and $\phi_{n-1-\beta}$ which have been obtained as Poisson solutions of Eq. (2.34), as

$$\phi_1 = \left(1 + \beta + \check{c}_1 \alpha\right) \phi_{n-\beta} - \left(\beta + \check{c}_1 \alpha\right) \phi_{n-1-\beta}, \tag{2.30}$$

$$\phi_2 = \left(1 + \beta + \check{c}_2 \alpha\right) \phi_{n-\beta} - \left(\beta + \check{c}_2 \alpha\right) \phi_{n-1-\beta}, \tag{2.31}$$

where, the extrapolated ϕ_i in the intermediate RK stages for $i = 1, 2$ are located at time instants $t = t_n + \check{c}_i\alpha\mathit{\Delta}t$ and $\phi_{n-\beta}$ and $\phi_{n-1-\beta}$, solutions of the Poisson equation, are thought as computed at $t_{n-\beta} = t_n - \beta\mathit{\Delta}t$ and $t_{n-1-\beta} = t_{n-1} - \beta\mathit{\Delta}t$, respectively (De Michele *et al.*, 2020) as shown in Fig. 2.3.

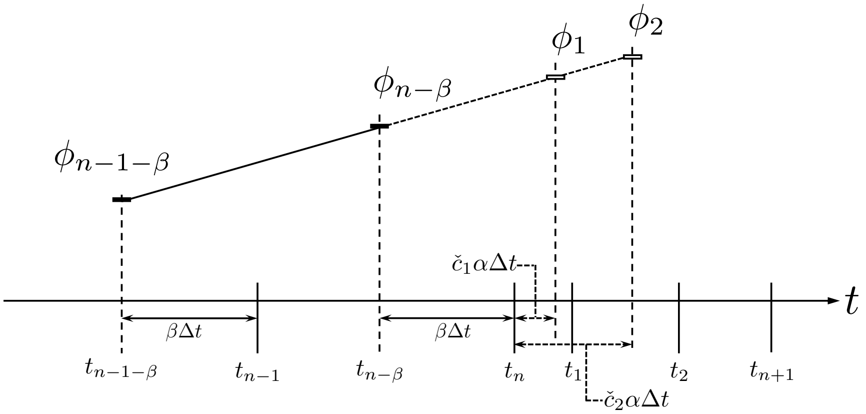

Figure 2.3: Schematic of the general $\alpha - \beta$ linear extrapolation for ϕ.

After extrapolating ϕ_1 and ϕ_2 using Eqs. (2.30) and (2.31), we compute the approximate velocity field U_i^* as

$$U_i^* = U_n + \mathit{\Delta}t \sum_{j=1}^{i} \breve{a}_{ij} F\left(U_{j-1}^* - \check{c}_{j-1}\mathit{\Delta}t\frac{G\phi_{j-1}}{\rho}\right) \qquad \text{for} \quad i = 1, 2, 3. \tag{2.32}$$

Finally, the divergence-free velocity field at t_{n+1} is obtained by applying the pressure-correction at the final stage (set $i = 3$ in Eq. (2.28)), as

$$U_{n+1} = U_{n+1}^* - \mathit{\Delta}t\frac{G\phi_{n+1-\beta}}{\rho}, \tag{2.33}$$

where $\phi_{n+1-\beta}$ is obtained by solving the Poisson equation,

$$DG\phi_{n+1-\beta} = \frac{\rho}{\mathit{\Delta}t}\left(DU_{n+1}^* + b_{n+1}\right), \tag{2.34}$$

which is obtained by taking the divergence of Eq. (2.33) and imposing the divergence-free condition for U_{n+1}.

For the Runge-Kutta time integration scheme, we use the coefficients for a three-stage, third-order explicit Runge-Kutta as described by SK (Sanderse & Koren, 2012):

$$\check{\mathbf{a}} = \begin{bmatrix} \frac{1}{3} & 0 & 0 \\ -1 & 2 & 0 \\ 0 & \frac{3}{4} & \frac{1}{4} \end{bmatrix}; \qquad \check{\mathbf{c}} = \begin{bmatrix} \frac{1}{3} \\ 1 \\ 1 \end{bmatrix}. \tag{2.35}$$

The pressure field p_{n+1} can then be computed using the update equation of SK (see Eq. (67) of Sanderse & Koren (2012)), as

$$p_{n+1} = -\frac{3}{2}\left\{\left[2 + 2\beta + \alpha\left(\check{c}_1 + \check{c}_2\right)\right]\phi_{n-\beta} - \left[2\beta + \alpha\left(\check{c}_1 + \check{c}_2\right)\right\}\phi_{n-1-\beta}\right] + 4\phi_{n+1-\beta}. \tag{2.36}$$

SK (Sanderse & Koren, 2012) note that the pressure field p_{n+1} is at best second-order accurate.

In summary, our new pressure-correction algorithm advances the numerical solution of the velocity field in time by integrating Eq. (2.21) with the following steps using Eqs. (2.32)-(2.34):

1. At the first stage ($i = 1$) of FastRK3, compute $F(U_n)$, and then compute U_1^* using Eq. (2.32),

2. For the second stage ($i = 2$) of FastRK3, compute $G\phi_1$ using Eq. (2.30) and $F(U_1^* - \check{c}_1 \Delta t G\phi_1)$, and then compute U_2^* using Eq. (2.32),

3. At the third stage ($i = 3$) of FastRK3, compute $G\phi_2$ using Eq. (2.31) and $F(U_2^* - \check{c}_2 \Delta t G\phi_2)$, and then compute $U_{n+1}^* = U_3^*$ using Eq. (2.32),

4. Compute $\phi_{n+1-\beta}$ by solving the Poisson equation (2.34) using U_{n+1}^* and a Poisson solver, e.g., the FastPoc method described by Aithal & Ferrante (2020) and in Sec. 2.3,

5. Compute U_{n+1} using Eq. (2.33), and, if the pressure is desired for post-processing, compute p_{n+1} using Eq. (2.36).

In order to perform the computations in parallel, the computational domain is decomposed such that the data is distributed in memory in the η-direction and contiguous in memory among computing cores in ξ- and ζ-directions. Also, we have implemented the numerical algorithms described in this section using Fortran 90, the message passing interface (MPI), FFTW (Frigo & Johnson, 2005), METIS (Karypis & Kumar, 2009), and HSL ME57 serial, direct linear-solver (HSL, 2013) for the parallel FFT-based Poisson solver, FastPoc described in Sec. 2.3.

2.2.1 Comparison of FastRK3 with LM and SK methods

The LM (Le & Moin, 1991), SK (Sanderse & Koren, 2012) and FastRK3 methods are schematically represented in Fig. 2.4. The schematic diagrams are analogous to Fig. 1 of Le & Moin (1991), where vertical lines correspond to the projection step which requires solving the Poisson equation for pressure. The typical implementations of RK3-based pressure-correction methods involve solving the Poisson equation thrice at every time step as indicated by the three solid vertical lines in figures 2.4a and 2.4b. The LM and FastRK3 schemes (dotted lines), on the other hand, require solution to the Poisson equation only once per time step at the last stage of RK3 ($i = 3$). In contrast with the LM method, however, we use the SK coefficients. A detailed comparison of the LM and FastRK3 algorithms are given in Appendix B. Further, we use linear extrapolation for pressure in time (Eqs. (2.30) and (2.31)) whereas LM method makes use of the constant extrapolation. Furthermore, LM method is semi-implicit, while FastRK3 is *explicit*. As a consequence, the time step $\mathit{\Delta} t$ has to be restricted by the convective and viscous limits to ensure numerical stability of FastRK3. The time step $\mathit{\Delta} t$ is given by

$$\mathit{\Delta} t \leq \min\left(\sqrt{3}\mathit{\Delta} t_c, \mathit{\Delta} t_\nu\right), \tag{2.37}$$

where,

$$\mathit{\Delta} t_c = \min\left(\frac{1}{\hat{U}}, \frac{1}{\hat{V}}, \frac{1}{\hat{W}}\right), \tag{2.38}$$

$$\mathit{\Delta} t_\nu = \frac{5\mathit{\Delta}_{\min}^2}{8\nu}, \tag{2.39}$$

and $\mathit{\Delta}_{\min}$ is the minimum spatial grid size and non-dimensional variables are used. It should be noted that convective time limit $\mathit{\Delta} t_c$ implicitly depends on the grid resolution via the contravariant velocity components $\left(\hat{U}, \hat{V}, \hat{W}\right)$ (see Eq. (2.7)). The present scheme is developed with the purpose of computing the solution of wall-bounded turbulent flows (i.e., high Re). The stability restriction imposed by the convective limit is more stringent than that imposed by the viscous limit, i.e., $\mathit{\Delta} t_c < \mathit{\Delta} t_\nu$ for those wall-bounded turbulent flows for which the following condition is satisfied:

$$\sqrt{3}\mathit{\Delta} x < \frac{5\mathit{\Delta}_{\min}^2}{8\nu}, \tag{2.40}$$

where, for simplicity, we have assumed uniform grid spacing in the streamwise direction, $\mathit{\Delta} x$. Note that $\mathit{\Delta} x$ and $\mathit{\Delta}_{\min}$ in terms of wall units, $\mathit{\Delta} x^+$ and $\mathit{\Delta}_{\min}^+$, are given by

$$\mathit{\Delta} x = \frac{\nu \mathit{\Delta} x^+}{u_\tau}; \;\; \mathit{\Delta}_{\min} = \frac{\nu \mathit{\Delta}_{\min}^+}{u_\tau}. \tag{2.41}$$

Substituting Eq. (2.41) in Eq. (2.40) gives the upper bound of friction velocity, u_τ:

$$u_\tau < \frac{5}{8\sqrt{3}} \frac{\left(\mathit{\Delta}_{\min}^+\right)^2}{\mathit{\Delta} x^+}, \tag{2.42}$$

which can be evaluated using the recommended guidelines for grid spacing to resolve the turbulence scales. Using FastRK3 vs LM has the advantage of reducing the computational time for being explicit vs semi-implicit without reducing the time-stepping.

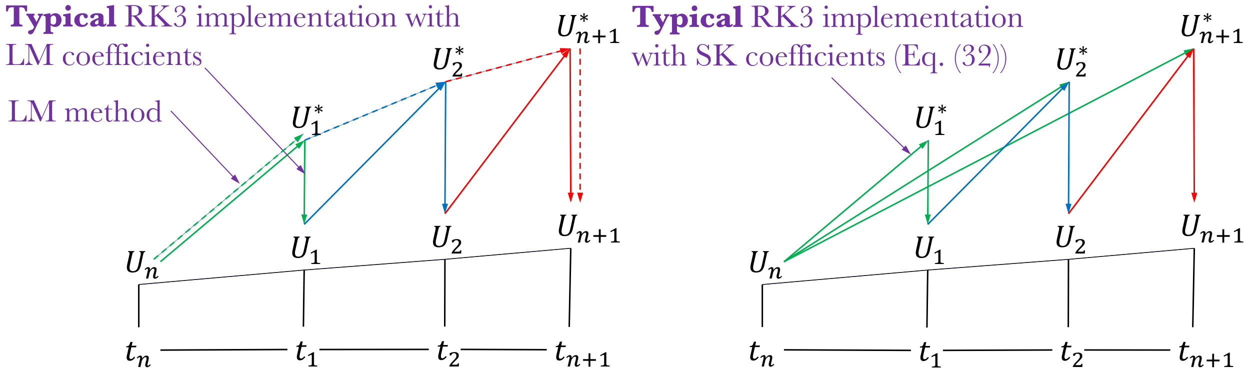

(a) LM method (Le & Moin, 1991)

(b) SK method (Sanderse & Koren, 2012)

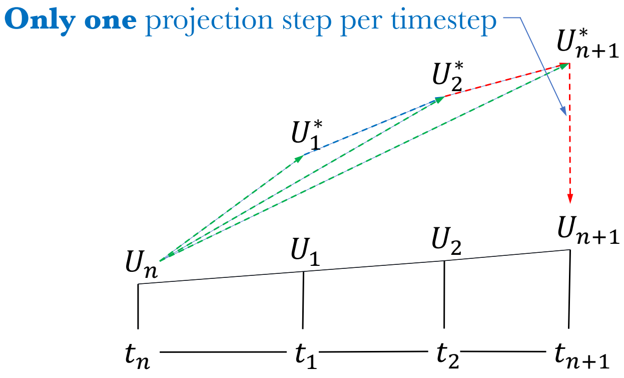

(c) Present method, FastRK3

Figure 2.4: Schematic diagrams of RK3 based pressure-correction methods: solid line, typical implementations with three projection steps per time step; dashed line, modified methods with one projection step per time step

2.3 FastPoc: a parallel fast Poisson solver for orthogonal curvilinear coordinates

Solution of the governing equations (2.15) and (2.16) with the projection-method described in Sec. 2.2 requires the numerical solution of the Poisson equation for pressure (2.34). By expanding Eq. (2.34) in the orthogonal curvilinear coordinates, we obtain:

$$\begin{aligned}&\frac{1}{\sqrt{g}}\left[\frac{\delta}{\delta\xi}\left(\frac{h_\eta h_\zeta}{h_\xi}\frac{\delta\phi_{n+1-\beta}}{\delta\xi}\right)+\frac{\delta}{\delta\eta}\left(\frac{h_\zeta h_\xi}{h_\eta}\frac{\delta\phi_{n+1-\beta}}{\delta\eta}\right)+\frac{\delta}{\delta\zeta}\left(\frac{h_\xi h_\eta}{h_\zeta}\frac{\delta\phi_{n+1-\beta}}{\delta\zeta}\right)\right]=\\&\qquad\frac{\rho}{\Delta t}\frac{1}{\sqrt{g}}\left[\frac{\delta}{\delta\xi}\left(\sqrt{g}\hat{U}^*_{\xi\,n+1}\right)+\frac{\delta}{\delta\eta}\left(\sqrt{g}\hat{U}^*_{\eta\,n+1}\right)+\frac{\delta}{\delta\zeta}\left(\sqrt{g}\hat{U}^*_{\zeta\,n+1}\right)\right],\end{aligned}\tag{2.43}$$

which upon dropping $1/\sqrt{g}$ from the two sides of the equation, takes the following form:

$$\frac{\delta}{\delta\xi}\left(\alpha\frac{\delta\phi_{n+1-\beta}}{\delta\xi}\right)+\frac{\delta}{\delta\eta}\left(\beta\frac{\delta\phi_{n+1-\beta}}{\delta\eta}\right)+\frac{\delta}{\delta\zeta}\left(\gamma\frac{\delta\phi_{n+1-\beta}}{\delta\zeta}\right)=\frac{\rho}{\Delta t}Q,\tag{2.44}$$

where

$$\alpha=\frac{h_\eta h_\zeta}{h_\xi};\quad \beta=\frac{h_\zeta h_\xi}{h_\eta};\quad \gamma=\frac{h_\xi h_\eta}{h_\zeta},\tag{2.45}$$

$$Q=\frac{\delta}{\delta\xi}\left(\sqrt{g}\hat{U}^*_{\xi\,n+1}\right)+\frac{\delta}{\delta\eta}\left(\sqrt{g}\hat{U}^*_{\eta\,n+1}\right)+\frac{\delta}{\delta\zeta}\left(\sqrt{g}\hat{U}^*_{\zeta\,n+1}\right).\tag{2.46}$$

For the flows over curved surfaces here considered, such as: surfaces of linear translation (e.g., curved ramps, Fig. D.2a, and bumps, Fig. D.2b) and surfaces of revolution (e.g., axisymmetric ramps, Fig. D.2c), the computational domain does not present variations in the azimuthal ζ direction, thus the coefficients α, β, and γ of Eq. (2.44) are independent of ζ, i.e.,

$$\begin{aligned}\alpha&=\alpha(\xi,\eta),\\ \beta&=\beta(\xi,\eta),\\ \gamma&=\gamma(\xi,\eta).\end{aligned}\tag{2.47}$$

The Poisson equation for pressure Eq. (2.44) can then be expressed as

$$\frac{\delta}{\delta\xi}\left(\alpha\frac{\delta\phi_{n+1-\beta}}{\delta\xi}\right)+\frac{\delta}{\delta\eta}\left(\beta\frac{\delta\phi_{n+1-\beta}}{\delta\eta}\right)+\gamma\frac{\delta^2\phi_{n+1-\beta}}{\delta\zeta^2}=\frac{\rho}{\Delta t}Q.\tag{2.48}$$

Eq. (2.48) is a variable-coefficient Poisson equation. Variable coefficient Poisson equations for pressure are typically solved using multigrid methods but these are computationally more expensive than direct FFT-based methods (e.g., Dodd & Ferrante (2014)). Thus, we have developed a direct FFT-based Poisson solver called FastPoc to solve Eq. (2.48).

Using the second-order central difference scheme and omitting the explicit indication of the time level $(n+1)$ of p, Eq. (2.48) is written in discretized form as

$$\begin{aligned}&\frac{1}{\varDelta\xi^2}\left[\alpha_{i+\frac{1}{2},j}(\phi_{i+1,j,k}-\phi_{i,j,k})-\alpha_{i-\frac{1}{2},j}(\phi_{i,j,k}-\phi_{i-1,j,k})\right]+\\&\frac{1}{\varDelta\eta^2}\left[\beta_{i,j+\frac{1}{2}}(\phi_{i,j+1,k}-\phi_{i,j,k})-\beta_{i,j-\frac{1}{2}}(\phi_{i,j,k}-\phi_{i,j-1,k})\right]+\\&\qquad\qquad\frac{\gamma_{i,j}}{\varDelta\zeta^2}\left[\phi_{i,j,k+1}+\phi_{i,j,k-1}-2\phi_{i,j,k}\right]=\frac{\rho}{\varDelta t}Q_{i,j,k},\end{aligned} \tag{2.49}$$

where α, β, and γ depend on i, j (indices for ξ and η) and do not depend on k (index for ζ) in accordance with Eq. (2.47). Consequently, we can perform real-to-complex FFT along the ζ-direction to reduce the three-dimensional system of linear equations to two-dimensional systems of linear equations whose coefficient matrices, A_m, are sparse, symmetric, and negative definite as follows:

$$\begin{aligned}&\bar{\phi}_m(i+1,j)\frac{\alpha_{i+\frac{1}{2}j}}{\varDelta\xi^2}+\bar{\phi}_m(i-1,j)\frac{\alpha_{i-\frac{1}{2}j}}{\varDelta\xi^2}+\bar{\phi}_m(i,j+1)\frac{\beta_{ij+\frac{1}{2}}}{\varDelta\eta^2}+\bar{p}_m(i,j-1)\frac{\beta_{ij-\frac{1}{2}}}{\varDelta\eta^2}\\&-\bar{\phi}_m(i,j)\left[\alpha_{i+\frac{1}{2}j}+\alpha_{i-\frac{1}{2}j}+\beta_{ij+\frac{1}{2}}+\beta_{ij-\frac{1}{2}}+\frac{2\gamma_{ij}}{\varDelta\zeta^2}\left(1-\cos\left[\frac{2\pi m}{N_\zeta}\right]\right)\right]=\frac{\rho}{\varDelta t}\bar{Q}_m(i,j),\end{aligned} \tag{2.50}$$

which can be expressed in matrix notation as

$$\mathrm{A}_m\overline{\phi}_m=\overline{b}_m, \tag{2.51}$$

for $m=0,\dots,N_\zeta-1$, and where the overbar denotes the Fourier modes of the variable (real-complex FFT) such that

$$\phi_{i,j,k}=\sum_{m=0}^{N_\zeta-1}\bar{p}_m(i,j)\;\omega_{N_\zeta}^{mk};\quad \omega_{N_\zeta}=\exp\left(\frac{2\pi\sqrt{-1}}{N_\zeta}\right). \tag{2.52}$$

We take advantage of the Hermitian symmetry of the Fourier modes and solve for only the non-redundant $N_\zeta/2+1$ planes: $m=0,\dots,N_\zeta/2$. The three-dimensional complex-valued data is then transposed such that it is distributed in the ζ-direction and contiguous in the η-direction. We have developed a 3D transpose algorithm, similarly to the all-to-all zero-copy method of Hoefler & Gottileb (Hoefler & Gottlieb, 2010) to perform such required

3D transpose of data among processors. The resulting two-dimensional systems of linear equations, Eq. (2.50), are then solved using the HSL ME57 direct, serial, linear-solver (HSL, 2013) which uses the $\mathrm{LDL^T}$ decomposition implemented using a multifrontal approach. The method consists of factorization of the coefficient matrix A_m into $\mathrm{L}_m\mathrm{D}_m\mathrm{L}_m^{\mathrm{T}}$ factors, where L_m are lower triangular matrices and D_m are diagonal matrices. The unknowns $\overline{\phi}_m$ are then obtained by performing forward substitutions $\mathrm{L}_m\mathrm{D}_m\overline{z}_m = \overline{b}_m$ and finally backward substitutions $\mathrm{L}_m^T\overline{\phi}_m = \overline{z}_m$. We use the fill-in reducing nested-dissection ordering (George, 1973; LeVeque, 2007) produced by METIS (Karypis & Kumar, 2009) for the sparse coefficient matrices to reduce the storage and computational costs of matrix factorization. Since the computational grid does not change during our simulations, we only need to perform the factorization of the coefficient matrix once during the initialization stage of the algorithm. Subsequently, we have to perform one serial forward and backward substitution each for every Fourier mode m at every time step to solve Eq. (2.50). The algorithm to solve for pressure, $\phi_{n+1-\beta}$ in parallel is here summarized.

1. Perform real-to-complex FFT along the ζ-direction of the right-hand side of Eq. (2.48),

2. Transpose the three-dimensional complex-valued data from being distributed in the η-direction such that the resulting data is distributed in the ζ-direction (and contiguous in the η-direction) since we need to solve the resulting $N_\zeta/2+1$ independent two-dimensional systems of linear equations, Eq. (2.50), for $m = 0, \ldots, N_\zeta/2$,

3. Solve the local (to the computing core) two-dimensional systems of linear equations for $m = 0, \ldots, N_\zeta/2$ using the HSL ME57 linear-solver (HSL, 2013) by performing one serial forward and backward substitution each for every Fourier mode m,

4. Transpose back the three-dimensional complex-valued data from being distributed in the ζ-direction to being distributed in the η-direction (and contiguous in the ζ-direction),

5. Perform complex-to-real inverse FFT of the resulting data along the ζ-direction to obtain $\phi_{n+1-\beta}$.

2.3.1 Comparison of FastPoc with multigrid methods

We compare the computational performance of the new direct Poisson solver FastPoc with *hypre* semi-coarsening multigrid (SMG) (Falgout *et al.*, 2006) for solving the variable coefficient Poisson equation, Eq. (2.49), to compute p. We chose the *hypre* SMG solver because in our computational tests it outperformed the other solvers included in the *hypre* library. Further, the *hypre* SMG has been shown to scale up to 100,000 cores Baker *et al.* (2012) and was also used to benchmark the performance of an FFT-based fast Poisson solver in Dodd & Ferrante (2014). We recognize that there are several multigrid methods and the present comparison is limited to *hypre* SMG.

For our test cases, we simulated the laminar flow over a curved ramp (Fig. D.2a) for which we prescribed a Blasius velocity profile Blasius (1908) at the inlet. Similarly to Dodd & Ferrante (2014), for the multigrid solution we used the previous p field (p_n) as an initial guess of the solution p_{n+1} to minimize the number of multigrid iterations. Table 2.1 shows the number of grid points, N_ξ, N_η, and N_ζ in the streamwise, wall-normal, and spanwise directions respectively, and the grid stretching parameter γ as defined in Ferrante & Elghobashi (2004) for three test cases A-C. In order to assess the suitability of these grids to study turbulent wall-bounded flows, we have also listed the distance of the closest grid point to the wall $\eta^+_{\min}$ in terms of wall units calculated at the used values of Re_{δ_0} also listed in Table 2.1. Cases B and C possess adequate grid resolutions required to perform direct numerical simulations of spatially developing wall-bounded turbulent flows. The simulations were performed on a supercomputer using Intel Xeon E5-2680v3 processors. We performed strong scaling analysis of the two Poisson solvers for cases A and B by keeping the problem size fixed and increasing the number of cores from 32 to 256. The *hypre* SMG solver required four iterations to converge to the tolerance of 10^{-6} for all core counts. Fig. 2.5 shows the average time taken by the two Poisson solvers to solve the discretized Poisson equation, Eq. (2.49), for cases A and B. We observed that the performance of the *hypre* SMG depends on the degree of grid compression near the wall, determined by the grid stretching parameter γ. For example, when we used 256 cores (16 nodes, 16 cores per node), case B required about 13% more time than case A to converge to the tolerance of 10^{-6}.

FastPoc, being a direct solver, ensures that the velocity field is divergence-free to machine precision at each time step and at every grid point (viz., the maximum velocity divergence, $|DU_{n+1}|_{\max}$, of $O(10^{-14})$ or smaller). The multigrid solver, in contrast, requires lowering its tolerance to achieve higher precision. However, we found that the *hypre* SMG solver was unable to converge to the tolerance of 10^{-14} in $O(10)$ iterations, therefore we restricted the tolerance for the multigrid convergence to 10^{-12}. Table 2.2 shows the wall clock time and the speedup of FastPoc and FastRK3 with respect to the multigrid solver for tolerances of 10^{-6} and 10^{-12} for case B: for $|DU_{n+1}|_{\max}$ of $O(10^{-6})$ or smaller, FastPoc is about thirty times faster than the multigrid solver and when the tolerance was reduced to $|DU_{n+1}|_{\max} < 10^{-12}$, the speedup increases to sixty. This is because the *hypre* SMG solver requires twelve iterations to converge to the tolerance of 10^{-12}. Likewise, FastRK3 is about four times faster than the multigrid based NS solver for $|DU_{n+1}|_{\max} < 10^{-6}$ and about seven times faster when the tolerance was reduced to $|DU_{n+1}|_{\max} < 10^{-12}$. Table 2.2 also shows that the solution to the Poisson equation requires more than 76% of the total solution time in the case of the multigrid based NS solver, while FastPoc takes about 10% of the total solution time of FastRK3.

Finally, Table 2.3 shows the total memory required by FastRK3 and the multigrid based NS solver. For case B when 256 cores (16 nodes, 16 cores per node) were used, FastRK3 and the multigrid solvers require about 342 GB and 336 GB of total memory, respectively. For case C, the total memory requirement of FastRK3 was 2651 GB, when 512 cores (32 nodes, 16 cores per node) were used. In contrast, the multigrid solver was unable to initialize for case C as the memory requirement exceeded the memory limit of 4096 GB using 512 cores (32 nodes, 16 cores per node). Table 2.4 shows the wall clock time per time step for FastPoc and FastRK3 for case C using 512 computing cores (32 nodes, 16 cores per node).

	N_ξ	N_η	N_ζ	γ	Re_{δ_0}	$\eta^+_{\min}$
Case A	1024	256	512	0.33	19,000	3.79
Case B	1024	256	512	0.66	19,000	0.28
Case C	2048	512	1024	0.66	38,000	0.26

Table 2.1: Number of grid points, N_ξ, N_η, and N_ζ, in the streamwise, wall-normal, and spanwise directions respectively, the grid stretching parameter γ (Ferrante & Elghobashi, 2004), the location of the closest grid point to the wall in wall units $\eta^+_{\min}$ for the two Reynolds numbers Re_{δ_0}, where δ_0 is the inflow boundary-layer thickness.

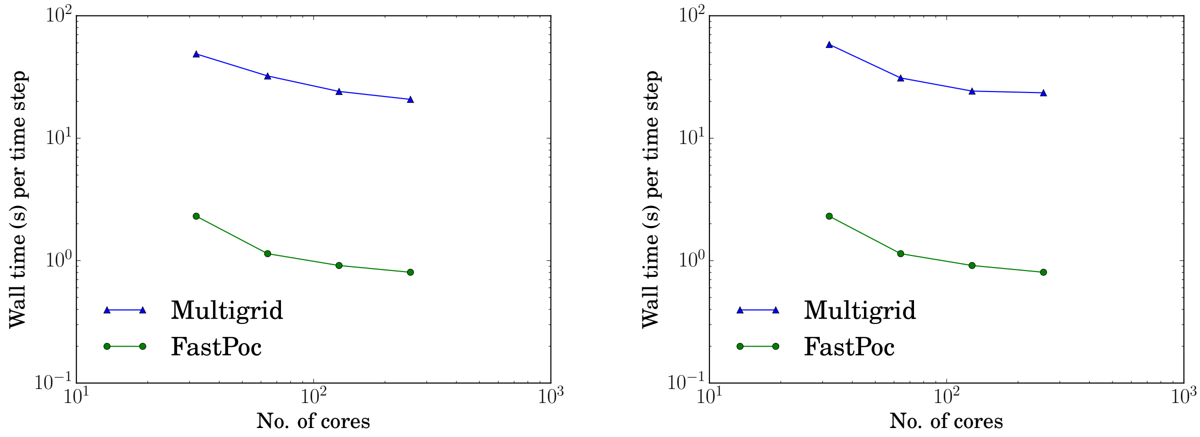

(a) Case A: $\gamma = 0.33$

(b) Case B: $\gamma = 0.66$

Figure 2.5: Strong scaling of multigrid solver and FastPoc on Intel Xeon E5-2680v3 (cases A and B)

SMG tolerance	Poisson solver			FastRK3 NS solver		
	SMG (s)	FastPoc (s)	Speedup	With SMG (s)	With FastPoc (s)	Speedup
$\lvert DU_{n+1}\rvert_{\max} < 10^{-6}$	23.48	0.80	29.35	30.59	7.93	3.86
$\lvert DU_{n+1}\rvert_{\max} < 10^{-12}$	48.02	0.80	60.03	55.11	7.93	6.95

Table 2.2: Wall clock time per time step (s) and speedup factor for the solution of the Poisson equation (middle column) and the NS equations (right column) on a 1024 × 512 × 256 grid (case B) using 256 computing cores (16 nodes, 16 cores per node) using Intel Xeon E5-2680v3.

	Case B	Case C
FastRK3 with multigrid	336 GB	Insufficient node memory
FastRK3 with FastPoc	342 GB	2651 GB

Table 2.3: Total memory requirement for cases B (using 256 cores, 16 nodes) and C (using 512 cores, 32 nodes) of FastRK3 and multigrid based solver

	FastPoc (s)	FastRK3 (s)
Case C	3.44	31.7

Table 2.4: Wall clock time per time step (s) for the solution of the Poisson equation (middle column) and the NS equations (right column) on a $2048 \times 1024 \times 512$ grid using 512 computing cores (32 nodes, 16 cores per node) on Intel Xeon E5-2680v3 (case C).

2.4 *Temporal accuracy of FastRK3*

Table 2.5 provides a summary of the RK-based projection methods in chronological order, and their order of temporal accuracy for free-shear and wall-bounded flows. The temporal accuracy of RK-based projection methods for which the Poisson solver for pressure is not solved for each stage of the RK integration method, similarly to FastRK3, depends on the accuracy of the extrapolation of the pressure-like scalar field ϕ at the intermediate stages of RK time integration. Le & Moin (1991) (LM) proposed a zeroth-order, i.e., constant extrapolation of ϕ while solving the Poisson equation for pressure only once per time step at the final stage of RK3. Capuano *et al.* (2016) proved numerically that the constant extrapolation of ϕ in combination with an explicit RK3 method, using the RK coefficients of Griffiths & Higham (2010), achieves second-order temporal accuracy for velocity of the Taylor-Green vortex flow. Sanderse & Koren (2012) noted that the pressure-like scalar field ϕ is a first-order approximation of the pressure p and is, thus, a second-order approximation at the midpoint of the stencil. Capuano *et al.* (2016) showed numerically, for a free-shear flow, that the temporal convergence rate of the underlying RK3 method can be recovered by using the midpoint rule while performing the linear extrapolation of ϕ. Recently, De Michele *et al.* (2020) analyzed numerically a family of linear extrapolation formulas to approximate ϕ at the intermediate stages of the RK method. Their general linear extrapolation formula depends on two parameters: α and β, as shown in Fig. 2.3. In order to advance the numerical solution in time of Δt from time t_n to t_{n+1} with the time instant of each RK stage as $t_i = t_n + \check{c}_i \Delta t$, the extrapolated ϕ_i in the intermediate RK stages for $i = 1, 2$ is located at time instants $t = t_n + \check{c}_i \alpha \Delta t$ where $\check{c}_i$ are the shifted RK3 coefficients (Sanderse & Koren, 2012). For the purpose of the extrapolation, in Fig. 2.3, $\phi_{n-\beta}$ and $\phi_{n-1-\beta}$, solutions of the Poisson equation, can be thought as computed at $t_{n-\beta} = t_n - \beta \Delta t$ and $t_{n-1-\beta} = t_{n-1} - \beta \Delta t$, respectively. Through numerical tests, De Michele *et al.* (2020) determined that the following $\alpha - \beta$ relationship,

$$\beta = -\frac{2}{3}\alpha + \frac{5}{6}, \tag{2.53}$$

has to be satisfied in order to preserve the temporal convergence rate of the underlying RK3 method for the velocity. However, a theoretical proof for the existence of such criterion, given in Eq. (2.53), was not provided. Furthermore, Capuano *et al.* (2016) and De Michele *et al.* (2020) reported temporal convergence results for free-shear flows and not wall-bounded flows (Table 2.5). Sanderse (2013) observed that there is an order reduction in the temporal accuracy for the case of wall-bounded flows due to the 'stiff' nature of the governing equations. To make their point, Sanderse (2013) studied the flow through a corner using grids with increasing refinement (see Sec. 7.3 of (Sanderse, 2013)). The computational problem becomes increasingly 'stiff' as the grid is refined. The test-case with a coarse, uniform grid showed no order reduction as the problem was non-stiff. Upon stretching the grid near the walls, Sanderse (2013) observed order reduction due to the numerical stiffness of the flow problem (Table 2.5). Prior to Sanderse (2013), the theoretical proof for such order reduction was given by Hairer & Wanner (1996) and Ascher & Petzold (1998), as well, more recently by Butcher (2016). Sanderse (2013) adopted an implicit RK method to solve the Navier-Stokes equations, while we adopt an explicit RK method in FastRK3 (Aithal & Ferrante, 2020). The derivation for order reduction given by Hairer & Wanner (1996) is agnostic to the type of the RK method employed, i.e., it applies to both implicit and explicit methods. Also, Sanz-Serna *et al.* (1986) showed the phenomenon of order reduction, both analytically and numerically, specifically for explicit RK methods like FastRK3. More recently, Karam *et al.* (2021) also developed a family of RK-based methods that do not require solving the Poisson equation for pressure at every stage (Table 2.5). Karam *et al.* (2021) developed these methods using the Stokes equation in order to eliminate the non-linear convection terms in the incompressible NS equations from their analytical derivation. Karam *et al.* (2021) reported numerical results showing 3rd-order temporal accuracy for velocity in a wall-bounded flow, i.e., the laminar channel flow (see Sec. 4.3 of (Karam *et al.*, 2021)). However, in this test-case, the divergence-free condition is satisfied identically, and, therefore, the r.h.s. of the Poisson equation for pressure in the projection method is theoretically zero making this test-case trivial. In our simulations of the laminar channel flow as in (Karam *et al.*, 2021), we observed that for the transient phase of the flow, the r.h.s. of the Poisson equation of pressure, is of $\mathcal{O}(10^{-12})$ in every cell of the computational domain except at the cells next to the inflow and outflow boundaries where it is of $\mathcal{O}(10^{-2})$. Since, as we will show in Sec.2.4.1, it is the order of the temporal accuracy of pressure that limits the order of accuracy of velocity, such test-case is trivial since the solution of the Poisson equation for pressure in the transient phase is practically inactive ($\nabla\phi^2 \approx 0 \Rightarrow \nabla\phi \approx$ constant) everywhere in the flow domain except near the inflow and outflow boundaries. Thus, we have italicized the 3$^{\text{rd}}$ order temporal convergence of Karam *et al.* (2021) for wall-bounded flows in Table 2.5 since it was obtained for a trivial test-case, and placed it under the non-stiff wall-bounded flows column since it used the same Reynolds number and a uniform grid with comparable grid refinement to the 'non-stiff' wall-bounded case studied by Sanderse (2013).

FastRK3 was developed to perform direct numerical simulations of turbulent flows, thus, we are primarily concerned with the temporal convergence rate for 'stiff' problems. In the present work, first we derive analytically the temporal convergence rate of FastRK3, and, then, we derive analytically the $\alpha - \beta$ relation, Eq. (2.53), in order to preserve the temporal convergence rate of the underlying RK3 method for the velocity. Finally, we report the results of the numerical analysis of the temporal convergence of FastRK3 obtained from simulating a free-shear and a 'stiff' wall-bounded flow, specifically, the Taylor-Green vortex and the lid-driven polar cavity flow.

In Aithal & Ferrante (2020), for FastRK3 we used the endpoint formulation (EP) for the extrapolation of ϕ_i, for $i = 1, 2$, where ϕ_i were defined at $t_n + \check{c}_i\Delta t$ as shown in Fig. 2.6a. Herein, for FastRK3 we use the general linear extrapolation formula for ϕ, shown in Fig. 2.3 and expressed in Eqs. (2.30) and (2.31). In Sec. 3.3, we report results of the temporal convergence of FastRK3 using EP ($\alpha = 1, \beta = 0$), midpoint formulation (MP) ($\alpha = 1/2, \beta = 1/2$) Capuano *et al.* (2016), shown in Figs. 2.6a and 2.6b, respectively, and a new extrapolation that we call standard approximation (SA) ($\alpha = 1, \beta = 1/6$).

2.4.1 Theoretical analysis on the temporal accuracy of FastRK3

In order to derive the 'global' temporal accuracy of FastRK3 over a period T, first, we derive the 'local error' introduced in one time step to advance the solution in time from t_n to time t_{n+1}. We assume that the RK3 coefficients are those provided by SK (Sanderse & Koren, 2012), who derived certain order conditions for the standard RK3 method. The way we

Reference	RK3 method		Temporal order of accuracy		
	# of Poisson solvers per time-step	Temporal integration	Free-shear flows	Wall-bounded flows	
				Non-stiff	Stiff
Le & Moin (1991)	1	Implicit	–	–	–
Sanderse & Koren (2012)	3	Explicit	3^{rd}	–	–
Sanderse (2013)	3	Implicit	3^{rd}	3^{rd}	2^{nd}
Capuano *et al.* (2016)	1	Explicit	3^{rd}	–	–
De Michele *et al.* (2020)	1	Explicit	3^{rd}	–	–
Karam *et al.* (2021)	1 or 2	Explicit	3^{rd}	$\mathit{3}^{rd}$	–

Table 2.5: Summary of RK3 methods for solving the incompressible Navier-Stokes equations and their order of temporal accuracy for velocity.

derive the error introduced at each of the three stages in FastRK3, Eqs. (2.30)-(2.34), is by deriving its error with respect to standard RK3 of SK (Sanderse & Koren, 2012), i.e., Eqs. (2.26)-(2.29). This approach was inspired by the proof provided by Nikitin (2006*b*) to study the temporal accuracy of their method.

First stage of RK3 The first stage ($i = 1$) of standard RK3 (Sanderse & Koren, 2012) is given by

$$\begin{aligned} \frac{\tilde{U}_1^* - \tilde{U}_n}{\varDelta t} &= \breve{a}_{11}\tilde{F}_n, \\ \frac{\tilde{U}_1 - \tilde{U}_1^*}{\varDelta t} &= -\check{c}_1\frac{G\tilde{\phi}_1}{\rho}, \end{aligned} \tag{2.54}$$

where, $\tilde{U}_n$ and $\tilde{U}_1$ are the arrays of discretized velocity components at t_n and $t_1 = t_n + \check{c}_1\varDelta t$, respectively, and $\tilde{U}_1^*$ is the array of the approximate velocity at t_1. $\tilde{F}_n$ represents the sum of

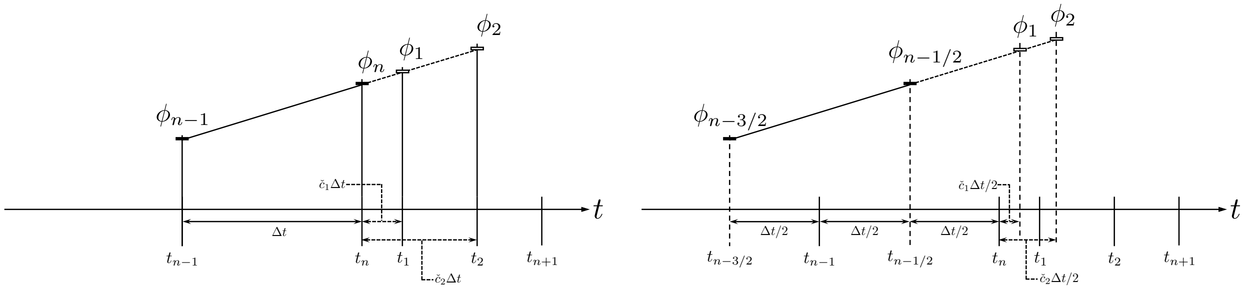

(a) EP extrapolation scheme: $\alpha = 1, \beta = 0$.

(b) MP extrapolation scheme: $\alpha = 1/2, \beta = 1/2$.

Figure 2.6: Endpoint (EP) and midpoint (MP) extrapolation schemes for ϕ.

discretized convection and diffusion of momentum, Eq. (2.22), at t_n, and, $\tilde{\phi}_1$ is the array of the discretized pressure-like scalar. Summing the two equations of Eq. (2.54) gives

$$\frac{\tilde{U}_1 - \tilde{U}_n}{\Delta t} = \breve{a}_{11}\tilde{F}_n - \check{c}_1 \frac{G\tilde{\phi}_1}{\rho}. \tag{2.55}$$

In standard RK3, in order to solve for $\tilde{U}_1$ using Eq. (2.55), the pseudo-pressure $\tilde{\phi}_1$ is obtained by solving the Poisson equation

$$DG\tilde{\phi}_1 = \frac{\rho}{\check{c}_1 \Delta t}\left(D\tilde{U}_1^* + b_1\right), \tag{2.56}$$

where $b_1 = b(t_1)$. Instead, in FastRK3, we use an approximation of $\tilde{\phi}_1$ at $t = t_n + \check{c}_1\alpha\Delta t$ computed via linear extrapolation Eq. (2.30) (i.e., $\phi_1 = \phi_1(\phi_{n-\beta}, \phi_{n-1-\beta})$ as depicted in Fig. 2.3), such that the velocity array U_1 of FastRK3 can be evaluated at time t_1 as

$$\frac{U_1 - \tilde{U}_n}{\Delta t} = \breve{a}_{11}\tilde{F}_n - \check{c}_1 \frac{G\phi_1}{\rho}. \tag{2.57}$$

Subtracting Eq. (2.55) from Eq. (2.57), we get

$$\frac{U_1 - \tilde{U}_1}{\Delta t} = \frac{\check{c}_1}{\rho}\left(G\tilde{\phi}_1 - G\phi_1\right). \tag{2.58}$$

Therefore, the instantaneous error $(U_1 - \tilde{U}_1)$ depends directly on how well ϕ_1 is approximating $\tilde{\phi}_1$. Since ϕ_1 is a linear extrapolation of ϕ, we can relate $G\phi_1$ and $G\tilde{\phi}_1$ as

$$G\tilde{\phi}_1 - G\phi_1 = c_{\phi_1}\Delta t + \mathcal{O}(\Delta t^2), \tag{2.59}$$

where c_{ϕ_1} is a vector with no dependence on Δt as shown in C. In our analysis of the third stage of FastRK3, we will determine the condition that c_{ϕ_1} has to satisfy in order to preserve the convergence rate of the underlying RK3 method. Substituting Eq. (2.59) in Eq. (2.58), and by multiplying the resulting equation by Δt, we get

$$U_1 - \tilde{U}_1 = \frac{\check{c}_1}{\rho}\left[c_{\phi_1}\Delta t^2 + \mathcal{O}(\Delta t^3)\right], \tag{2.60}$$

which shows that the velocity U_1 is a second-order approximation of $\tilde{U}_1$.

Next, we derive the difference between the discretized divergence of velocity DU_1 and $D\tilde{U}_1$. Applying the discrete divergence operator D to Eq. (2.58) gives

$$\frac{DU_1 - D\tilde{U}_1}{\Delta t} = \frac{\check{c}_1}{\rho} D\left(G\tilde{\phi}_1 - G\phi_1\right), \tag{2.61}$$

and using Eq. (2.59) in Eq. (2.61) gives

$$\frac{DU_1 - D\tilde{U}_1}{\Delta t} = \frac{\check{c}_1}{\rho} D\left(c_{\phi_1}\Delta t + \mathcal{O}(\Delta t^2)\right), \tag{2.62}$$

and, thus,

$$DU_1 - D\tilde{U}_1 \sim \mathcal{O}(\Delta t^2), \tag{2.63}$$

which shows that DU_1 is a second-order approximation of $D\tilde{U}_1$.

Next, we compare the fluxes computed using FastRK3 and standard RK3, using the definition of F given in Eq. (2.22),

$$F_1 - \tilde{F}_1 = [C(U_1) - C(\tilde{U}_1)] + VU_1 - V\tilde{U}_1. \tag{2.64}$$

Since V is a linear operator and using Eq. (2.60), we have

$$VU_1 - V\tilde{U}_1 = V\left[U_1 - \tilde{U}_1\right] \sim \frac{\check{c}_1}{\rho}\left[c_{\phi_1}\Delta t^2 + \mathcal{O}(\Delta t^3)\right]. \tag{2.65}$$

Further, since U_1 is a second-order approximation of $\tilde{U}_1$ from Eq. (2.60), it can be shown that

$$C(U_1) - C(\tilde{U}_1) \sim \frac{\check{c}_1}{\rho}\left[c_{\phi_1}\Delta t^2 + \mathcal{O}(\Delta t^3)\right]. \tag{2.66}$$

Therefore, using Eqs. (2.60), (2.65) and (2.66) in Eq. (2.64), we get

$$F_1 - \tilde{F}_1 \sim \frac{\check{c}_1}{\rho}\left[c_{\phi_1}\Delta t^2\right] + \mathcal{O}(\Delta t^3). \tag{2.67}$$

Second stage of RK3 Next, the second stage ($i = 2$) of standard RK3 (Sanderse & Koren, 2012) is given by

$$\frac{\tilde{U}_2 - \tilde{U}_n}{\Delta t} = \breve{a}_{21}\tilde{F}_n + \breve{a}_{22}\tilde{F}_1 - \breve{c}_2\frac{G\tilde{\phi}_2}{\rho}, \tag{2.68}$$

where $\tilde{U}_2$ is the discretized velocity at $t_2 = t_n + \breve{c}_2\Delta t$. $\tilde{F}_1$ represents the combined discretized convective and diffusion of momentum, Eq. (2.22), at t_1 computed using $\tilde{U}_1$, and $\tilde{\phi}_2$ is the array of discretized pseudo-pressure. Similarly to the first stage of standard RK3, the second stage would also require solving the Poisson equation, Eq. (2.29), to obtain $\tilde{\phi}_2$. Instead, we use an approximate discretized array for ϕ_2 at $t = t_n + \breve{c}_2\alpha\Delta t$ (i.e., $\phi_2 = \phi_2(\tilde{\phi}_{n-\beta}, \tilde{\phi}_{n-1-\beta})$ as depicted in Fig. 2.3), such that the velocity array U_2 of FastRK3 can be evaluated at time t_2, as

$$\frac{U_2 - \tilde{U}_n}{\Delta t} = \breve{a}_{21}\tilde{F}_n + \breve{a}_{22}\tilde{F}_1 - \breve{c}_2\frac{G\phi_2}{\rho}, \tag{2.69}$$

where, F_1 represents the combined discretized convective and diffusion terms computed using U_1. Subtracting Eq. (2.68) from Eq. (2.69) results in

$$\frac{U_2 - \tilde{U}_2}{\Delta t} = \breve{a}_{22}\left(F_1 - \tilde{F}_1\right) + \frac{\breve{c}_2}{\rho}\left(G\tilde{\phi}_2 - G\phi_2\right). \tag{2.70}$$

Similarly to the first stage of FastRK3, since ϕ_2 is a linear extrapolation of ϕ, we can relate $G\phi_2$ and $G\tilde{\phi}_2$ as

$$G\tilde{\phi}_2 - G\phi_2 = c_{\phi_2}\Delta t + \mathcal{O}(\Delta t^2), \tag{2.71}$$

where c_{ϕ_2} is a vector with no dependence on Δt similarly to c_{ϕ_1} as proved in C. In our analysis of the third stage of FastRK3, we will determine the condition that c_{ϕ_2} has to satisfy in order to preserve the temporal accuracy of the underlying RK3 method. Hence, the instantaneous error of the discretized velocity U_2 at t_2 is given by substituting Eqs. (2.67) and (2.71) in Eq. (2.70) as

$$U_2 - \tilde{U}_2 \sim \frac{\breve{c}_2}{\rho}\left[c_{\phi_2}\Delta t^2\right] + \mathcal{O}(\Delta t^3) \tag{2.72}$$

and, thus,

$$U_2 - \tilde{U}_2 \sim \mathcal{O}(\Delta t^2). \tag{2.73}$$

Further, similarly to the first stage of FastRK3 above in Eq. (2.63), it can be shown that the accuracy of the discretized divergence of velocity U_2 is given by

$$DU_2 - D\tilde{U}_2 \sim \mathcal{O}(\Delta t^2). \tag{2.74}$$

Next, we compare the fluxes computed using FastRK3 and standard RK3, using the definition of F given in Eq. (2.22),

$$F_2 - \tilde{F}_2 = \left[C(U_2) - C(\tilde{U}_2)\right] + \left[VU_2 - V\tilde{U}_2\right]. \tag{2.75}$$

Similarly to the analysis in the first stage of FastRK3, using Eq. (2.72), it can be shown that

$$C(U_2) - C(\tilde{U}_2) \sim \frac{\check{c}_2}{\rho}\left[c_{\phi_2}\Delta t^2 + \mathcal{O}(\Delta t^3)\right]. \tag{2.76}$$

Thus, using Eqs. (2.65), (2.72) and (2.76) in Eq. (2.75), we get

$$F_2 - \tilde{F}_2 \sim \frac{\check{c}_2}{\rho}\left[c_{\phi_2}\Delta t^2\right] + \mathcal{O}(\Delta t^3). \tag{2.77}$$

Third stage of RK3 Finally, the third stage ($i = 3$) of standard RK3 (Sanderse & Koren, 2012) is given by

$$\frac{\tilde{U}_{n+1} - \tilde{U}_n}{\Delta t} = \breve{a}_{32}\tilde{F}_1 + \breve{a}_{33}\tilde{F}_2 - \frac{G\tilde{\phi}_3}{\rho}, \tag{2.78}$$

where $\tilde{U}_{n+1}$ is the discretized velocity at $t_{n+1} = t_n + \Delta t$, and $\tilde{\phi}_3$ is the array of the discretized pseudo-pressure. Note that the discretized velocity at the third stage of RK3, $\tilde{U}_{n+1}$, differs from the exact velocity, denoted as $\bar{U}_{n+1}$, at t_{n+1} by $\mathcal{O}(\Delta t^4)$ as reported in Sec. 312 of (Butcher, 2016), i.e.,

$$\tilde{U}_{n+1} = \bar{U}_{n+1} + \mathcal{O}(\Delta t^4). \tag{2.79}$$

The velocity field at the third stage of FastRK3, using Eqs. (2.32) and (2.33), is given by

$$\frac{U_{n+1} - \tilde{U}_n}{\Delta t} = \breve{a}_{32}F_1 + \breve{a}_{33}F_2 - \frac{G\phi_3}{\rho}, \tag{2.80}$$

where, F_2 represents the combined discrete convection and diffusion of momentum, Eq. (2.22), computed using U_2. It should be noted that we *do* solve the Poisson equation for pseudo-pressure, ϕ, only at this final stage of FastRK3. In order to compute the accuracy of the third stage of FastRK3, we first determine the difference $(DG\tilde{\phi}_3 - DG\phi_3)$ as shown below. Applying the discrete divergence operator D to Eqs. (2.78) and (2.80) gives, respectively,

$$\frac{D\tilde{U}_{n+1} - D\tilde{U}_n}{\Delta t} = D\left(\check{a}_{32}\tilde{F}_1 + \check{a}_{33}\tilde{F}_2\right) - \frac{DG\tilde{\phi}_3}{\rho}, \tag{2.81}$$

$$\frac{DU_{n+1} - D\tilde{U}_n}{\Delta t} = D\left(\check{a}_{32}F_1 + \check{a}_{33}F_2\right) - \frac{DG\phi_3}{\rho}, \tag{2.82}$$

and, thus, using Eq. (2.21) in Eq. (2.81) and (2.82) and rearranging the terms in the resulting equations gives the following Poisson equations for $\tilde{\phi}_3$ and ϕ_3, respectively,

$$\frac{DG\tilde{\phi}_3}{\rho} = D\left(\check{a}_{32}\tilde{F}_1 + \check{a}_{33}\tilde{F}_2\right) + \frac{b_{n+1} - b_n}{\Delta t}, \tag{2.83}$$

$$\frac{DG\phi_3}{\rho} = D\left(\check{a}_{32}F_1 + \check{a}_{33}F_2\right) + \frac{b_{n+1} - b_n}{\Delta t}. \tag{2.84}$$

Note that the solution ϕ_3 of Eq. (2.84) for FastRK3, varies from the solution $\tilde{\phi}_3$ of Eq. (2.83) for standard RK3 in the interior grid points, while satisfying the prescribed boundary conditions. This is because the terms appearing on the r.h.s. of Eq. (2.84) are F_1 and F_2 rather than $\tilde{F}_1$ and $\tilde{F}_2$ as in Eq. (2.83). Subtracting Eq. (2.83) from Eq. (2.84) gives

$$\frac{DG\phi_3}{\rho} - \frac{DG\tilde{\phi}_3}{\rho} = D\left[\check{a}_{32}(F_1 - \tilde{F}_1) + \check{a}_{33}(F_2 - \tilde{F}_2)\right]. \tag{2.85}$$

Using Eqs. (2.67) and (2.77) in the r.h.s. of Eq. (2.85) gives

$$\frac{DG\phi_3}{\rho} - \frac{DG\tilde{\phi}_3}{\rho} \sim D\left[\frac{\check{a}_{32}\check{c}_1}{\rho}\left(c_{\phi_1}\Delta t^2\right) + \frac{\check{a}_{33}\check{c}_2}{\rho}\left(c_{\phi_2}\Delta t^2\right)\right] + \mathcal{O}(\Delta t^3), \tag{2.86}$$

and, rearranging the r.h.s. of Eq. (2.86) gives

$$\frac{DG\phi_3}{\rho} - \frac{DG\tilde{\phi}_3}{\rho} \sim \frac{D}{\rho}\left[\check{a}_{32}\check{c}_1 c_{\phi_1} + \check{a}_{33}\check{c}_2 c_{\phi_2}\right]\Delta t^2 + \mathcal{O}(\Delta t^3). \tag{2.87}$$

This result, Eq. (2.87), shows that, for general RK3 coefficients, $\check{a}_{ij}$ and $\check{c}_i$, the difference between $DG\phi$ of FastRK3 and of standard RK3 is of $\mathcal{O}(\Delta t^2)$. However, the RK3 coefficients we use in FastRK3, specified in Eq. (2.35) in accordance to (Sanderse & Koren, 2012), satisfy the relation

$$\check{a}_{32}\check{c}_1 = \check{a}_{33}\check{c}_2, \tag{2.88}$$

and, thus, substituting Eq. (2.88) in Eq. (2.87) gives

$$\frac{DG\phi_3}{\rho} - \frac{DG\tilde{\phi}_3}{\rho} \sim \frac{D}{\rho}\breve{a}_{32}\breve{c}_1 \left[c_{\phi_1} + c_{\phi_2}\right] \Delta t^2 + \mathcal{O}(\Delta t^3). \tag{2.89}$$

Therefore, Eq. (2.89) shows that the accuracy of $DG\phi$ of FastRK3 vs standard RK3 in the third stage depends on the sum $c_{\phi_1} + c_{\phi_2}$, i.e., the *sum* of the of errors introduced by linear extrapolations of $G\phi$ in the first two stages of RK3, Eqs. (2.59) and (2.71). Depending on the type of linear extrapolation of ϕ used, the possible values of the vector coefficients c_{ϕ_1} and c_{ϕ_2} are such that

$$\begin{aligned} &\text{Case A:}\ \ c_{\phi_1} + c_{\phi_2} \neq 0, \\ &\text{Case B:}\ \ c_{\phi_1} + c_{\phi_2} = 0,\ \ c_{\phi_1} \neq 0 \text{ and } c_{\phi_2} \neq 0 \\ &\text{Case C:}\ \ c_{\phi_1} = c_{\phi_2} = 0. \end{aligned} \tag{2.90}$$

For cases B and C of Eq. (2.90), i.e., $c_{\phi_1} + c_{\phi_2} = 0$, Eq. (2.89) gives

$$D\left(G\phi_3 - G\tilde{\phi}_3\right) \sim \mathcal{O}(\Delta t^3). \tag{2.91}$$

Equation (2.91) shows that, for the cases B and C of Eq. (2.90), the error on pressure gradient introduced by FastRK3 (by computing the Poisson equation for pressure and using the linear extrapolation for stage 1 and 2 for ϕ_i) versus the standard RK3 (for which the Poisson equation is solved at each stage of RK3) is of third order. In Sec. 2.4.2, we show the conditions for which the linear extrapolations of $G\phi$ satisfy the conditions of cases B and C of Eq. (2.90).

The instantaneous error $U_{n+1} - \tilde{U}_{n+1}$ is computed by subtracting Eq. (2.78) from Eq. (2.80),

$$\frac{U_{n+1} - \tilde{U}_{n+1}}{\Delta t} = \breve{a}_{32}\left(F_1 - \tilde{F}_1\right) + \breve{a}_{33}\left(F_2 - \tilde{F}_2\right) - \frac{\left(G\phi_3 - G\tilde{\phi}_3\right)}{\rho}, \tag{2.92}$$

and, then, by using Eqs. (2.67), (2.77), (2.88) and (2.91) in Eq. (2.92) gives

$$\frac{U_{n+1} - \tilde{U}_{n+1}}{\Delta t} \sim \mathcal{O}(\Delta t^3), \tag{2.93}$$

to finally give

$$U_{n+1} - \tilde{U}_{n+1} \sim \mathcal{O}(\mathit{\Delta} t^4), \tag{2.94}$$

which shows that U_{n+1} is a fourth-order approximation of $\tilde{U}_{n+1}$. Given Eq. (2.79), Eq. (2.94) implies that U_{n+1} is still a fourth-order accurate approximation of the exact velocity $\bar{U}_{n+1}$, i.e.,

$$U_{n+1} - \bar{U}_{n+1} \sim \mathcal{O}(\mathit{\Delta} t^4). \tag{2.95}$$

Thus far, we have derived the error of FastRK3 to advance the numerical solution of one time-step. Next, we determine its global error at time T. When the stability constraints of the method discussed in Eq. (34) of (Aithal & Ferrante, 2020) are satisfied, as well as, the RK3 coefficients satisfy Eq. (2.88), and the linear extrapolation of ϕ satisfies cases B or C of Eq. (2.90), then, the error introduced at each time step of FastRK3 is of $\mathcal{O}(\mathit{\Delta} t^4)$, according to Eq. (2.95), without growing or diminishing in time (LeVeque, 2007). In order to integrate the governing equations from time $t = 0$ to $t = T = N\mathit{\Delta} t$, FastRK3 performs the RK3 steps (2.32)-(2.34) for N times. Therefore, the resulting global error of FastRK3 at time T is the sum of the one time-step error for all N time steps i.e.,

$$U_N - \bar{U}_N \sim N\ \mathcal{O}(\mathit{\Delta} t^4) = \frac{T}{\mathit{\Delta} t}\ \mathcal{O}(\mathit{\Delta} t^4) = \mathcal{O}(\mathit{\Delta} t^3). \tag{2.96}$$

Therefore, under the specified conditions above, FastRK3 is third-order accurate in the global temporal error for velocity. As verification of the main theoretical results of this section, we provide the numerical verification of Eqs. (2.59), (2.71), (2.79), (2.91) and (2.96) by reporting the temporal errors computed from simulating the Taylor-Green vortex flow using FastRK3 and standard RK3 in Sec. 3.3.2. Similarly to Sanderse & Koren (2012), we note that the third-order temporal convergence rate for velocity, derived in Eq. (2.96), is valid for numerically 'non-stiff' problems. The numerically 'stiff' problems, however, exhibit order reduction as proved analytically by Hairer & Wanner (1996) for RK methods independently of being implicit or explicit, and by Sanz-Serna *et al.* (1986) specifically for explicit RK methods.

2.4.2 Theoretical derivation of the $\alpha - \beta$ relation

In this section, first, we derive analytically the $\alpha - \beta$ relation, Eq. (2.53), that was found numerically using the four-stage RK4 method by De Michele *et al.* (2020). Then, we show that the $\alpha - \beta$ relation is equivalent to the condition that the linear extrapolation of ϕ needs to satisfy to ensure that FastRK3 recovers the temporal convergence rate of the underlying RK3 method, i.e., the condition specified in Eq. (2.90) for cases B and C.

Let us now derive the $\alpha - \beta$ relation for a general RK method with $s\,(\geq 3)$ number of stages, such that the results can be applied to the RK3 and RK4 methods. We start from generalizing the constraint to ensure that the final-stage $DG\phi$ of FastRK3, expressed via Eq. (2.87), is third-order accurate, i.e., $\breve{a}_{32}\breve{c}_1 c_{\phi_1} + \breve{a}_{33}\breve{c}_2 c_{\phi_2} = 0$ for RK3, as

$$\sum_{i=1}^{s-1} \breve{a}_{si+1}\breve{c}_i c_{\phi_i} = 0. \tag{2.97}$$

Similarly to Eq. (2.88) for RK3, also for the coefficients used by De Michele *et al.* (2020) for RK4, the products $\breve{a}_{si+1}\breve{c}_i$ (no sum on i) are equal to each other for all $i = 1, \ldots, s-1$. Therefore, for such choice of RK coefficients, i.e.,

$$\breve{a}_{si+1}\breve{c}_i = \text{constant for} \;\; i = 1, \ldots, s-1, \tag{2.98}$$

where i is the stage of the RK method, Eq. (2.97) simplifies to

$$\sum_{i=1}^{s-1} c_{\phi_i} = 0, \tag{2.99}$$

which is a generalization of cases B and C of Eq. (2.90) for an RK method with s steps. Next, the exact solution of ϕ, $\bar{\phi}(t)$, is given in (Sanderse & Koren, 2012) from the exact pressure solution, $p(t)$, as

$$\bar{\phi}(t_i) = \frac{1}{\breve{c}_i \mathit{\Delta} t} \int_{t_n}^{t_i} p(t)dt, \tag{2.100}$$

of which $\tilde{\phi}_i$ are first-order approximations at t_i in general when using the coefficients of explicit RK methods (Sanderse & Koren, 2012), e.g., Eq. (2.35) for RK3 ($s = 3$). By the midpoint method (Fig. 2.6b) we know that $\tilde{\phi}_i$ are second-order approximations for the exact $\bar{\phi}$ at $t_n + \check{c}_i \frac{\Delta t}{2}$:

$$\tilde{\phi}_i = \bar{\phi}\left(t_n + \check{c}_i \frac{\Delta t}{2}\right) + \mathcal{O}\left(\Delta t^2\right). \tag{2.101}$$

In order to maintain this second-order accuracy at the midpoint for FastRK3 in which we do not solve Eq. (2.29), we linearly extrapolate from $\tilde{\phi}_{n-\frac{1}{2}}$ at $t_{n-\frac{1}{2}}$ and $\tilde{\phi}_{n-\frac{3}{2}}$ at $t_{n-\frac{3}{2}}$ to $\tilde{\phi}_i$ at $t_n + \check{c}_i \frac{\Delta t}{2}$ (as depicted in Fig. 2.6b) as

$$\phi_i = \left(1 + \frac{\check{c}_i + 1}{2}\right)\tilde{\phi}_{n-\frac{1}{2}} - \left(\frac{\check{c}_i + 1}{2}\right)\tilde{\phi}_{n-\frac{3}{2}}. \tag{2.102}$$

The general linear extrapolation of ϕ (Fig. 2.3) is given in (De Michele *et al.*, 2020) as

$$\phi_i = (1 + \beta + \alpha\check{c}_i)\tilde{\phi}_{n-\frac{1}{2}} - (\beta + \alpha\check{c}_i)\tilde{\phi}_{n-\frac{3}{2}}. \tag{2.103}$$

As the ϕ_i defined in Eq. (2.102) are second-order approximations to $\bar{\phi}(t_n + \check{c}_i \frac{\Delta t}{2})$, the stage-wise first-order error, ϵ_i, introduced by the general linear extrapolation (2.103) is given by subtracting Eq. (2.102) from Eq. (2.103) as

$$\epsilon_i = \left[\left(\beta - \frac{1}{2}\right) + \check{c}_i\left(\alpha - \frac{1}{2}\right)\right]\tilde{\phi}_{n-\frac{1}{2}} - \left[\left(\beta - \frac{1}{2}\right) + \check{c}_i\left(\alpha - \frac{1}{2}\right)\right]\tilde{\phi}_{n-\frac{3}{2}}. \tag{2.104}$$

In order to limit the total error relative to the exact $\bar{\phi}$ introduced at each time step by the linear extrapolation, Eq. (2.103) to $\mathcal{O}(\Delta t^2)$, which we will show is identical to the condition imposed in Eq. (2.99), we impose that the *sum* of the errors ϵ_i, as expressed in Eq. (2.104), for the s stages of RK to be zero, i.e.,

$$\sum_{i=1}^{s-1} \epsilon_i = 0. \tag{2.105}$$

Eq. (2.105) represents a generalization of case B of Eq. (2.90) and therefore ensures that the error on $DG\phi$ introduced by FastRK3 versus the standard RK3, given in Eq. (2.91), is of third order. Substituting Eq. (2.104) in Eq. (2.105) gives

$$(s-1)\left(\beta - \frac{1}{2}\right) + \left(\alpha - \frac{1}{2}\right)\sum_{i=1}^{s-1} \check{c}_i = 0. \tag{2.106}$$

Substituting the corresponding $\check{c}_i$ of RK3, Eq. (2.35), or RK4 (De Michele *et al.*, 2020) and $s = 3$ or $s = 4$, respectively, into Eq. (2.106), we get

$$\beta = -\frac{2}{3}\alpha + \frac{5}{6}, \tag{2.107}$$

which is identical to Eq. (2.53), i.e., the $\alpha - \beta$ condition that De Michele *et al.* (2020) found numerically using the forth-order RK scheme, RK4. Therefore, for any linear extrapolation of ϕ that satisfies the $\alpha - \beta$ relation Eq. (2.106), it follows that the sum of errors introduced by pressure extrapolation in each time step is $\mathcal{O}(\Delta t^2)$, and, thus, from Eqs. (2.92) and (2.96) the 'local' and 'global' temporal accuracy of velocity are fourth and third order, respectively.

Let us now consider the equivalence of Eqs. (2.99) and (2.105). We know from Eqs. (2.59) and (2.71) that the intermediate pressure gradients $G\phi_i$ of FastRK3 are, at worst, first-order approximations of $G\tilde{\phi}_i$ of standard RK3. However, for the specific type of linear extrapolation corresponding to case C of Eq. (2.90), in which $c_{\phi_1} = 0$ and $c_{\phi_2} = 0$, $G\phi_i$ will be second-order approximations of $G\tilde{\phi}_i$, according to Eqs. (2.59) and (2.71). Further, in Sec. 3.3.2 we show numerically that this linear extrapolation of ϕ_i that corresponds to case C of Eq. (2.90) and approximates standard RK3 with second-order accuracy, also satisfies the $\alpha - \beta$ relation, Eq. (2.106), viz., $\alpha = 1$, $\beta = 1/6$. This means that the errors with respect to the exact values, $G\bar{\phi}(t_n + \check{c}_i\frac{\Delta t}{2})$, of this standard RK3 approximation (SA) of $G\phi_i$ sum to $\mathcal{O}(\Delta t^2)$. Thus, we can say that the errors of $G\tilde{\phi}_i$ with respect to the exact values, $G\bar{\phi}(t_n + \check{c}_i\frac{\Delta t}{2})$, also sum to $\mathcal{O}(\Delta t^2)$. This implies that Eqs. (2.99) and (2.105) are interchangeable constraints since they can be derived from each other. It then follows that any extrapolation formula satisfying Eq. (2.105), and therefore Eq. (2.106), will also satisfy Eq. (2.99). For the specific case of the FastRK3 method ($s = 3$) with any extrapolation formula satisfying Eq. (2.107), the coefficients c_{ϕ_1} and c_{ϕ_2} of Eqs. (2.59) and (2.71) will follow the relationship given by case B of Eq. (2.90), such that the sum of the errors of $G\phi_i$ with respect to the exact values, $G\bar{\phi}(t_n + \check{c}_i\frac{\Delta t}{2})$, is $\sim \mathcal{O}(\Delta t^2)$.

2.4.3 Summary of theoretical results

Herein, we provide a summary of the main theoretical results of Sec. (2.4.1) and (2.4.2).

1. For a general three-step RK method where the pseudo-pressure ϕ is linearly extrapolated with c_{ϕ_1} and c_{ϕ_2} defined in Eqs. (2.59) and (2.71), the following condition, derived from Eq. (2.87),

   $$\breve{a}_{32}\breve{c}_1 c_{\phi_1} + \breve{a}_{33}\breve{c}_2 c_{\phi_2} = 0, \tag{2.108}$$

   must be satisfied in order for the method to be third-order accurate in time for velocity as expressed by Eq. (2.96). For an s-step RK method, by understanding how the error introduced by pressure extrapolation propagates through its stages, in Eq. (2.108) can be generalized as

   $$\sum_{i=1}^{s-1} \breve{a}_{si+1}\breve{c}_i c_{\phi_i} = 0. \tag{2.109}$$

2. For an s-step RK method ($s \geq 3$) in which

   $$\breve{a}_{s1}\breve{c}_1 = \breve{a}_{s2}\breve{c}_2 = \ldots = \breve{a}_{ss}\breve{c}_{s-1}, \tag{2.110}$$

   (e.g., the RK3 coefficients given by SK (Sanderse & Koren, 2012) or the RK4 method used by De Michele *et al.* (2020)), the condition expressed in Eq. (2.109) simplifies to

   $$\sum_{i=1}^{s-1} c_{\phi_i} = 0. \tag{2.111}$$

   Satisfying Eq. (2.111) ensures that the net error of $DG\phi_s - DG\tilde{\phi}_s$ in the final stage of RK is of $\mathcal{O}\left(\Delta t^3\right)$ as shown for $s = 3$ in Eqs. (2.87)-(2.91). Therefore, the 'local' and 'global' temporal accuracy of velocity are fourth and third order, respectively, independently of the number of stages s of RK as shown for $s = 3$ in Eqs. (2.92) and (2.96). Note that such upper bounds on the order of the temporal accuracy are determined by the choice of linearly extrapolating the pressure at the intermediate RK stages, Eqs. (2.30) and (2.31).

3. For a general s-step RK method, we have derived the generalized form of the $\alpha - \beta$ relation, i.e., Eq. (2.106),

$$(s-1)\left(\beta - \frac{1}{2}\right) + \left(\alpha - \frac{1}{2}\right)\sum_{i=1}^{s-1} \check{c}_i = 0. \tag{2.112}$$

Chapter 3

VERIFICATION, VALIDATION AND CONVERGENCE RATES OF FASTRK3

3.1 Verification and spatial convergence rates

In this section, we verify FastRK3 by simulating three canonical flows, two of which have analytical solutions. From these test-cases, we compute the temporal and spatial orders of accuracy of FastRK3 and determine if FastRK3 conserves the discrete kinetic energy. We present results from the lid-driven polar cavity in Sec. 3.1.1 and 3.1.1, the laminar boundary-layer over a flat plate in Sec. 3.1.2, and the Jeffery-Hamel flow in Sec. 3.1.3. We compute the temporal convergence rate of the solver for an unsteady problem by simulating the unsteady lid-driven polar cavity flow (Sec. 3.1.1), the conservation of discrete kinetic energy in the inviscid limit (Sec. 3.1.1), and the spatial convergence rate for steady problems by simulating the laminar boundary-layer over a flat plate (Sec. 3.1.2) and the Jeffery-Hamel flow (Sec. 3.1.3).

3.1.1 Unsteady lid-driven polar cavity

We simulated the lid-driven polar cavity flow with a velocity magnitude of the lid that is sinusoidal in time. The computational domain was given by $R_i \leq r \leq R_o$ and $-\alpha/2 \leq \theta \leq \alpha/2$ with a mesh of 256×192 grid points. No-slip boundary conditions, as described in Sec. 4.1.2, were applied at the four boundaries of the domain. For the moving wall at $r = R_i$ we prescribed an azimuthal velocity of $U_\theta = U_i \cos(\omega t)$. The flow was simulated up to $t_{\max} = 40$ corresponding to 87,869 time steps. The time step Δt was set as $\Delta t/\Delta_{t_\nu} = 0.25$. The fluid flow in the azimuthal direction, θ, is caused by viscous diffusion of momentum in the radial direction, r. The dimensionless physical and flow parameters were set as:

$$\mathrm{R}_i = 1.0, \quad \mathrm{R}_o = 2.0, \quad \alpha = 1, \quad U_i = 1, \quad \omega = 2\pi/T, \quad T = 10, \quad \mathrm{Re}_i = \frac{U_i \ \mathrm{R}_i}{\nu} = 280. \tag{3.1}$$

In order to prove whether or not there is a loss of accuracy in FastRK3 by not performing the Poisson solver at each stage as in standard RK3, we computed the relative error between FastRK3 and the standard RK3 method (Sanderse & Koren, 2012) for this unsteady test case. The relative error for a generic flow variable σ at $t_{\max}$ was computed as

$$\epsilon = \frac{||\sigma_{\mathrm{RK3}} - \sigma_{\mathrm{FastRK3}}||_2}{||\sigma_{\mathrm{RK3}}||_2}. \tag{3.2}$$

The relative errors, ϵ, for U_r, U_θ and p are 2.06×10^{-3}, 8.75×10^{-4} and 3.65×10^{-3}, respectively. Figure 3.1 shows excellent agreement between the streamlines of the numerical solution from standard RK3 and FastRK3. Figures 3.2 and 3.3 show the radial (U_r) and azimuthal (U_θ) velocity profiles and pressure profiles respectively along four radial lines $\theta = \pi/18, -\pi/18, \pi/9$, and $-\pi/9$ from the two methods. All these results show excellent agreement between the solutions of FastRK3 and the standard RK3 (Sanderse & Koren, 2012).

Conservation of kinetic energy in the inviscid limit We have analyzed numerically whether FastRK3 is energy conserving in the inviscid limit. We used the solution of the unsteady lid-driven polar cavity at Re=280 and $t = 40$, with the same parameters as described in Sec. 3.1.1, as the initial condition of a new simulation in which we set $\mathrm{Re} = \infty$. Figure. 3.4 shows the time development of the change in kinetic energy

$$K = \sum_{\xi=1}^{N_\xi} \sum_{\eta=1}^{N_\eta} \sum_{\zeta=1}^{N_\zeta} U_\xi^2 h_\xi^2 + U_\eta^2 h_\eta^2 + U_\zeta^2 h_\zeta^2 \tag{3.3}$$

where U_ξ, U_η and U_ζ represent the discrete contravariant velocity component along ξ-, η- and ζ- directions respectively, normalized by the initial kinetic energy K_0. The plot of Fig. 3.4 shows that the kinetic energy in the inviscid limit slightly decreases in time of 0.24% in 10,983 time steps due to the dissipative nature of the explicit third-order Runge-Kutta based schemes (Nikitin, 2006*a*).

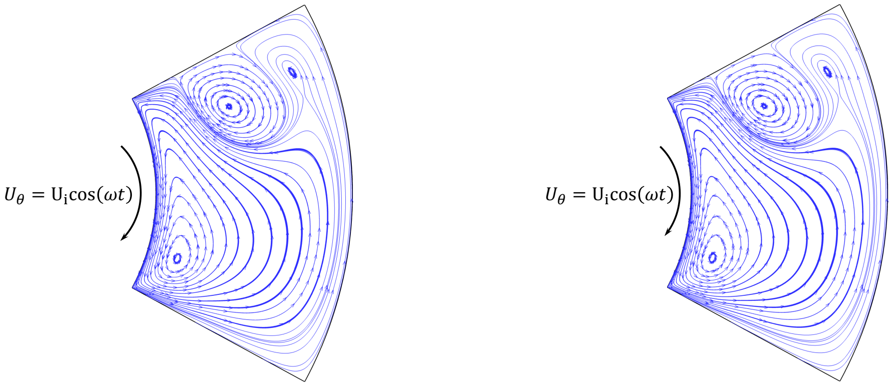

(a) Streamlines of the numerical solution for $\mathrm{Re}_i = 280$ from standard RK3 at $t_{\max} = 40$

(b) Streamlines of the numerical solution for $\mathrm{Re}_i = 280$ from FastRK3 at $t_{\max} = 40$

Figure 3.1: Lid-driven polar cavity flow

3.1.2 Laminar boundary-layer over a flat plate

Next, we verified FastRK3 by simulating the laminar boundary-layer over a flat plate and by comparing with the velocity profiles obtained from the numerical simulation to the Blasius solution (Blasius, 1908). We prescribed a uniform flow, U_∞, at the inlet upstream of the leading edge of the plate. We set up a rectangular computational domain with streamwise and wall-normal lengths $L_x = 10$ and $L_y = 3.6$, respectively. At the bottom boundary, the section $0 \leq x < 5$ was a plane of symmetry ($\delta U/\delta y = \delta p/\delta y = 0$), and the section $5 \leq x \leq 10$ was the no-slip wall (flat plate). We used a computational mesh of 192×96 grid points gradually stretched in the wall-normal ($\eta = y$) direction with the grid stretching parameter $\gamma = 0.66$ (Ferrante & Elghobashi, 2004) and in the streamwise direction with the grid stretching parameter $\gamma = 0.33$ (Ferrante & Elghobashi, 2004), to have finer mesh in the regions of highest velocity gradients near the bottom boundary and near the leading edge of the flat-plate at $x = 0$. The time step Δt was set as $\Delta t/\Delta t_\nu = 0.125$. Fig. 3.5 shows the streamwise and wall-normal components of velocity where the Reynolds number

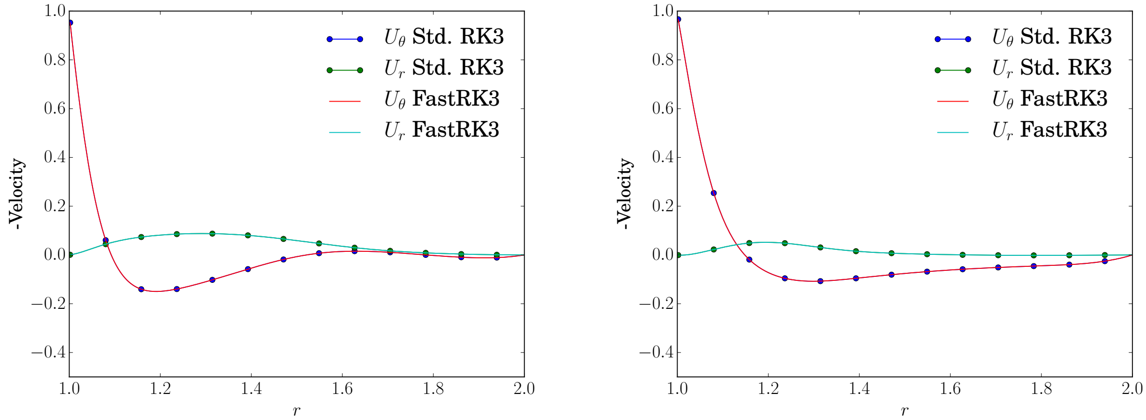

(a) $\theta = \pi/18$, $\mathrm{Re}_i = 280$ (b) $\theta = -\pi/18$, $\mathrm{Re}_i = 280$

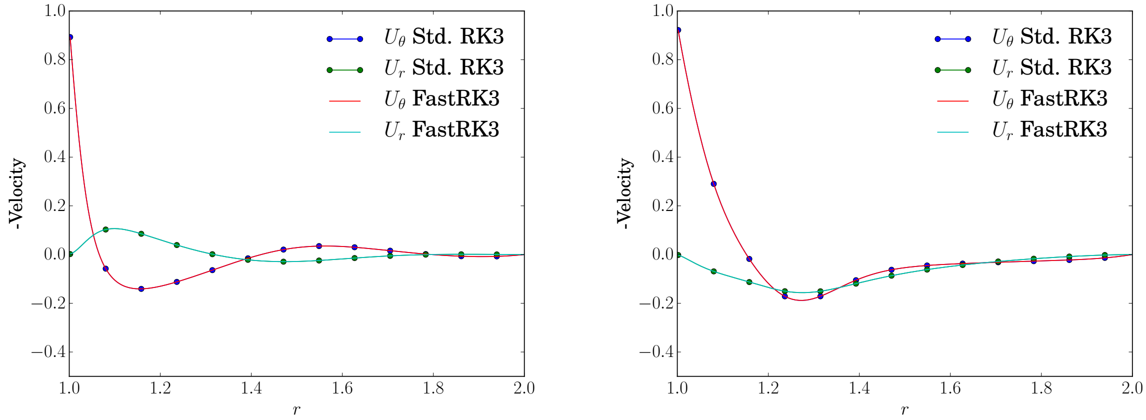

(c) $\theta = \pi/9$, $\mathrm{Re}_i = 280$ (d) $\theta = -\pi/9$, $\mathrm{Re}_i = 280$

Figure 3.2: Comparison of FastRK3 and standard RK3 solutions for U_θ and U_r along radial lines for the lid-driven polar cavity at $t_{\max} = 40$.

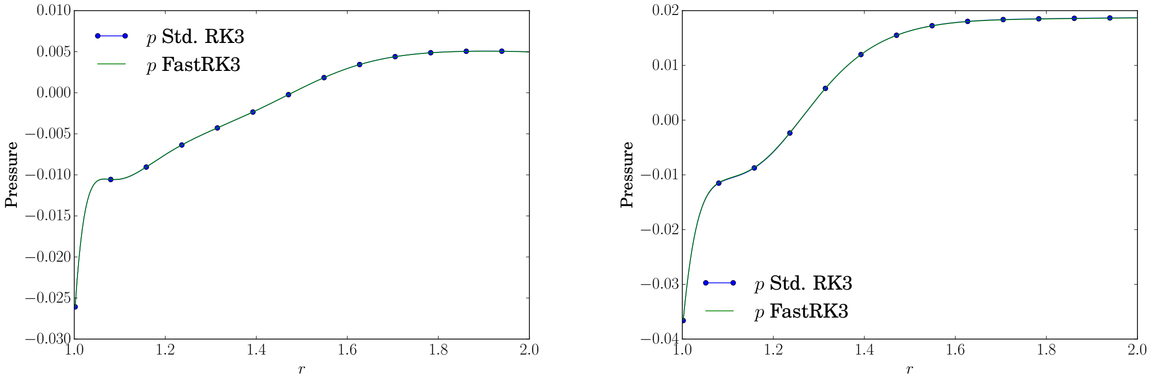

(a) $\theta = \pi/18$, $\mathrm{Re}_i = 280$

(b) $\theta = -\pi/18$, $\mathrm{Re}_i = 280$

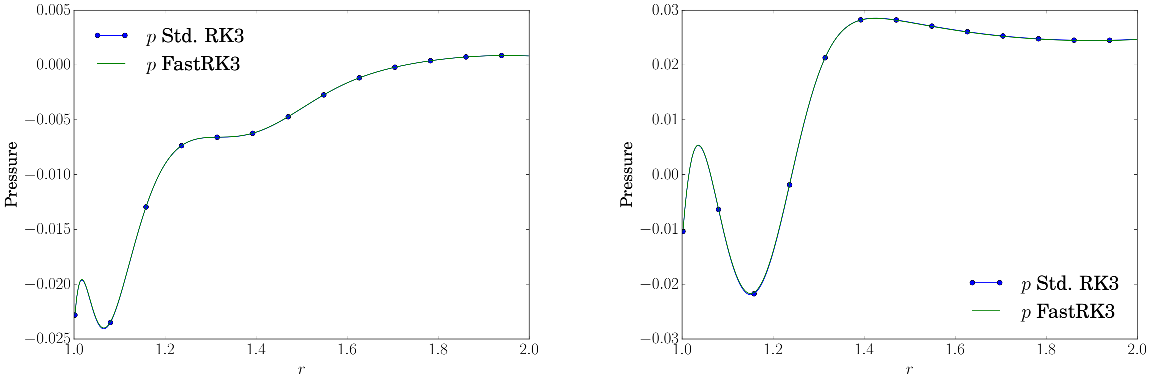

(c) $\theta = \pi/9$, $\mathrm{Re}_i = 280$

(d) $\theta = -\pi/9$, $\mathrm{Re}_i = 280$

Figure 3.3: Comparison of FastRK3 and standard RK3 solutions for p along radial lines for the lid-driven polar cavity at $t_{\max} = 40$.

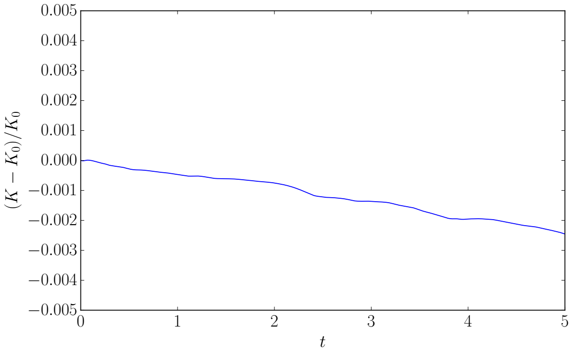

Figure 3.4: Time development of the change in kinetic energy, $K - K_0$, normalized by the initial kinetic energy, K_0, for the sinusoidal lid-driven polar cavity for Re$=\infty$ and setting at $t = 0$ as initial condition the solution at $t = 40$ of the sinusoidal lid-driven cavity at Re=280 with the same parameters as described in Sec. 3.1.1.

is $\mathrm{Re}_x = 764$. The relative error for a generic flow variable σ between the analytical solution, σ_{ex}, and its numerical approximation, σ_{num}, was computed as follows:

$$\epsilon = \frac{||\sigma_{\mathrm{ex}} - \sigma_{\mathrm{num}}||_2}{||\sigma_{\mathrm{ex}}||_2}. \tag{3.4}$$

The relative error ϵ between the numerical and analytical x- and y- components of velocity are 8.9×10^{-3} and 9.5×10^{-3}, respectively.

Then, we assessed the spatial accuracy of FastRK3 by simulating the laminar boundary-layer flow over a flat plate. We simulated the flow on meshes of 32×8, 64×16, 128×32, and 256×64 grid points. We prescribed a Blasius velocity profile at the inlet and the Reynolds number based on the inlet boundary-layer thickness is $\mathrm{Re}_{\delta_0} = 1000$. For this test, we set up a rectangular computational domain with streamwise and wall-normal lengths $L_x = 10\delta_0$ and $L_y = 3.6\delta_0$, respectively. The CFL number was kept constant with $\mathit{\Delta} t/\mathit{\Delta} x = 0.01$. The spatial accuracy of the solver, n, was computed as follows (Oberkampf & Roy, 2010):

$$n = \frac{\ln\left(\frac{E_{8\mathit{\Delta} y,4\mathit{\Delta} y}}{E_{4\mathit{\Delta} y,2\mathit{\Delta} y}}\right)}{\ln\left(\frac{8\mathit{\Delta} y-4\mathit{\Delta} y}{4\mathit{\Delta} t-2\mathit{\Delta} y}\right)} = \frac{\ln\left(\frac{E_{8\mathit{\Delta} y,4\mathit{\Delta} y}}{E_{4\mathit{\Delta} y,2\mathit{\Delta} y}}\right)}{\ln\left(2\right)}, \tag{3.5}$$

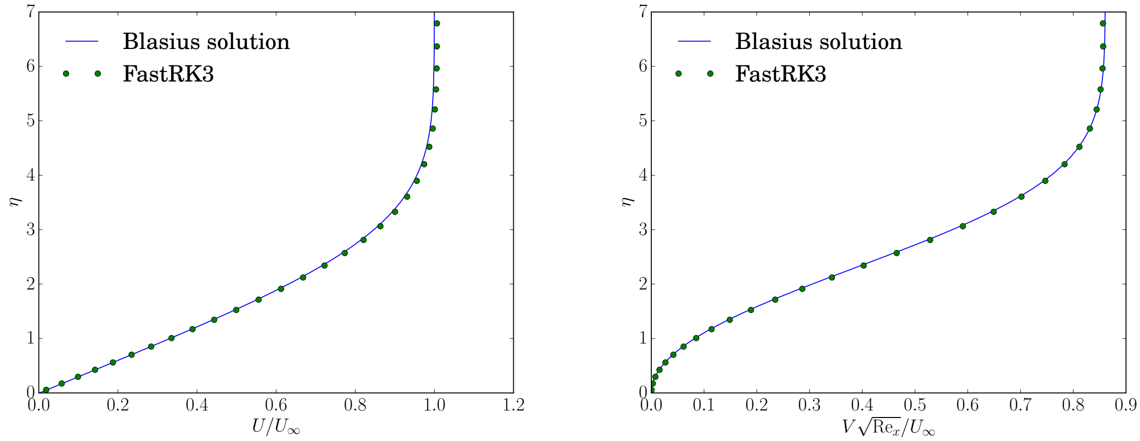

(a) U-component of velocity

(b) V-component of velocity

Figure 3.5: Comparison of FastRK3 vs. Blasius solution for flat plate boundary layer for $\mathrm{Re}_x = 764$: (a) U/U_∞ and (b) $V\sqrt{\mathrm{Re}_x}/U_\infty$ as functions of the self-similar variable, $\eta = y\sqrt{\mathrm{Re}_x}/x$.

where, $E_{8\Delta y,4\Delta y}$, $E_{4\Delta y,2\Delta y}$ and $E_{2\Delta y,\Delta y}$ are the L_2 norms of the errors between successive grids for a generic flow variable σ:

$$\begin{aligned} E_{8\Delta y,4\Delta y} &= ||\sigma_{8\Delta y} - \sigma_{4\Delta y}||_2, \\ E_{4\Delta y,2\Delta y} &= ||\sigma_{4\Delta y} - \sigma_{2\Delta y}||_2, \\ E_{2\Delta y,\Delta y} &= ||\sigma_{2\Delta y} - \sigma_{\Delta y}||_2. \end{aligned} \tag{3.6}$$

Figure 3.6 shows L_2 norms of errors between successive solutions as a function of the number of grid points in y for the streamwise and wall-normal velocity components ($U(y)/U_\infty$, $V(y)/U_\infty$). Table 3.1 shows L_2 norms of $E_{4\Delta y,2\Delta y}$ and $E_{2\Delta y,\Delta y}$, and the computed order of accuracy, n, for the streamwise and wall-normal velocity components ($U(y)/U_\infty$, $V(y)/U_\infty$). The convergence rates for the streamwise $U(y)$ and wall-normal $V(y)$ components of velocity are 1.94 and 2.03, respectively. These results confirm that FastRK3 is second-order accurate in space, consistently with our second-order spatial discretization of the governing Eqs. (2.15) and (2.16).

	$E_{4\Delta y,2\Delta y}$	$E_{2\Delta y,\Delta y}$	n
$U(y)/U_\infty$	1.45e-2	3.79e-3	1.94
$V(y)/U_\infty$	4.52e-1	1.11e-1	2.03

Table 3.1: L_2 norm of spatial errors and spatial convergence rate (or spatial order of accuracy), n, for streamwise velocity (U) and wall-normal velocity (V) for laminar boundary-layer flow over a flat plate.

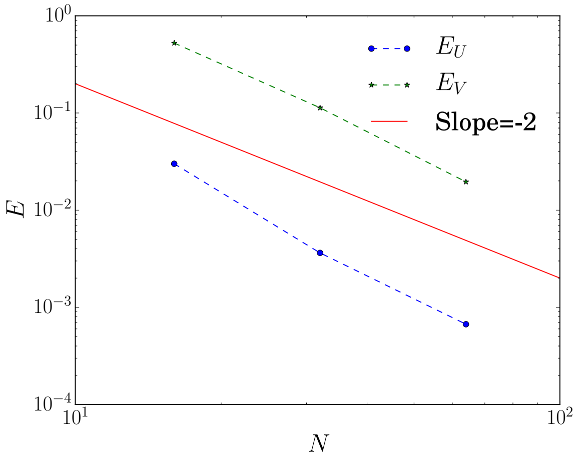

Figure 3.6: Spatial error convergence for laminar boundary layer flow over a flat plate.

3.1.3 Jeffery-Hamel flow

Our last verification case of FastRK3 was the Jeffery-Hamel flow (Jeffery, 1915; Hamel, 1917) for which the flow schematic is shown in Fig. 3.7a. The test is defined by the radial flow generated by a point source and bounded by two walls diverging from the point source with a semi-aperture angle α. The generated grid is curved in the azimuthal direction θ as shown in Fig. 3.7b.

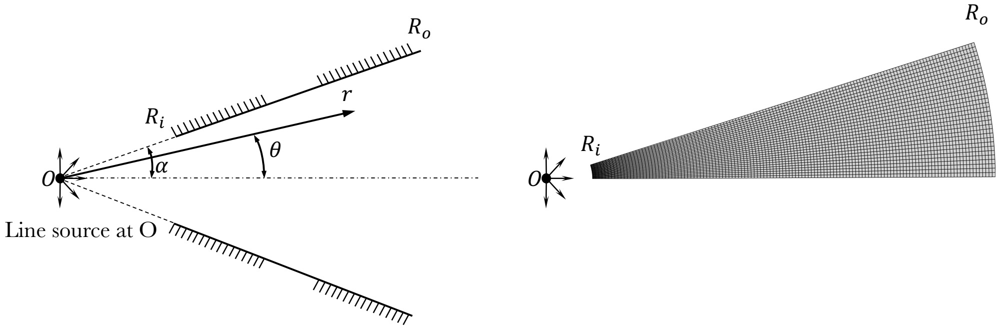

(a) Jeffery-Hamel flow schematic

(b) Computational grid for Jeffery-Hamel flow

Figure 3.7: Jeffery-Hamel flow

The similarity solution of the radial flow U_r as a function of the similarity variable $\eta = \theta/\alpha$ is given by White & Corfield (2006) as

$$\frac{U_r(r,\theta)}{U_{\max}(r)} = f(\eta), \tag{3.7}$$

where $U_{\max}(r)$ is the maximum radial velocity $U_r(r,\theta)$ for a fixed r, which corresponds to $U_{\max}(r) = U_r(r,\theta = 0) \propto 1/r$, and $f(\eta)$ satisfies the following third-order nonlinear differential equation,

$$f''' + 2\alpha \text{ Re } ff' + 4\alpha^2 f' = 0, \tag{3.8}$$

with the appropriate boundary conditions:

$$f(0) = 1,\ f'(0) = 0 \text{ and } f(1) = 0. \tag{3.9}$$

For our numerical test-case, we simulated the flow in the computational domain defined by $R_i \leq r \leq R_o$ and $0 \leq \theta \leq \alpha$ using a mesh of 128×32 grid points (Fig. 3.7b). We imposed the condition of symmetry at the bottom boundary of the domain representing the centerline of the flow, and no-slip boundary conditions at the top of the computational domain (Fig. 3.7a). The inflow conditions at $r = R_i$ were prescribed by assigning the similarity solution, Eq. (3.7), computed for $r = R_i$ and we prescribed convective conditions (see Sec. 4.1.2) at the outflow ($r = R_o$). We set the following computational and flow parameters:

$$\mathrm{R}_i = 1, \quad \mathrm{R}_o = 10, \quad \alpha = \pi/10, \mathrm{Re} = \frac{U_{\max}(r)\ r\ \alpha}{\nu} = 100/\pi \quad (\alpha\ \mathrm{Re} = 10),$$
$$\Delta t/\Delta t_\nu = 0.25. \tag{3.10}$$

Fig. 3.8a shows the radial velocity profile as a function of the similarity variable η obtained using FastRK3 and the analytical solution, Eq. (3.7). The numerical solution is in excellent agreement with the analytical solution of the Jeffery-Hamel flow with the relative error $\epsilon = 3.1 \times 10^{-3}$, which also verifies FastRK3 over curved meshes.

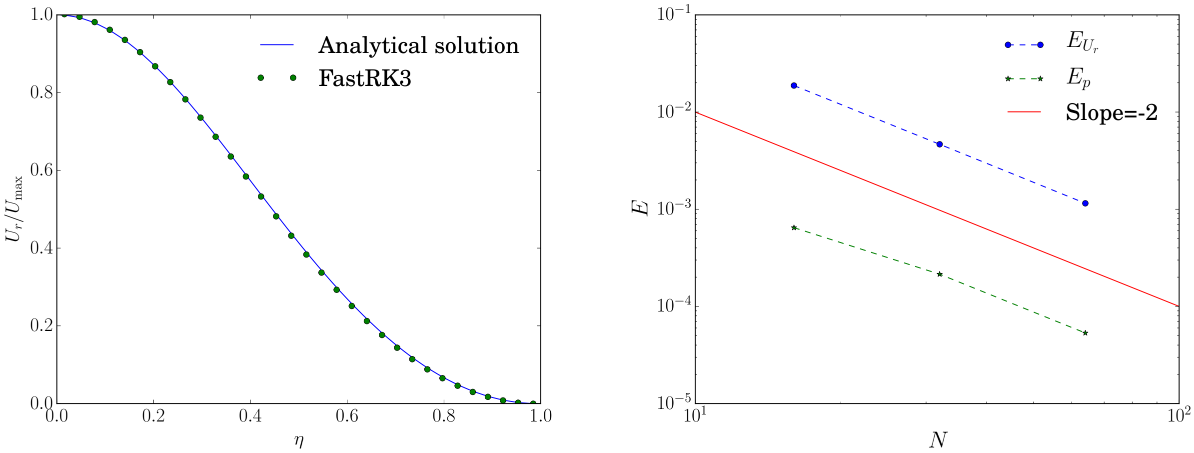

(a) Comparison of velocity (U_r) with solution to Jeffery-Hamel flow: $U_r/U_{\max}$ as a function of η.

(b) Spatial error convergence for Jeffrey-Hamel flow.

Figure 3.8: Jeffery-Hamel flow

We also assessed the effect of curved grid lines on the spatial convergence rate of FastRK3 with the Jeffery-Hamel flow. The dimensionless physical and flow parameters are given in

	$E_{4\varDelta\theta,2\varDelta\theta}$	$E_{2\varDelta\theta,\varDelta u\theta}$	n
$U_r(\theta)/U_\infty$	4.61e-3	1.15e-3	2.02
$p(\theta)/\rho U_\infty^2$	2.17e-4	5.33e-5	2.00

Table 3.2: L_2 norm of spatial errors and spatial convergence rates (or spatial order of accuracy), n, for radial velocity (U_r) and pressure (ϕ) for Jeffery-Hamel flow.

Eq. (3.10). We simulated the flow on meshes of 32×8, 64×16, 128×32 and 256×64 grid points. Figure 3.8b shows L_2 norms of errors between successive solutions as a function of number of grid points in r for radial velocity and pressure ($U_r(\theta)/U_\infty$, $\phi(\theta)/\rho U_\infty^2$). Table 3.1 shows L_2 norms of $E_{4\varDelta\theta,2\varDelta\theta}$ and $E_{2\varDelta\theta,\varDelta\theta}$, and the observed order of accuracy, n, for radial velocity and pressure ($U_r(\theta)/U_\infty$, $p(\theta)/\rho U_\infty^2$). The computed convergence rate n for the radial component of velocity U_r and pressure ϕ are 2.02 and 2.27, respectively. This verifies that, consistently with the discretization of Eqs. (2.15) and (2.16), FastRK3 is second-order accurate in space for velocity and pressure.

3.2 Validation

3.2.1 Lid-driven polar cavity

In order to validate FastRK3, we performed simulations of the lid-driven polar cavity flow for which experimental data by Fuchs & Tillmark (1985) is available, and we used the same geometrical and grid parameters as described in Sec. 3.1.1. The dimensionless physical and flow parameters matching the experiments (Fuchs & Tillmark, 1985) were set as:

$$\mathrm{R}_i = 1.0, \quad \mathrm{R}_o = 2.0, \quad \alpha = 1, \quad U_i = 1, \quad \mathrm{Re}_i = \frac{U_0\,\mathrm{R}_i}{\nu} = 280,\ 340,\ 380,\ \text{and } 410, \tag{3.11}$$

and the time step $\varDelta t$ was prescribed as $\varDelta t/\varDelta t_\nu = 0.125$. The flow was initialized with zero velocity in the interior of the cavity and was advanced in time until reaching the steady state solution with a residual computed using the infinity-norm, $||\phi_n - \phi_{n-1}||_\infty$ smaller than

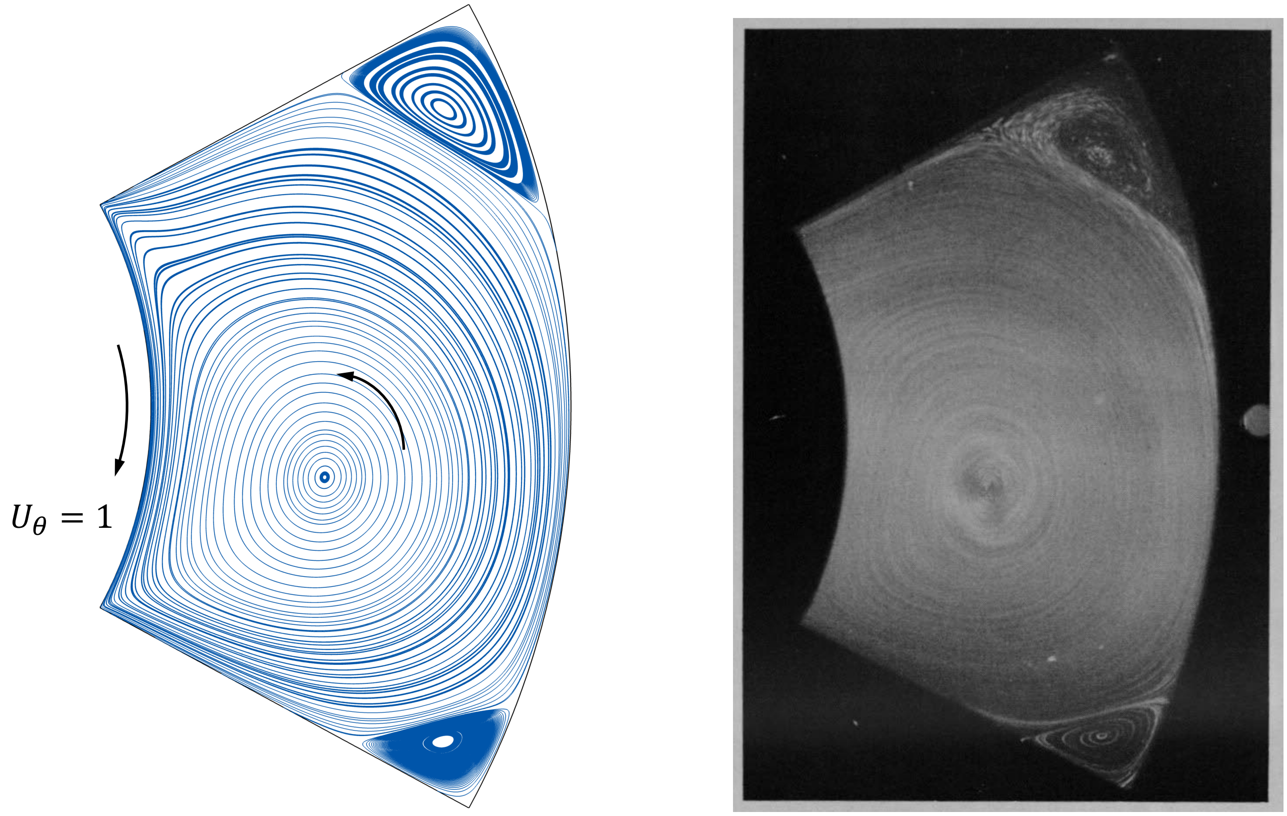

(a) Streamlines of the numerical solution for $\mathrm{Re}_i = 350$

(b) Flow visualization from the experiments of Fuchs & Tillmark for $\mathrm{Re}_i = 350$ (Fig. 7 of Fuchs & Tillmark (1985))

Figure 3.9: Lid-driven polar cavity flow

2×10^{-8}. Figures 3.9a and 3.9b show very good agreement between the streamlines of the numerical solution and the flow visualization of the experiments of the lid-driven polar cavity flow, respectively. The position of the center of the largest vortex in the numerical solution and experiments differs by about 3%. Figure 3.10 shows the radial (U_r) and azimuthal (U_θ) velocity profiles along four radial lines $\theta = \pi/18, -\pi/18, \pi/9$, and $-\pi/9$ and $\mathrm{Re}_i = 410$, 280, 380, and 340, respectively, in comparison with the experimental data of Fuchs & Tillmark (1985). In all four cases, we obtained very good agreement with the experimental results of Fuchs & Tillmark (1985), which also validates FastRK3.

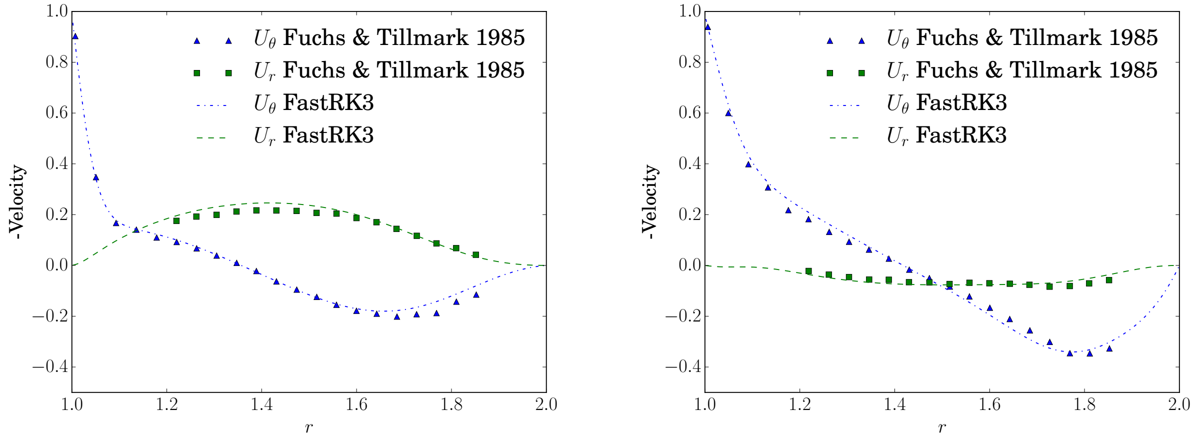

(a) $\theta = \pi/18$, $\mathrm{Re}_i = 410$ (b) $\theta = -\pi/18$, $\mathrm{Re}_i = 280$

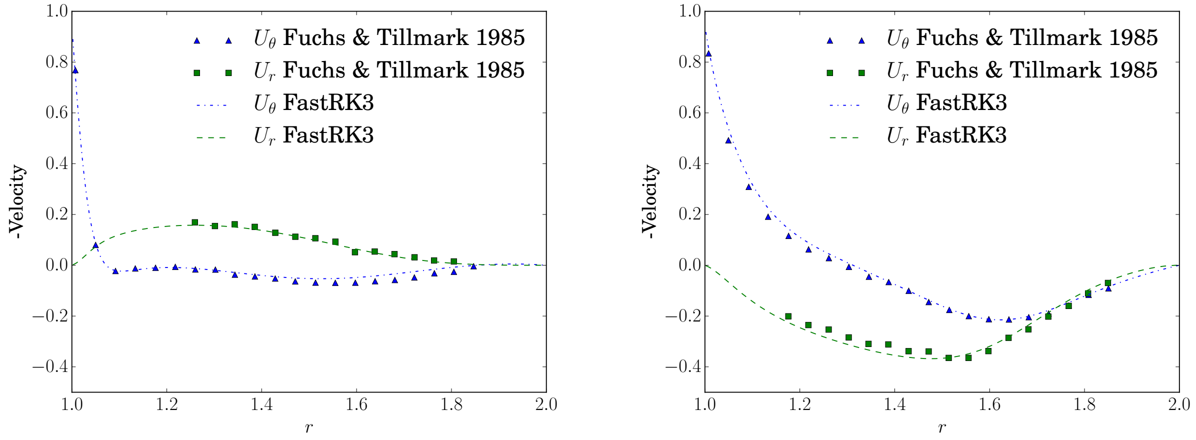

(c) $\theta = \pi/9$, $\mathrm{Re}_i = 380$ (d) $\theta = -\pi/9$, $\mathrm{Re}_i = 340$

Figure 3.10: Comparison of U_θ and U_r along radial lines for the lid-driven polar cavity.

3.3 Numerical analysis on the temporal accuracy of FastRK3

3.3.1 Definition of errors

In this section, in order to verify numerically the order for the temporal accuracy of FastRK3, which was derived theoretically in Sec. 2.4.1, we define three types of errors that we report for our numerical tests in Sec. 3.3.2 and 3.3.3. First, the error, $E_{\tilde{\eta}}$ or E_{η} for standard RK3 or FastRK3, respectively, between two successive time step sizes Δt_1 and Δt_2 for a generic flow variable η is defined as follows:

$$E_{\eta} = ||\eta_{\Delta t_1} - \eta_{\Delta t_2}||_2 \,, \tag{3.12}$$

where $||\cdot||_2$ is the L_2 norm. Next, to determine the relative error $\tilde{E}_{\eta}$ between the values of a generic flow variable η computed using FastRK3 and $\tilde{\eta}$ computed using standard RK3, we first calculate the errors, $\tilde{E}_{\eta,1}$ and $\tilde{E}_{\eta,2}$, as

$$\tilde{E}_{\eta,1} = ||\tilde{\eta}_{\Delta t_1} - \eta_{\Delta t_1}||_2 \,, \tag{3.13}$$

$$\tilde{E}_{\eta,2} = ||\tilde{\eta}_{\Delta t_2} - \eta_{\Delta t_2}||_2 \,, \tag{3.14}$$

and, then, take the absolute value of their difference to compute $\tilde{E}_{\eta}$ as

$$\tilde{E}_{\eta} = \left|\tilde{E}_{\eta,2} - \tilde{E}_{\eta,1}\right| \tag{3.15}$$

Finally, when comparing the solution of FastRK3 with the analytical solution, $\bar{\eta}$, the error $\bar{E}_{\eta}$, is computed as follows. First,

$$\bar{E}_{\eta,1} = ||\bar{\eta} - \eta_{\Delta t_1}||_2 \,, \tag{3.16}$$

$$\bar{E}_{\eta,2} = ||\bar{\eta} - \eta_{\Delta t_2}||_2 \,, \tag{3.17}$$

and, then, $\bar{E}_{\eta}$ is calculated as

$$\bar{E}_{\eta} = \left|\bar{E}_{\eta,2} - \bar{E}_{\eta,1}\right| . \tag{3.18}$$

The error $\bar{E}_{\tilde{\eta}}$ of the standard RK3 solution $\tilde{\eta}$ with respect to the analytical solution $\bar{\eta}$ is computed analogously to Eqs. (3.16)-(3.18) by replacing η with $\tilde{\eta}$.

3.3.2 Numerical verification of theoretical results: Taylor-Green vortex

Periodic boundary conditions In this section, we report numerical results to verify the key results of the theoretical analysis on the temporal accuracy of FastRK3 provided in Sec. 2.4.1, specifically Eqs. (2.59), (2.71), (2.91), and (2.96). For this purpose, we have performed numerical simulations of the two-dimensional Taylor-Green vortex Taylor (1923) using standard RK3 (SK Sanderse & Koren (2012), Eqs. (2.26), (2.28), (2.29)) and FastRK3 (Aithal & Ferrante (2020), Eqs. (2.32), (2.33), (2.34)) methods while applying periodic boundary conditions. The analytical solution of the Taylor-Green vortex flow for x- and z-components of the non-dimensional velocity components, $\bar{u}$ and $\bar{w}$, respectively, are given by

$$\bar{u} = -\omega_0 \frac{k_z}{k^2} \cos\left(k_x x\right) \sin\left(k_z z\right) e^{-k^2 t/\mathrm{Re}}, \tag{3.19}$$

$$\bar{w} = -\omega_0 \frac{k_x}{k^2} \sin\left(k_x x\right) \cos\left(k_z z\right) e^{-k^2 t/\mathrm{Re}}, \tag{3.20}$$

where ω_0 is the amplitude of the initial non-dimensional vorticity, k_x and k_z are non-dimensional wave-numbers of the vortices in the x and z directions such that $k^2 = k_x^2 + k_z^2$. In our test cases, we used $\omega_0 = 100$, $k_x = k_z = 2\pi$ and $\mathrm{Re} = 200$. By requiring $\phi_{n-\frac{3}{2}}$ in order to advance the solution in time, FastRK3 is not a self-starting method, thus, we use standard RK3 to perform the time integration of the first time step from the set initial conditions. All simulations were performed using a 128^2 mesh over a square domain of non-dimensional side-length of unity, for six different time steps, up to a non-dimensional time $T = 1.75008$, at which the magnitude of the maximum vorticity has decayed to about half of its initial value. The smallest non-dimensional time step used was $\Delta t_{\min} = 1.5 \times 10^{-5}$ which corresponds to a total number of time steps $N = 116,672$ and CFL ≈ 0.015. The time step of the other five simulations was sequentially doubled up to $\Delta t_{\max} = 4 \times 10^{-4}$ which corresponds to $N = 3,646$ and CFL ≈ 0.5. Further, for FastRK3, we performed simulations using three different linear extrapolations of ϕ for the first two-stages of RK3: endpoint extrapolation (EP) (Fig. 2.6a), midpoint extrapolation (MP) (Fig. 2.6b), and standard RK3 approximation (SA). The summary of these three extrapolations and their $\alpha - \beta$ coefficients are given in Table 3.3. These three cases were chosen to show that the theoretically predicted accuracy of

FastRK3 for cases A, B and C of Eq. (2.90) is matched by the numerical results of FastRK3 using the EP, MP and SA linear extrapolations, respectively.

Linear extrapolation	α	β	$\alpha - \beta$ relation, Eq. (2.106)	Eq. (2.90)	$\tilde{E}_{G\phi_3}$	$E_{U_{n+1}}$
Endpoint (EP)	1	0	No	Case A	$\mathcal{O}\left(\Delta t^2\right)$	$\mathcal{O}\left(\Delta t^2\right)$
Midpoint (MP)	$\frac{1}{2}$	$\frac{1}{2}$	Yes	Case B	$\mathcal{O}\left(\Delta t^3\right)$	$\mathcal{O}\left(\Delta t^3\right)$
Std. RK3 approx. (SA)	1	$\frac{1}{6}$	Yes	Case C	$\mathcal{O}\left(\Delta t^3\right)$	$\mathcal{O}\left(\Delta t^3\right)$

Table 3.3: FastRK3 test-cases: type of linear extrapolation of ϕ, α and β values, whether the $\alpha - \beta$ relation, Eq. (2.106), is satisfied or not, case of Eq. (2.90), and theoretical global convergence rates of the errors $\tilde{E}_{G\phi_3}$ and $E_{U_{n+1}}$.

Figure 3.11 shows the global error $\bar{E}_{\tilde{U}_i}$ for $i = 1, 2,$ and 3 of the velocity fields computed using the standard RK3 method, for the comparison with the analytical solution of the Taylor-Green vortex. Figure 3.11 shows that $\tilde{U}_1$, $\tilde{U}_2$ and $\tilde{U}_3 = \tilde{U}_{n+1}$ are, respectively, first-, second- and third-order approximations of the exact solution $\bar{U}(t)$. Note that for the third stage, the convergence rate flattens for $\Delta t < 5 \times 10^{-5}$ because the error is reaching the zero-machine value. These results verify Eq. (2.79) used in the theoretical proof of Sec. 2.4.1.

Next, we analyze the stage-wise accuracy of the gradient of pseudo-pressure, $\tilde{E}_{G\phi_1}$, $\tilde{E}_{G\phi_2}$ and $\tilde{E}_{G\phi_3}$ of FastRK3 relative to standard RK3. Figures 3.12a and 3.12b show that the convergence rates of the first and second stages, $\tilde{E}_{G\phi_1}$ and $\tilde{E}_{G\phi_2}$, are first order for both the endpoint and midpoint formulations. Since the midpoint extrapolation of $G\phi$, given in Eqs. (2.30) and (2.31) for $\alpha = 1/2$ and $\beta = 1/2$, satisfies the $\alpha - \beta$ relation, Eq. (2.106), the sum of errors of $G\phi$ introduced by the pressure extrapolation at each time step is $\mathcal{O}(\Delta t^2)$, Eq. (2.90, Case B). Therefore, $\tilde{E}_{G\phi_3}$ for the midpoint formulation is third-order accurate, in agreement with the analytical relation Eq. (2.91) and Table 3.3. In contrast, the endpoint formulation does not satisfy the $\alpha - \beta$ relation, Eq. (2.106), and hence shows a reduction

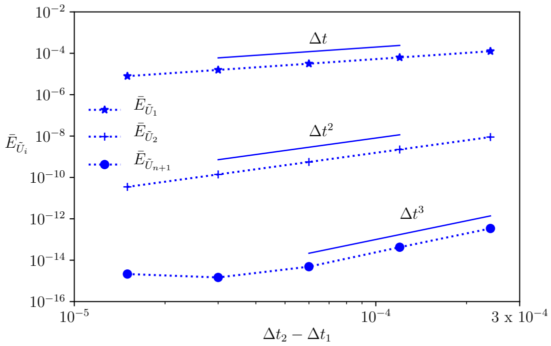

Figure 3.11: Stage-wise error $\bar{E}_{\tilde{U}_i}$ of velocities $\tilde{U}_1$, $\tilde{U}_2$ and $\tilde{U}_3 = \tilde{U}_{n+1}$ (Eq. (2.79)) computed using standard RK3 in comparison with the analytical solution of the Taylor-Green vortex with periodic boundary conditions.

in the convergence rate at the third stage of FastRK3 $\tilde{E}_{G\phi_{n+1}}$, Eq. (2.90, Case A). We also performed a parametric study of α and β to minimize the errors $\tilde{E}_{G\phi_1}$ and $\tilde{E}_{G\phi_2}$. Figure 3.12c shows that for $\alpha = 1$, $\beta = \frac{1}{6}$, which also satisfies the $\alpha - \beta$ relation Eq. (2.106), $G\phi_1$ and $G\phi_2$ are both second-order approximations of $\tilde{G\phi_1}$ and $\tilde{G\phi_2}$, i.e., $c_{\phi_1} = c_{\phi_2} = 0$, Eq. (2.90, Case C). As a result, the error $\tilde{E}_{G\phi_3}$ of FastRK3 SA is third-order accurate, in agreement with the analytical relation (2.91) and Table 3.3. Since we have shown numerically that standard RK3 $\tilde{G\phi_1}$ and $\tilde{G\phi_2}$ can be approximated to second-order by an extrapolation which satisfies the $\alpha - \beta$ relation, we can say that the errors of $\tilde{G\phi_1}$ and $\tilde{G\phi_2}$ relative to the exact solutions $\bar{\phi}(t_n + \check{c}_1 \frac{\Delta t}{2})$ and $\bar{\phi}(t_n + \check{c}_2 \frac{\Delta t}{2})$ sum to $\mathcal{O}(\Delta t^2)$. Now that we have established this relationship between the standard RK3 solutions and the exact solutions, it follows that any extrapolation formulation that produces errors relative to standard RK3 which sum to $\mathcal{O}(\Delta t^2)$, i.e. Eq. (2.90, case B), must also produce errors relative to the exact solutions which sum to $\mathcal{O}(\Delta t^2)$. Thus, we can confirm the point made in Sec. 2.4.2 that Eqs. (2.99) and (2.105) are interchangeable constraints.

Figure 3.13 shows the pressure error (E_p, comparing successive solutions) and velocity error ($\bar{E}_U$, comparing the numerical solution against the analytical solution) for the simulations of the Taylor-Green vortex using FastRK3 with EP, MP, and SA extrapolations, and standard RK3 methods. Figure 3.13a shows that E_p for the midpoint formulation is second-order accurate similarly to standard RK3, while the endpoint formulation shows order-reduction to first-order. This order reduction is due to the fact that the net extrapolation error for the endpoint formulation is first-order. Conversely, the midpoint formulation (MP) and the standard RK3 approximation (SA) which produce third-order solutions for $G\phi_3$ achieve third-order accuracy for velocity (Fig. 3.13b, MP and EP), confirming Eq. (2.96) (Figs. 3.12b and 3.12c). Further, Fig. 3.13b shows that the endpoint formulation (EP) is limited to a second-order solution for the velocity as a result of its second-order solution for $G\phi_{n+1}$ (Fig. 3.12a). Also, Fig. 3.13b, shows that there is an increase in the magnitude of error between standard RK3 and FastRK3 MP as a result of not satisfying the divergence free constraint on U_1 and U_2 to machine precision. However, FastRK3 MP and FastRK3 SA are able to maintain the order of accuracy of standard RK3 for both velocity and pressure as shown in Figs. 3.13b and 3.13a, respectively. Additionally, the relative error for the $x-$component of velocity between the FastRK3 MP solution and the standard RK3 solution, is negligible, e.g., for $\varDelta t = 6 \times 10^{-5}$:

$$\frac{\left|\left|\tilde{U} - U\right|\right|_2}{\left|\left|\tilde{U}\right|\right|_2} = 5.95 \times 10^{-11}. \tag{3.21}$$

Note that the SA coefficients, $\alpha = 1$, $\beta = \frac{1}{6}$, minimize the errors of $\phi-$extrapolation for the Taylor-Green vortex and may vary for other flows. Because of such dependence, we recommend implementing the FastRK3 MP as it is generally third-order accurate in time for velocity and second-order for pressure for free shear flows.

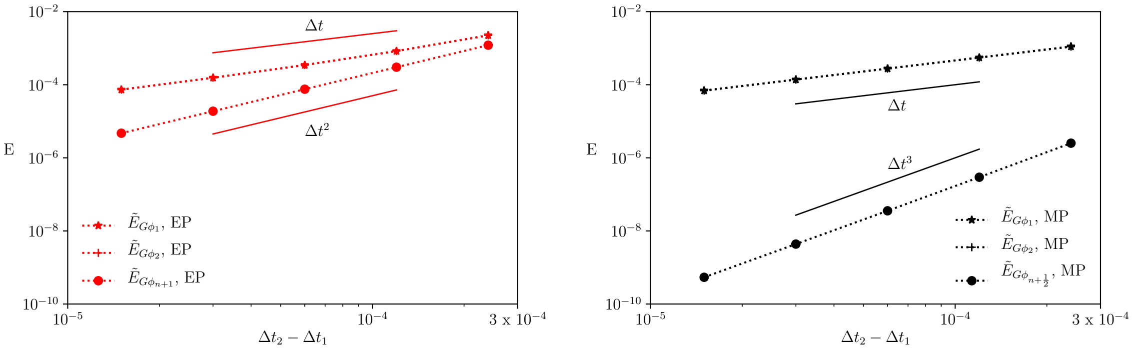

(a) Pressure gradient $G\phi$, endpoint method

(b) Pressure gradient $G\phi$, midpoint method

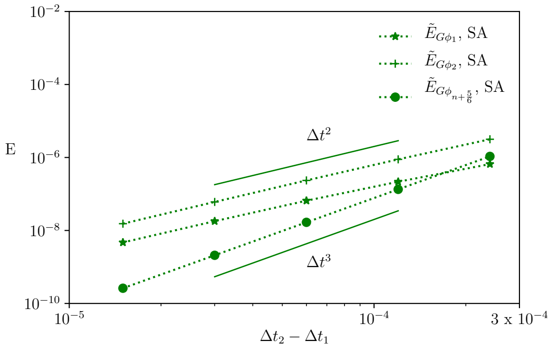

(c) Pressure gradient $G\phi$, standard RK3 approximation method

Figure 3.12: Stage-wise error $\tilde{E}_{G\phi_i}$ of the pressure gradient with respect to standard RK3 for FastRK3 using EP, MP and SA extrapolations of ϕ in (a), (b) and (c), respectively, corresponding to cases A, B and C of Eq. (2.90) and Table 3.3 for the Taylor-Green vortex with periodic boundary conditions.

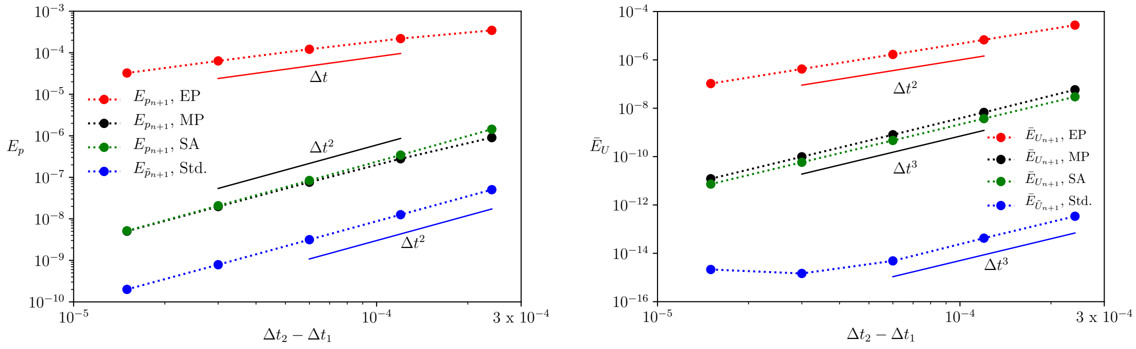

(a) Pressure

(b) Velocity

Figure 3.13: Pressure and velocity errors, E_p (compared with successive solutions) and $\bar{E}_U$ (compared with analytical solution), at the final third-stage of FastRK3 with EP, MP and SA extrapolations and of standard RK3 (Table 3.3) for the Taylor-Green vortex with periodic boundary conditions.

Unsteady Dirichlet boundary conditions Additionally, we have performed numerical simulations of the two-dimensional Taylor-Green vortex flow with unsteady Dirichlet boundary conditions using FastRK3 while keeping the same parameters of the TGV test-case which had periodic boundary conditions and was discussed above. Figure 3.14, similarly to Fig. 3.13, shows the pressure (E_p) and velocity ($\bar{E}_U$) errors at the third-stage of FastRK3 using EP, MP and SA extrapolations of ϕ. Figure 3.14a shows that E_p is first-order accurate for EP extrapolation and second-order accurate for MP and SA extrapolations. Further, Fig. 3.14b shows that $\bar{E}_U$ is second-order accurate for EP extrapolation and third-order accurate for MP and SA extrapolations. Therefore, also with the choice of unsteady Dirichlet boundary conditions (Fig. 3.14), the order of temporal accuracy of FastRK3, for both pressure and velocity, remains the same as that obtained using periodic boundary conditions (Fig. 3.13).

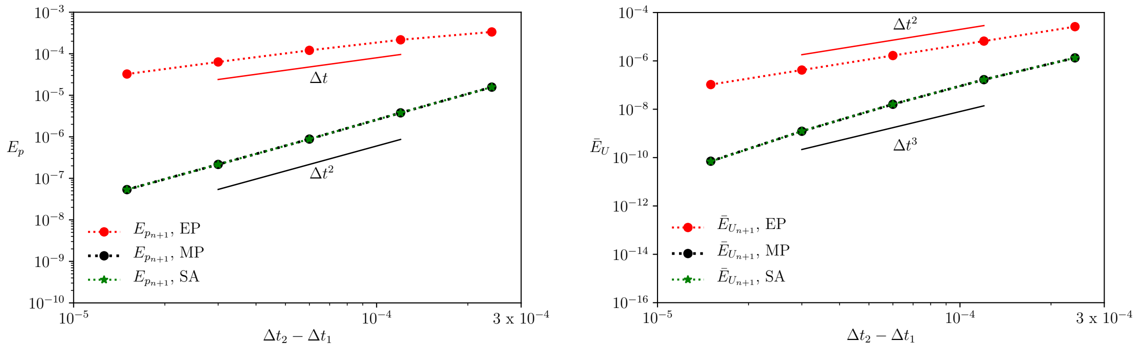

(a) Pressure

(b) Velocity

Figure 3.14: Pressure and velocity errors, E_p (compared with successive solutions) and $\bar{E}_U$ (compared with analytical solution), at the final third-stage of FastRK3 with EP, MP and SA extrapolations (Table 3.3) for the Taylor-Green vortex with unsteady Dirichlet boundary conditions.

3.3.3 Lid-driven polar cavity

In order to test the temporal accuracy of FastRK3 for wall-bounded flows, we have simulated the transient phase of the flow in a lid-driven polar cavity (Fig. 3.15) for which the lid is impulsively started from rest and kept at a constant velocity in time, i.e., quiescent initial conditions $U_\theta(r, t = 0) = U_r(r, t = 0) = 0$, and the lid azimuthal velocity $U_\theta(r = R_i, t \geq 0^+) = U_i = 1$. The computational domain was given by $R_i \leq r \leq R_o$ and $-\alpha/2 \leq \theta \leq \alpha/2$ with an orthogonal grid of 256×192 grid points, in the radial and azimuthal directions, respectively. No-slip boundary conditions, as described in Aithal & Ferrante (2020), were applied at the four boundaries of the domain. The fluid flow in the azimuthal direction, θ, is caused by viscous diffusion of momentum in the radial direction, r. The dimensionless physical and flow parameters were set as:

$$\mathrm{R}_i = 1.0, \quad \mathrm{R}_o = 2.0, \quad \alpha = 1, \quad U_i = 1, \quad \mathrm{Re}_i = \frac{U_i\ \mathrm{R}_i}{\nu} = 280. \tag{3.22}$$

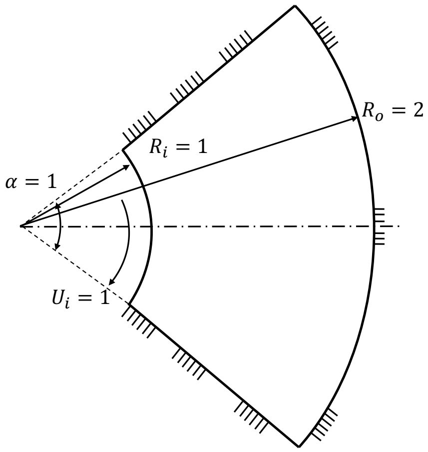

Figure 3.15: Flow schematic of the lid-driven polar cavity

All simulations for five different time steps were performed up to a non-dimensional time $T = 1.0$. The smallest time step used was $\Delta t_{\min} = 1.1\times10^{-4}$ which corresponds to $N = 17572$ time steps and CFL$= 3.125 \times 10^{-2}$. The CFL of the other four simulations was sequentially doubled up to $\text{CFL}_{\max} = 0.5$ which corresponds to $N = 1097$ and $\Delta t = 9.1 \times 10^{-4}$. We performed simulations using FastRK3 MP and standard RK3. Figure 3.16 shows the global errors E_{U_r}, E_{U_θ} and E_p, as defined in Eq. (3.12), between successive solutions respectively for U_r/U_i, U_θ/U_i and p computed using standard RK3 (Fig. 3.16a) and FastRK3 MP (Fig. 3.16b). The average temporal convergence rates of Std. RK3 and FastRK3 are given in Table 3.4. We observe a loss of accuracy from third-order to second-order for both methods from the Taylor-Green vortex results of Fig. 3.13 to the lid-driven cavity flow results of Fig. 3.16, which is consistent with the temporal order reduction discussed in 'stiff' wall-bounded flows for RK-based methods by Sanderse (2013), for the Adams-Bashforth method by Aithal & Ferrante (2020), and for explicit RK methods as shown by Sanz-Serna *et al.* (1986). We should also mention that for trivial and non-stiff problems such as the Stokes' first problem or the laminar channel flow, FastRK3 produces 3rd-order temporal accuracy as standard RK3. In summary, FastRK3 with MP shows the same order of temporal accuracy for velocity and pressure at the last stage of standard RK3, and the results are consistent with the results summarized in Table 2.5.

Std. RK3			FastRK3		
$\tilde{U}_\theta$	$\tilde{U}_r$	$\tilde{p}$	U_θ	U_r	p
1.94	1.91	1.74	1.94	1.91	1.94

Table 3.4: Average temporal order of accuracy for Std. RK3 and FastRK3

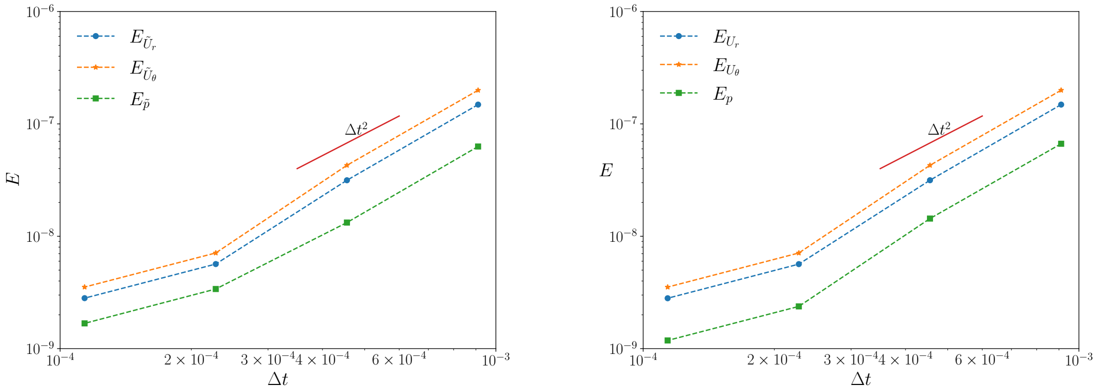

(a) Std. RK3 $\left(\tilde{U}_r, \tilde{U}_\theta, \tilde{p}\right)$.

(b) FastRK3 (U_r, U_θ, p).

Figure 3.16: Global errors between successive solutions of the radial and azimuthal velocities, and pressure for (a) standard RK3 and (b) FastRK3 using MP extrapolation for the lid-driven polar cavity flow.

3.4 Summary

We have developed a new projection-method, called FastRK3 to integrate the NS equations in time for simulating incompressible flows over curved walls. FastRK3 solves the orthogonal formulation of the incompressible NS equations in curvilinear coordinates rather than the general curvilinear coordinates. This choice has allowed us to develop an FFT-based Poisson solver for pressure, called FastPoc, for the grids whose components of the metric tensor are independent of one spatial direction. In summary, we have:

- adopted the orthogonal formulation of the incompressible NS equations in curvilinear coordinates, Eqs. (2.15)-(2.16),
- developed an explicit and direct pressure-correction method, FastRK3, that requires solving the Poisson equation for pressure only once per time step, Eqs. (2.32)-(2.34),
- developed FastPoc, an FFT-based, direct Poisson solver for pressure (Sec. 2.3) for the grids whose components of the metric tensor are independent of one spatial direction: surfaces of linear translation (e.g., curved ramps, and bumps) and surfaces of revolution (e.g., axisymmetric ramps),
- shown that FastPoc is thirty to sixty times faster than *hypre* SGS multigrid for tolerance set at 10^{-6} and 10^{-12}, respectively, and the entire NS solver, FastRK3, is four to seven times faster when using FastPoc rather than multigrid accordingly to these set tolerance values (Sec. 2.3.1),
- verified and validated FastRK3 for wall-bounded flows (Sec. 3.1 and 3.2.1),
- shown that FastRK3, while solving the Poisson equation for pressure only once per time step versus thrice of standard RK3, produces nearly identical results as those of standard RK3 with an L_2 norm difference for the velocity components and pressure of $\mathcal{O}(10^{-3})$ (Sec. 3.1.1),
- shown that FastRK3 is second-order accurate in space for velocity and pressure (Sec. 3.1),
- shown that reduction of the kinetic energy in the inviscid limit for the unsteady lid-driven polar cavity flow is 0.24% in 10,983 time steps (Sec. 3.1.1),

- derived analytically the temporal accuracy of FastRK3 (Sec. 2.4.1),
  - derived the condition that the RK coefficients need to satisfy in order to preserve the temporal accuracy of the underlying RK3 method, Eq. (2.88),
  - shown analytically that the temporal accuracy of velocity in the final stage of FastRK3 depends on the sum of errors introduced by the linear extrapolation of $G\phi$, Eq. (2.89),
  - derived the condition that the linear extrapolation of $G\phi$ needs to satisfy in order to preserve the temporal accuracy of the underlying RK3 method, i.e., cases B and C of Eq. (2.90),
  - derived analytically the $\alpha-\beta$ relation, Eq. (2.107), using the conditions Eqs. (2.98) and (2.99), and, generalized it to an s-stage RK method as in Eq. (2.106) (Sec. 2.4.2),
- verified numerically the temporal accuracy of FastRK3 (Sec. 3.3)
  - verified the key analytical results of the proof of the temporal accuracy of FastRK3 by reporting the numerical results obtained for the Taylor-Green vortex flow (Sec. 3.3.2),
  - shown numerically that FastRK3 (MP and SA) is third-order accurate in time for velocity and second-order accurate in time for pressure for free-shear flows with both periodic and unsteady Dirichlet boundary conditions (Sec. 3.3.2),
  - shown numerically that FastRK3 MP is second-order accurate in time for velocity and pressure for 'stiff' wall-bounded flows (Sec. 3.3.3).

The advancements stated above prove that FastRK3 is apt for simulations of wall-bounded laminar and turbulent flows over curved walls. FastRK3 can be employed in existing incompressible and low-Mach number NS solvers (e.g., DNS and RANS solvers) to simulate flows over curved surfaces (e.g., Aithal & Ferrante (2019)), and improve their computational performance. The new method can also be extended to simulate particle-, droplet-, and bubble-laden flows in wakes and over curved surfaces with the use of the appropriate methodology to simulate the multiphase flow (e.g., Dodd & Ferrante (2014)). Finally, the time integration methodology of FastRK3, Eqs. (2.32)-(2.34), to solve the discretized incompressible NS equations, Eq. (2.21), can be used independently from the formulation used to write the governing equations (e.g., Cartesian, orthogonal, etc.) and to perform its spatial discretization (e.g., finite difference and finite volume).

Chapter 4

DNS OF TURBULENT BOUNDARY LAYER SEPARATING OVER A CURVED WALL

4.1 Simulation setup

4.1.1 Computational domain and grid

In this chapter, we investigate the turbulent flow of a spatially developing turbulent boundary layer (SDTBL) separating over the circular arc experimentally studied by Song & Eaton (2004). First, we validate FastRK3 by comparing our DNS results with the experimental results of Song & Eaton (2004). Next, we analyze our DNS results to explain the physical mechanisms of turbulent flow separation.

Song & Eaton (2004) studied experimentally the Reynolds number effects on the separation, reattachment, and recovery of turbulent flows over a ramp. Figure 4.1 shows a schematic of the flow domain used in their experiments. The ramp is a circular arc with a radius R of 127 mm. The ramp height h and length L were 21 mm and 70 mm, respectively. Song & Eaton (2004) define a reference station (x_r) two ramp-lengths upstream of the ramp. They varied the Reynolds number based on the momentum thickness at x_r from $\mathrm{Re}_{\theta_0} = 1100$ to 20,100. We use their results at $\mathrm{Re}_{\theta_0} = 1100$ in the present validation study. We place the inflow plane of the DNS at the reference station with the Reynolds number based on inflow boundary layer thickness $Re_{\delta_0} = \tilde{U}_\infty \tilde{\delta}_0 / \tilde{\nu} = 9000$ where, $\tilde{U}_\infty$, $\tilde{\delta}_0$ and $\tilde{\nu}$ are the dimensional free-stream velocity, the dimensional inflow boundary layer thickness at the inflow plane and the dimensional kinematic viscosity, respectively. Since we use the free-stream velocity and inflow boundary layer thickness as reference velocity and length scales to non-dimensionalize the NS equations, $Re_{\delta_0} = 1/\nu = 9000$, where the quantities not accented with $\sim$ are dimensionless: $U_\infty = 1$, $\delta_0 = 1$ and ν is the dimensionless kinematic viscosity, such that the resulting inflow $\mathrm{Re}_{\theta_0} = 1100$. This is the result of performing a separate "Code A" simulation of the SDTBL over a flat plate to generate the turbulent inflow conditions at the desired Re_{θ_0} (see Sec. 4.1.3). The dimensional inflow boundary layer thickness at the inflow plane is $\tilde{\delta}_0$=25.6 mm. All dimensions are non-dimensionalized by $\tilde{U}_\infty$ and $\tilde{\delta}_0$. Throughout this chapter, all variables are dimensionless unless they are accented with $\sim$. The ramp profile used in the experiments has a discontinuity of its first-derivative at the location where the circular arc ends intersecting the horizontal wall (Fig. 4.1). We eliminate this discontinuity by using spline interpolation in a small region ($0.9 \leq x/L \leq 1$) in order to generate a smooth orthogonal mesh over the ramp (Fig. 4.2). Figure 4.2 shows the computational domain used in our simulations. The length scales non-dimensionalized by the boundary layer thickness at the inflow plane are

$$L_r = 5.47\delta_0,\ L = 2.73\delta_0,\ L_s = 13.67\delta_0,\ R = 4.96\delta_0,\ h = 0.82\delta_0. \tag{4.1}$$

The dimensions of the computational domain, L_ξ, L_η and L_ζ, normalized by δ_0, and the number of grid points, N_x, N_y and N_z in the streamwise, wall-normal and spanwise directions, respectively, are listed in Table 4.1. The orthogonal grid generator is discussed in detail in Appendix D. As shown in Fig. 4.2, we define the coordinate system such that the streamwise coordinate (ξ or x) of the leading edge of the ramp is set to zero and the wall-normal coordinate (η or y) are always zero at the wall. The non-dimensional quantities in wall-units carry the superscript '+', i.e., $\langle\hat{U}\rangle^+ = \langle\hat{U}\rangle/u_\tau$ and $\eta^+ = \eta u_\tau/\nu$, where $\langle\ldots\rangle$ represents the spatial averaging in the spanwise ζ-direction in addition to time averaging of the enclosed quantity, $u_\tau = \sqrt{\tau_w/\rho}$ is the friction velocity, τ_w is the wall shear stress, and ρ is the fluid density. The zero subscript refers to the conditions at the inflow plane where $\mathrm{Re}_{\theta_0} = 1100$ at $x/L = -2$ from the ramp as in the experiments.

The grid spacing is $\varDelta\xi^+ = 8$, $\varDelta\eta^+_{\mathrm{min}} = 0.7$ and $\varDelta\zeta^+ = 12$, where the grid in the wall-normal direction is stretched gradually to have a fine grid close to the wall. We use the grid-stretching function given by Ferrante & Elghobashi (2004) and the grid stretching parameter is $\gamma = 0.66$. The turbulent inflow conditions were generated with the method of Ferrante &

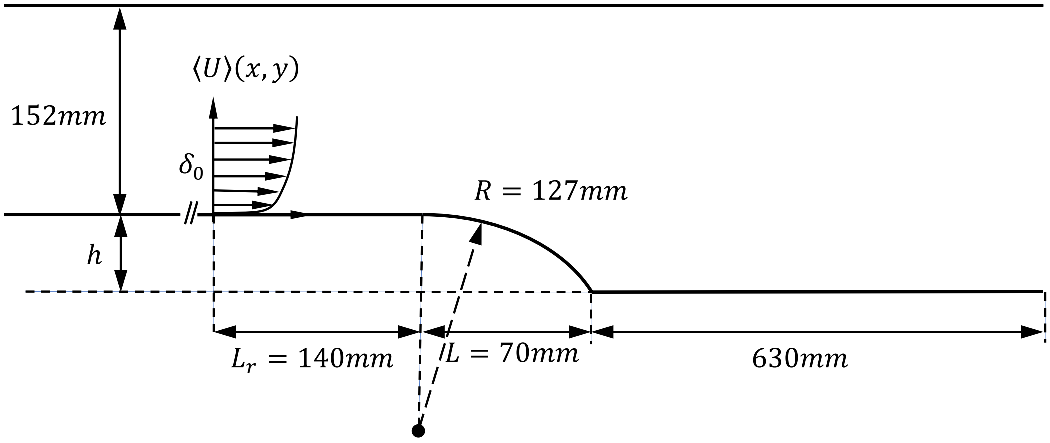

Figure 4.1: Flow schematic of the experiment of Song & Eaton (2004).

Elghobashi (2004). In order to have enough grid resolution to resolve the mixing layer created by the flow separation over the curved ramp, we keep the maximum value of $\Delta < 3.58\eta_k$, where $\Delta = \sqrt[3]{\Delta\xi\Delta\eta\Delta\zeta}$ and η_k is the Kolmogorov scale. Pope (2000) notes that the peak dissipation occurs at $24\eta_k$ and the bulk of the dissipation occurs in the range $[8\eta_k, 60\eta_k]$. Therefore, the employed computational grid resolves most of the dissipation spectrum. The timestep size is $\Delta t = 0.03\ \nu/u_\tau^2$ and we advance the solution up to $T = 450 \approx 8100\nu/u_\tau^2$ and compute the statistics every ten timesteps during the time interval $150 \leq t \leq 450$ which corresponds to 25 flow-throughs at a non-dimensional velocity of 0.9 U_∞.

L_x	L_y	L_z	N_x	N_y	N_z
$20\delta_0$	$4\delta_0$	$10\delta_0$	1024	128	512

Table 4.1: The dimensions of the computational domain, L_x, L_y and L_z, and the number of grid points, N_x, N_y and N_z in the streamwise, wall-normal and spanwise directions, respectively.

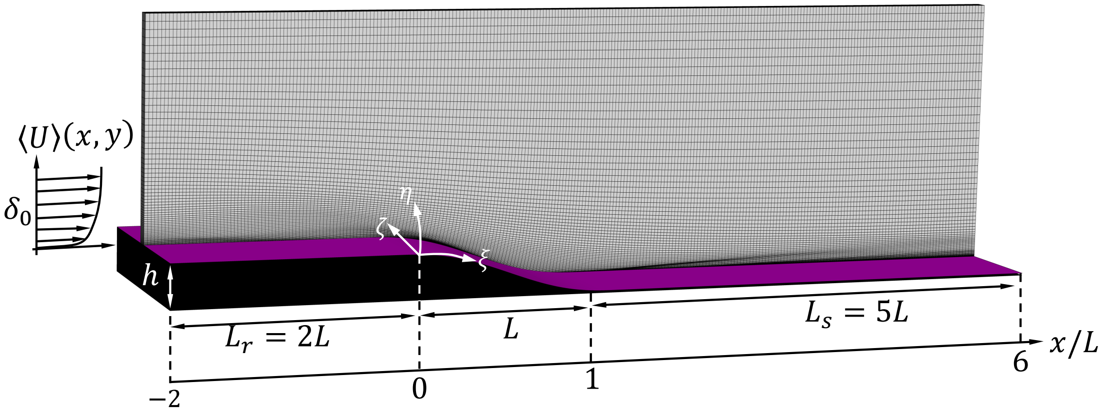

Figure 4.2: Computational domain used in the present DNS.

4.1.2 Boundary conditions

Figure 4.3 shows a schematic of the boundaries of the computational domain on which we impose the following boundary conditions to simulate SDTBL over the ramp. Note that FastRK3, described in Sec. 2.2 requires special considerations for imposing convective outflow boundary conditions which is described herein. Since for spatial discretization FastRK3 uses the second-order central difference scheme, only one plane of ghost cells is required at each boundary.

Spanwise planes Periodic boundary conditions are applied in the spanwise ζ-direction for ϕ_i and the three velocity components $\hat{U}_i$ and $\hat{U}_i^*$ for the three stages $i = 1, 2, 3$ of the RK3 scheme.

Inflow plane At the inflow plane, we impose a Neumann condition for ϕ_i:

$$\frac{\delta \phi_i}{\delta \xi} = 0 \quad \text{at} \quad \xi = -2L, \quad \text{for} \quad i = 1, 2, 3, \tag{4.2}$$

where $\delta/\delta\xi$ is the finite difference operator in the ξ-direction. For simulating turbulent flows we extend the method of Ferrante & Elghobashi (2004) to orthogonal coordinates in order

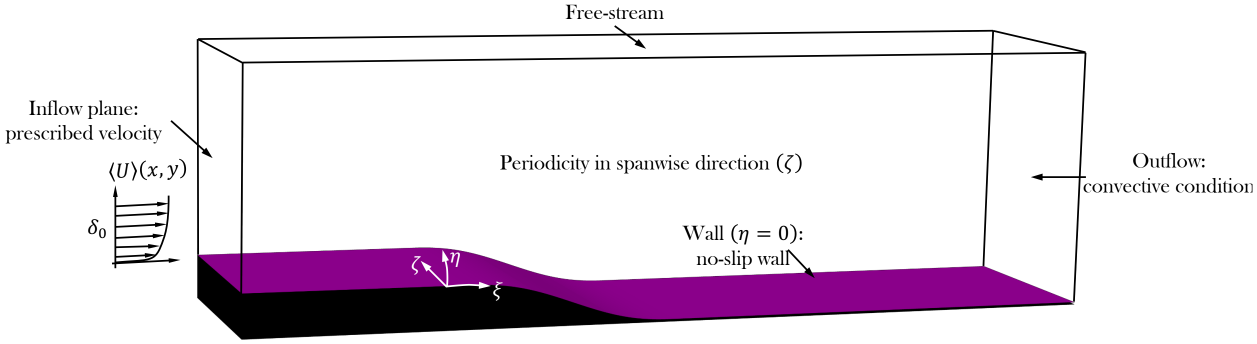

Figure 4.3: A schematic of the computational domain for the simulation of incompressible flows over curved walls, the boundary conditions are also shown.

to generate and apply turbulent inflow conditions, as described in Sec. 4.1.3.

Free-stream plane We impose the Neumann condition for ϕ_i and the velocity components at the free-stream plane,

$$\frac{\delta \phi_i}{\delta \eta} = 0 \quad \text{and} \quad \frac{\delta \hat{U}_i}{\delta \eta} = \frac{\delta \hat{U}_i^*}{\delta \eta} = 0 \quad \text{at} \quad \eta = L_\eta, \quad \text{for} \quad i = 1, 2, 3, \tag{4.3}$$

where $\delta/\delta\eta$ is the finite difference operator in the η-direction.

Outflow plane At the outflow plane, a zero pressure gradient in the streamwise ξ-direction ($\delta\phi_i/\delta\xi = 0$) is applied at $\xi = L_\xi$ for $i = 1, 2, 3$ of the RK3 scheme. In order to apply the outflow boundary conditions to the velocity components, we consider the following convective condition (Lowery & Reynolds, 1986):

$$\frac{d\hat{U}}{dt} + \hat{U}_c(\eta, t)\ G_\xi \hat{U} = 0, \tag{4.4}$$

where $G_\xi \hat{U}$ is the ξ-component (normal to the outflow plane) of $G\hat{U}$, and $\hat{U}_c(\eta, t)$ is the convective velocity at the outflow plane which is computed as the instantaneous streamwise velocity component averaged in the homogeneous spanwise ζ-direction. We use the same coefficients $\breve{\mathbf{a}}$ and $\breve{\mathbf{c}}$ defined in Eq. (2.24) to integrate Eq. (4.4) in time. We first define the array $f(\hat{U})$ as

$$f(\hat{U}) = \hat{U}_c G_\xi \hat{U}, \tag{4.5}$$

and then advance the velocity U_i at the outflow plane in time by integrating Eq. (4.4) using the RK3 scheme, Eq. (2.26), as

$$\hat{U}_i = \hat{U}_n - \Delta t \sum_{j=1}^{i} \breve{a}_{ij} f(\hat{U}_{j-1}) \quad \text{for} \quad i = 1, 2, 3. \tag{4.6}$$

No-slip wall The no-slip boundary condition is applied to the velocity field at the wall (Fig. 4.3) for the three steps of RK3 ($i = 1, 2, 3$):

$$\hat{U}_n = \hat{U}_i = 0. \tag{4.7}$$

We apply a zero pressure gradient in the wall-normal η-direction ($\delta\phi_i/\delta\eta = 0$) for $i = 1, 2, 3$ of the RK3 scheme.

4.1.3 Generating turbulent inflow conditions

The DNS of a spatially-developing turbulent boundary layer (SDTBL) requires that the inflow velocity satisfy the three-dimensional, unsteady Navier-Stokes equations. The prescribed inflow values of the three time-dependent velocity components, therefore, must be obtained *a priori* by an auxiliary DNS of the same flow. This auxiliary DNS, denoted as Code A, must be synchronized with the main simulation, denoted as Code B, such that at each time step, the values of the three velocity components on a plane at a fixed streamwise location in the auxiliary domain are copied to the inlet plane of the main simulation. Ferrante & Elghobashi (2004) developed a method for generating inflow conditions for DNS of SDTBLs where the instantaneous fluctuating velocity field on a selected plane in Code A is used as the instantaneous inflow conditions for Code B.

In order to perform DNS of SDTBLs separating over curved walls, we have incorporated in FastRK3, the method of Ferrante & Elghobashi (2004) for generating turbulent inflow

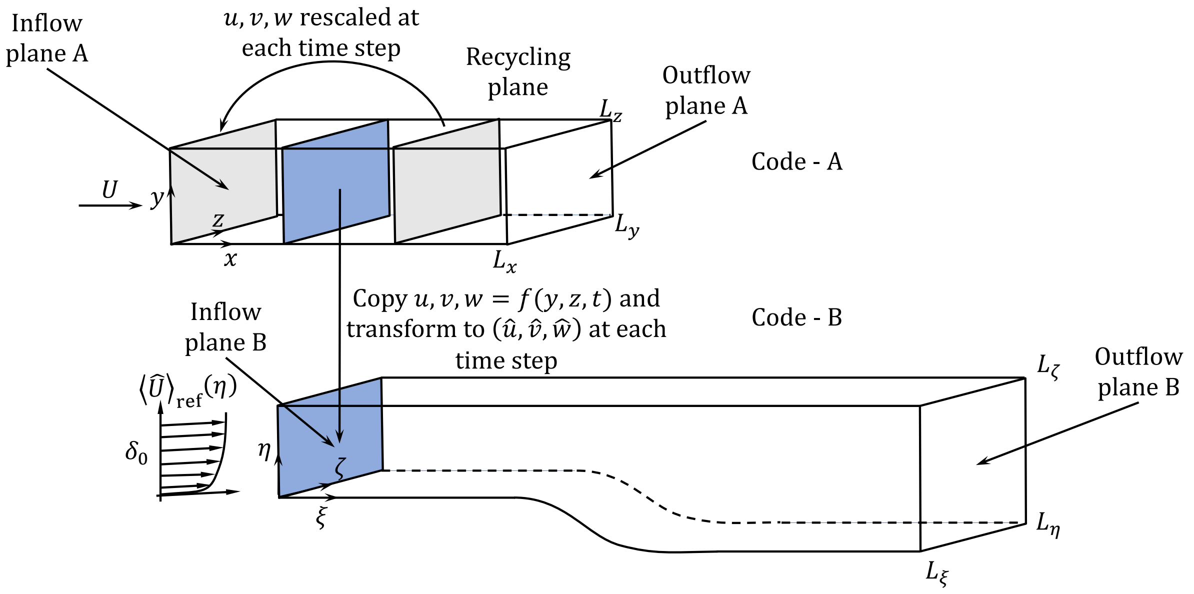

Figure 4.4: Schematic of the computational domains of the auxiliary simulation (Code A) and the main simulation (Code B).

conditions. Figure 4.4 shows the schematic of the computational domains of the auxiliary simulation (Code A) and the main simulation (Code B). The Cartesian components of the instantaneous fluctuating velocity field on the selected plane in Code A, (u, v, w) are transformed to the contravariant components $(\hat{u}, \hat{v}, \hat{w})$ using Eq. (2.7). The mean streamwise velocity at the inflow plane of Code B, denoted as $U_{\text{ref}}(y)$, is then computed using the law-of-the-wall (Coles, 1956; Prandtl, 1925; von Kármán, 1930). The procedure to compute $U_{\text{ref}}(y)$ is explained in Appendix A of Ferrante & Elghobashi (2004). Note that we use a non-dimensional free-stream velocity $U_\infty = 1$ in our simulations similarly to Ferrante & Elghobashi (2004). The velocity $U_{\text{ref}}(y)$ is then transformed to its contravariant components $\hat{U}^i_{\text{ref}}$. Finally, the fluid velocity at the inlet is given by the sum of the mean and fluctuation components, $\hat{U}^i = \hat{U}^i_{\text{ref}} + \hat{u}^i$.

4.2 Results

In this section, we analyze the DNS results of a SDTBL separating over the circular arc of Song & Eaton (2004) at $\mathrm{Re}_{\theta_0} = 1100$. Since we solve the governing equations in orthogonal curvilinear coordinates, we obtain the contravariant components of the velocity field from FastRK3. Therefore, we can analyze the flow physics in both orthogonal curvilinear coordinates and Cartesian coordinates. However, we need to transform the contravariant components of the flow properties of interest to their Cartesian components. The transformation equation for vectors is given in Eq. (2.7). In the case of a second-order tensor, say $\hat{A}^{ij}$, the Cartesian components A^{ij} are given by

$$A^{ij} = \frac{\partial x^i}{\partial \xi^m} \frac{\partial x^j}{\partial \xi^n} \hat{A}^{mn}. \tag{4.8}$$

Further, the Cartesian coordinates all have the physical dimensions of length but this is not true in general for curvilinear coordinates (for e.g., polar coordinates r and θ have different physical dimensions). Thus, the contravariant components of velocity $\hat{U}^i = \partial \xi^i / \partial t$ would not all have the same dimensions. The physical components of the contravariant velocity vector $\hat{U}^i$, which has the same physical dimensions as velocity $\mathbf{U}$ are given by (Aris, 1962)

$$\hat{U}^i_p = \hat{U}^i h_i, \quad (\text{no sum on } i), \tag{4.9}$$

where, h_i are the scale factors defined in Eq. (2.13). The above equation can be extended to a second-order tensor, say $\hat{A}^{ij}$. The physical components $\hat{A}^{ij}_p$ are given by

$$\hat{A}^{ij}_p = \hat{A}^{ij} h_i h_j, \quad (\text{no sum on } i \text{ and } j). \tag{4.10}$$

Note that this conversion of curvilinear components to physical components ensures that they have the same physical dimensions as their Cartesian counterparts. The physical components are then non-dimensionalized as any other Cartesian variable. Henceforth, we omit the explicit indication of the subscript $\cdot_p$ for physical components of the quantities in the orthogonal curvilinear coordinates for simplicity of notations. We distinguish the Cartesian components of tensors from the physical components in the orthogonal curvilinear coordinates by denoting the former with subscript, for example A_{11}, while we denote the latter with a hat and superscript, for example, $\hat{A}^{11}$.

In Sec. 4.2.1, we validate FastRK3 by comparing with the experimental results of Song & Eaton (2004). In Secs. 4.2.2 and 4.2.3, we discuss the mean profiles of pressure and velocity, and the profiles of turbulence kinetic energy and Reynold stresses, respectively, in both Cartesian and curvilinear orthogonal coordinates. In Secs. 4.2.4 and 4.2.6, we analyze the budgets of the turbulence kinetic energy and Reynold stresses to identify the key mechanisms of turbulence in the separated flow over the curved ramp. Finally, we summarize all the findings in Sec. 4.3.

4.2.1 Validation for a turbulent separated flow

Reynolds stresses Figure 4.5 shows the comparison for the vertical profiles of the Reynolds stresses between the experiments by Song & Eaton (2004) and our DNS at the leading edge of the ramp $x/L = 0$. The DNS profiles are obtained by spatial averaging in the spanwise (ζ) direction and time-averaging over a nondimensional time $t = 150 \approx 5400\nu/u_\tau^2$. We see that the Reynolds stress profiles are close to the experimental profiles.

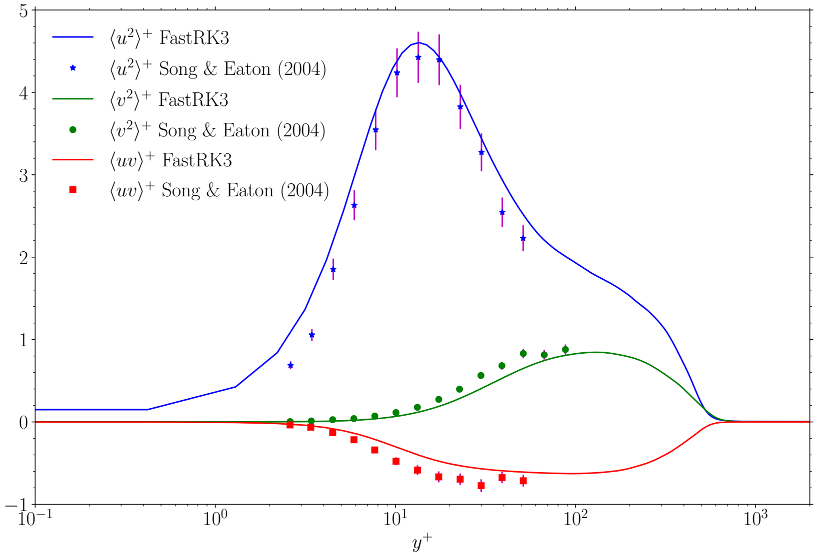

Figure 4.5: Comparison of the Reynolds stress profiles at the leading edge of the ramp, $x/L = 0$ with the experimental data of Song & Eaton (2004). Experimental error bars are also shown in magenta.

Coefficient of friction Figure 4.6 shows the streamwise development of mean skin friction coefficient c_f. We get good agreement with the experimental values up to the trailing edge of the ramp, $x/L = 1$. The mean skin friction coefficient in (Song & Eaton, 2004) was computed using the log-law fitting of the mean velocity profile to estimate the wall-shear stress, which is inaccurate for separated flows considering that the mean velocity profile deviates significantly from the log-law in the separated and post-reattachment (recovery) regions. Indeed, in Sec. 4.2.2, the DNS results show that the mean velocity profiles differ significantly from the log-law in such regions. Further, part of the discrepancy in the c_f values downstream of the trailing edge of the ramp may also be due to the slight changes we applied to smoothen the geometry with the spline interpolation to avoid the discontinuity in its first derivative as described in Sec. 4.1.1.

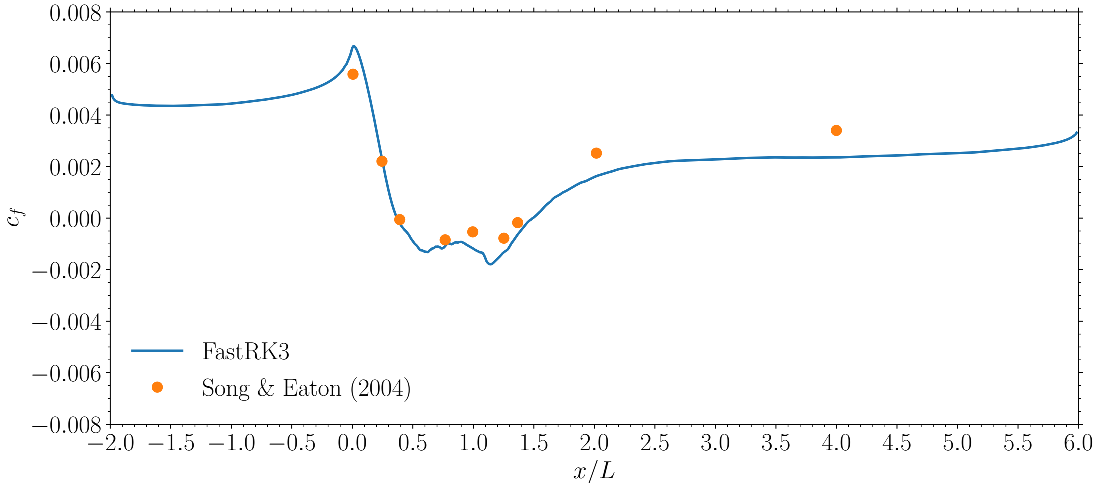

Figure 4.6: Comparison of the c_f profile for the flow over circular arc with experimental values of Song & Eaton (2004).

Separation bubble properties The mean separation and reattachment locations, x_{sep}/L and x_{rea}/L, respectively, are listed in Table 4.2. We get good agreement of x_{sep}/L with the experimental value. Due to the smoothening of the ramp profile using spline interpolation at $x/L = 1$, we see a discrepancy in the value of x_{rea}/L with respect ot the experimental values. Table 4.2 also shows the good agreement of the DNS and experimental results for the separation bubble properties at $x/L = 1$: separation bubble, S, height at which the maximum reverse flow velocity U_N is reached, N and the ratio U_N/U_e, where U_e is the edge velocity of the boundary layer.

	x_{sep}/L	x_{rea}/L	S	N	U_N/U_e
Song & Eaton (2004)	0.40	1.36	$0.21\delta_0$	$0.07\delta_0$	-0.12
FastRK3	0.37	1.49	$0.21\delta_0$	$0.06\delta_0$	-0.10

Table 4.2: Comparison of the DNS results with the experiments of Song & Eaton (2004) of the mean separation and reattachment locations, x_{sep}/L and x_{rea}/L, respectively, and the separation bubble properties at $x/L = 1$: separation bubble, S, height at which the maximum reverse flow velocity U_N is reached, N and the ratio U_N/U_e, where U_e is the edge velocity of the boundary layer.

4.2.2 Mean velocity profiles

Figure 4.7 shows the contours of the mean Cartesian streamwise ($\langle U\rangle/U_\infty$) and wall-normal ($\langle V\rangle/U_\infty$) components of velocity. Figure 4.7b shows the separation bubble along with the streamlines and the isoline where $\langle U\rangle = 0$. The mean pressure contour $\langle p\rangle$ is shown in Fig. 4.8a. Figure 4.8 shows the profiles of mean Cartesian streamwise ($\langle U\rangle/U_\infty$) and wall-normal ($\langle V\rangle/U_\infty$) components of velocity. We identify eight streamwise stations (A-H) where each station is represented by a different color as shown in Fig. 4.8. The separation x_{sep} and reattachment x_{rea} points are denoted by magenta and green, respectively. The streamwise locations of the stations (A-H) are shown in Table 4.3. Figure 4.10 also shows the spatial development of the skin friction coefficient c_f. Figure 4.11 shows the profiles of mean Cartesian x-component of velocity, $\langle U\rangle/U_\infty$ (Fig. 4.11a), and y-component of velocity, $\langle V\rangle/U_\infty$ (Fig. 4.11b). Figure 4.13 shows the profiles of mean Cartesian x-component of velocity, $\langle U\rangle_0^+$ (Fig. 4.13a), and y-component of velocity, $\langle V\rangle_0^+$ (Fig. 4.13b), normalized by the viscous scales at station A. The log-law is indicated by the solid black line in Fig. 4.13a. We notice that the profiles of mean x-component of velocity, $\langle U\rangle_0^+$, deviates considerably from the log-law in the separation and recovery regions, i.e., at stations C-H. The velocity profiles at B are already affected by the presence of the ramp and show deviations from the flat-plate behavior of station A. Typically, $\langle V\rangle/U_\infty \ll 1$ for flat-plate TBL, however, we see that $|\langle V\rangle|/U_\infty \approx \mathcal{O}(1)$ at stations B-G. The flow decelerates due to the adverse pressure gradient and eventually separates at C. We observe reversed flow ($\langle U\rangle < 0$) at stations D and E and the flow reattaches at F. The flow, then, starts to returning towards its characteristics (e.g., mean velocity profiles and Reynolds stresses) of a zero-pressure-gradient (ZPG) SDTBL, as seen in stations G and H. Figure 4.9 shows the profiles of mean contravariant streamwise ($\langle \hat{U}\rangle/U_\infty$) and wall-normal ($\langle \hat{V}\rangle/U_\infty$) components of velocity. Figure 4.14 shows the profiles of mean ξ-component of velocity, $\langle \hat{U}\rangle/U_\infty$ (Fig. 4.14a), and η-component of velocity, $\langle \hat{V}\rangle/U_\infty$ (Fig. 4.14b). Figure 4.16 shows the profiles of mean ξ-component of velocity, $\langle \hat{U}\rangle_0^+$ (Fig. 4.16a), and η-component of velocity, $\langle \hat{V}\rangle_0^+$ (Fig. 4.16b), normalized by the viscous scales at station A. The behavior of Cartesian and contravariant component of mean streamwise velocity are similar. However, $\langle \hat{V}\rangle/U_\infty$ is affected more by the presence of the ramp than $\langle V\rangle/U_\infty$ stations B-H (Figs. 4.11b and 4.14b).

Station	A	B	C	D	E	F	G	H
Location (x)	$-2L/\delta_0$	0	x_{sep}	$0.5L/\delta_0$	L/δ_0	x_{rea}	$2L/\delta_0$	$4L/\delta_0$

Table 4.3: Streamwise locations of eight stations (A-H) identified in Fig. 4.9.

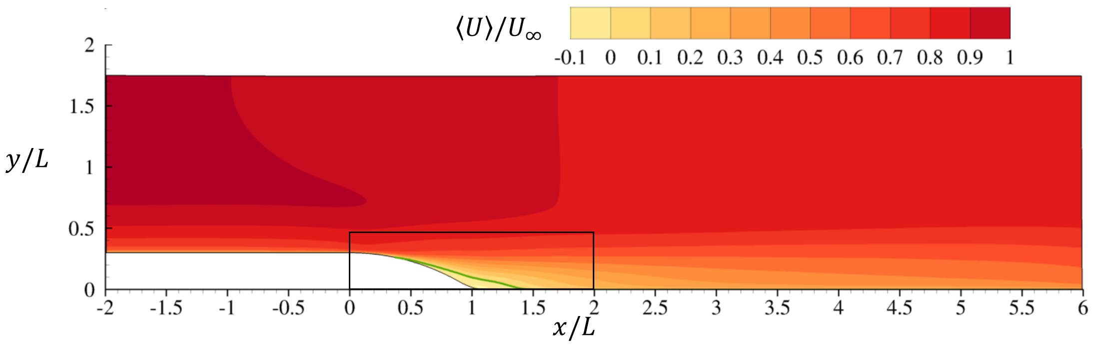

(a) Color contours of the mean Cartesian x-component of velocity $\langle U\rangle/U_\infty$ and the isoline (green) where $\langle U\rangle = 0$.

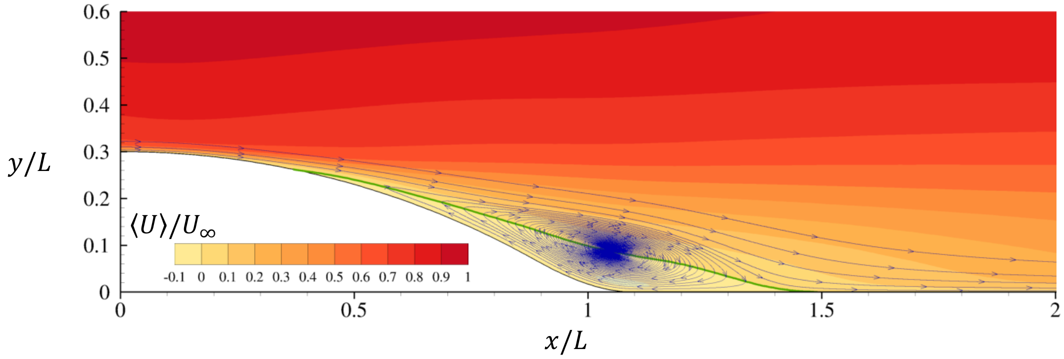

(b) The subdomain of Fig. 4.7a showing the separation bubble along with the streamlines and isoline (green) where $\langle U\rangle = 0$.

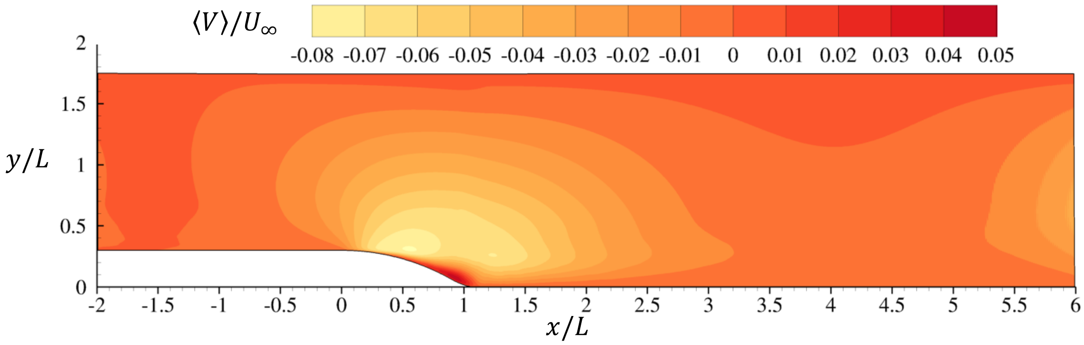

(c) Color contours of the mean Cartesian y-component of velocity $\langle V\rangle/U_\infty$.

Figure 4.7: Color contours of x- and y-components of mean Cartesian velocity.

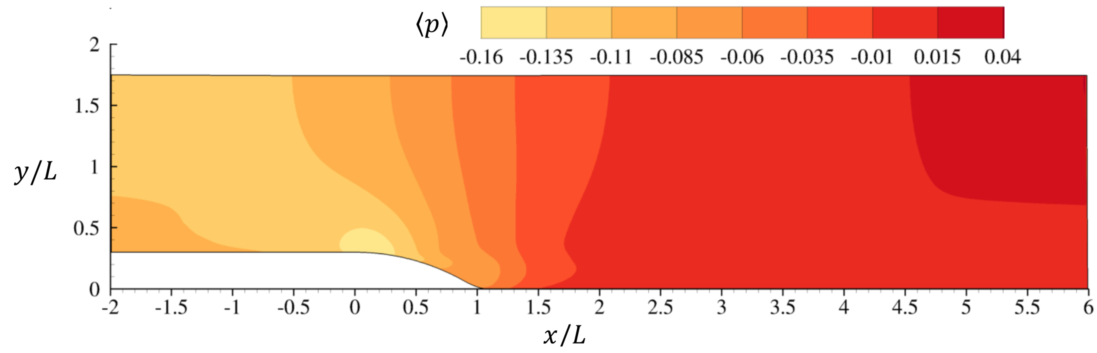

(a) Color contours of the mean pressure $\langle p\rangle$.

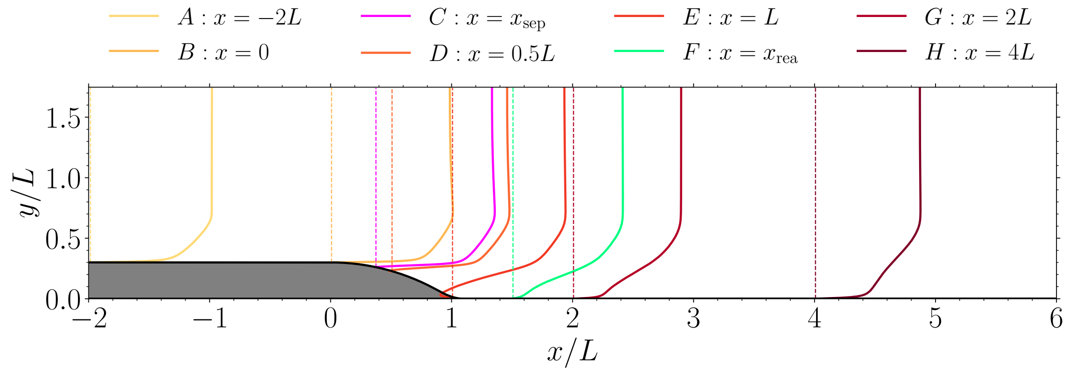

(b) Mean Cartesian x-component of velocity $\langle U\rangle/U_\infty$ (solid lines) at streamwise stations: A-H (dotted lines).

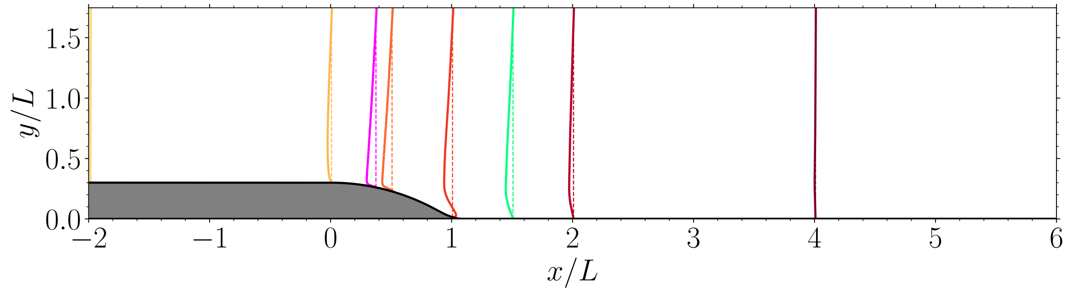

(c) Mean Cartesian y-component of velocity $\langle V\rangle/U_\infty$ (solid lines) at streamwise stations: A-H (dotted lines).

Figure 4.8: (a) Color contours of mean pressure, and (b) and (c) profiles of the mean Cartesian x- and y- components of velocity, respectively, at streamwise stations A-H.

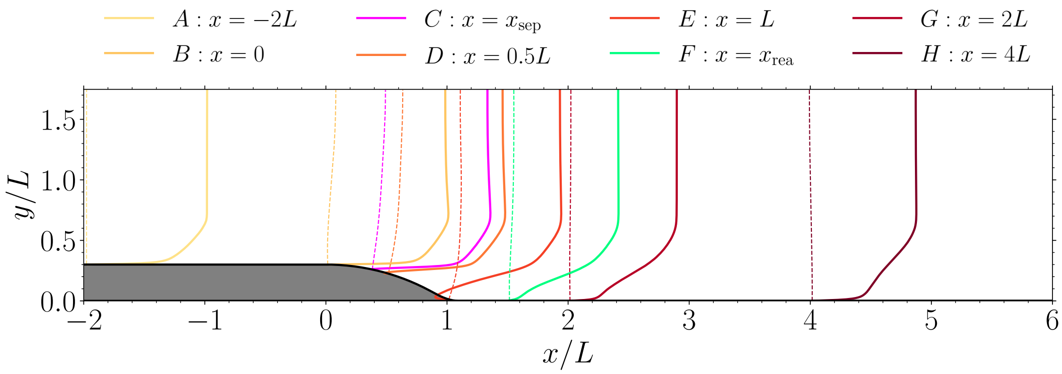

(a) Mean contravariant ξ-component of velocity $\langle \hat{U} \rangle / U_\infty$ (solid lines) along the grid lines (dotted lines) at streamwise stations: A-H.

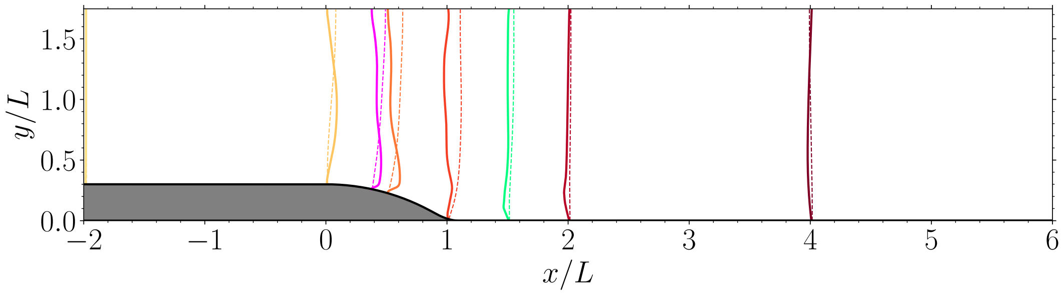

(b) Mean contravariant η-component of velocity $\langle \hat{V} \rangle / U_\infty$ (solid lines) along the grid lines (dotted lines) at streamwise stations: A-H.

Figure 4.9: (a) and (b) profiles of the mean contravariant ξ- and η-components of velocity, respectively.

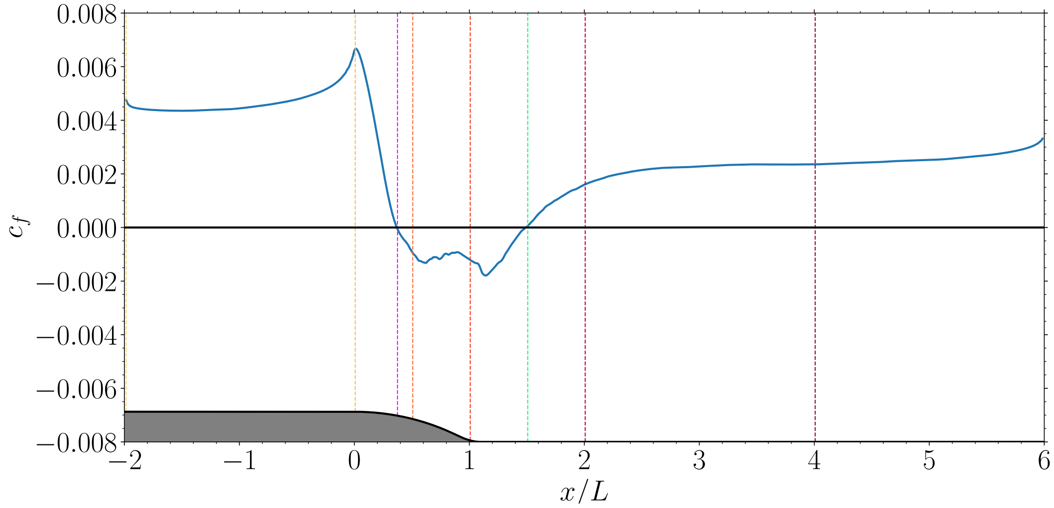

Figure 4.10: Spatial development of the skin friction coefficient c_f along the streamwise direction.. The streamwise stations (A-H) are also shown.

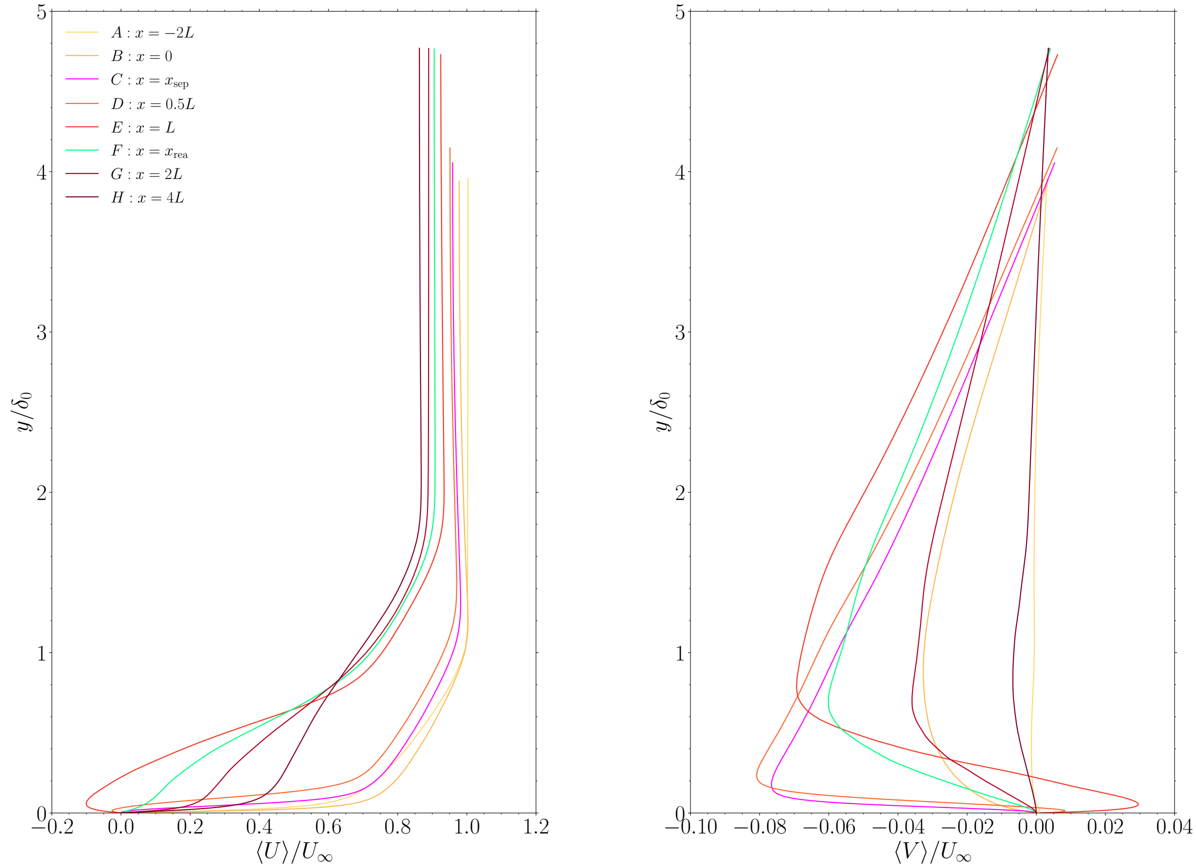

(a) $\langle U \rangle / U_\infty$ (b) $\langle V \rangle / U_\infty$

Figure 4.11: Profiles of the (a) mean x-component of velocity, $\langle U \rangle / U_\infty$ and (b) mean y-component of velocity, $\langle V \rangle / U_\infty$, at stations A-H.

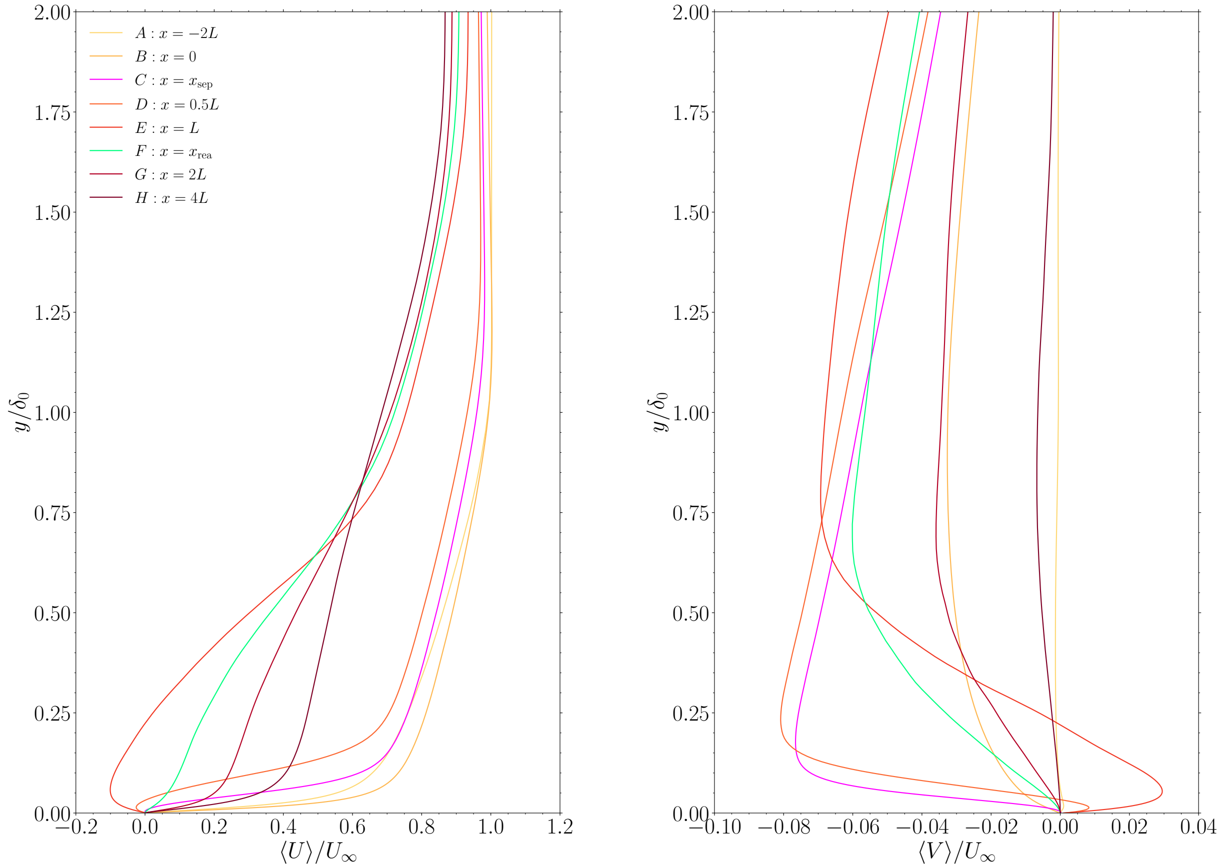

(a) $\langle U \rangle / U_\infty$

(b) $\langle V \rangle / U_\infty$

Figure 4.12: Zoomed-in profiles of the (a) mean x-component of velocity, $\langle U \rangle / U_\infty$, and (b) mean y-component of velocity, $\langle V \rangle / U_\infty$, at stations A-H.

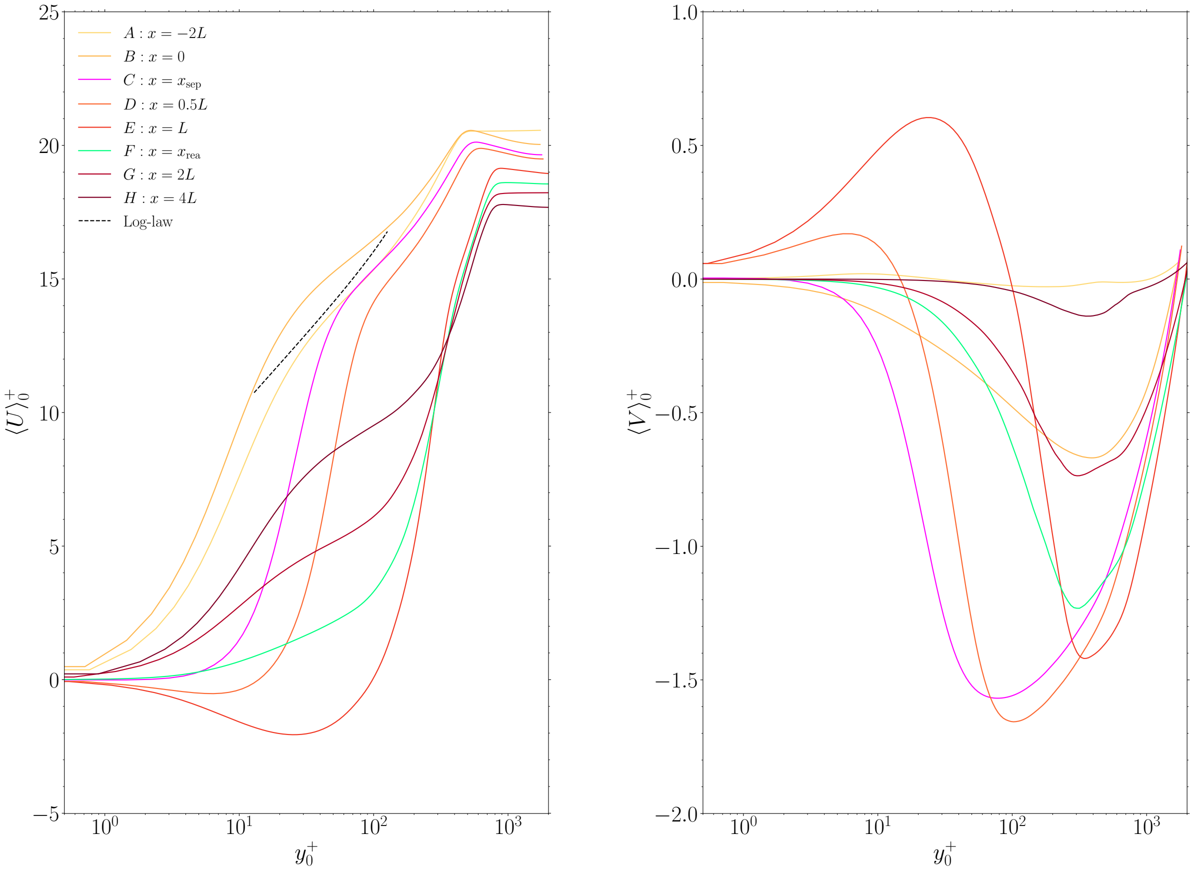

(a) $\langle U \rangle_0^+$

(b) $\langle V \rangle_0^+$

Figure 4.13: Profiles of the (a) mean x-component of velocity, $\langle U \rangle_0^+$, and (b) mean y-component of velocity, $\langle V \rangle_0^+$, at stations A-H. The dashed black line in (a) indicates the von Kármán (1930) log-law. Wall units are normalized by viscous scales at $x_0 = -2L$.

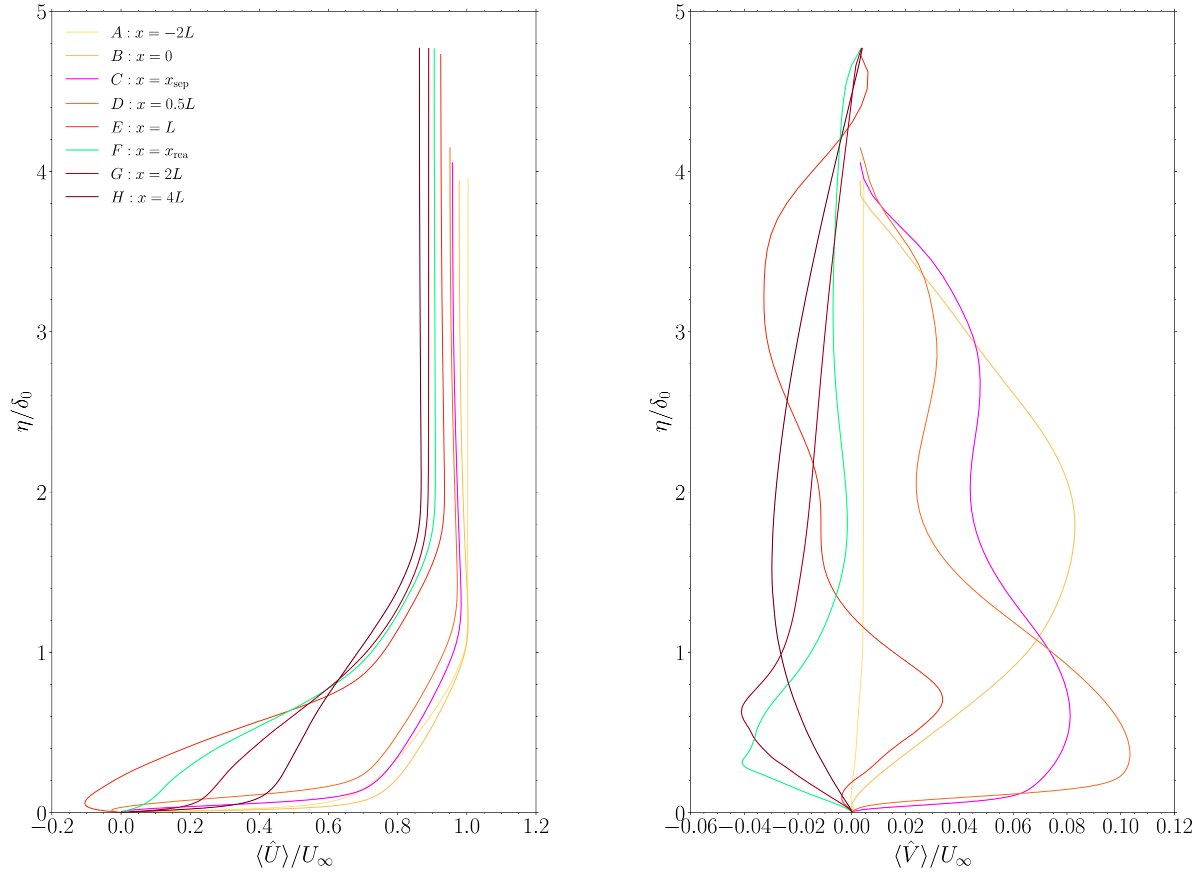

(a) $\langle \hat{U} \rangle / U_\infty$

(b) $\langle \hat{V} \rangle / U_\infty$

Figure 4.14: Profiles of the (a) mean ξ-component of velocity, $\langle \hat{U} \rangle / U_\infty$, and (b) mean η-component of velocity, $\langle \hat{V} \rangle / U_\infty$, at stations A-H.

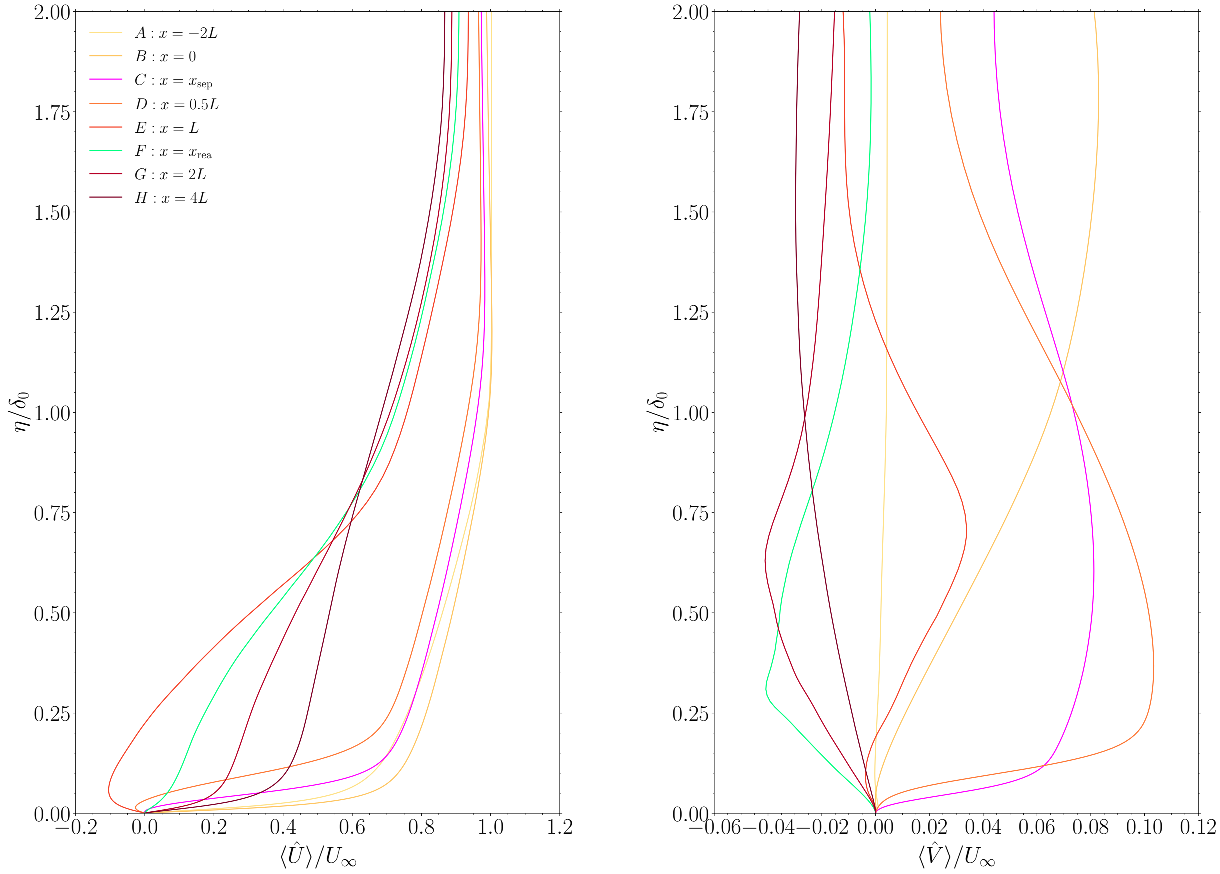

(a) $\langle \hat{U} \rangle / U_\infty$

(b) $\langle \hat{V} \rangle / U_\infty$

Figure 4.15: Zoomed-in profiles of the (a) mean ξ-component of velocity, $\langle \hat{U} \rangle / U_\infty$, and (b) mean η-component of velocity, $\langle \hat{V} \rangle / U_\infty$, at stations A-H.

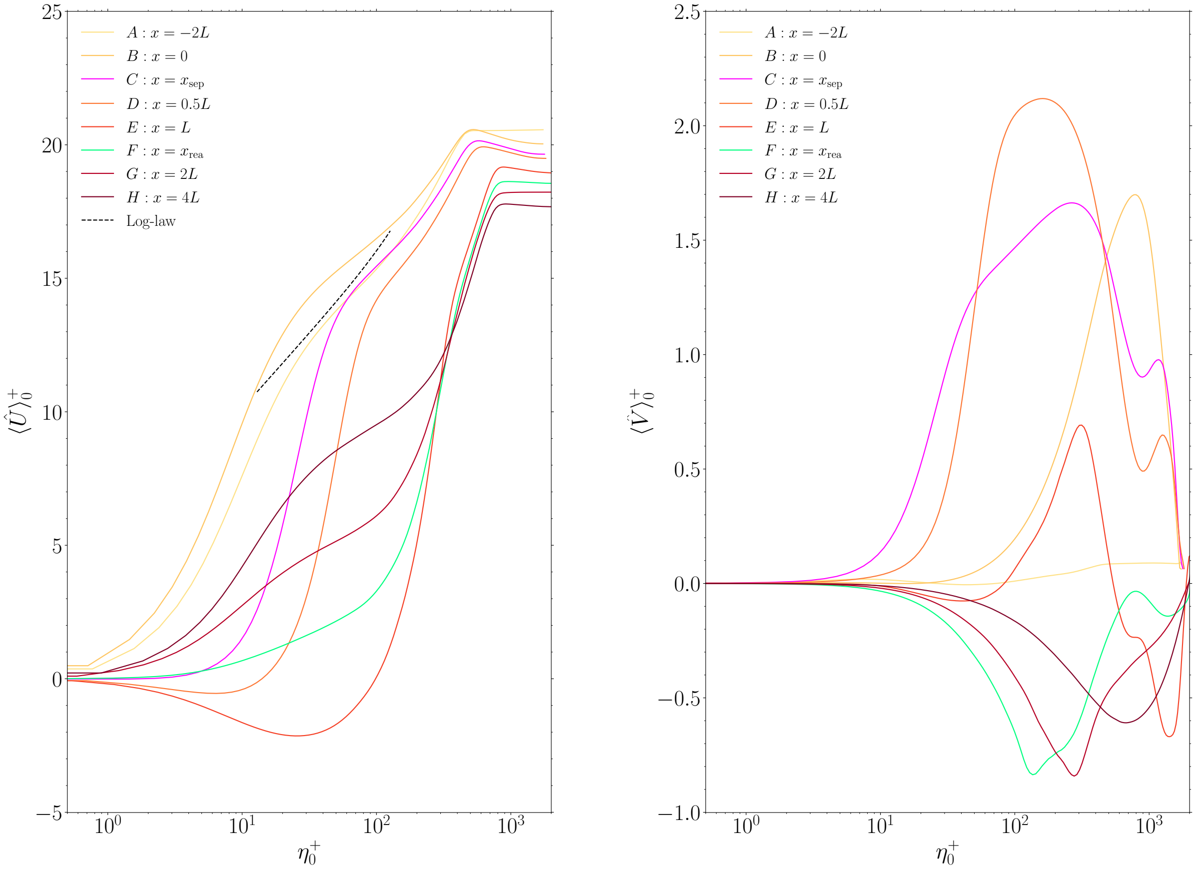

(a) $\langle \hat{U} \rangle_0^+$

(b) $\langle \hat{V} \rangle_0^+$

Figure 4.16: Profiles of the (a) mean ξ-component of velocity, $\langle \hat{U} \rangle_0^+$, and (b) mean η-component of velocity, $\langle \hat{V} \rangle_0^+$, at stations A-H. The dashed black line in (a) indicates the von Kármán (1930) log-law. Wall units are normalized by viscous scales at $x_0 = -2L$.

4.2.3 Turbulence kinetic energy and Reynolds stresses

Turbulence kinetic energy Figures 4.17 and 4.18 show the profiles at stations A-H and color contours, respectively, of the turbulence kinetic energy (TKE), k_0^+, normalized by the viscous scales at $x_0 = -2L$. In the region upstream of the ramp ($x < 0$), the peak values of TKE are observed at $y_0^+ \approx 10$. The TKE profile at station A, as shown in Fig. 4.17, has the typical shape and magnitude of that for ZPG-SDTBL at this Reynolds number (see, e.g., Spalart (1988); DeGraaff & Eaton (2000); Pope (2000); Ferrante & Elghobashi (2004)). However, in the separated region and in the recovery region of the flow ($x > 0.4L$), the peak TKE shifts away from the wall at $y_0^+ \gtrsim 200$. The maximum value of TKE, out of the stations A-H, is obtained in the separted region at station E at distance of $y_0^+ \approx 200$ from the wall as shown in Fig. 4.17. Further, as seen in Fig. 4.18, the peak TKE increases by at least a factor of three in the separated region when compared with the attached region, i.e., from $k_{0_{\max}}^+ \approx 3.5$ at station A to $k_{0_{\max}}^+ \approx 13$ at station E. Downstream of the reattachment location, at station F, the profiles of TKE tend to recover towards the ZPG flat-plate boundary layer profiles. As the flow begins to recover, the TKE profile at station H in the near-wall region of $y_0^+ < 20$ begins to resemble that of a ZPG flat-plate boundary layer by showing a peak at $y_0^+ \approx 10$, while showing another peak at $y_0^+ \approx 265$ being advected from the TKE produced upstream in shear-layer region.

Reynolds stresses in Cartesian coordinates The Cartesian components of Reynolds stresses $\langle u_i u_j \rangle_0^+$ shown in Figs. 4.19 and 4.20 (left column) also exhibit a similar behavior to the TKE. At station A and B, the profiles of the Reynolds stresses are very similar to those of a ZPG flat-plate boundary layer (see, e.g., Spalart (1988); DeGraaff & Eaton (2000); Pope (2000); Ferrante & Elghobashi (2004)). From station C down to station F, such profiles deviate from their ZPG counterparts, and their peaks shift away from the wall from $y_0^+ \approx 20$ to $y_0^+ \approx 200$ due to the hear layer initiated by the ramp at $x/L = 0$. Downstream of the reattachment location (station G and H), we see the Reynolds stress profiles gradually returning towards the shape of the profiles characteristic of a ZPG SDTBL. The profiles of $\langle u^2 \rangle_0^+$ and

$\langle w^2 \rangle_0^+$ in the near wall region of $y_0^+ < 20$ resembles that of a typical ZPG flat-plate boundary layer. The return of the profiles of $\langle uv \rangle_0^+$ and $\langle v^2 \rangle_0^+$ to their ZPG flat-plate boundary layer behavior is slower as the profiles still exhibit peaks in the region away from the wall at $y_0^+ \gtrsim 200$. This is consistent with the observation of Song & Eaton (2004) that the recovery rate of the Reynolds stresses to their characteristic ZPG flat-plate boundary layer profiles, ordered from fastest to slowest, is $\langle u^2 \rangle$, $\langle uv \rangle$, and $\langle v^2 \rangle$. Similarly to the TKE, we see the peak values of the Reynolds stresses increase by at least a factor of two in the separated region when compared with the attached region, i.e., from $\left[\langle u^2 \rangle_{0\max}^+, \langle v^2 \rangle_{0\max}^+, \langle w^2 \rangle_{0\max}^+, -\langle uv \rangle_{0\max}^+\right] \approx [6, 1, 1.5, 0.75]$ at station A to $\left[\langle u^2 \rangle_{0\max}^+, \langle v^2 \rangle_{0\max}^+, \langle w^2 \rangle_{0\max}^+, -\langle uv \rangle_{0\max}^+\right] \approx [12, 6.5, 7.5, 5.5]$ at station E. For the stations A-H, the maximum value of $\langle u^2 \rangle_0^+$ is at station D, while the maximum values of $\langle v^2 \rangle_0^+$, $\langle w^2 \rangle_0^+$, $-\langle uv \rangle_0^+$ are all at station E. Further, Table 4.4 shows the exact positions of the peak values for the Cartesian components of the Reynolds stresses.

	$\langle u^2 \rangle_0^+$	$\langle v^2 \rangle_0^+$	$\langle w^2 \rangle_0^+$	$-\langle uv \rangle_0^+$
x-location (x/L)	0.6	0.9	1.1	0.8
y-location (y_0^+)	69.5	121.9	201.3	95.0

Table 4.4: Positions identified by the x- and y-locations of peak values for the Cartesian components of the Reynolds stresses: $\langle u^2 \rangle_0^+$, $\langle v^2 \rangle_0^+$, $\langle w^2 \rangle_0^+$ and $-\langle uv \rangle_0^+$.

Reynolds stresses in orthogonal curvilinear coordinates The physical components of the contravariant Reynolds stresses $\langle \hat{u}^i \hat{u}^j \rangle_0^+$ are shown in Figs. 4.19 and 4.20 (right column). Since TKE is a scalar and $2k$ is an invariant of the Reynolds stress tensor, the profile of k_0^+ is the same in Cartesian and orthogonal curvilinear coordinates. Also, due to the linear translation of the computational domain along the ζ direction, the profile of $\langle w^2 \rangle_0^+$ is also unaffected by the coordinate transformation (Figs. 4.20a and 4.20b). The profiles of the physical components of the contravariant Reynolds stresses over the ramp, i.e., at stations C, D and E, differ from the Cartesian components due to the fact that the grid lines are curved and so the Cartesian and curvilinear components of velocity differ from each other. The profile of $\langle \hat{u}^2 \rangle_0^+$ at stations C, D and E have greater magnitudes than the Cartesian profiles but show the same qualitative behavior (Figs. 4.19a and 4.19b). On the other hand, profile of $\langle \hat{v}^2 \rangle_0^+$ at stations C, D and E have smaller magnitudes than the Cartesian profiles (Figs. 4.19c and 4.19d) since the TKE is an invariant with coordinate transformation. The profiles of $\langle \hat{v}^2 \rangle_0^+$ and $-\langle \hat{u}\hat{v} \rangle_0^+$ (Figs. 4.20c and 4.20d) differ the most from their corresponding Cartesian profiles. The magnitude of $\langle \hat{v}^2 \rangle_0^+$ for $y_0^+ \lesssim 50$ at stations C, D and E is smaller than that of $\langle v^2 \rangle_0^+$ and the maximum value of $\langle \hat{v}^2 \rangle_0^+$ is obtained at the reattachment location, station F while for $\langle v^2 \rangle_0^+$ its peak is at station E. Further, Table 4.5 shows the exact positions of the peak values for the physical components of the Reynolds stresses in orthogonal curvilinear coordinates.

At the separation location (station C, Fig. 4.20d), the profile of $-\langle \hat{u}\hat{v} \rangle_0^+$ has a negative value, i.e., $\langle \hat{u}\hat{v} \rangle_0^+ > 0$ in the region $\hat{\eta}_0^+ < 26$. Abe *et al.* (2012) and Abe (2019) also report obtaining positive values in the profile of $\langle uv \rangle$ in the case of the so-called 'pressure-gradient induced flow separation' in a flat-plate turbulent boundary layer. In their case, the positive values in the profile of $\langle uv \rangle$ were near the top of a 'large' separation bubble where the streamlines have a convex curvature (see Figs. 3(e) and 5(b) of Abe *et al.* (2012)).

The behavior of the turbulence kinetic energy and the Reynolds stresses in both Cartesian and curvilinear coordinates will be explained in subsequent sections, Sec. 4.2.5 and Sec. 4.2.6, by analyzing the budget equations of the Reynolds stresses.

For the first time, we notice that the profiles of the Reynolds stresses in orthogonal curvilinear coordinates over the curved region of the ramp share some similarities with the Reynolds stresses, the terms of their budget equations, and mean velocity gradient (Sec. 4.2.6) in the region with suction velocity (APG) of a pressure-gradient induced turbulent flow separation over a flat plate (Abe *et al.*, 2012; Abe, 2017; Kitsios *et al.*, 2017). This is because in the computational domain after the coordinate transformation of the curved physical domain is equivalent to a Cartesian domain over a flat plate with imposed APG conditions. Such a comparison is only possible because (i) we employ a structured orthogonal grid (Appendix D) over the curved ramp in our simulations, and (ii) FastRK3 solves the governing equations written in orthogonal curvilinear coordinates. That said, we will note in Sec. 4.2.5 and 4.2.6, the differences between the Reynolds stress budgets and mean velocity gradients in Cartesian coordinates and those in orthogonal curvilinear coordinates over the curved ramp due to the curvature that would not be possible to simulate using a flat wall with an imposed APG to force separation.

	$\langle \hat{u}^2 \rangle_0^+$	$\langle \hat{v}^2 \rangle_0^+$	$\langle \hat{w}^2 \rangle_0^+$	$-\langle \hat{u}\hat{v} \rangle_0^+$
ξ-location (ξ/L)	0.7	1.5	1.1	1.3
η-location (η_0^+)	81.0	143.2	201.3	182.5

Table 4.5: Positions identified by the ξ- and η-locations of peak values for the physical components of the Reynolds stresses in orthogonal curvilinear coordinates: $\langle \hat{u}^2 \rangle_0^+$, $\langle \hat{v}^2 \rangle_0^+$, $\langle \hat{w}^2 \rangle_0^+$ and $-\langle \hat{u}\hat{v} \rangle_0^+$.

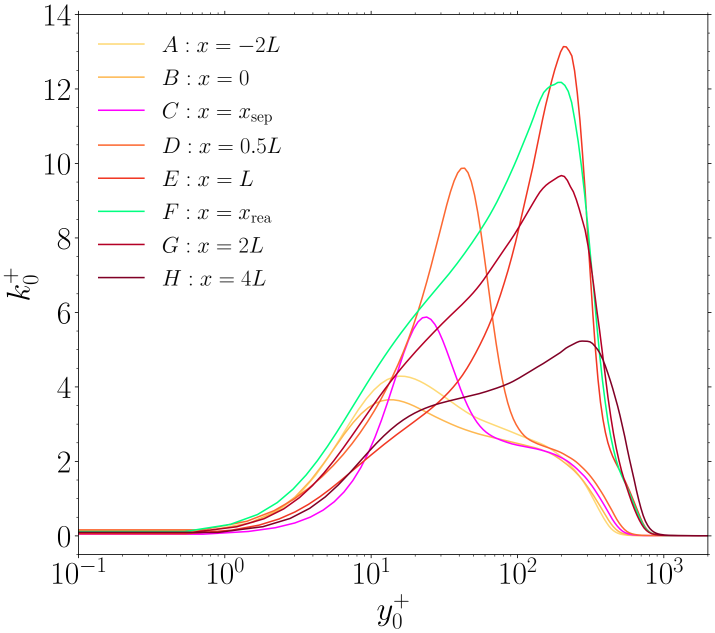

Figure 4.17: Profiles of turbulence kinetic energy, k_0^+ at stations A-H. Wall units are normalized by viscous scales at $x_0 = -2L/\delta_0$.

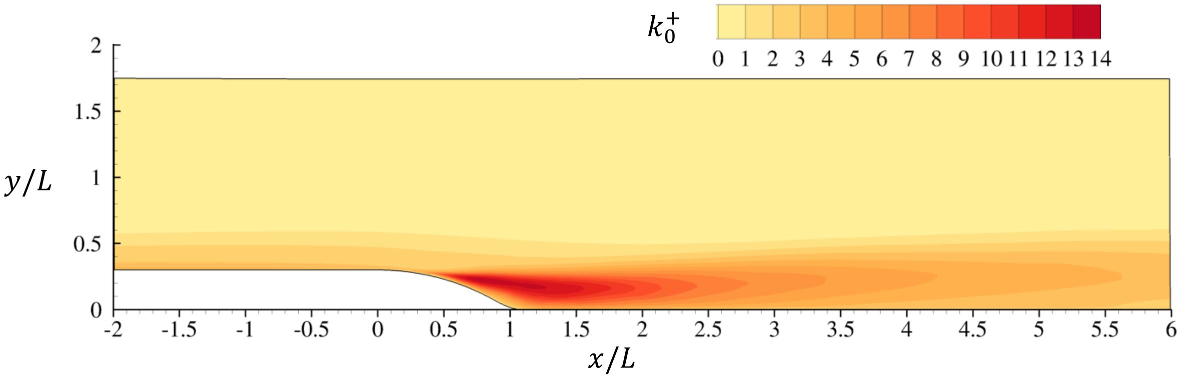

Figure 4.18: Color contours of the turbulence kinetic energy k_0^+ .Wall units are normalized by viscous scales at $x_0 = -2L/\delta_0$.

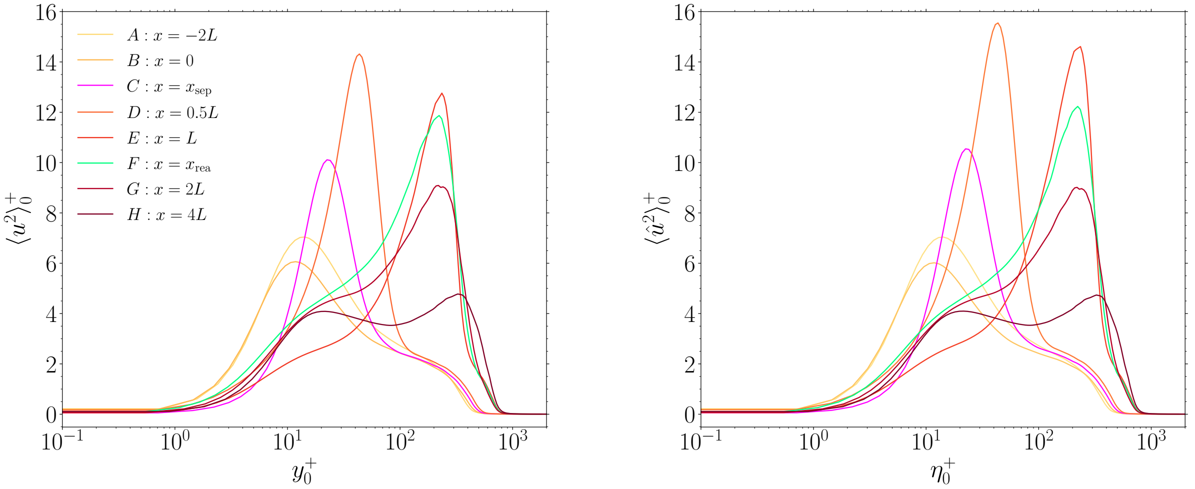

(a) $\langle u^2 \rangle_0^+$ (b) $\langle \hat{u}^2 \rangle_0^+$

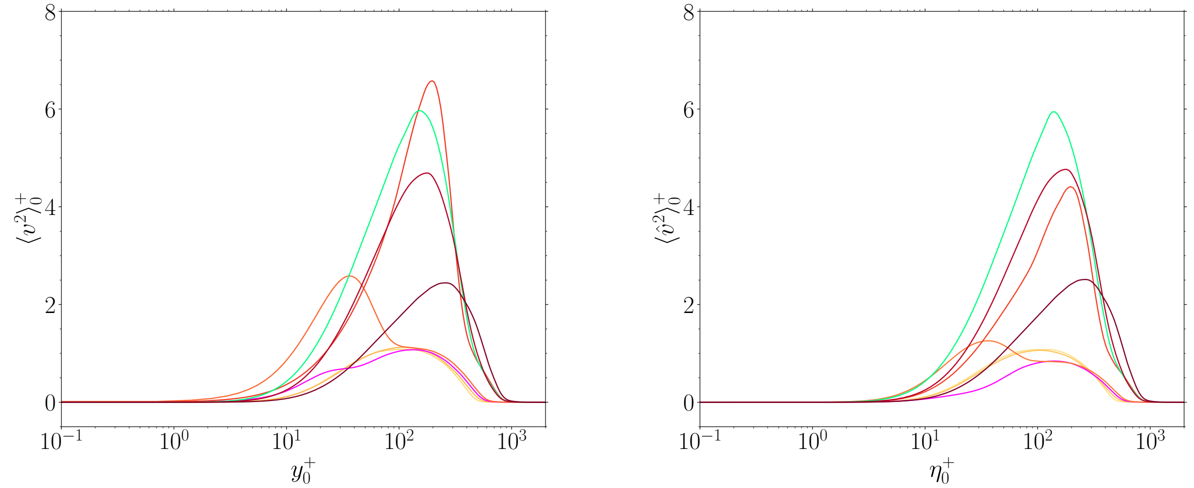

(c) $\langle v^2 \rangle_0^+$ (d) $\langle \hat{v}^2 \rangle_0^+$

Figure 4.19: Cartesian (left column) and contravariant (right column) components of Reynolds stresses, $\langle u^2 \rangle_0^+$ and $\langle v^2 \rangle_0^+$, at stations A-H. Wall units are normalized by viscous scales at $x_0 = -2L/\delta_0$.

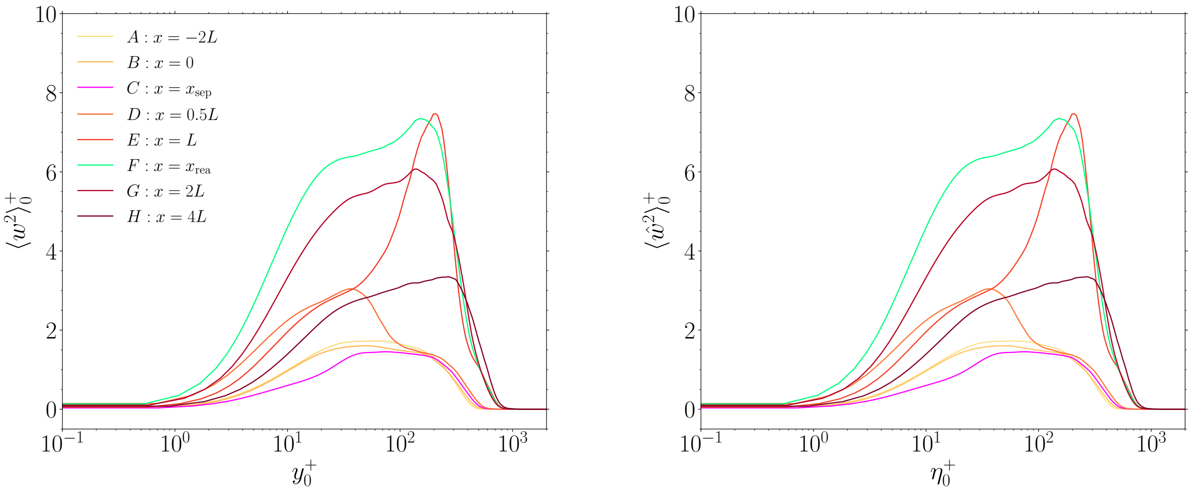

(a) $\langle w^2 \rangle_0^+$ (b) $\langle \hat{w}^2 \rangle_0^+$

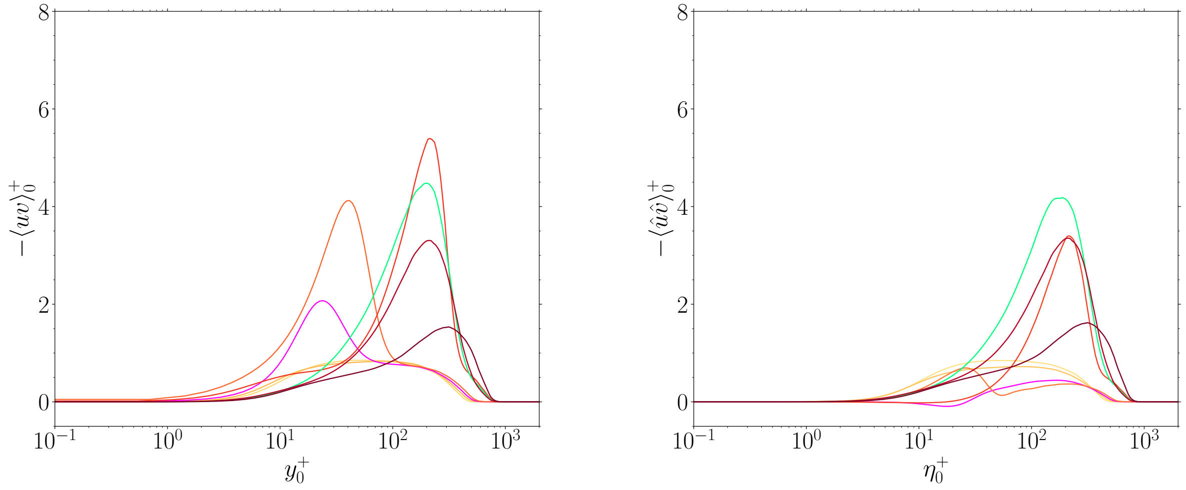

(c) $\langle -uv \rangle_0^+$ (d) $-\langle \hat{u}\hat{v} \rangle_0^+$

Figure 4.20: Cartesian (left column) and contravariant (right column) components of Reynolds stresses, $\langle w^2 \rangle_0^+$ and $-\langle uv \rangle_0^+$, at stations A-H. Wall units are normalized by viscous scales at $x_0 = -2L/\delta_0$.

4.2.4 Turbulence kinetic energy budget

The budget equation of the turbulence kinetic energy k can be obtained by taking the dot product of the velocity fluctuation $\mathbf{u}(\boldsymbol{x},t)$ with the momentum equation for the velocity fluctuation (Eq. (5.138) of Pope (2000)) and then by taking the mean, $\langle\ldots\rangle$, of each term of the resulting equation which for a statistically stationary turbulent flow results in:

$$\underbrace{-\langle\mathbf{U}\rangle\cdot\nabla k}_{\text{mean flow convection}} \underbrace{-\frac{1}{2}\nabla\cdot\langle\mathbf{u}(\mathbf{u}\cdot\mathbf{u})\rangle}_{\text{turbulent convection}} + \underbrace{2\nu\nabla\cdot\langle\mathbf{u}\cdot\mathbf{s}\rangle}_{\text{viscous diffusion}} + \mathscr{P} + \mathit{\Pi} - \epsilon = 0, \tag{4.11}$$

where $\mathbf{u}(\boldsymbol{x},t)$ is the velocity fluctuation:

$$\mathbf{u}(\boldsymbol{x},t) = \mathbf{U}(\boldsymbol{x},t) - \langle\mathbf{U}(\boldsymbol{x},t)\rangle\,, \tag{4.12}$$

and $\mathbf{s} = \mathbf{s} = 1/2\left(\nabla\mathbf{u} + \nabla\mathbf{u}^T\right)$ is the strain rate tensor of the velocity fluctuation $\mathbf{u}$, $\mathscr{P}$ and ϵ are the production and dissipation of k, respectively. Note that for the SDTBL separating over a curved wall that we study (Fig. 4.2), the flow is statistically stationary and homogeneous in the spanwise direction z, thus, the mean $\langle\ldots\rangle$ is taken as average in time and in the spanwise direction of the enclosed quantity. The terms corresponding to the mean and turbulent convection and the viscous diffusion of k are indicated in Eq. (4.11). The production of k, $\mathscr{P}$, is

$$\mathscr{P} = -\langle\mathbf{u}\mathbf{u}\rangle : \overline{\mathbf{S}}, \tag{4.13}$$

where the strain rate tensor of the mean flow, $\overline{\mathbf{S}}$, in Eq. (4.13) is defined as

$$\overline{\mathbf{S}} = \frac{1}{2}\left(\nabla\langle\mathbf{U}\rangle + \nabla\langle\mathbf{U}^T\rangle\right). \tag{4.14}$$

the pressure transport of k, $\mathit{\Pi}$, is

$$\mathit{\Pi} = \frac{1}{\rho}\nabla\cdot\langle\mathbf{u}p'\rangle, \tag{4.15}$$

where p' is the pressure fluctuation,

$$p' = p - \langle p\rangle, \tag{4.16}$$

and the dissipation of k, ϵ, is

$$\epsilon = 2\nu\langle \mathbf{s} : \mathbf{s} \rangle. \tag{4.17}$$

FastRK3 solves the orthogonal formulation of the incompressible NS equations and computes the contravariant components of the fluid velocity (Sec. 2.2). In order to compute the turbulence statistics of the flow over the curved wall, we derive, for the first time, the budget equations of the turbulence kinetic energy and of all components of Reynolds stresses in orthogonal coordinates using the analytical techniques introduced in Sec. 2. We transform the transport equations for the TKE and all the components of the Reynolds stresses to the orthogonal curvilinear coordinates and these equations are derived in Appendix F. Each of the terms of the transport equations of the TKE and the Reynolds stresses are then transformed to their Cartesian components as discussed in Sec. 4.2 using Eq. (4.8). Figures 4.21 and 4.22 show the budget of TKE, k_0^+, at the stations A-H. The positions of maximum values of k, $-\langle uv \rangle$ and $\partial\langle U \rangle/\partial y$ are denoted by triangles on horizontal axis. Further, we examine the budgets of the individual components of TKE, i.e., $\langle u^2 \rangle$, $\langle v^2 \rangle$ and $\langle w^2 \rangle$, in Sec. 4.2.5 and 4.2.6, in order to explain the physical mechanisms of turbulence in a separated flow.

TKE budget at station A and B ($\mathbf{x = -2L}$ and $\mathbf{x = 0}$) Figures 4.21a and 4.21b show the budget of TKE, k_0^+, at A($x = -2L$) and B ($x = 0$), respectively. The budget of k_0^+ at stations A and B exhibit similar characteristics as that of a flat-plate turbulent boundary layer of Spalart (1988) discussed by Pope (2000) in their Chapter 7, Sec. 7.3.5, Fig. 7.34. Dissipation reaches its peak value at the wall, while production peaks in the buffer layer at $y_0^+ \approx 11$. TKE production is larger than viscous dissipation around the y-location of peak TKE and the transport terms take care of balancing the budget by carrying the excess energy produced and not dissipated to other regions of the flow. The viscous diffusion term diffuses TKE primarily towards the wall.

TKE budget at station C and D ($\mathbf{x = x_{sep}}$ and $\mathbf{x = 0.5}$) Figures 4.21c and 4.21d show the budget of TKE, k_0^+, at stations C ($x = x_{\text{sep}}$) and D ($x = 0.5L$), respectively. The location of peak production of TKE, at stations C and D, shifts away from the wall and is obtained at $y_0^+ \approx 23$ and $y_0^+ \approx 40$, respectively. Further, the maximum value of production, at stations C and D, are, respectively, three times and four times their counterparts at station A. The pressure transport term is still smaller than the other terms, while the mean and turbulent convection are more significant in the separated region.

TKE budget at station E and F ($\mathbf{x = L}$ and $\mathbf{x = x_{rea}}$) Figures 4.22a and 4.22b show the budget of TKE, k_0^+, at stations E ($x = L$) and F ($x = x_{\text{sep}}$), respectively. The budget of k_0^+ at station E ($x = L$) differs greatly from that of a ZPG SDTBL. The peak production is obtained at $y_0^+ \approx 240$ which is indicative of the fact that the strongest turbulence in the flow has shifted away from the wall due to the shear layer created in the flow by the flow separation over the curved ramp. The peak dissipation is still obtained at the wall, and the viscous diffusion term transports kinetic energy primarily towards the wall. The budget of k_0^+ at station F ($x = x_{\text{rea}}$) mostly follows the same trend as that at station E ($x = L$), except the peak value of TKE production at station F is smaller than that at station E, and peak the value of viscous dissipation at the wall is greater at station F than at station E ($x = L$).

TKE budget at station G and H ($\mathbf{x = 2L}$ and $\mathbf{x = 4L}$) Figures 4.22c and 4.22d show the budget of TKE, k_0^+, at stations G ($x = 2L$) and H ($x = 4L$), respectively. In the near wall region ($y_0^+ \leq 70$), the TKE budgets tend to return towards the ZPG SDTBL. However, the peak production of TKE at station G ($x = 2L$) is still obtained at $y_0^+ \approx 220$. The TKE budget at station H ($x = 4L$) resembles that of a typical ZPG SDTBL albeit with values about half of those at station A ($x = -2L$).

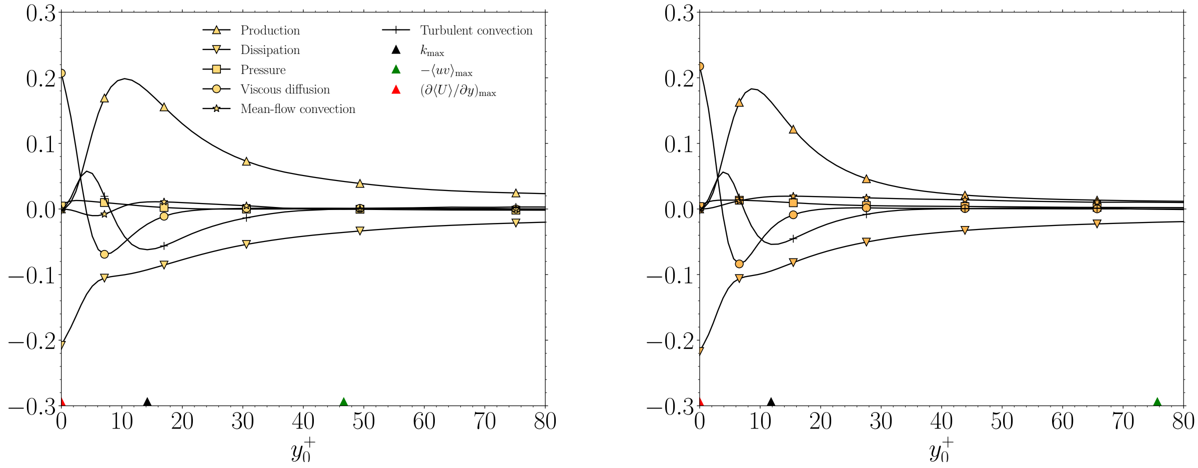

(a) Station A ($x = x_0 = -2L$)

(b) Station B ($x = 0$)

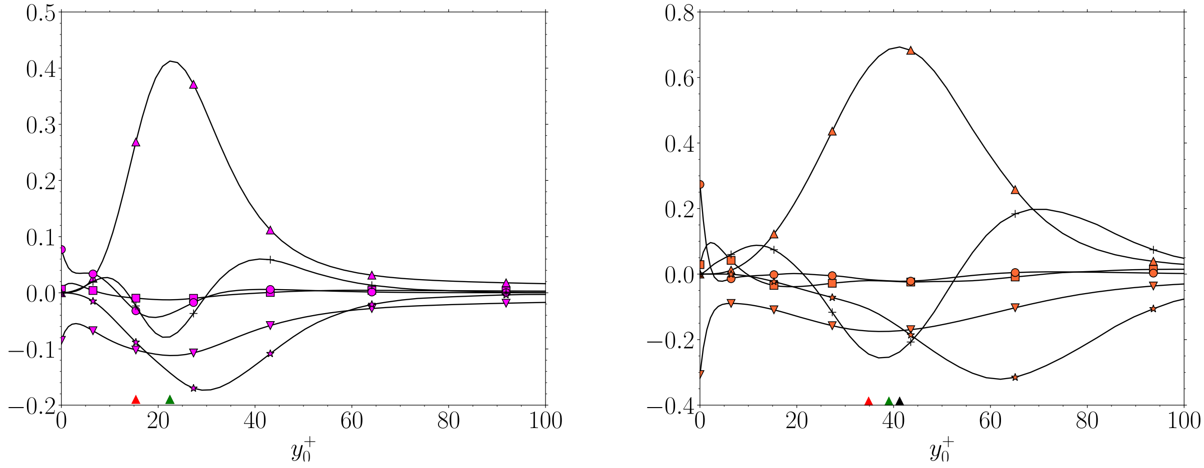

(c) Station C ($x = x_{\text{sep}}$)

(d) Station D ($x = 0.5L$)

Figure 4.21: Budget of turbulence kinetic energy, k, at stations A-D, normalized by viscous scales at $x_0 = -2L$. Positions of maximum values of k, $-\langle uv \rangle$ and $\partial \langle U \rangle / \partial y$ are denoted by triangles on horizontal axis.

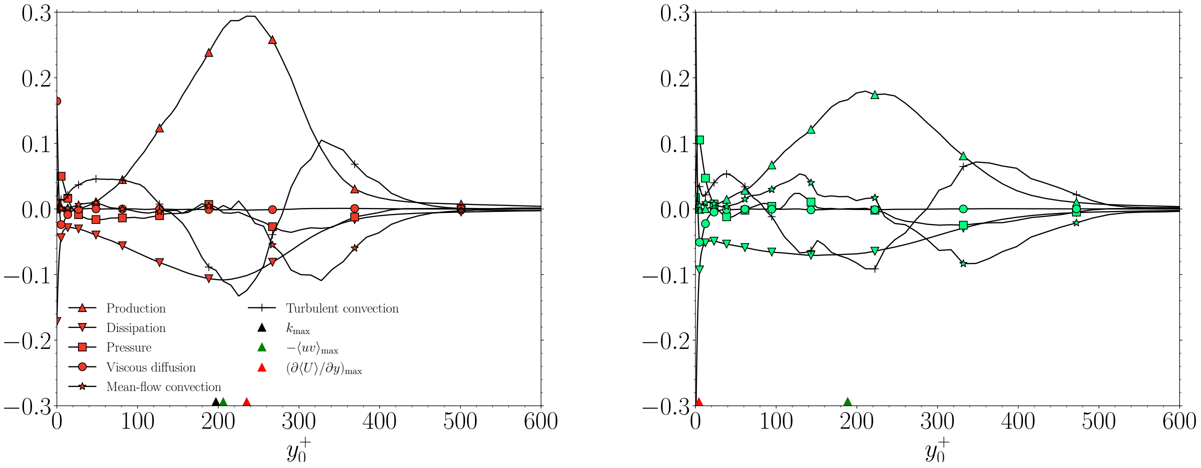

(a) Station E ($x = L$) (b) Station F ($x = x_{\mathrm{rea}}$)

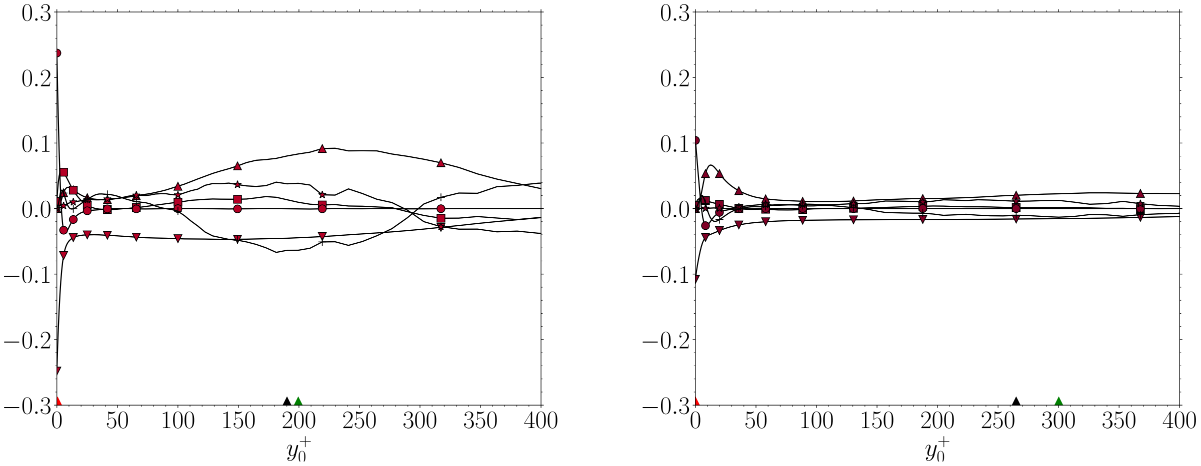

(c) Station G ($x = 2L$) (d) Station H ($x = 4L$)

Figure 4.22: Budget of turbulence kinetic energy, k, at stations E-H, normalized by viscous scales at $x_0 = -2L$. Positions of maximum values of k, $-\langle uv \rangle$ and $\partial\langle U \rangle/\partial y$ are denoted by triangles on horizontal axis.

4.2.5 Reynolds stress budget in Cartesian coordinates

Next, we explain the changes occurring to the terms of the Reynolds stress budget due to flow separation with respect to a ZPG SDTBL.

Reynolds stress budgets in Cartesian coordinates We investigate the Reynolds stress balances to better understand the dynamics of turbulence in this separated flow over the curved wall. The transport equation for the Reynolds stresses in a statistically stationary turbulent flow is (Pope, 2000)

$$-\underbrace{\langle\mathbf{U}\rangle\cdot\nabla\langle\mathbf{uu}\rangle}_{\text{mean flow convection}}-\underbrace{\nabla\cdot\langle\mathbf{uuu}\rangle}_{\text{turbulent convection}}+\underbrace{\nu\nabla^2\langle\mathbf{uu}\rangle}_{\text{viscous diffusion}}+\mathscr{P}+\boldsymbol{\Pi}-\boldsymbol{\epsilon}=0, \tag{4.18}$$

where where $\mathbf{u}(\boldsymbol{x},t)$ is the velocity fluctuation from its mean $\langle\mathbf{U}(\boldsymbol{xi},t)\rangle$ as shown in Eq. (4.12). The terms corresponding to the mean flow convection tensor, the turbulent convection tensor and the viscous diffusion tensor are indicated in Eq. (4.18). $\mathscr{P}$ is the production tensor

$$\mathscr{P}\equiv-\langle\mathbf{uu}\rangle\cdot\nabla\langle\mathbf{U}\rangle-\langle\mathbf{uu}\rangle\cdot\nabla\langle\mathbf{U}\rangle^T, \tag{4.19}$$

$\boldsymbol{\Pi}$ is the velocity-pressure-gradient tensor

$$\boldsymbol{\Pi}\equiv-\frac{1}{\rho}\left\langle\mathbf{u}\nabla p'+\mathbf{u}\nabla p'^T\right\rangle, \tag{4.20}$$

where p' is the pressure fluctuation which is defined in Eq. (4.16), and $\boldsymbol{\epsilon}$ is the dissipation tensor

$$\boldsymbol{\epsilon}\equiv2\nu\left\langle\nabla\mathbf{u}\cdot\nabla\mathbf{u}^T\right\rangle. \tag{4.21}$$

The transformation of each of the terms of Eq. (4.18) to orthogonal curvilinear coordinates is discussed in Appendix F.

We start he analysis of the Reynolds stress budgets by looking at the production tensor (4.19). Since production of Reynolds stresses is mainly affected by the mean shear, we first analyze the gradient of mean velocity, $\nabla\langle\mathbf{U}\rangle$.

Gradient of mean velocity Figure 4.23 shows the profiles of the four terms of the gradient of mean velocity, $\nabla\langle \mathbf{U}\rangle$, normalized by the viscous scales at A ($x_0 = -2L$) for the stations A-H. At stations A, B, G and H, the derivatives of the mean velocity components in the y-direction are greater than those in the x-direction, i.e., $|\partial\langle U\rangle_0^+/\partial y| \gg |\partial\langle V\rangle_0^+/\partial y| > |\partial\langle U\rangle_0^+/\partial x| > |\partial\langle V\rangle_0^+/\partial x|$, which is characteristic of a ZPG TBL. The velocity derivatives $\partial\langle V\rangle_0^+/\partial x \ll 1$ and $\partial\langle V\rangle_0^+/\partial y \ll 1$ at stations where the wall is flat, namely, stations A, B, F, G and H. At station A, $\partial\langle U\rangle_0^+/\partial y$ is unity and maximum at the wall since we used the viscous scales at that location for the normalization of such term.

Over the curved ramp, at stations C, D and E, we have $|\partial\langle U\rangle_0^+/\partial y| \gg |\partial\langle V\rangle_0^+/\partial y| > |\partial\langle U\rangle_0^+/\partial x| > |\partial\langle V\rangle_0^+/\partial x|$. Therefore, $\partial\langle U\rangle_0^+/\partial y$ and $\partial\langle V\rangle_0^+/\partial y$ are the two significant components of the velocity gradient in the separated region over the curved ramp. The velocity gradient at the wall where separation (station C) occurs is zero. At stations D and E, $\partial\langle U\rangle_0^+/\partial y < 0$ for $y < 10$ and $y < 45$, respectively, due to the reversed flow in the separated region. At these stations, the adverse pressure gradient decelerates the flow, thus, $\partial\langle U\rangle_0^+/\partial x$ is negative for $y < 6$ and $y < 25$, respectively. The mean shear gradually $\partial\langle U\rangle_0^+/\partial y$ increases, from zero in the case of station C, and from negative values in the case of stations D and E, at the wall to positive values farther away from the wall, past the inflection point of the mean velocity profile of $\langle U\rangle$ (Fig. 4.13a). Therefore, in the separated region, the maximum value of $\partial\langle U\rangle_0^+/\partial y$ occurs away from the wall for $y_0^+ > 10$. At station C, the velocity derivative $\partial\langle V\rangle_0^+/\partial y$ starts from the value of zero at the wall and takes on negative values away from the wall, i.e., $\partial\langle V\rangle_0^+/\partial y < 0$ as the flow turns downwards $\langle V\rangle < 0$ (Fig. 4.13b). At stations D and E, where the separation bubble near the wall occurs (Fig. 4.7b), the flow is reversed ($\langle U\rangle < 0$) and, thus, it moves upwards, i.e., $\langle V\rangle > 0$ in the near-wall region (Fig. 4.13b). Therefore, the velocity derivative $\partial\langle V\rangle_0^+/\partial y > 0$ for $y_0^+ < 6$ and $y_0^+ < 30$ at stations D and E, respectively. The profile of $\partial\langle V\rangle_0^+/\partial y$ then changes its sign from positive to negative past this location of maximum $\langle V\rangle$ velocity as the flow along y gradually changes its direction to flow downward, i.e., $\langle V\rangle < 0$ (Fig. 4.13b).

In the reattachment (station F) and the recovery region (stations G and H), we have

$|\partial\langle U\rangle_0^+/\partial y| \gg |\partial\langle V\rangle_0^+/\partial y| > |\partial\langle U\rangle_0^+/\partial x| > |\partial\langle V\rangle_0^+/\partial x|$. Therefore, $\partial\langle U\rangle_0^+/\partial y$ is the most significant component of the mean velocity gradient tensor. The velocity gradient at the wall where reattachment (station F) occurs is zero. At stations G and H, i.e., downstream of the reattachment location, the peak values of $\partial\langle U\rangle_0^+/\partial y$ are obtained at the wall, similarly to stations A and B. However, unlike as at stations A, B and H, the profile of $\partial\langle U\rangle_0^+/\partial y$ does not smoothly decay to zero for $y_0^+ > 60$ at stations F and G. The velocity derivative $\partial\langle V\rangle_0^+/\partial y$ is only significant at stations F and G. Therefore,downstream of station G, the flow gradually regains the chief characteristic of a ZPG SDTBL where $\partial\langle U\rangle_0^+/\partial y$ is the only significant mean velocity derivative.

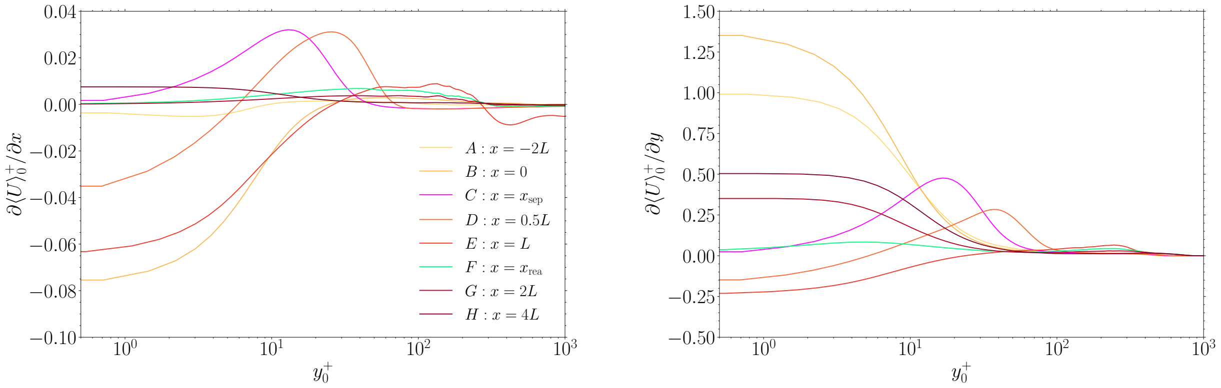

(a) $\partial\langle U\rangle_0^+/\partial x$ (b) $\partial\langle U\rangle_0^+/\partial y$

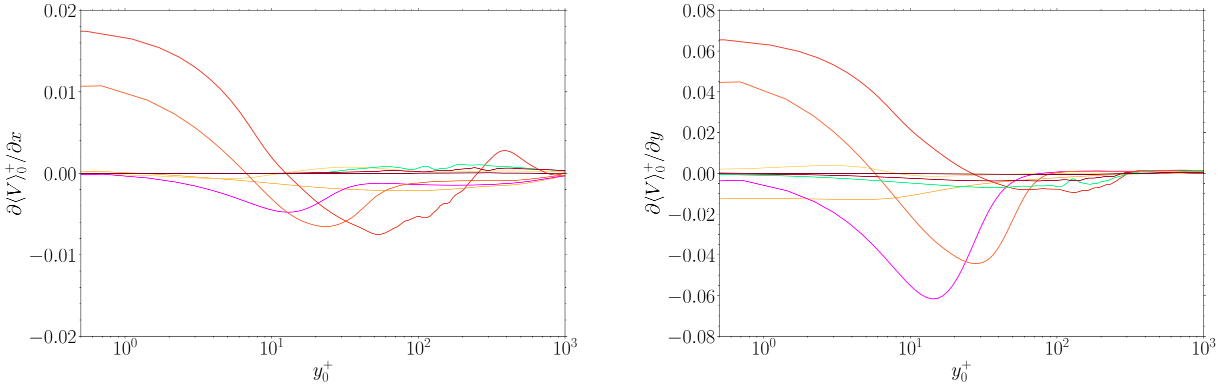

(c) $\partial\langle V\rangle_0^+/\partial x$ (d) $\partial\langle V\rangle_0^+/\partial y$

Figure 4.23: Cartesian components of the components of the mean velocity gradient, $\nabla\langle\mathbf{U}\rangle$, at stations A-H, normalized by viscous scales at $x_0 = -2L$.

Reynolds stress budget at station A and B ($\mathbf{x = -2L}$ and $\mathbf{x = 0}$) Figures 4.24 and 4.25 show the budgets of the Reynolds stress components at stations A and B. The triangles on the horizontal axis in the figures denote the y_0^+ positions where the maximum values of relevant flow properties occur. The Reynolds stress budgets at stations A and B exhibit similar characteristics as that of a turbulent boundary layer over a flat-plate as discussed by Pope (2000) in their Chapter 7, Sec. 7.3.5, Figs. 7.35-7.38. The main source of production of Reynolds stress in a flat-plate turbulent boundary layer is $\mathscr{P}_{11}$, production of $\langle u^2 \rangle$, as shown in (Figs. 4.24a and 4.24b), while $\mathscr{P}_{22}$ (Figs. 4.24c and 4.24d) and $\mathscr{P}_{33}$ (Figs. 4.25a and 4.25b) are negligible. Therefore, most of the TKE production in this region occurs through the production of $\langle u^2 \rangle$. Over most of the boundary layer, the velocity-pressure-gradient term, $\mathit{\Pi}_{11}$, is the main sink of $\langle u^2 \rangle$, while $\mathit{\Pi}_{22}$ and $\mathit{\Pi}_{33}$ are the main sources of $\langle v^2 \rangle$ and $\langle w^2 \rangle$, respectively. Therefore, the primary role of the velocity-pressure-gradient tensor is as a sink of $\langle u^2 \rangle$ and as a source of $\langle v^2 \rangle$ and $\langle w^2 \rangle$. Further, the dissipation of $\langle v^2 \rangle$ and $\langle w^2 \rangle$, viz., ϵ_{22} and ϵ_{33}, are approximately balanced by $\mathit{\Pi}_{22}$ and $\mathit{\Pi}_{33}$. Finally, in the shear-stress budget, $-\langle uv \rangle$, the production $-\mathscr{P}_{12}$ is approximately balanced by $-\mathit{\Pi}_{12}$, while the dissipation $-\epsilon_{12}$ is negligible, except near the wall or $y_0^+ < 10$.

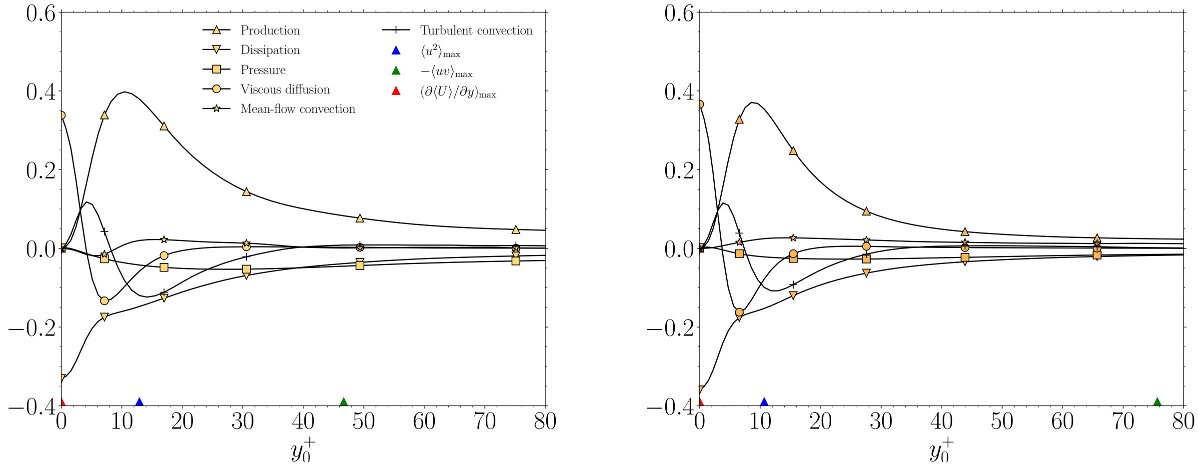

(a) Budget of $\langle u^2 \rangle$, at station A ($x = x_0 = -2L$)

(b) Budget of $\langle u^2 \rangle$, at station B ($x = 0$)

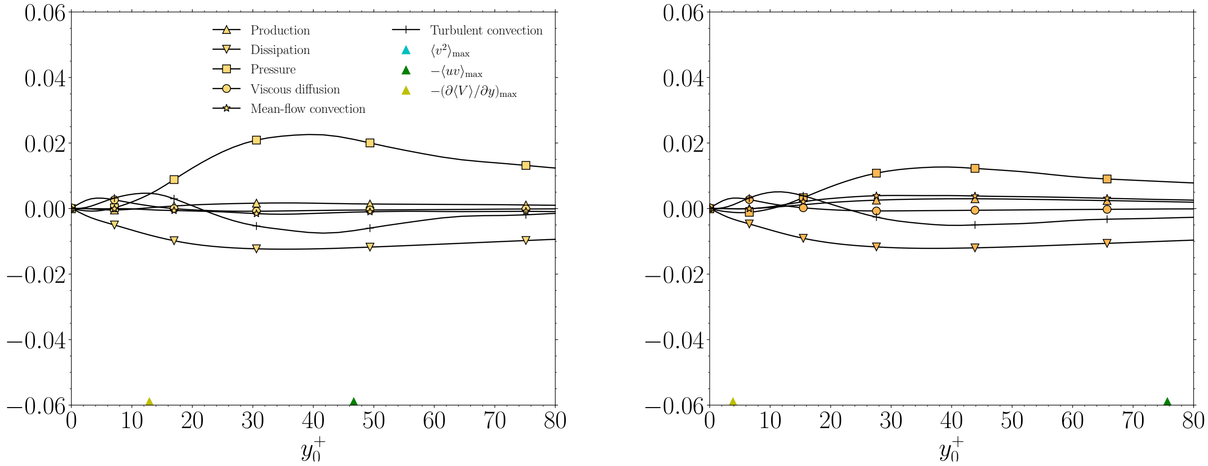

(c) Budget of $\langle v^2 \rangle$, at station A ($x = x_0 = -2L$)

(d) Budget of $\langle v^2 \rangle$, at station B ($x = 0$)

Figure 4.24: Budget of $\langle u^2 \rangle$ (in (a) and (b)) and $\langle v^2 \rangle$ (in (c) and (d)) at stations A and B, normalized by viscous scales at $x_0 = -2L$ (Eq. 4.18). Colored triangles on the horizontal axis denote the positions of maximum values of $\langle u^2 \rangle$, $-\langle uv \rangle$, $\partial \langle U \rangle / \partial y$ (in (a) and (b)) and maximum values of $\langle v^2 \rangle$, $-\langle uv \rangle$ and $\partial \langle V \rangle / \partial y$ (in (c) and (d)).

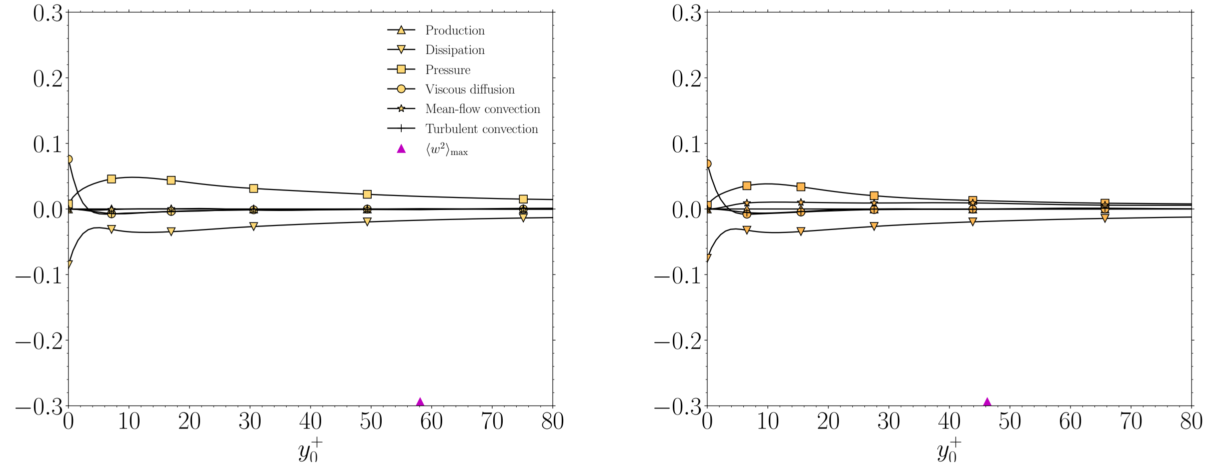

(a) Budget of $\langle w^2\rangle$, at station A ($x = x_0 = -2L$)

(b) Budget of $\langle w^2\rangle$, at station B ($x = 0$)

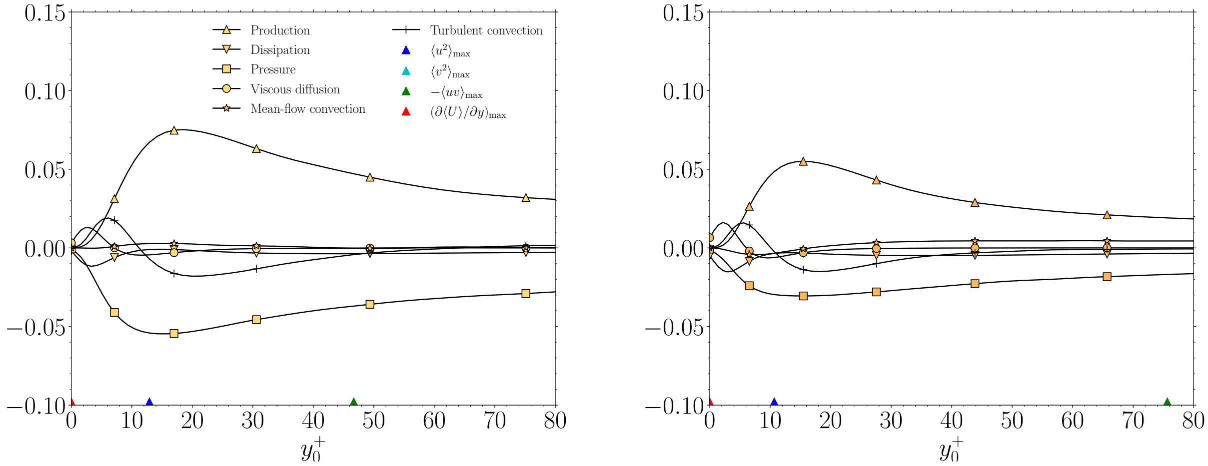

(c) Budget of $-\langle uv\rangle$, at station A ($x = x_0 = -2L$)

(d) Budget of $-\langle uv\rangle$, at station B ($x = 0$)

Figure 4.25: Budget of $\langle w^2\rangle$ (in (a) and (b)) and $-\langle uv\rangle$ (in (c) and (d)) at stations A and B, normalized by viscous scales at $x_0 = -2L$ (Eq. 4.18). Colored triangles on the horizontal axis denote the positions of maximum values of $\langle w^2\rangle$ (in (a) and (b)) as well as $\langle u^2\rangle$, $\langle v^2\rangle$, $-\langle uv\rangle$ and $\partial\langle U\rangle/\partial y$ (in (c) and (d)).

Reynolds stress budget at station C and D ($\mathbf{x = x_{sep}}$ and $\mathbf{x = 0.5L}$) Figures 4.27 and 4.28 show the budgets of the Reynolds stress components at stations C and D. The budgets of the Reynolds stress are quite different from those of a ZPG SDTBL as those just described of station A. For example, the peak value of production of $\langle u^2 \rangle$ at stations C and D is at least two times that of at stations A and B. In order to analyze further such change, we notice that the production of $\langle u^2 \rangle$, $\mathscr{P}_{11}$, is written from (4.19) as

$$\mathscr{P}_{11} = 2\left(-\langle u^2 \rangle \frac{\partial \langle U \rangle}{\partial x} - \langle uv \rangle \frac{\partial \langle U \rangle}{\partial y}\right). \tag{4.22}$$

The two terms on the r.h.s. of Eq. (4.22) at stations C and D are shown in Figs. 4.29a and 4.29b, respectively and the main source of $\mathscr{P}_{11}$ is $\partial \langle U \rangle / \partial x$. The peak production of $\langle u^2 \rangle$ at stations C ($y_0^+ \approx 22$) and D ($y_0^+ \approx 40$) are obtained further away from the wall compared to A and B ($y_0^+ \approx 10$). The production of $\langle u^2 \rangle$ at C and D peaks close to the position of maximum mean shear $\partial \langle U \rangle / \partial y$ ($y_0^+ \approx 16$ for station C, and $y_0^+ \approx 36$ for station D).

Similarly to stations A and B, also at stations C and D (4.27 and 4.28) the velocity-pressure-gradient term, $\mathit{\Pi}_{11}$, is a sink of $\langle u^2 \rangle$, and $\mathit{\Pi}_{22}$ and $\mathit{\Pi}_{33}$ are sources of $\langle v^2 \rangle$ and $\langle w^2 \rangle$, respectively. The pressure term $\mathit{\Pi}_{33}$ is the main source of $\langle w^2 \rangle$ since its production $\mathscr{P}_{33}$ is zero. However unlike stations A and B, at stations C and D, the production of $\langle v^2 \rangle$ is non-negligible. The production of $\langle v^2 \rangle$, $\mathscr{P}_{22}$, is written from (4.19) as

$$\mathscr{P}_{22} = 2\left(-\langle uv \rangle \frac{\partial \langle V \rangle}{\partial x} - \langle v^2 \rangle \frac{\partial \langle V \rangle}{\partial y}\right). \tag{4.23}$$

The terms of Eq. (4.23) at stations C and D are shown in Figs. 4.29c and 4.29d, respectively. Since, $-\langle uv \rangle > 0$ (Fig. 4.20c) and $\partial \langle V \rangle / \partial x < 0$ for $y_0^+ > 7$ for both stations C and D (Fig. 4.23c), the first term $-\langle uv \rangle \partial \langle V \rangle / \partial x < 0$ and does not contribute to the bulk of production of $\langle v^2 \rangle$. Therefore, $\partial \langle V \rangle / \partial y$ is the main source of production since $-\langle v^2 \rangle$ is always negative and $\partial \langle V \rangle / \partial y < 0$ at station C and for $y_0^+ > 6$ at station D (Fig. 4.23d). Hence, the production of $\langle v^2 \rangle$ peaks at $y_0^+ \approx 20$ and 32 for stations C and D, respectively, around the location of minimum $\partial \langle V \rangle / \partial y$ at $y_0^+ \approx 12$ and 25 for stations C and D, respectively, as shown in Figs. 4.27c and 4.27d.

Further, at stations C and D where the wall is curved, the viscous diffusion and dissipation of $\langle v^2 \rangle$ and $-\langle uv \rangle$ are not equal to zero as in the upstream flat-plate regions of the flow, i.e., at stations A and B. In order to explain that, next, we analyze the behavior of such terms in a turbulent flow over a flat-plate and curved-wall regions. In a flat-plate turbulent boundary layer, the velocities

$$u = v = w = 0 \;\forall (x, z) \text{ at the wall } (y = 0). \tag{4.24}$$

Therefore, the velocity derivatives at the flat-wall

$$\left.\frac{\partial u}{\partial x}\right|_{y=0} = \left.\frac{\partial w}{\partial z}\right|_{y=0} = 0, \tag{4.25}$$

and the continuity equation, $\nabla \cdot \mathbf{u} = 0$, yields

$$\left.\frac{\partial v}{\partial y}\right|_{y=0} = 0. \tag{4.26}$$

Further, from Eq. (4.24) we have

$$\left.\frac{\partial v}{\partial x}\right|_{y=0} = \left.\frac{\partial v}{\partial z}\right|_{y=0} = 0. \tag{4.27}$$

The viscous diffusion of $\langle v^2 \rangle$ and $-\langle uv \rangle$ are, respectively, written from Eq. (4.18) as

$$\begin{aligned} \nu \nabla^2 \langle v^2 \rangle &= \nu \left\langle \frac{\partial}{\partial x}\left(\frac{\partial v^2}{\partial x}\right) + \frac{\partial}{\partial y}\left(\frac{\partial v^2}{\partial y}\right) + \frac{\partial}{\partial z}\left(\frac{\partial v^2}{\partial z}\right) \right\rangle, \\ &= \nu \left\langle \frac{\partial}{\partial x}\left(2v\frac{\partial v}{\partial x}\right) + \frac{\partial}{\partial y}\left(2v\frac{\partial v}{\partial y}\right) + \frac{\partial}{\partial z}\left(2v\frac{\partial v}{\partial z}\right) \right\rangle, \end{aligned} \tag{4.28}$$

$$\begin{aligned} -\nu \nabla^2 \langle uv \rangle &= -\nu \left\langle \frac{\partial}{\partial x}\left(\frac{\partial uv}{\partial x}\right) + \frac{\partial}{\partial y}\left(\frac{\partial uv}{\partial y}\right) + \frac{\partial}{\partial z}\left(\frac{\partial uv^2}{\partial z}\right) \right\rangle, \\ &= -\nu \left\langle \frac{\partial}{\partial x}\left(u\frac{\partial v}{\partial x} + v\frac{\partial u}{\partial x}\right) + \frac{\partial}{\partial y}\left(u\frac{\partial v}{\partial y} + v\frac{\partial u}{\partial y}\right) + \frac{\partial}{\partial z}\left(u\frac{\partial v}{\partial z} + v\frac{\partial u}{\partial z}\right) \right\rangle, \end{aligned} \tag{4.29}$$

which, using Eqs. (4.26) and (4.27), result in

$$\nu \nabla^2 \langle v^2 \rangle = -\nu \nabla^2 \langle uv \rangle = 0 \;\forall (x, z) \text{ at the wall } (y = 0). \tag{4.30}$$

The viscous dissipation of $\langle v^2 \rangle$ and $-\langle uv \rangle$ are, respectively, written from Eq. (4.18) as

$$\epsilon_{22} = 2\nu \left\langle \left(\frac{\partial v}{\partial x}\right)^2 + \left(\frac{\partial v}{\partial y}\right)^2 + \left(\frac{\partial v}{\partial z}\right)^2 \right\rangle, \tag{4.31}$$

$$-\,\epsilon_{12} = -2\nu \left\langle \left(\frac{\partial u}{\partial x}\frac{\partial v}{\partial x}\right) + \left(\frac{\partial u}{\partial y}\frac{\partial v}{\partial y}\right) + \left(\frac{\partial u}{\partial z}\frac{\partial v}{\partial z}\right) \right\rangle, \tag{4.32}$$

which, using Eqs. (4.26) and (4.27), result in

$$\epsilon_{22} = -\epsilon_{12} = 0 \ \forall (x, z) \text{ at the wall } (y = 0). \tag{4.33}$$

Hence, from Eqs. (4.30) and (4.33), the viscous diffusion and dissipation of $\langle v^2 \rangle$ and $-\langle uv \rangle$, at the wall in the flat-plate regions of the flow, i.e., stations A and B and as we shall see later in this section, at stations F, G and H, are zero (Fig. 4.24c and 4.24d). In the curved wall region $0 \leq x \leq L$, instead, we have the contravariant component of velocity fluctuation $\hat{u} = \hat{v} = w = 0 \ \forall (\xi, z)$ at the wall $(\eta = 0)$. However, the velocity derivatives at the curved wall $(\eta = 0)$

$$\left.\frac{\partial u}{\partial x}\right|_{\eta=0} \neq 0 \quad \text{and} \quad \left.\frac{\partial w}{\partial z}\right|_{\eta=0} = 0 \tag{4.34}$$

and, thus, from the continuity equation, $\nabla \cdot \mathbf{u} = 0$, we get

$$\left.\frac{\partial v}{\partial y}\right|_{\eta=0} \neq 0. \tag{4.35}$$

Hence, from Eqs. (4.28) and (4.31), the viscous diffusion and dissipation of $\langle v^2 \rangle$ and $-\langle uv \rangle$, at the curved-wall section, i.e., stations C and D are not equal zero (Fig. 4.27c and 4.27d). The viscous diffusion of $\langle w^2 \rangle$ is written from Eq. (4.18) as

$$\begin{aligned} \nu \nabla^2 \langle w^2 \rangle &= \nu \left\langle \frac{\partial}{\partial x}\left(\frac{\partial w^2}{\partial x}\right) + \frac{\partial}{\partial y}\left(\frac{\partial w^2}{\partial y}\right) + \frac{\partial}{\partial z}\left(\frac{\partial w^2}{\partial z}\right) \right\rangle, \\ &= \nu \left\langle \frac{\partial}{\partial x}\left(2w\frac{\partial w}{\partial x}\right) + \frac{\partial}{\partial y}\left(2w\frac{\partial w}{\partial y}\right) + \frac{\partial}{\partial z}\left(2w\frac{\partial w}{\partial z}\right) \right\rangle, \end{aligned} \tag{4.36}$$

and, the viscous dissipation of $\langle w^2 \rangle$ is written from Eq. (4.18) as

$$\epsilon_{33} = 2\nu \left\langle \left(\frac{\partial w}{\partial x}\right)^2 + \left(\frac{\partial w}{\partial y}\right)^2 + \left(\frac{\partial w}{\partial z}\right)^2 \right\rangle, \tag{4.37}$$

Since $w = 0 \ \forall z$ at the wall in the curved-wall section, the viscous diffusion and dissipation of $\langle w^2 \rangle$, Eqs. (4.36) and (4.37), at the curved-wall section, as well, are zero (Fig. 4.28a and 4.28b). Figure 4.26 summarizes these different results regarding the derivatives of velocity fluctuations at the wall in a SDTBL over a flat-wall versus a curved-wall, just discussed through Eqs. (4.24)-(4.37). In this regard, we notice that differently from what we observe in the turbulent flow separating over a curved wall, in the case of 'pressure-gradient-induced turbulent flow separation' over a flat-plate, as studied for example by Abe (2017), the viscous diffusion and dissipation of $\langle v^2 \rangle$ and $-\langle uv \rangle$ at the wall are zero since $u = v = w = 0 \ \forall (x, z)$ at the wall ($y = 0$). Later in this section, we will discuss the similarities and differences of the Reynolds stress budgets of our DNS from the SDTBL separating over the curved wall in orthogonal curvilinear coordinates with those of 'pressure-gradient-induced turbulent flow separation' over a flat-plate.

The mean flow convection and turbulent convection of the Reynolds stress in Figs. 4.27 and 4.28 indicate enhanced transport compared to that at station A and B, shown in Fig. 4.24 and 4.25, due to the shear layer created by the flow separation over the curved ramp (Fig. 4.8b). Since the mean flow convection depends on the gradient of the Reynolds stress and $|\langle V \rangle| \gg 0$ at $y_0^+ > 10$ and 20 at station C and D, respectively, the bulk of mean flow convection is obtained above the peaks of their respective components of Reynolds stress, i.e., at $y_0^+ > \langle u_i u_j \rangle_{\max}$ (Figs. 4.27 and 4.28). Note that the profiles of the mean flow convection and turbulent convection in the shear layer region of the flow, $10 < y_0^+ < 100$ of stations C and D in Figs. 4.27 and 4.28 are similar to that of the turbulent mixing layer, Fig. 21 of Rogers & Moser (1994).

Finally, regarding the budget of $-\langle uv \rangle$, its production, $-\mathscr{P}_{12}$, is written from (4.19) as

$$-\mathscr{P}_{12} = \left(\langle u^2 \rangle \frac{\partial \langle V \rangle}{\partial x} + \langle uv \rangle \frac{\partial \langle U \rangle}{\partial x} + \langle uv \rangle \frac{\partial \langle V \rangle}{\partial y} + \langle v^2 \rangle \frac{\partial \langle U \rangle}{\partial y} \right). \tag{4.38}$$

Figures 4.28c and 4.28d show that $-\mathscr{P}_{12}$ is approximately two and six times larger at stations C and D, respectively, that that at station A. In order to understand such increase, we show the terms of Eq. (4.38) at stations C and D in Figs. 4.30a and 4.30b. Since $\langle uv \rangle < 0$ and $\langle v^2 \rangle > 0$, $-\mathscr{P}_{12}$ is sustained by the mean shear $\partial \langle U \rangle / \partial y > 0$ and the velocity derivative $\partial \langle V \rangle / \partial y < 0$. Since $\langle u^2 \rangle > 0$ and $\langle uv \rangle < 0$, the mean shear terms $\partial \langle V \rangle / \partial x < 0$ and the velocity derivative $\partial \langle U \rangle / \partial x > 0$ contribute to reducing the production $-\mathscr{P}_{12}$ as shown in

Figs. 4.30a and 4.30b. The dissipation, $-\epsilon_{12}$, is negligible except near the wall while the production is balanced by the velocity-pressure transport, $-\Pi_{12}$.

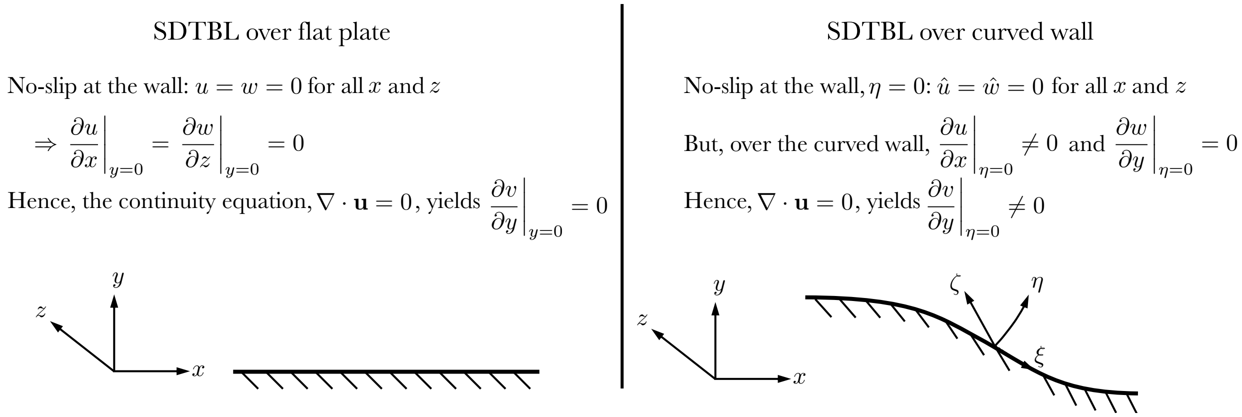

SDTBL over flat plate

No-slip at the wall: $u = w = 0$ for all x and z

$$\Rightarrow \left.\frac{\partial u}{\partial x}\right|_{y=0} = \left.\frac{\partial w}{\partial z}\right|_{y=0} = 0$$

Hence, the continuity equation, $\nabla \cdot \mathbf{u} = 0$, yields $\left.\dfrac{\partial v}{\partial y}\right|_{y=0} = 0$

SDTBL over curved wall

No-slip at the wall, $\eta = 0$: $\hat{u} = \hat{w} = 0$ for all x and z

But, over the curved wall, $\left.\dfrac{\partial u}{\partial x}\right|_{\eta=0} \neq 0$ and $\left.\dfrac{\partial w}{\partial y}\right|_{\eta=0} = 0$

Hence, $\nabla \cdot \mathbf{u} = 0$, yields $\left.\dfrac{\partial v}{\partial y}\right|_{\eta=0} \neq 0$

Figure 4.26: Derivatives of velocity fluctuations at the wall in Cartesian coordinates at the wall for flat plate (left) and curved plate (right).

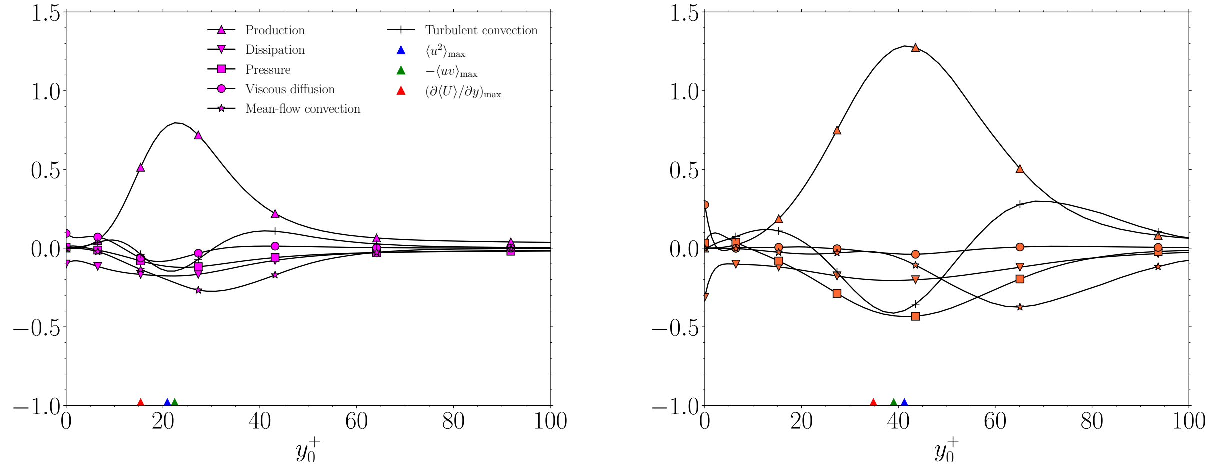

(a) Budget of $\langle u^2 \rangle$, at station C ($x = x_{\text{sep}}$)

(b) Budget of $\langle u^2 \rangle$, at station D ($x = 0.5L$)

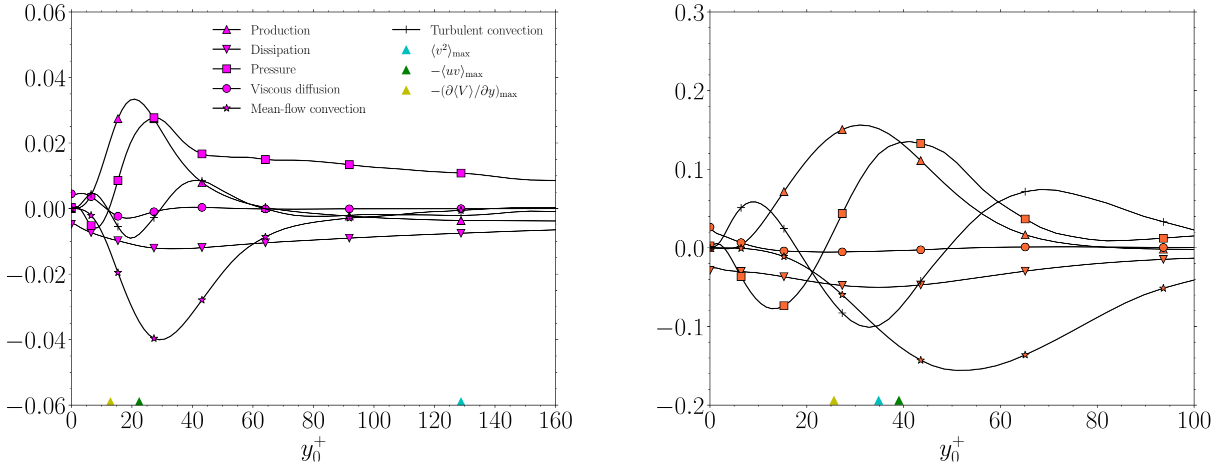

(c) Budget of $\langle v^2 \rangle$, at station C ($x = x_{\text{sep}}$)

(d) Budget of $\langle v^2 \rangle$, at station D ($x = 0.5L$)

Figure 4.27: Budget of $\langle u^2 \rangle$ (in (a) and (b)) and $\langle v^2 \rangle$ (in (c) and (d)) at stations C and D, normalized by viscous scales at $x_0 = -2L$ (Eq. 4.18). Colored triangles on the horizontal axis denote the positions of maximum values of $\langle u^2 \rangle$, $-\langle uv \rangle$, $\partial \langle U \rangle / \partial y$ (in (a) and (b)) and maximum values of $\langle v^2 \rangle$, $-\langle uv \rangle$ and $\partial \langle V \rangle / \partial y$ (in (c) and (d)).

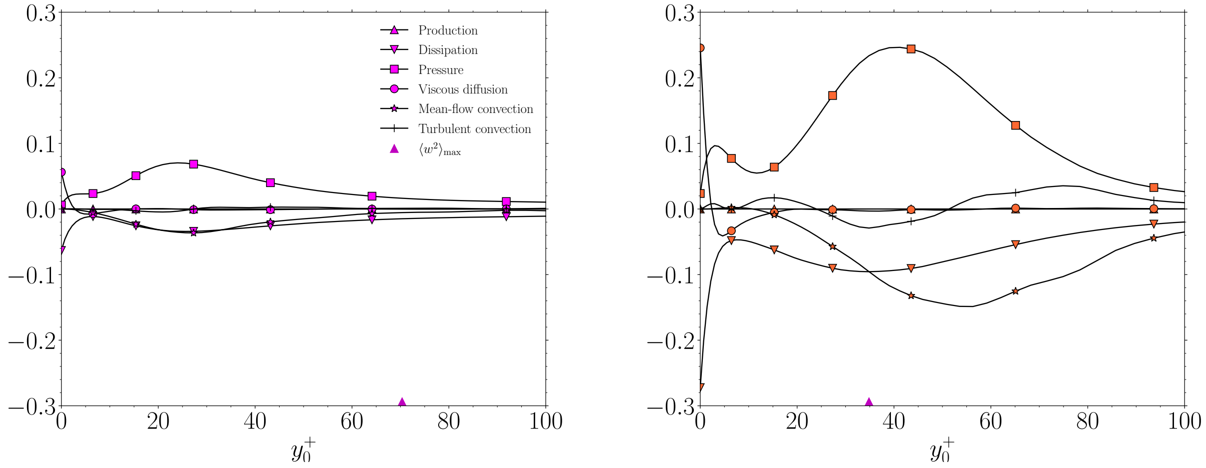

(a) Budget of $\langle w^2\rangle$, at station C ($x = x_{\mathrm{sep}}$)

(b) Budget of $\langle w^2\rangle$, at station D ($x = 0.5L$)

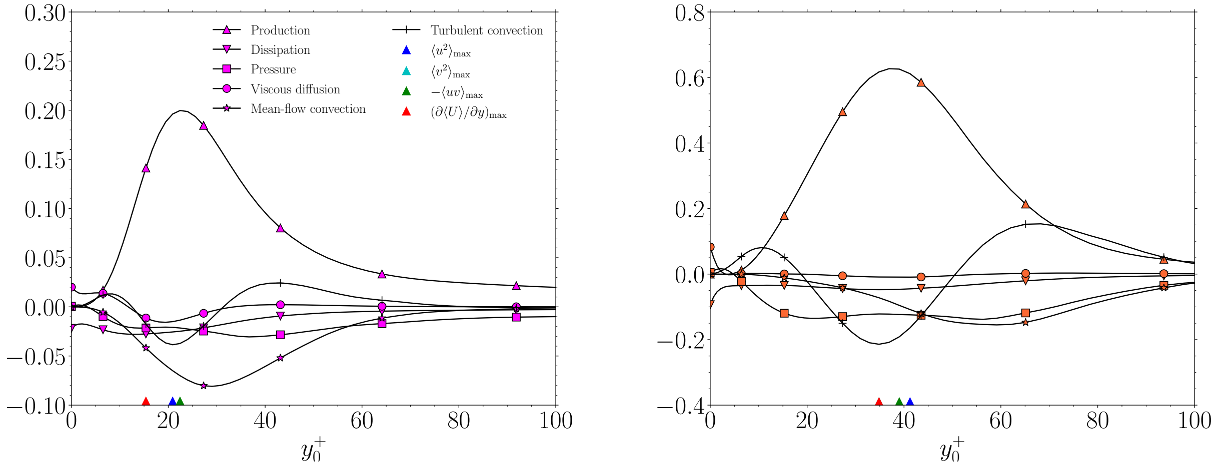

(c) Budget of $-\langle uv\rangle$, at station C ($x = x_{\mathrm{sep}}$)

(d) Budget of $-\langle uv\rangle$, at station D($x = 0.5L$)

Figure 4.28: Budget of $\langle w^2\rangle$ (in (a) and (b)) and $-\langle uv\rangle$ (in (c) and (d)) at stations C and D, normalized by viscous scales at $x_0 = -2L$ (Eq. 4.18). Colored triangles on the horizontal axis denote the positions of maximum values of $\langle w^2\rangle$ (in (a) and (b)) as well as $\langle u^2\rangle$, $\langle v^2\rangle$, $-\langle uv\rangle$ and $\partial\langle U\rangle/\partial y$ (in (c) and (d)).

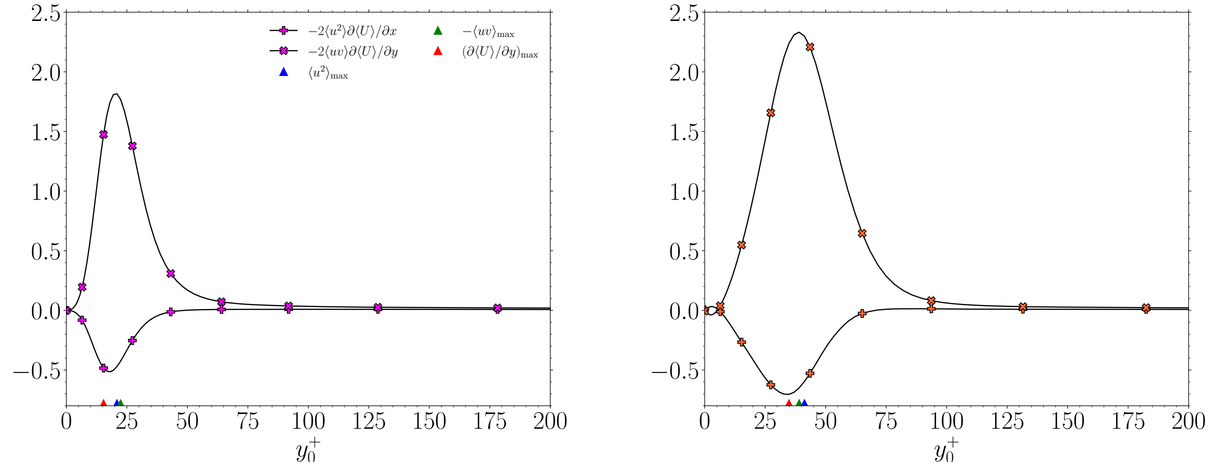

(a) Terms of $\mathscr{P}_{11}$, production of $\langle u^2\rangle$, at station C (b) Terms of $\mathscr{P}_{11}$, production of $\langle u^2\rangle$, at station D

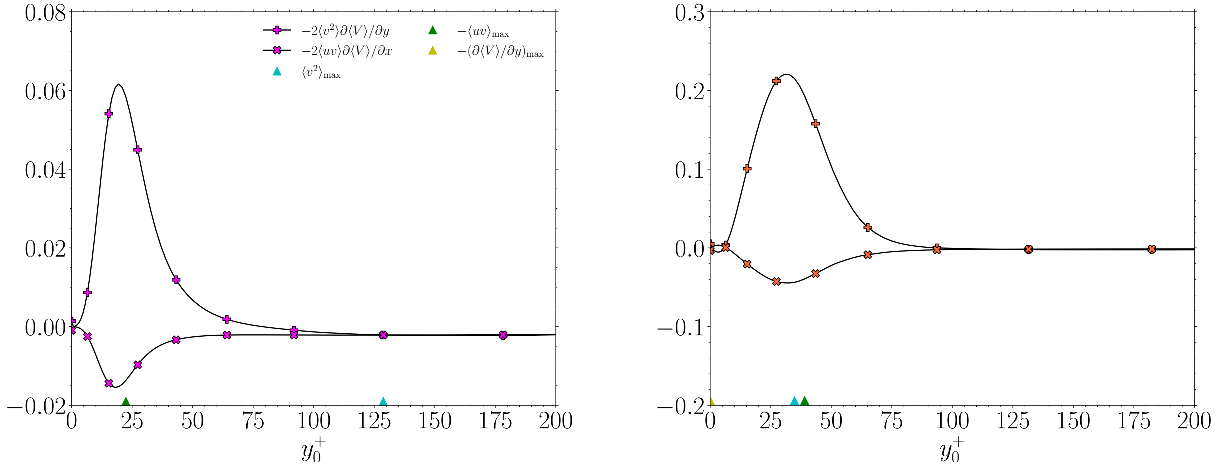

(c) Terms of $\mathscr{P}_{22}$ production of , $\langle v^2\rangle$, at station C (d) Terms of $\mathscr{P}_{22}$, production of $\langle v^2\rangle$, at station D

Figure 4.29: Terms contributing to $\mathscr{P}_{11}$, production of $\langle u^2\rangle$ (Eq. (4.22), (a) and (b)), and $\mathscr{P}_{22}$, production of $\langle v^2\rangle$ (Eq. (4.23), (c) and (d)) at stations C and D, normalized by viscous scales at $x_0 = -2L$. Colored triangles on the horizontal axis denote the positions of maximum values of $\langle u^2\rangle$, $-\langle uv\rangle$, $\partial\langle U\rangle/\partial y$ (in (a) and (b)) and maximum values of $\langle v^2\rangle$, $-\langle uv\rangle$ and $\partial\langle V\rangle/\partial y$ (in (c) and (d)).

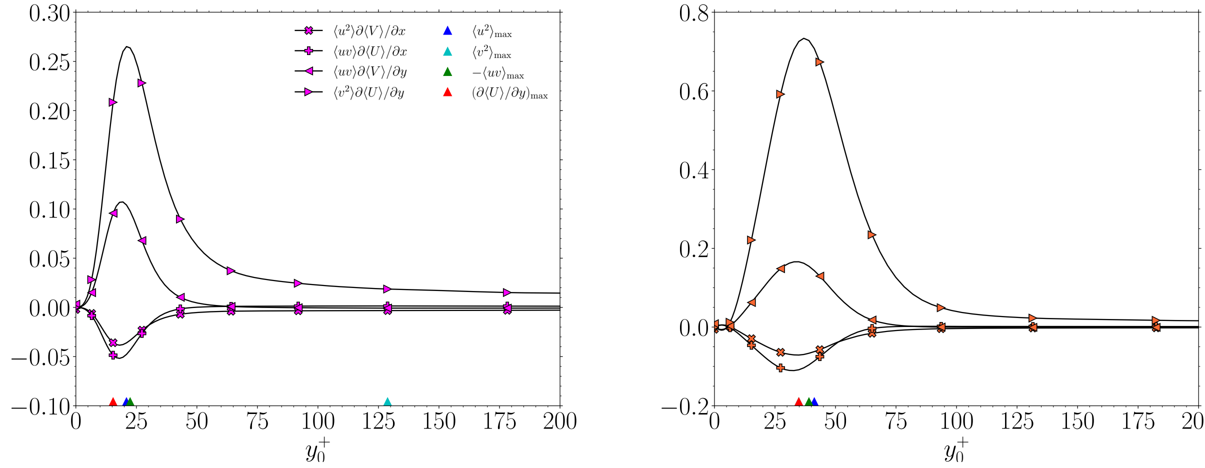

(a) Terms of $-\mathscr{P}_{12}$, production of $-\langle uv\rangle$, at station C (b) Terms of $-\mathscr{P}_{12}$, production of $-\langle uv\rangle$, at station D

Figure 4.30: Terms contributing to $-\mathscr{P}_{12}$ (4.38), production of $-\langle uv\rangle$, at stations C and D, normalized by viscous scales at $x_0 = -2L$. Colored triangles on the horizontal axis denote the positions of maximum values of $\langle u^2\rangle$, $\langle v^2\rangle$, $-\langle uv\rangle$ and $\partial\langle U\rangle/\partial y$.

Reynolds stress budget at station E and F ($\mathbf{x = L}$ and $\mathbf{x = x_{rea}}$) Figures 4.31 and 4.32 show the budgets of the Reynolds stress components at stations E and F. The terms contributing to the production of $\langle u^2\rangle$, $\mathscr{P}_{11}$, given in Eq. (4.22), at stations E and F are shown in Figs. 4.33a and 4.33b. The peak values of $\mathscr{P}_{11}$ at stations E and F are comparable to that of station A. The peak $\mathscr{P}_{11}$ at stations E and F ($y_0^+ \approx 240$) occur further away from the wall compared to stations A and B ($y_0^+ \approx 10$). The balance of $\langle u^2\rangle$ at the location of peak production at station E, i.e., $\mathscr{P}_{11} - \epsilon_{11} - \mathit{\Pi}_{11}$, is smaller than that at station D, and, hence, the maximum value of $\langle u^2\rangle$ is obtained at station D from all the stations analyzed A-H (Fig. 4.19a). The production of $\langle u^2\rangle$ peaks near the position of maximum mean shear $\partial\langle U\rangle/\partial y$ in the case of station E ($y_0^+ \approx 235$) and near its local maxima at station F ($y_0^+ \approx 230$, Table 4.4).

Similarly to the other stations the velocity-pressure-gradient term, $\mathit{\Pi}_{11}$, is a sink of $\langle u^2\rangle$, and, $\mathit{\Pi}_{22}$ and $\mathit{\Pi}_{33}$ are sources of $\langle v^2 \rangle$ and $\langle w^2 \rangle$, respectively. The pressure term $\mathit{\Pi}_{33}$ is the main source of $\langle w^2 \rangle$ since the production $\mathscr{P}_{33}$ is zero. Similarly to stations C and D, the production of $\langle v^2 \rangle$, at stations E and F, is non-negligible.

The terms contributing to the production of $\langle v^2 \rangle$, $\mathscr{P}_{22}$, given in Eq. (4.23), at station E and F are shown in Figs. 4.33c and 4.33d. The velocity derivative $\partial \langle V \rangle / \partial y$ is a source of production of $\langle v^2 \rangle$ in the region where $\partial \langle V \rangle / \partial y < 0$, i.e., for $20 < y_0^+ < 300$ at E and for $2 < y_0^+ < 300$ at station F (Fig. 4.23d). However, unlike C and D, $\partial \langle V \rangle / \partial x$ is also source of $\mathscr{P}_{22}$ in the region where $\partial \langle V \rangle / \partial y > 0$, i.e., for $y_0^+ > 210$ at E and for $y_0^+ > 20$ at station F (Fig. 4.23c). As a result, the balance of $\langle v^2 \rangle$ at the location of peak production at station E, i.e., $\mathit{\Pi}_{22} + \mathscr{P}_{22} - \epsilon_{22}$, is greater than that at station D, and, hence, the maximum value of $\langle v^2 \rangle$ is obtained at station E from of all the analyzed stations A-H (Fig. 4.19c and Table 4.4).

Further, similarly to station C and D, the viscous diffusion and dissipation of $\langle v^2 \rangle$ and $-\langle uv \rangle$ at the wall at station E are not equal to zero (Fig. 4.31c). However, this is not the case at station F since that is in a flat-plate region and is not located in the curved-wall region as stations C, D and E (Fig. 4.31d). Further, the mean flow convection and turbulent convection of the Reynolds stress in Figs. 4.31 and 4.32 indicate enhanced transport compared to that at stations A and B due to shear layer created by the flow separation over the curved ramp and these profiles resemble those of the turbulent mixing layer, e.g., see Fig. 21 of Rogers & Moser (1994) for $60 < y_0^+ < 500$. The bulk of mean flow convection is obtained above the peaks of their respective components of Reynolds stress, i.e., at $y_0^+ > \langle u_i u_j \rangle_{\max}$ (Figs. 4.31 and 4.32). Finally, in the shear-stress budget, the peak production $-\mathscr{P}_{12}$ is approximately three times greater at stations E and F than at station A. The terms contributing to $-\mathscr{P}_{12}$, given in Eq. (4.38), at stations E and F are shown in Figs. 4.34a and 4.34b which show that the main term contributing to $-\mathscr{P}_{12}$ at stations E and F is the last term of Eq. (4.38), i.e., $\langle v^2 \rangle \partial \langle U \rangle / \partial y$. Also, at stations E and F, the dissipation, $-\epsilon_{12}$, is negligible and the production, $-\mathscr{P}_{12}$ is balanced by $-\mathit{\Pi}_{12}$.

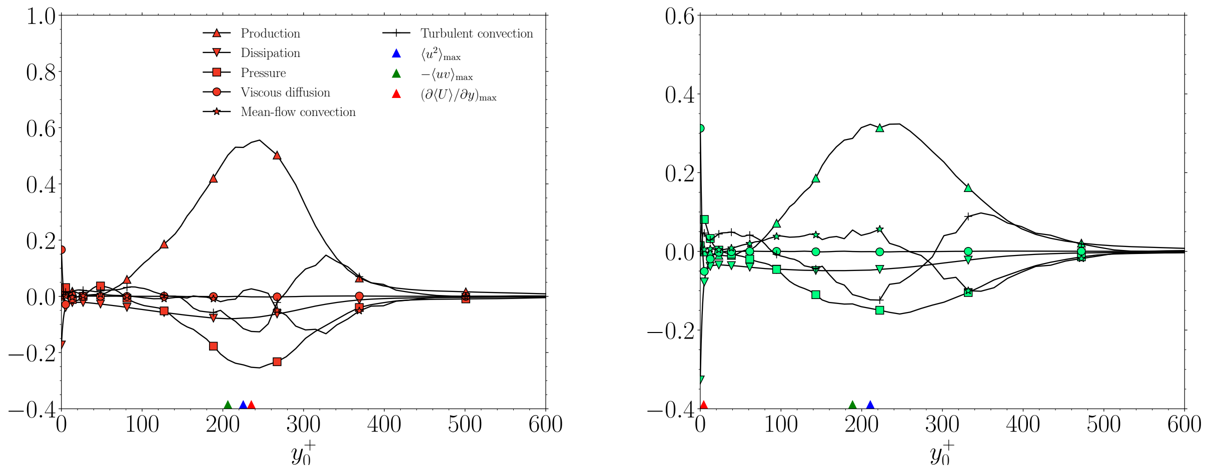

(a) Budget of $\langle u^2 \rangle$, at station E ($x = x_L$)

(b) Budget of $\langle u^2 \rangle$, at station F ($x = x_{\mathrm{rea}}$)

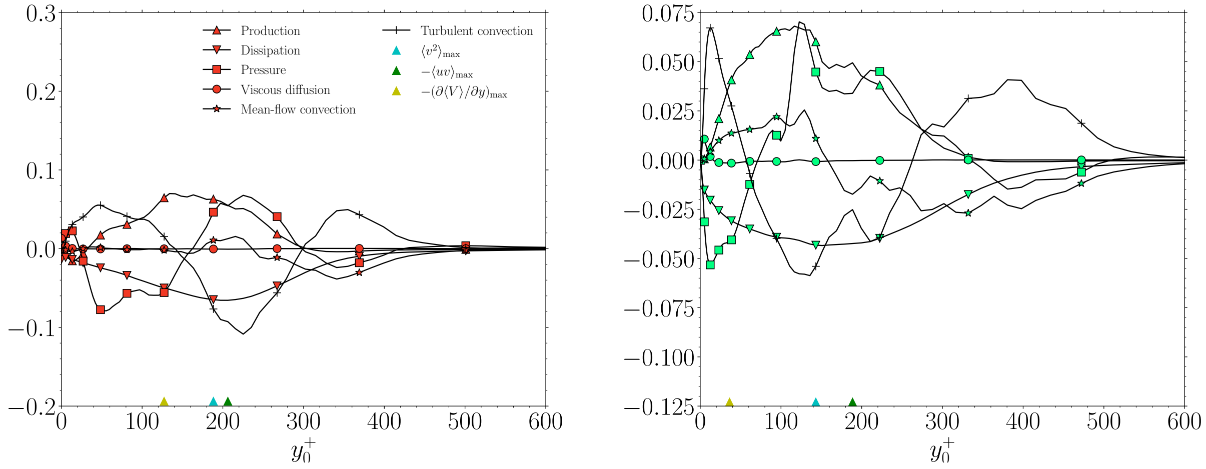

(c) Budget of $\langle v^2 \rangle$, at station E ($x = L$)

(d) Budget of $\langle v^2 \rangle$, at station F ($x = x_{\mathrm{rea}}$)

Figure 4.31: Budget of $\langle u^2 \rangle$ (in (a) and (b)) and $\langle v^2 \rangle$ (in (c) and (d)) at stations E and F, normalized by viscous scales at $x_0 = -2L$ (Eq. 4.18). Colored triangles on the horizontal axis denote the positions of maximum values of $\langle u^2 \rangle$, $-\langle uv \rangle$, $\partial \langle U \rangle / \partial y$ (in (a) and (b)) and maximum values of $\langle v^2 \rangle$, $-\langle uv \rangle$ and $\partial \langle V \rangle / \partial y$ (in (c) and (d)).

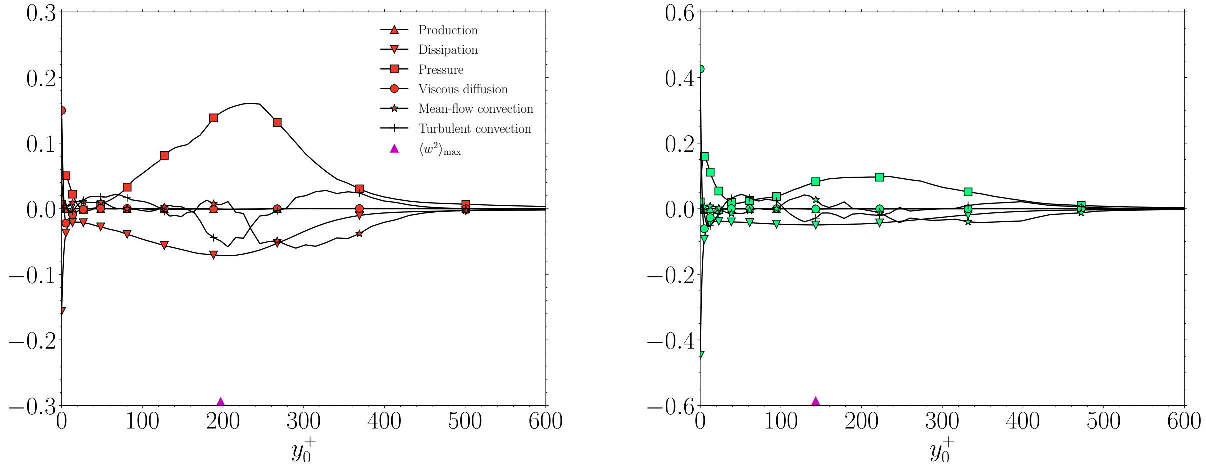

(a) Budget of $\langle w^2 \rangle$, at station E ($x = L$)

(b) Budget of $\langle w^2 \rangle$, at station F ($x = x_{\text{rea}}$)

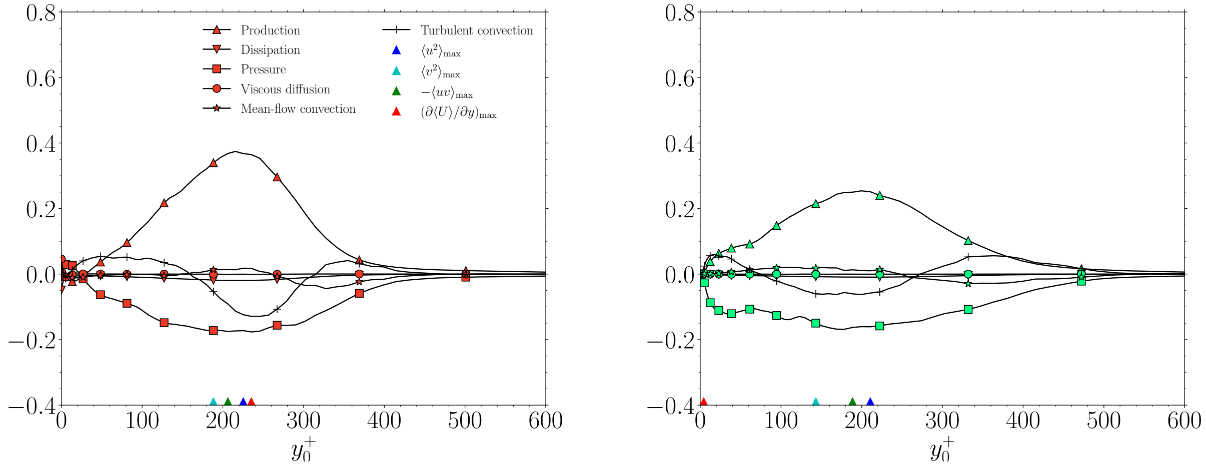

(c) Budget of $-\langle uv \rangle$, at station E ($x = L$)

(d) Budget of $-\langle uv \rangle$, at station F ($x = x_{\text{rea}}$)

Figure 4.32: Budget of $\langle w^2 \rangle$ (in (a) and (b)) and $-\langle uv \rangle$ (in (c) and (d)) at stations E and F, normalized by viscous scales at $x_0 = -2L$ (Eq. 4.18). Colored triangles on the horizontal axis denote the positions of maximum values of $\langle w^2 \rangle$ (in (a) and (b)) as well as $\langle u^2 \rangle$, $\langle v^2 \rangle$, $-\langle uv \rangle$ and $\partial \langle U \rangle / \partial y$ (in (c) and (d)).

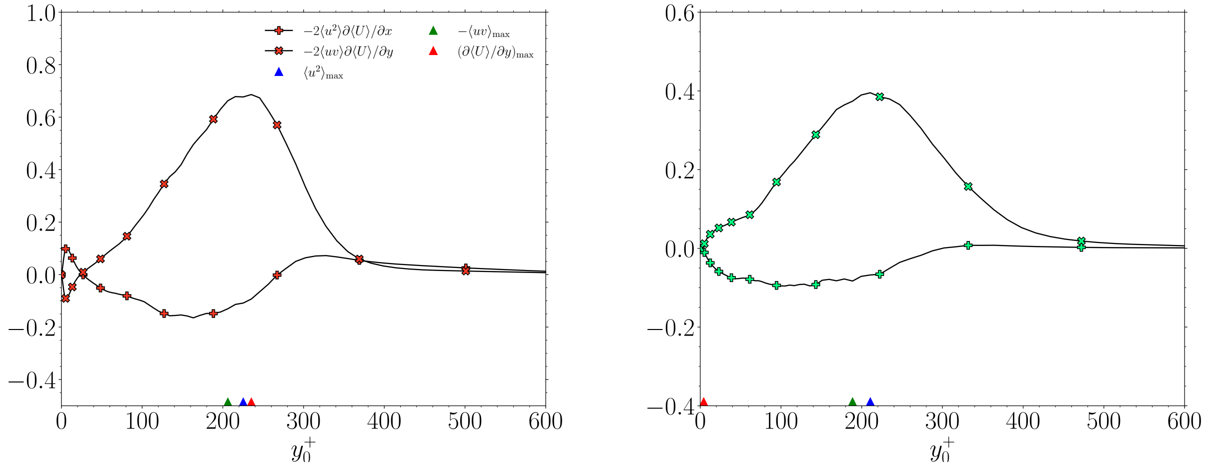

(a) Terms of $\mathscr{P}_{11}$, production of $\langle u^2\rangle$, at station E (b) Terms of $\mathscr{P}_{11}$, production of $\langle u^2\rangle$, at station F

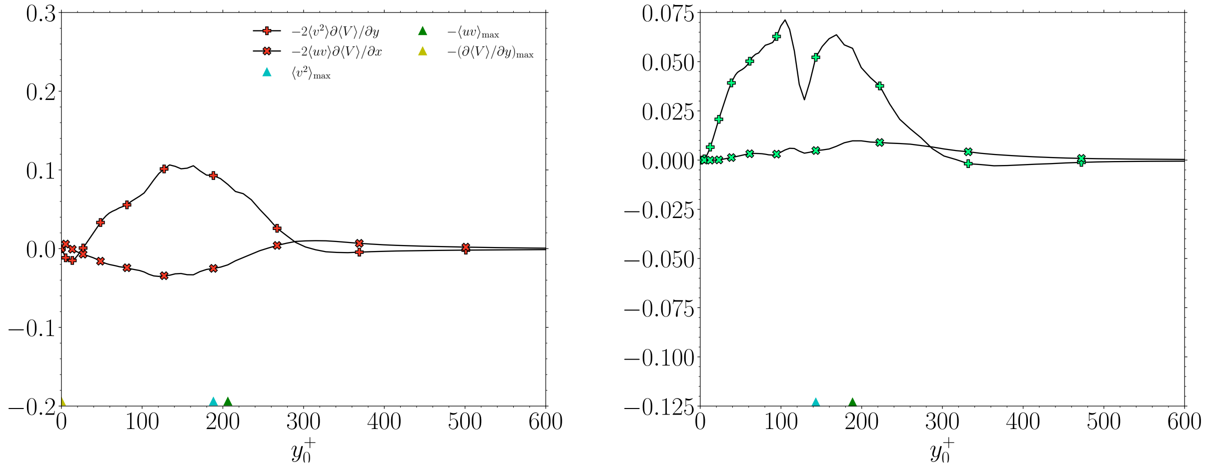

(c) Terms of $\mathscr{P}_{22}$, production of $\langle v^2\rangle$, at station E (d) Terms of $\mathscr{P}_{22}$, production of $\langle v^2\rangle$, at station F

Figure 4.33: Terms contributing to $\mathscr{P}_{11}$, production of $\langle u^2\rangle$ (Eq. (4.22), (a) and (b)) and $\mathscr{P}_{22}$, production of $\langle v^2\rangle$ (Eq. (4.23), (c) and (d)) normalized by viscous scales at $x_0 = -2L$. Colored triangles on the horizontal axis denote the positions of maximum values of $\langle u^2\rangle$, $-\langle uv\rangle$, $\partial\langle U\rangle/\partial y$ (in (a) and (b)) and maximum values of $\langle v^2\rangle$, $-\langle uv\rangle$ and $\partial\langle V\rangle/\partial y$ (in (c) and (d)).

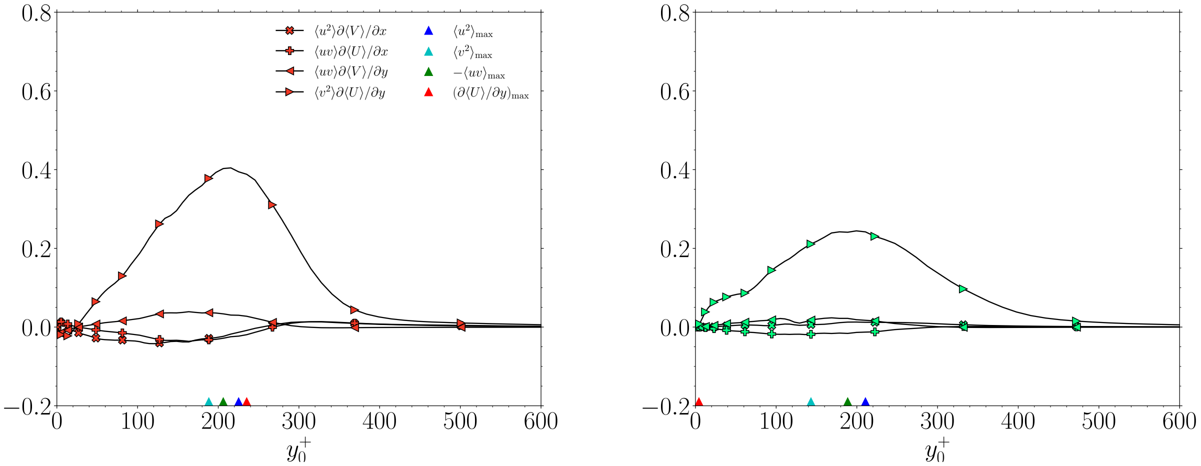

(a) Terms of $-\mathscr{P}_{12}$, production of $-\langle uv\rangle$, at station E (b) Terms of $-\mathscr{P}_{12}$, production of $-\langle uv\rangle$, at station F

Figure 4.34: Terms contributing to $-\mathscr{P}_{12}$ (4.38), $\mathscr{P}_{12}$, production of $-\langle uv\rangle$, normalized by viscous scales at $x_0 = -2L$. Colored triangles on the horizontal axis denote the positions of maximum values of $\langle u^2\rangle$, $\langle v^2\rangle$, $-\langle uv\rangle$ and $\partial\langle U\rangle/\partial y$.

Reynolds stress budget at station G and H ($\mathbf{x = 2L}$ and $\mathbf{x = 4L}$) Figures 4.35 and 4.36 show the budgets of the Reynolds stress components at stations G and H. The stations E and F are approximately $0.5L$ and $2.5L$ downstream of the reattachment location $x_{\text{rea}} = 1.49L$. The budgets of $\langle u^2\rangle$ and $\langle w^2\rangle$ in the near-wall region at $y_0^+ < 60$ for stations G and H tend towards their respective characteristic shapes of a ZPG SDTBL. The budgets of $\langle u^2\rangle$ and $\langle w^2\rangle$ in the outer boundary layer at $y_0^+ > 60$ for station G are similar to those of the turbulent mixing layer, Figs. 21a and 21 of Rogers & Moser (1994). The terms contributing to the production of $\langle u^2\rangle$, $\mathscr{P}_{11}$, given in Eq. (4.22), at stations G and H are shown in Figs. 4.37a and 4.37b. The peak of $\mathscr{P}_{11}$ at station F ($y_0^+ \approx 240$) is obtained further away from the wall compared to station A ($y_0^+ \approx 10$). The profiles of $\partial\langle U\rangle/\partial y$ at stations G and H peak at the wall. However, unlike in the ZPG region as at station A, the profiles do not smoothly decay to zero in the outer region of the turbulent boundary layer. Consequently, there is a local peak of production at station H at $y_0^+ \approx 350$, which leads to the two peaks in the profile of $\langle u^2 \rangle$. Similarly to the other stations, over most of the boundary layer, the velocity-pressure-gradient term, $\mathit{\Pi}_{11}$ is a sink of $\langle u^2 \rangle$ and $\mathit{\Pi}_{22}$ and $\mathit{\Pi}_{33}$ are sources of $\langle v^2 \rangle$ and $\langle w^2 \rangle$, respectively. The pressure term $\mathit{\Pi}_{33}$ is the main source of $\langle w^2 \rangle$ since the production $\mathscr{P}_{33}$ is zero. The local maxima of the pressure term $\mathit{\Pi}_{33}$ at $y_0^+ \approx 250$ and $y_0^+ \approx 320$ for stations G and H, respectively, combined with the high rate of dissipation ϵ_{33} in the near wall region results in the peak of $\langle w^2 \rangle$ occurring farther away from the wall at $y_0^+ \approx 130$ for station G, and at $y_0^+ \approx 255$ for station H. The terms contributing to the production of $\langle v^2 \rangle$, $\mathscr{P}_{22}$, given in Eq. (4.23), at stations G and H are shown in Figs. 4.37c and 4.37d. The production of $\langle v^2 \rangle$ at station H is negligible, which is not the case at station G. The mean vertical velocity derivatives at station G are $\partial \langle V \rangle / \partial y < 0$ for $2 < y_0^+ < 250$ (Fig. 4.23d) and $\partial \langle V \rangle / \partial x > 0$ for $y_0^+ > 20$ (Fig. 4.23c). As a result, the production of $\langle v^2 \rangle$ at station G is non-negligible. The budgets of $\langle v^2 \rangle$ and $-\langle uv \rangle$ at station G are similar to that of the turbulent mixing layer, e.g., see Figs. 21b and 21d of Rogers & Moser (1994). The budget of $\langle v^2 \rangle$ at station H exhibits a similar trend to that of a ZPG SDTBL albeit with the pressure-velocity-gradient term $\mathit{\Pi}_{22}$ reaching its maximum value at $y_0^+ \approx 300$ and with enhanced transport terms, compared to those at stations A and B. Finally, in the shear-stress budget, the dissipation, ϵ_{12}, is negligible except in the near-wall region and the production is balanced by $\mathit{\Pi}_{12}$. The terms contributing to the production of $-\langle uv \rangle$, $\mathscr{P}_{12}$, given in Eq. (4.38), at stations G and H are shown in Figs. 4.38a and 4.38b. Therefore, we see the same trends as that of a ZPG flat-plate boundary layer in the near wall region, however the peak production of $-\langle uv \rangle$ occurs farther away from the wall, at $y_0^+ \approx 220$ for station G. At station H, the production $\mathscr{P}_{12}$ peaks at $y_0^+ \approx 20$ and has another local maximum at $y_0^+ \approx 220$, which results in producing the peak of $-\langle uv \rangle$ occurring at $y_0^+ \approx 300$.

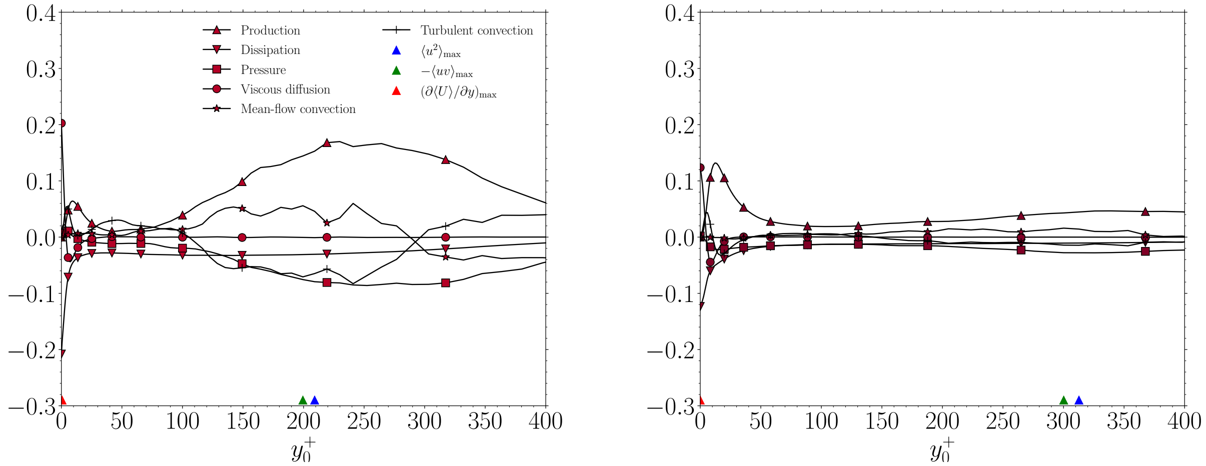

(a) Budget of $\langle u^2\rangle$, at station G ($x = 2L$)

(b) Budget of $\langle u^2\rangle$, at station H ($x = 4L$)

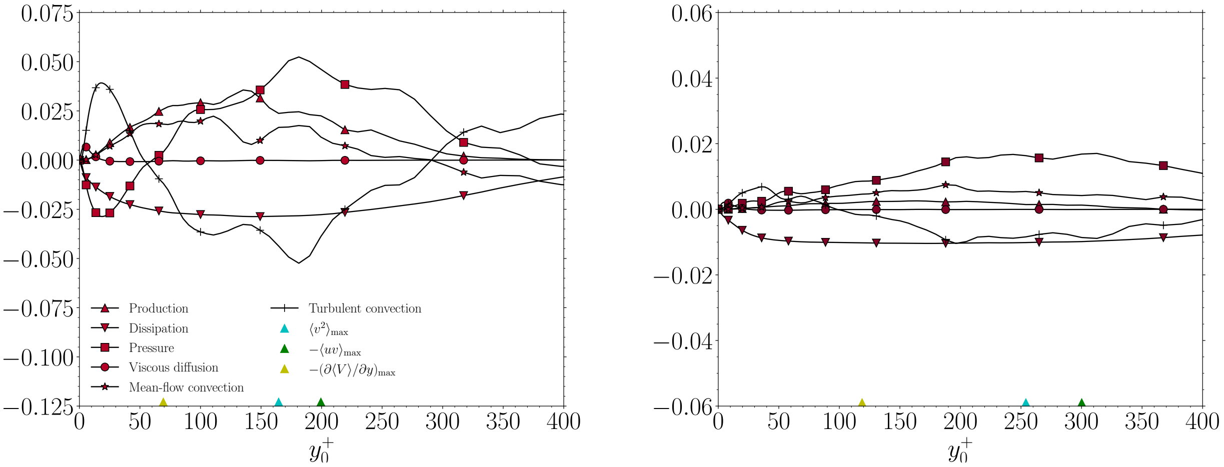

(c) Budget of $\langle v^2\rangle$, at station G ($x = 2L$)

(d) Budget of $\langle v^2\rangle$, at station H ($x = 4L$)

Figure 4.35: Budget of $\langle u^2\rangle$ (in (a) and (b)) and $\langle v^2\rangle$ (in (c) and (d)) at stations G and H, normalized by viscous scales at $x_0 = -2L$ (Eq. 4.18). Colored triangles on the horizontal axis denote the positions of maximum values of $\langle u^2\rangle$, $-\langle uv\rangle$, $\partial\langle U\rangle/\partial y$ (in (a) and (b)) and maximum values of $\langle v^2\rangle$, $-\langle uv\rangle$ and $\partial\langle V\rangle/\partial y$ (in (c) and (d)).

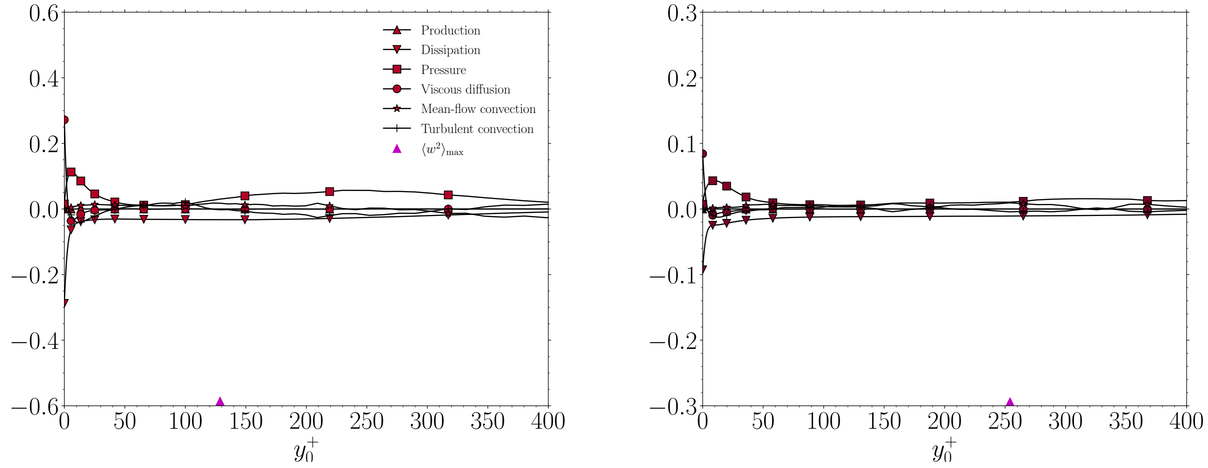

(a) Budget of $\langle w^2 \rangle$, at station G ($x = 2L$)

(b) Budget of $\langle w^2 \rangle$, at station H ($x = 4L$)

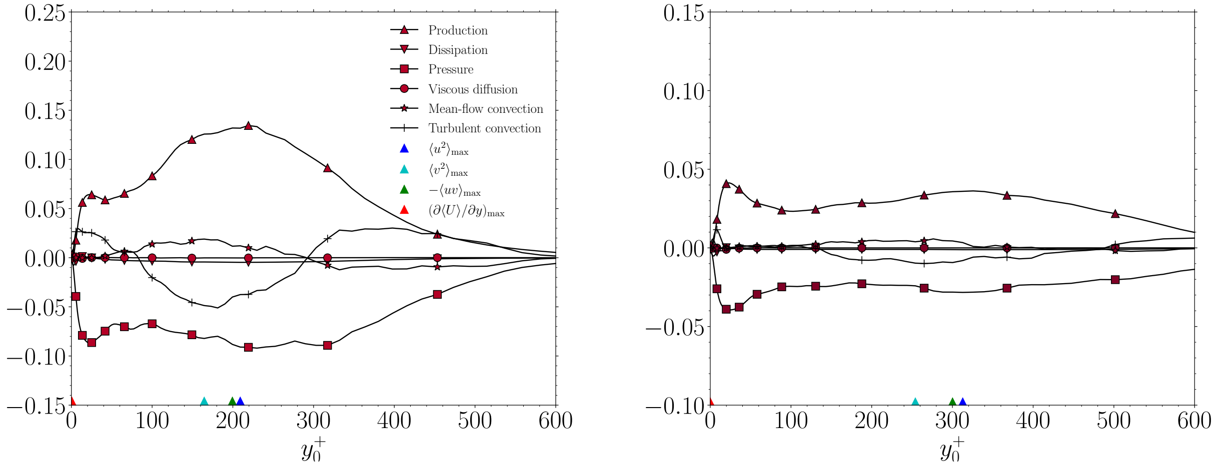

(c) Budget of $-\langle uv \rangle$, at station G ($x = 2L$)

(d) Budget of $-\langle uv \rangle$, at station H ($x = 4L$)

Figure 4.36: Budget of $\langle w^2 \rangle$ (in (a) and (b)) and $-\langle uv \rangle$ (in (c) and (d)) at stations G and H, normalized by viscous scales at $x_0 = -2L$ (Eq. 4.18). Colored triangles on the horizontal axis denote the positions of maximum values of $\langle w^2 \rangle$ (in (a) and (b)) as well as $\langle u^2 \rangle$, $\langle v^2 \rangle$, $-\langle uv \rangle$ and $\partial \langle U \rangle / \partial y$ (in (c) and (d)).

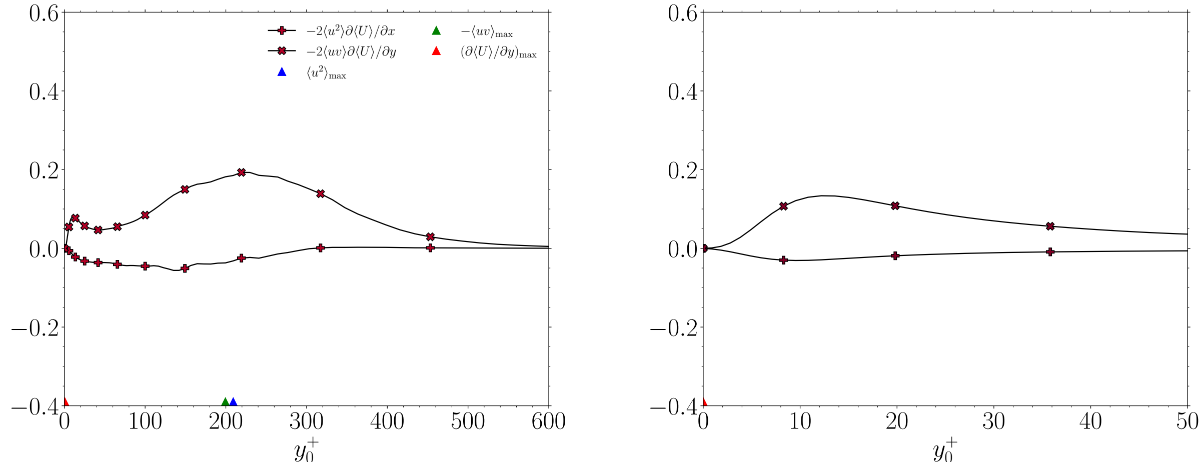

(a) Terms of $\mathscr{P}_{11}$, production of $\langle u^2\rangle$, at station G (b) Terms of $\mathscr{P}_{11}$, production of $\langle u^2\rangle$, at station H

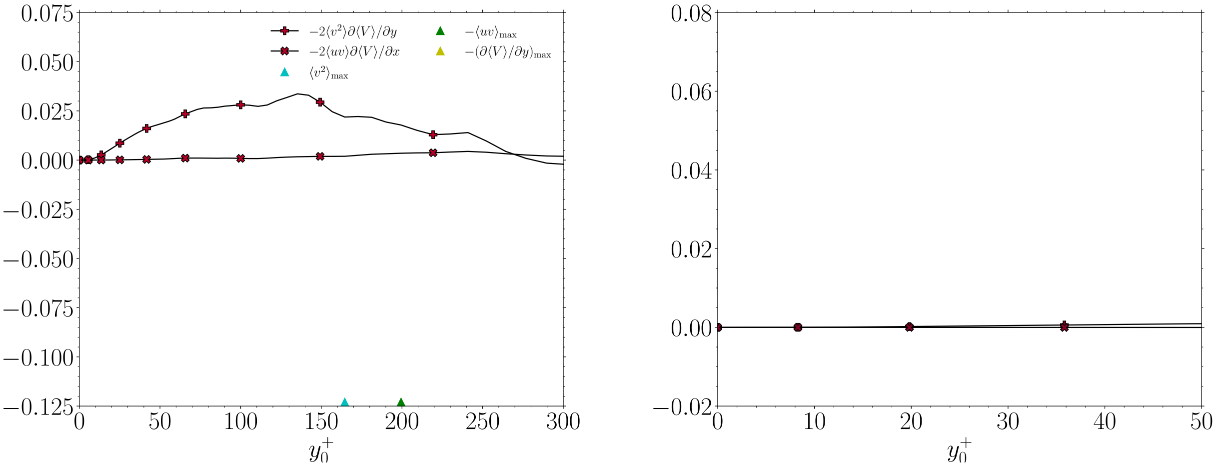

(c) Terms of $\mathscr{P}_{22}$, production of $\langle v^2\rangle$, at station G (d) Terms of $\mathscr{P}_{22}$, production of $\langle v^2\rangle$, at station H

Figure 4.37: Terms contributing to $\mathscr{P}_{11}$, production of $\langle u^2\rangle$ (Eq. (4.22), (a) and (b)) and $\mathscr{P}_{22}$, production of $\langle v^2\rangle$ (Eq. (4.23), (c) and (d)) normalized by viscous scales at $x_0 = -2L$. Colored triangles on the horizontal axis denote the positions of maximum values of $\langle u^2\rangle$, $-\langle uv\rangle$, $\partial\langle U\rangle/\partial y$ (in (a) and (b)) and maximum values of $\langle v^2\rangle$, $-\langle uv\rangle$ and $\partial\langle V\rangle/\partial y$ (in (c) and (d)).

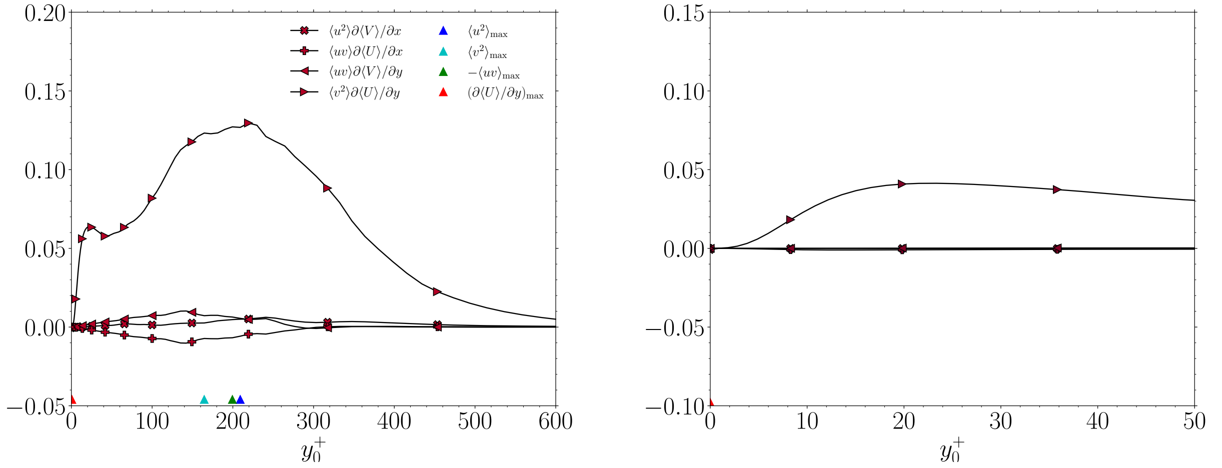

(a) Terms of $-\mathscr{P}_{12}$, production of $\langle uv\rangle$, at station G (b) Terms of $-\mathscr{P}_{12}$, production of $\langle uv\rangle$, at station H

Figure 4.38: Terms contributing to $-\mathscr{P}_{12}$ (4.38), production of $-\langle uv\rangle$, normalized by viscous scales at $x_0 = -2L$. Colored triangles on the horizontal axis denote the positions of maximum values of $\langle u^2\rangle$, $\langle v^2\rangle$, $-\langle uv\rangle$ and $\partial\langle U\rangle/\partial y$.

4.2.6 Reynolds stress budgets in orthogonal curvilinear coordinates

In this section, we analyze the budgets of the physical components of contravariant Reynolds stresses over the curved ramp, i.e., at stations C, D and E (Table 4.3, Figs. 4.9 and 4.10). Specifically, we study the budgets of $\langle\hat{u}^2\rangle$, $\langle\hat{v}^2\rangle$ and $-\langle\hat{u}\hat{v}\rangle$, since the profile of $\langle w^2\rangle_0^+$ is unaffected by the coordinate transformation since $\zeta = z$. The transport equation for the Reynolds stresses in a statistically stationary turbulent flow is given in Eq. (4.18) and the orthogonal formulation of each of the terms of this equation is given in Eqs. (F.1)-(F.6) of Appendix F. Similarly to the analysis of the Reynolds stress budgets in Cartesian coordinates of Sec. 4.2.5, we first analyze the orthogonal curvilinear components of the gradient of mean velocity.

Gradient of mean velocity in orthogonal curvilinear coordinates at stations C, D and E ($x = x_{\mathbf{sep}}$, $x = 0.5L$ and $x = L$) Figure 4.39 shows for stations C, D and E, the profiles of the four physical components of the gradient of mean contravariant velocity, $\nabla_i\langle\hat{U}^j\rangle$, normalized by the viscous scales at station A. Similarly to the Cartesian components, at stations A, B, G and H, the derivatives of the mean velocity components in the η-direction are greater than those in the ξ-direction, i.e., $\nabla_\eta\langle\hat{U}\rangle_0^+ \gg \nabla_\eta\langle\hat{V}\rangle_0^+ > \nabla_\xi\langle\hat{U}\rangle_0^+ > \nabla_\xi\langle\hat{V}\rangle_0^+$. Similarly to the Reynolds stresses discussed in Sec. 4.2.3, the profiles of physical components of the gradient of the mean contravariant velocity (Fig. 4.39) over the curved ramp, i.e., at stations C, D and E, are the ones that differ from their corresponding Cartesian profiles (Fig. 4.23). The velocity gradient at the wall where separation occurs (station C) is zero. Away from the wall, at ($\eta_0^+ \gtrsim 5$) for station D and ($\eta_0^+ \gtrsim 20$) for station E, $\nabla_\xi\langle\hat{U}\rangle_0^+ < 0$ and $\nabla_\eta\langle\hat{U}\rangle_0^+ > 0$ (Figs. 4.39a and 4.39b). Finally, $\nabla_\eta\langle\hat{V}\rangle_0^+ > 0$ and it is non-negligible farther away from the wall, and $\nabla_\xi\hat{V}_0^+ < 0$ and it is the least significant component of the mean velocity gradient (Figs. 4.39c and 4.39d). The physical components of the mean velocity gradients in orthogonal curvilinear coordinates at C, D and E exhibit similar behavior to those reported for the region of pressure-gradient-induced separation over a flat-plate via suction velocity APG, see Figs. 7b and 7d of Kitsios *et al.* (2017).

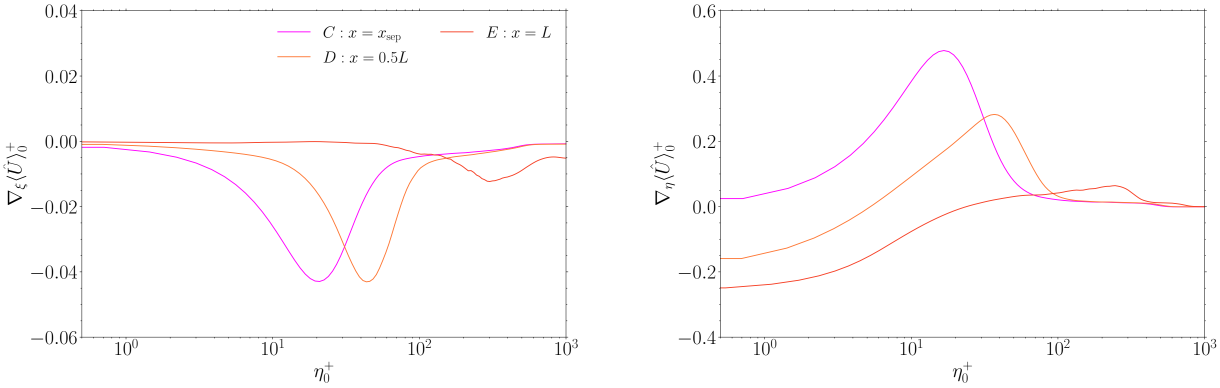

(a) $\nabla_\xi \langle \hat{U} \rangle_0^+$ (b) $\nabla_\eta \langle \hat{U} \rangle_0^+$

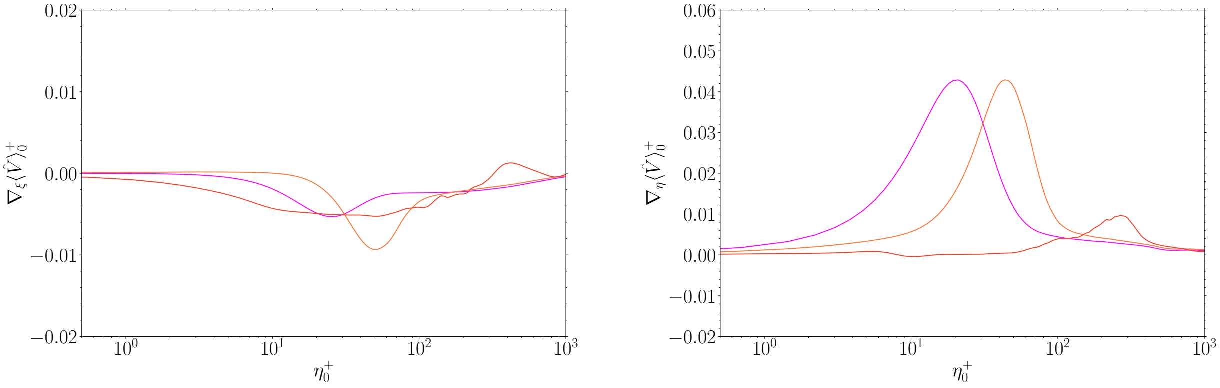

(c) $\nabla_\xi \langle \hat{V} \rangle_0^+$ (d) $\nabla_\eta \langle \hat{V} \rangle_0^+$

Figure 4.39: Physical components of the gradient of mean contravariant velocity, $\nabla_i \langle \hat{U}^j \rangle$, normalized by viscous scales at $x_0 = -2L$, for stations A-H.

Reynolds stress budgets in orthogonal curvilinear coordinates at stations C, D and E ($x = x_{\mathbf{sep}}$, $x = 0.5L$ and $x = L$) Figures 4.40, 4.42 and 4.44 show the Reynolds stress budgets, at stations C, D and E, of $\langle \hat{u}^2 \rangle$, $\langle \hat{v}^2 \rangle$ and $-\langle \hat{u}\hat{v} \rangle$, respectively. Herein, we analyze the changes occurring in the budgets of these Reynolds stresses over the curved wall due to the coordinate transformation over the curved ramp. The triangles on the horizontal axis in the figures denote the η_0^+ positions where the maximum values of relevant flow properties occur.

For stations C, D and E, the budget of $\langle\hat{u}^2\rangle$, shown in Fig. 4.40, is similar to its Cartesian counterpart of $\langle u^2\rangle$, shown in Figs. 4.27a, 4.27b and 4.31a. Further, we have seen in Sec. 4.2.3 that the $\langle\hat{u}^2\rangle_0^+$ profiles (Fig. 4.19b) at stations C, D and E have greater magnitudes than that of the Cartesian profiles (Figs. 4.19a) but show the same qualitative behavior. We notice that this increased magnitude of the $\langle\hat{u}^2\rangle_0^+$ profile is due to the greater production of $\langle\hat{u}^2\rangle$ compared to $\langle u^2\rangle$. The production of $\langle\hat{u}^2\rangle$, $\hat{\mathscr{P}}^{11}$, is written from (F.4) as

$$\hat{\mathscr{P}}^{11} = 2\left[-\langle\hat{u}^2\rangle\nabla_\xi\langle\hat{U}\rangle - \langle\hat{u}\hat{v}\rangle\nabla_\eta\langle\hat{U}\rangle\right]. \tag{4.39}$$

The two terms on the r.h.s. of Eq. (4.39) at stations C, D and E are shown in Fig. 4.41. The first term of Eq. (4.39), $-\langle\hat{u}^2\rangle\nabla_\eta\langle\hat{U}\rangle$, is the main source for the production $\mathscr{P}^{11}$ of $\langle\hat{u}^2\rangle$ at stations C and D, and is also significant at station E. This is because $-\langle\hat{u}^2\rangle$ is always negative and $\nabla_\xi\langle\hat{U}\rangle < 0$ at station C, and for $\eta_0^+ \gtrsim 5$ and 20 at stations D and E, respectively (Fig. 4.39a). At station C, the second term of Eq. (4.39), $-\langle\hat{u}\hat{v}\rangle\nabla_\eta\langle\hat{U}\rangle$, is a sink for the production $\hat{\mathscr{P}}^{11}$ of $\langle\hat{u}^2\rangle$ because it is negative, since for $\eta_0^+ < 26$, $\langle\hat{u}\hat{v}\rangle > 0$ and $\nabla_\eta\langle\hat{U}\rangle > 0$ (Fig. 4.39b). However, at stations D and E, this term is positive and contributes as a source to the production of $\langle\hat{u}^2\rangle$ since $\nabla_\eta\langle\hat{U}\rangle < 0$ and $\nabla_\eta\langle\hat{U}\rangle > 0$ for $\eta_0^+ \gtrsim 5$ and 20 at stations D and E, respectively (Fig. 4.39b). At stations C, D and E, due to greater production $\hat{\mathscr{P}}^{11}$ compared to $\mathscr{P}^{11}$, the balance of $\hat{\mathscr{P}}^{11} - \hat{\mathit{\Pi}}^{11} - \hat{\epsilon}^{11}$ is greater than $\mathscr{P}^{11} - \mathit{\Pi}^{11} - \epsilon^{11}$, and, hence, $\langle\hat{u}^2\rangle$ is greater than $\langle u^2\rangle$.

Over the curved ramp, at stations C, D and E, the budgets of $\langle\hat{v}^2\rangle$ (Fig. 4.42) and $-\langle\hat{u}\hat{v}\rangle$ (Fig. 4.44) differ greatly from the budgets of their Cartesian counterparts, $\langle v^2\rangle$ (Figs. 4.27c, 4.27d and 4.31c) and $-\langle uv\rangle$ (Figs. 4.28c, 4.28d and 4.32c), respectively. Firstly, the viscous diffusion and dissipation of $\langle\hat{v}^2\rangle$ and $-\langle\hat{u}\hat{v}\rangle$ are zero at the wall ($\eta = 0$), analogously to the Cartesian profiles in a turbulent flat-plate boundary layer, since $\partial\hat{v}/\partial\xi = \partial\hat{v}/\partial\eta = \partial\hat{v}/\partial\zeta = 0$ (Fig. 4.26, Eqs. (F.3) and (F.6)). The velocity-pressure-gradient term, $\hat{\mathit{\Pi}}^{22}$, is the major source of $\langle\hat{v}^2\rangle$, analogously to $\mathit{\Pi}_{22}$ for $\langle v^2\rangle$. Strikingly, the production $\hat{\mathscr{P}}^{22}$ is negative indicating that it is a sink of $\langle\hat{v}^2\rangle$. The production of $\langle\hat{v}^2\rangle$, $\hat{\mathscr{P}}^{22}$, is written from Eq. (F.4) as

$$\hat{\mathscr{P}}^{22} = 2\left[-\langle\hat{u}\hat{v}\rangle\nabla_\xi\langle\hat{V}\rangle - \langle\hat{v}^2\rangle\nabla_\eta\langle\hat{V}\rangle\right]. \tag{4.40}$$

The profiles of the two terms on the r.h.s. of Eq. (4.40) at stations C, D and E are shown in Fig. 4.43. Figure 4.43 shows that the contribution of the first term on the r.h.s. of Eq. (4.40) to $\hat{\mathscr{P}}^{22}$ is negligible with respect to the second term. $\nabla_\xi\langle\hat{V}\rangle$, which appears in the first term on the r.h.s. of Eq. (4.40), $-\langle\hat{u}\hat{v}\rangle\nabla_\xi\langle\hat{V}\rangle$, has the smallest magnitude of all the components of mean velocity gradient (Fig. 4.39) and is mostly negative at stations C, D and E (Fig. 4.39c). Therefore, in the zones where $-\langle\hat{u}\hat{v}\rangle > 0$, $-\langle\hat{u}\hat{v}\rangle\nabla_\xi\langle\hat{V}\rangle$ is negative and is a sink for the production, $\hat{\mathscr{P}}^{22}$. This occurs for $y_0^+ > 26$ at station C and over most of the boundary layer at stations D and E (Fig. 4.20d). In the second term on the r.h.s. of Eq. (4.40), $\langle\hat{v}^2\rangle$ is always positive as well as $\nabla_\eta\langle\hat{V}\rangle > 0$ over the boundary layer at stations C, D and E. Therefore, the second term on the r.h.s. of Eq. (4.40), $-\langle\hat{v}^2\rangle\nabla_\eta\langle\hat{V}\rangle < 0$, and, is the major cause of negative production of $\langle\hat{v}^2\rangle$ (Fig. 4.43). Hence, the profile of $\langle\hat{v}^2\rangle_0^+$ at stations C, D and E have smaller magnitudes than the Cartesian profiles (Figs. 4.19c and 4.19d). The negative production of $\langle\hat{v}^2\rangle$ was also reported in Figs. 14b and 14d of Abe (2017) in the APG region of a pressure-gradient-induced turbulent flow separation over a flat-plate. The smaller value of $\langle\hat{v}^2\rangle$ than $\langle v^2\rangle$ also results in its diminished convection with respect to that of its Cartesian counterpart .

The production of $-\langle\hat{u}\hat{v}\rangle$, $-\hat{\mathscr{P}}^{12}$, is written from (F.4) as

$$-\hat{\mathscr{P}}^{12} = \left[\langle\hat{u}^2\rangle\nabla_\xi\langle\hat{V}\rangle + \langle\hat{u}\hat{v}\rangle\nabla_\xi\langle\hat{U}\rangle + \langle\hat{u}\hat{v}\rangle\nabla_\eta\langle\hat{V}\rangle + \langle\hat{v}^2\rangle\nabla_\eta\langle\hat{U}\rangle\right]. \tag{4.41}$$

The profiles of the terms on the r.h.s. of Eq. (4.41) at stations C, D and E are shown in Fig. 4.45. In the first term on the r.h.s. of Eq. (4.40), $\langle\hat{u}^2\rangle\nabla_\xi\langle\hat{V}\rangle$, we have seen that $\nabla_\xi\langle\hat{V}\rangle$ has the smallest magnitude of all the components of mean velocity gradient (Fig. 4.39) and is mostly negative at stations C, D and E (Fig. 4.39c). At the same time, $\langle\hat{u}^2\rangle$ is always positive and is the largest component of the Reynolds stresses. Therefore, we see from Fig. 4.45 that $\langle\hat{u}^2\rangle\nabla_\xi\langle\hat{V}\rangle < 0$ and is a sink of $-\hat{\mathscr{P}}^{12}$. In the second term on the r.h.s. of Eq. (4.40), $\langle\hat{u}\hat{v}\rangle\nabla_\xi\langle\hat{U}\rangle$, $\nabla_\xi\langle\hat{U}\rangle$ is mostly negative at stations C, D and E (Fig. 4.39a). Therefore, $\langle\hat{u}\hat{v}\rangle\nabla_\xi\langle\hat{U}\rangle$, is positive and is a source for the production $-\hat{\mathscr{P}}^{12}$ of $-\langle\hat{u}\hat{v}\rangle$ when $-\langle\hat{u}\hat{v}\rangle > 0$. This occurs for $y_0^+ > 26$ at station C and over most of the boundary layer at stations D and E (Fig. 4.20d). Since $-\langle\hat{u}\hat{v}\rangle$ is the least significant component of the Reynolds stresses (Fig. 4.20d), Figure 4.43 shows that the second term on the r.h.s. of Eq. (4.40) is a minor contributor to $-\hat{\mathscr{P}}^{12}$. In the third term on the r.h.s. of Eq. (4.40), $\langle\hat{u}\hat{v}\rangle\nabla_\eta\langle\hat{V}\rangle$, $\nabla_\eta\langle\hat{V}\rangle$ is mostly positive at stations C, D and E (Fig. 4.39d). Therefore, $\langle\hat{u}\hat{v}\rangle\nabla_\xi\langle\hat{U}\rangle$ is negative and is a sink of the production $-\hat{\mathscr{P}}^{12}$, when $-\langle\hat{u}\hat{v}\rangle > 0$, which occurs for $y_0^+ > 26$ at station C and over most of the boundary layer at stations D and E (Fig. 4.20d). Therefore, Figure 4.43 shows that this term is a minor sink of $-\hat{\mathscr{P}}^{12}$. In the final term on the r.h.s. of Eq. (4.40), $\langle\hat{v}^2\rangle\nabla_\eta\langle\hat{U}\rangle$, $\langle\hat{v}^2\rangle$ is always positive. Further, $\nabla_\eta\langle\hat{U}\rangle$ has the largest magnitude among all the components of mean velocity gradient (Fig. 4.39), and is mostly positive at station C, and positive for $\eta_0^+ \gtrsim 5$ at station D and for $\eta_0^+ \gtrsim 20$ at station E (4.39b). Therefore, $\langle\hat{v}^2\rangle\nabla_\eta\langle\hat{U}\rangle$ is positive and is the main source of $-\hat{\mathscr{P}}^{12}$ (Fig. 4.45). This term was also identified as the primary source of $-\hat{\mathscr{P}}^{12}$ in Sec. 3.3, pp 582 of Abe (2017) in the APG region of a pressure-gradient-induced turbulent flow separation over a flat plate. At station C, the magnitude of the two terms $\langle\hat{v}^2\rangle\nabla_\eta\langle\hat{U}\rangle$ and $\langle\hat{u}^2\rangle\nabla_\xi\langle\hat{V}\rangle$ are comparable, resulting in a smaller $-\hat{\mathscr{P}}^{12}$ than at stations D and E. Since there are two sources of production $\mathscr{P}_{12}$, of $-\langle uv\rangle$, namely, $\langle v^2\rangle\partial\langle U\rangle/\partial y$ and $\langle uv\rangle\partial\langle V\rangle/\partial y$, the magnitude of $-\langle uv\rangle$ is greater than its contravariant counterpart $-\langle\hat{u}\hat{v}\rangle$ at stations C, D and E (Figs. 4.20c and 4.20d). The dissipation $-\hat{\epsilon}^{12}$ is negligible and the production $-\hat{\mathscr{P}}^{22}$ is mainly balanced by the velocity-pressure-gradient term, $-\hat{\Pi}^{12}$.

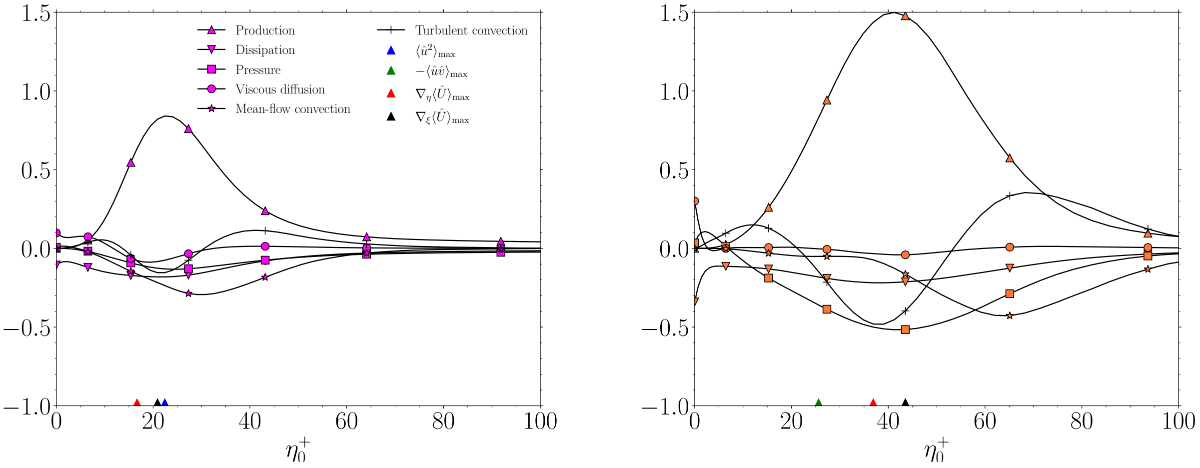

(a) Budget of $\langle \hat{u}^2 \rangle$, at station C ($x = x_{\text{sep}}$)

(b) Budget of $\langle \hat{u}^2 \rangle$, at station D ($x = 0.5L$)

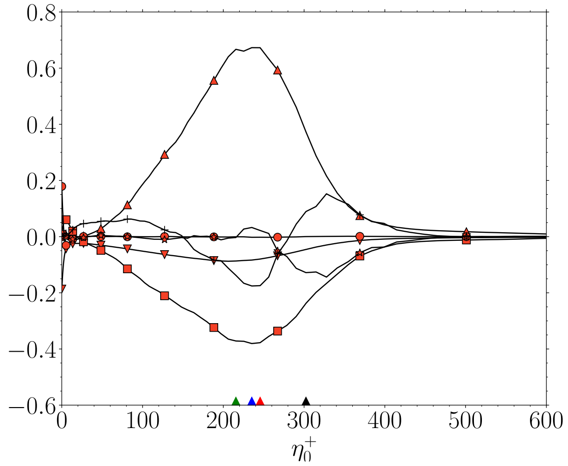

(c) Budget of $\langle \hat{u}^2 \rangle$, at station E ($x = L$)

Figure 4.40: Budget of $\langle \hat{u}^2 \rangle$ at stations C, D and E, normalized by viscous scales at $x_0 = -2L$ (Eq. 4.18). Colored triangles on the horizontal axis denote the positions of maximum values of $\langle \hat{u}^2 \rangle$, $-\langle \hat{u}\hat{v} \rangle$, $\nabla_\eta \langle \hat{U} \rangle$.

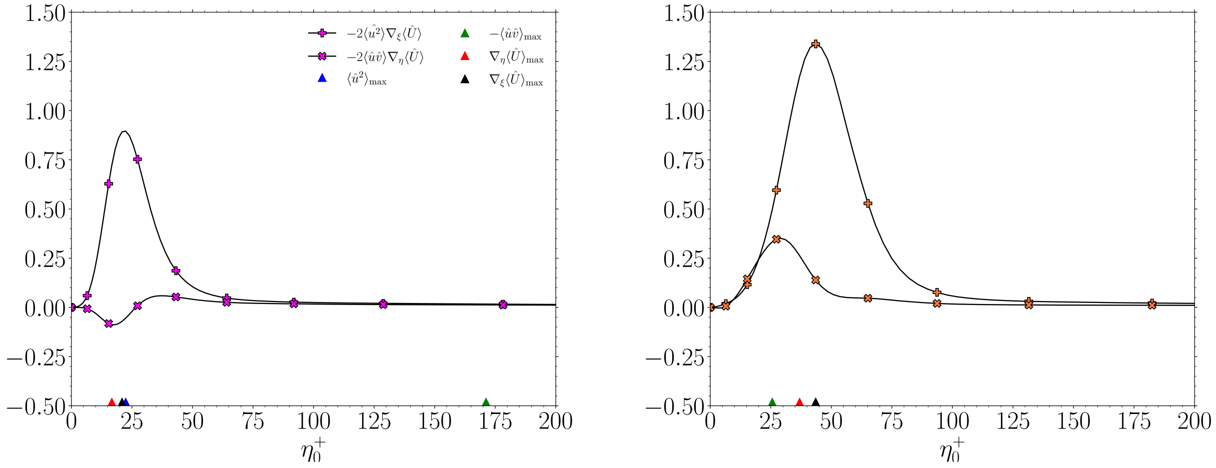

(a) Terms of $\hat{\mathscr{P}}^{11}$, production of $\langle\hat{u}^2\rangle$, at station C (b) Terms of $\hat{\mathscr{P}}^{11}$, production of $\langle\hat{u}^2\rangle$, at station D

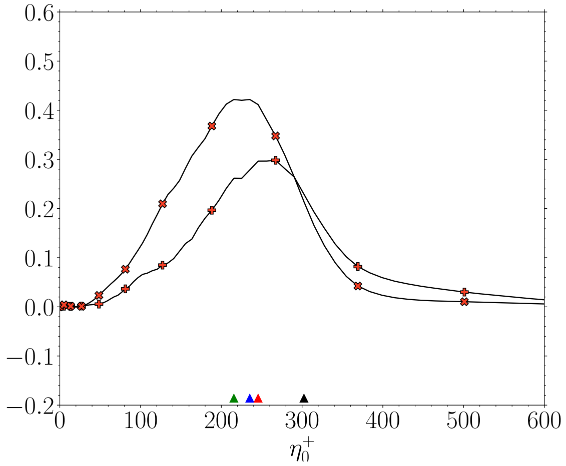

(c) Terms of $\hat{\mathscr{P}}^{11}$, production of $\langle\hat{u}^2\rangle$, at station E

Figure 4.41: Terms contributing to $\hat{\mathscr{P}}^{11}$, production of $\langle\hat{u}^2\rangle$ (4.39), normalized by viscous scales at $x_0 = -2L$. Colored triangles on the horizontal axis denote the positions of maximum values of $\langle\hat{u}^2\rangle$, $-\langle\hat{u}\hat{v}\rangle$, $\nabla_\eta\langle\hat{U}\rangle$.

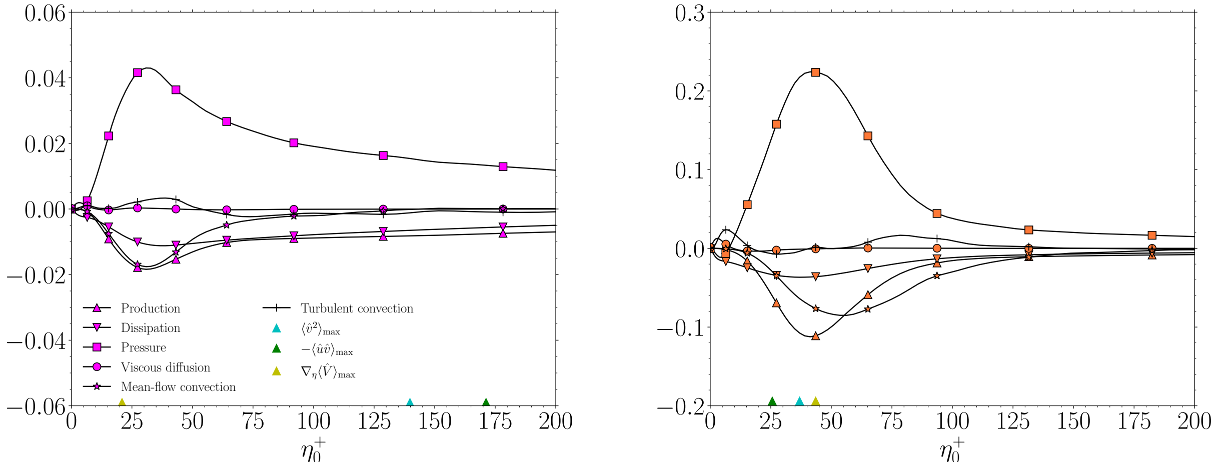

(a) Budget of $\langle\hat{v}^2\rangle$, at station C ($x = x_{\text{sep}}$)

(b) Budget of $\langle\hat{v}^2\rangle$, at station D ($x = 0.5L$)

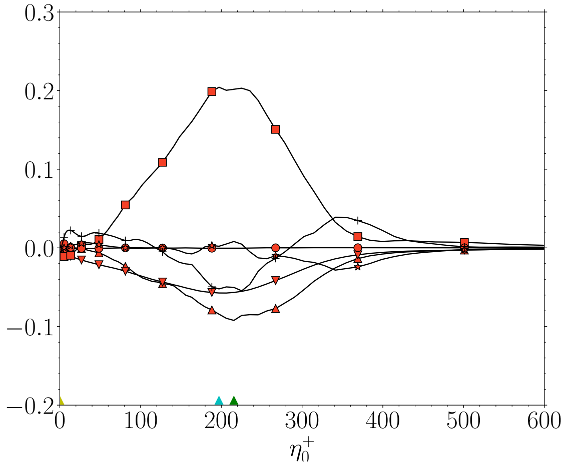

(c) Budget of $\langle\hat{v}^2\rangle$, at station E ($x = L$)

Figure 4.42: Budget of $\langle\hat{v}^2\rangle$ at stations C, D and E, normalized by viscous scales at $x_0 = -2L$ (Eq. 4.18). Colored triangles on the horizontal axis denote the positions of maximum values of $\langle\hat{v}^2\rangle$, $-\langle\hat{u}\hat{v}\rangle$ and $\nabla_\eta\langle\hat{V}\rangle$.

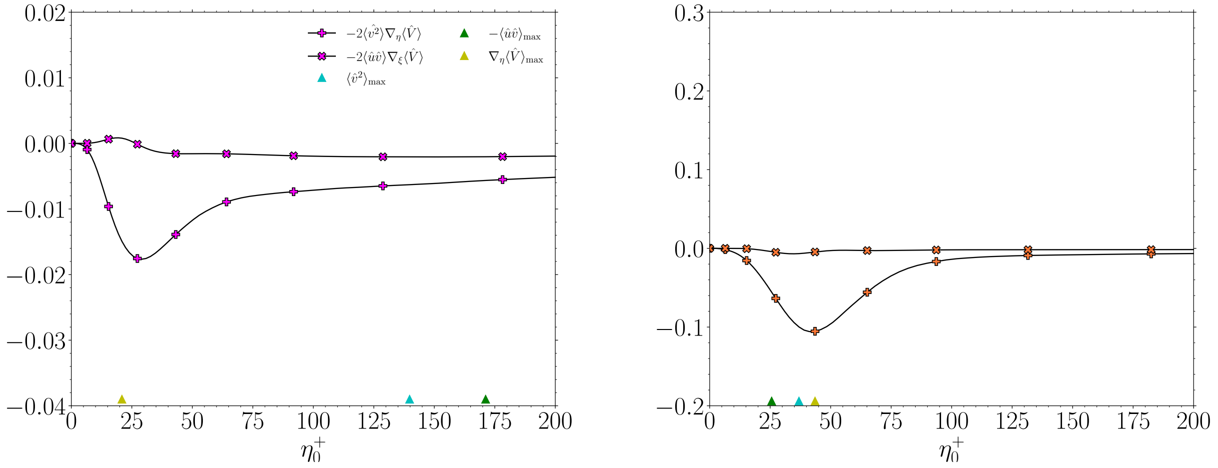

(a) Terms of $\hat{\mathscr{P}}^{22}$, production of $\langle\hat{v}^2\rangle$, at station C (b) Terms of $\hat{\mathscr{P}}^{22}$, production of $\langle\hat{v}^2\rangle$, at station D

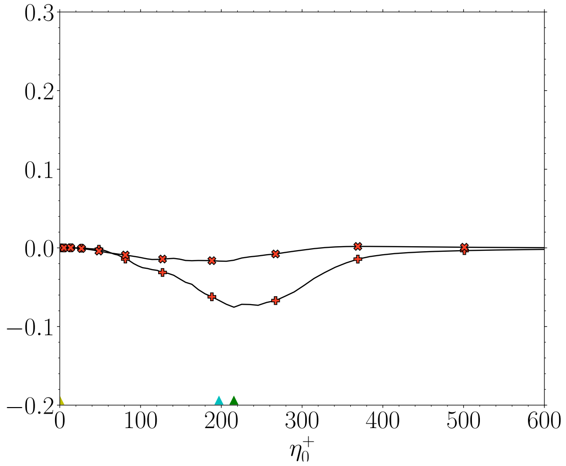

(c) Terms of $\hat{\mathscr{P}}^{22}$, production of $\langle\hat{v}^2\rangle$, at station E

Figure 4.43: Terms contributing to $\hat{\mathscr{P}}^{22}$, production of $\langle\hat{v}^2\rangle$ (4.40), normalized by viscous scales at $x_0 = -2L$. Colored triangles on the horizontal axis denote the positions of maximum values of $\langle\hat{v}^2\rangle$, $-\langle\hat{u}\hat{v}\rangle$, $\nabla_\eta\langle\hat{V}\rangle$.

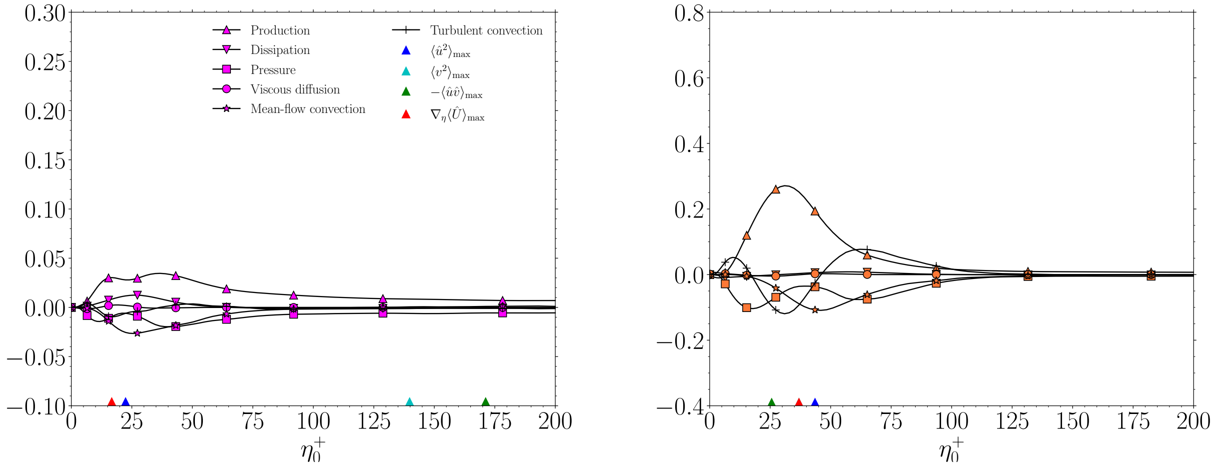

(a) Budget of $-\langle \hat{u}\hat{v} \rangle$, at station C ($x = x_{\text{sep}}$)

(b) Budget of $-\langle \hat{u}\hat{v} \rangle$, at station D ($x = 0.5L$)

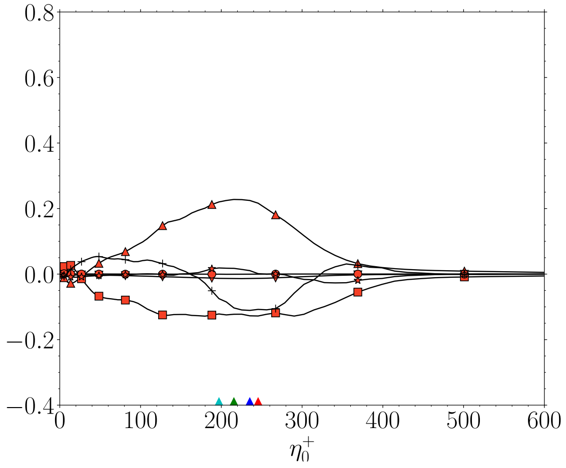

(c) Budget of $-\langle \hat{u}\hat{v} \rangle$, at station E ($x = L$)

Figure 4.44: Budget of $-\langle \hat{u}\hat{v} \rangle$ at stations C, D and E, normalized by viscous scales at $x_0 = -2L$. Colored triangles on the horizontal axis denote the positions of maximum values of $\langle \hat{u}^2 \rangle$, $\langle \hat{v}^2 \rangle$, $-\langle \hat{u}\hat{v} \rangle$, $\nabla_\eta \langle \hat{U} \rangle$.

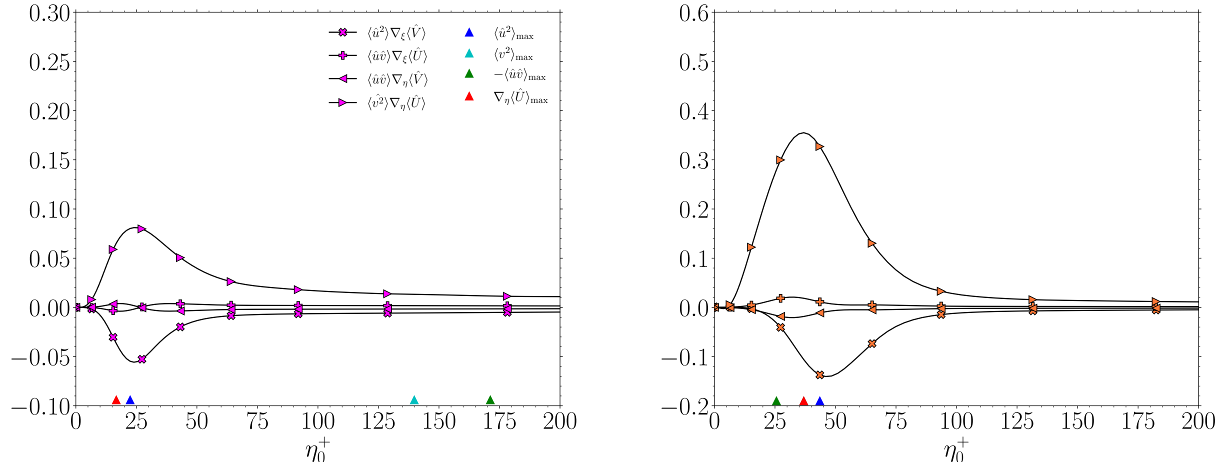

(a) Terms of $-\hat{\mathscr{P}}^{12}$, production of $-\langle\hat{u}\hat{v}\rangle$, at station C (b) Terms of $-\hat{\mathscr{P}}^{12}$, production of $-\langle\hat{u}\hat{v}\rangle$, at station D

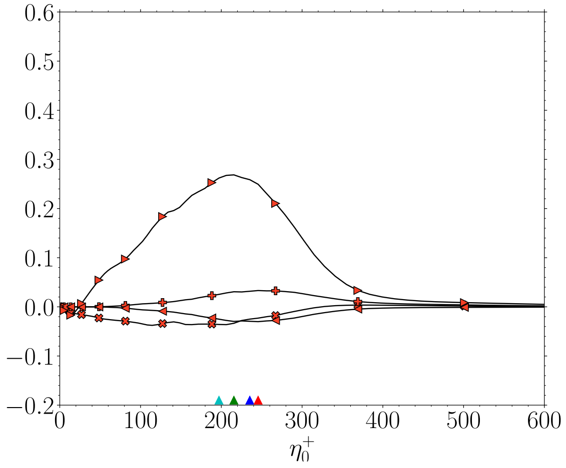

(c) Terms of $-\hat{\mathscr{P}}^{12}$, production of $-\langle\hat{u}\hat{v}\rangle$, at station E

Figure 4.45: Terms contributing to $-\hat{\mathscr{P}}^{12}$, production of $-\langle\hat{u}\hat{v}\rangle$ (4.41), normalized by viscous scales at $x_0 = -2L$. Colored triangles on the horizontal axis denote the positions of maximum values of $\langle\hat{u}^2\rangle$, $\langle\hat{v}^2\rangle$, $-\langle\hat{u}\hat{v}\rangle$, $\nabla_\eta\langle\hat{U}\rangle$.

4.2.7 Physical mechanisms in SDTBL separating over a curved ramp

In Sec. 4.2.5, we have explained the changes occurring to the terms of the Reynolds stress budget due to flow separation with respect to a ZPG SDTBL. Further, in Sec. 4.2.6, we analyzed the differences between the Reynolds stress budgets in Cartesian and orthogonal curvilinear coordinates over the curved ramp, i.e., at stations C, D an E. Herein, we summarize the key physical mechanisms of turbulence in SDTBL over a curved ramp based on our findings of the present study.

Flat plate region upstream of the ramp: stations A and B At stations A and B, upstream of the ramp, the Reynolds stress budgets exhibit similar characteristics as that of a ZPG SDTBL over a flat plate. In this region, $\partial\langle U\rangle/\partial y$ is the only significant component of the mean velocity gradient as shown in Fig. 4.23. Therefore, $\mathscr{P}_{11}$ is the main source of production of TKE while $\mathscr{P}_{22}$ and $\mathscr{P}_{33}$ are negligible (Figs. 4.24 and 4.25). The peak production, $\mathscr{P}_{11}$, occurs close to the wall at $y_0^+ \approx 10$, which is the region of maximum TKE. Over most of the boundary layer, the velocity-pressure-gradient term, $\mathit{\Pi}_{11}$, is a sink of $\langle u^2\rangle$ while $\mathit{\Pi}_{22}$ and $\mathit{\Pi}_{33}$ are the main sources of $\langle v^2\rangle$ and $\langle w^2\rangle$, respectively. Therefore, the primary role of the velocity-pressure-gradient tensor is as a sink of $\langle u^2\rangle$ while being a source of $\langle v^2\rangle$ and $\langle w^2\rangle$. The dissipation of $\langle v^2\rangle$ and $\langle w^2\rangle$, i.e., ϵ_{22} and ϵ_{33}, respectively, are approximately balanced by $\mathit{\Pi}_{22}$ and $\mathit{\Pi}_{33}$. Finally, in the shear-stress budget, the production $\mathscr{P}_{12}$, whose main source is the mean shear $\partial\langle U\rangle/\partial y$, is approximately balanced by $\mathit{\Pi}_{12}$ while the dissipation ϵ_{12} is negligible, except near the wall. These pathways of production and dissipation of the Reynolds stresses in this region are shown in Fig. 4.46a.

Curved ramp region: stations C, D and E (Cartesian coordinates) The convex shape of the ramp leads to the APG (Fig. 4.8a) in the turbulent flow. Due to the APG, the streamwise velocity $\langle U\rangle$ in the boundary layer decreases in the x-direction over the ramp, i.e., the flow slows down (Fig. 4.7a) and separates ($\partial\langle\hat{U}\rangle/\partial\eta = 0$ for $\eta = 0$) at station C, $x_{\text{sep}} = 0.37L$. After that for $x > x_{\text{sep}}$, the flow is reversed in the near-wall region and forms a separation bubble (Fig. 4.7b) until it reattaches ($\partial\langle\hat{U}\rangle/\partial\eta = 0$ for $\eta = 0$) at station F, $x_{\text{rea}} = 1.49L$ (Fig. 4.10). Because of the separation bubble over the curved (Fig. 4.7b), the flow moves upwards in the section of the bubble closer to the wall where the flow is reversed, thus, the y-component of the mean velocity, $\langle V\rangle_0^+ > 0$ for $y_0^+ < 5$ at station D and $y_0^+ < 100$ at station E (Fig. 4.13b). Above this region in the upper section of the bubble, the flow turns downwards, thus $\langle V\rangle < 0$ (Fig. 4.13b). Therefore, in addition to the mean shear $\partial\langle U\rangle_0^+/\partial y$, the mean velocity derivative $-\partial\langle V\rangle_0^+/\partial y$ is significant in this curved ramp region. As a result, the production of $\langle v^2\rangle$, $\mathscr{P}_{22}$, is non-negligible (Figs. 4.29c, 4.29d and 4.33c) when $\partial\langle V\rangle/\partial y < 0$ (Fig. 4.23d). Similarly to station A, $\partial\langle U\rangle_0^+/\partial y$ is the main source of $\mathscr{P}_{11}$ (Figs. 4.29a, 4.29b and 4.33a) and $\mathit{\Pi}_{11}$ is a sink of $\langle u^2\rangle$ while $\mathit{\Pi}_{22}$ and $\mathit{\Pi}_{33}$ are sources of $\langle v^2\rangle$ and $\langle w^2\rangle$, respectively. In the case of $\langle w^2\rangle$, $\mathit{\Pi}_{33}$ is its main source since the production $\mathscr{P}_{33}$ is zero. Therefore, the TKE production in this curved ramp region occurs through the production of both $\langle u^2\rangle$ and $\langle v^2\rangle$. Further, the viscous diffusion and dissipation of $\langle v^2\rangle$ and $-\langle uv\rangle$, in the curved ramp region, are not equal to zero at the wall, since $\partial v/\partial y \neq 0$, for $\eta = 0$ (Fig. 4.26). The profiles of the mean flow convection and turbulent convection in the shear layer region of the flow ($y_0^+ < 100$ for stations C and D and $y_0^+ < 500$ for station E) are similar to those reported for a turbulent mixing layer in Fig. 21 by Rogers & Moser (1994). Hence, this curved ramp region of the flow is characterized by enhanced transport of the Reynolds stresses compared to that at station A, due to the mixing layer created in the flow by the flow separation. Finally, in the budget of $-\langle uv\rangle$, the main sources of production $-\mathscr{P}_{12}$ are the mean shear $\partial\langle U\rangle/\partial y$ as well as the mean velocity derivative $\partial\langle V\rangle_0^+/\partial y$ (Figs. 4.30a, 4.30b and 4.34a). The dissipation $-\epsilon_{12}$ is negligible except near the wall while the production is balanced by $-\mathit{\Pi}_{12}$ (Figs. 4.28c, 4.28d and 4.32c). The pathways of production and dissipation of the Reynolds stresses explained herein for the separated flow over the curved ramp in this region are summarized in the schematic of Fig. 4.46b.

Curved ramp region: stations C, D and E (orthogonal curvilinear coordinates)

The budget of $\langle\hat{u}^2\rangle$ (Fig. 4.40) is similar to its Cartesian counterpart of $\langle u^2\rangle$ (Figs. 4.27a, 4.27b and 4.31a), but with increased production of $\langle \hat{u}^2 \rangle$ compared to $\langle u^2 \rangle$. This is because the velocity derivative $\nabla_\xi \langle \hat{U} \rangle$ contributes to the production of $\langle \hat{u}^2 \rangle$ (Figs. 4.41), in addition to the mean shear $\nabla_\eta \langle \hat{U} \rangle$, which is not the case for $\langle u^2 \rangle$ (Figs. 4.29a, 4.29b and 4.33a). Therefore, at stations C, D and E, due to greater production $\hat{\mathscr{P}}^{11}$ than $\mathscr{P}^{11}$, the balance of $\hat{\mathscr{P}}^{11} - \hat{\Pi}^{11} - \hat{\epsilon}^{11}$ is greater than $\mathscr{P}^{11} - \Pi^{11} - \epsilon^{11}$, and, hence, $\langle \hat{u}^2 \rangle$ is greater than $\langle u^2 \rangle$.

We notice that the budgets of $\langle \hat{v}^2 \rangle$ and $-\langle \hat{u}\hat{v} \rangle$ differ greatly from the budget of their Cartesian counterparts $\langle v^2 \rangle$ and $-\langle uv \rangle$, respectively. First, the viscous diffusion and dissipation of $\langle \hat{v}^2 \rangle$ (Fig. 4.42) and $-\langle \hat{u}\hat{v} \rangle$ (Fig. 4.44) are zero at the wall, analogously to the Cartesian profiles in a turbulent flat-plate boundary layer, since $\partial \hat{v}/\partial \xi = \partial \hat{v}/\partial \eta = \partial \hat{v}/\partial \zeta = 0$ at $\eta = 0$ (Fig. 4.26, Eqs. (F.3) and (F.6)). In the budget of $\langle \hat{v}^2 \rangle$, the velocity-pressure-gradient term $\hat{\Pi}^{22}$ is the major source of $\langle \hat{v}^2 \rangle$ analogously to Π_{22} for $\langle v^2 \rangle$. However, the production $\hat{\mathscr{P}}^{22}$ is negative (Fig. 4.43) indicating that it is a sink of $\langle \hat{v}^2 \rangle$. The main source of negative $\hat{\mathscr{P}}^{22}$ is the velocity derivative $\nabla_\eta \langle \hat{V} \rangle > 0$. The negative production of $\langle v^2 \rangle$ was also reported in Figs. 14b and 14d of Abe (2017) in the APG region of a pressure-gradient-induced turbulent flow separation over a flat plate. Hence, the profile of $\langle \hat{v}^2 \rangle_0^+$ at stations C, D and E have smaller magnitudes than their respective Cartesian counterparts. In the budget of $-\langle \hat{u}\hat{v} \rangle$, the mean shear $\nabla_\eta \langle \hat{U} \rangle > 0$ is the main source of $-\hat{\mathscr{P}}^{12}$ (Fig. 4.45). This term was also identified as the primary source of $-\hat{\mathscr{P}}^{12}$ in Sec. 3.3, pp 582 of Abe (2017). However, the mean shear $\nabla_\xi \langle \hat{V} \rangle < 0$ for most of the boundary layer at stations C, D and E (Fig. 4.39c), and decreases $-\hat{\mathscr{P}}^{12}$. Further, at station C, the magnitude of these two competing terms are comparable resulting in a smaller $-\hat{\mathscr{P}}^{12}$ than at stations D and E. Since there are two sources of production $-\mathscr{P}_{12}$ of $-\langle uv \rangle$, namely, $\partial \langle U \rangle / \partial y$ and $\partial \langle V \rangle / \partial y$ (Figs. 4.30 and 4.34b), whose combined magnitude makes $-\mathscr{P}_{12} > -\hat{\mathscr{P}}^{12}$ (Figs. 4.28c, 4.28d, 4.32c and 4.44), $-\langle uv \rangle$ is greater than the contravariant $-\langle \hat{u}\hat{v} \rangle$ at stations C, D and E (Figs. 4.20c and 4.20d). The pathways of production and dissipation of the Reynolds stresses in the region over the ramp are shown in Fig. 4.47.

Herein, in Sec. 4.2.6, we have shown, for the first time, the similarities between the profiles of the Reynolds stress budgets and mean velocity gradients in orthogonal curvilinear coordinates over the curved region and those in the APG region of a pressure-gradient induced turbulent flow separation over a flat plate. Such a comparison has been possible only because (i) we employ a structured orthogonal grid (Appendix D) over the curved ramp in our simulations, and (ii) FastRK3 solves the governing equations written in orthogonal curvilinear coordinates.That said, we have also in Sec. 4.2.5 and 4.2.6, the differences between the Reynolds stress budgets and mean velocity gradients in Cartesian coordinates and those in orthogonal curvilinear coordinates over the curved ramp.

Reattachment and recovery region: stations F, G and H The Reynolds stress budgets at the reattachment location, station F, are similar to those at stations C, D and E, in the curved ramp region of the flow, with the exception that the viscous diffusion and dissipation of $\langle v^2 \rangle$ and $-\langle uv \rangle$ are equal to zero at the wall ($\eta = 0$) (Figs. 4.31 and 4.32). This is because station F is located in the flat-plate region downstream of the ramp (Figs. 4.8b and 4.26). Downstream of the reattachment location, at stations G and H, the budgets of $\langle u^2 \rangle$ and $\langle w^2 \rangle$ at $y_0^+ < 60$ tend towards their shapes characteristic of ZPG SDTBL. The budgets of $\langle u^2 \rangle$ and $\langle w^2 \rangle$ at $y_0^+ > 60$ for station G are similar to those reported for a turbulent mixing layer in Figs. 21a and 21c by Rogers & Moser (1994). The profiles of the mean shear $\partial \langle U \rangle / \partial y$ at stations G and H peak at the wall, however, unlike in the ZPG region (station A), the profiles do not smoothly decay to zero at $y_0^+ > 50$ and exhibit a local maximum at $y_0^+ \approx 240$ since the profile of mean x-component of velocity is still yet to regain its characteristic ZPG SDTBL shape. Therefore, the peak production of $\langle u^2 \rangle$ at F ($y_0^+ \approx 240$) is obtained further away from the wall compared to A ($y_0^+ \approx 10$). Consequently, there is a local peak of production at station H at $y_0^+ \approx 350$ (Fig. 4.35b), which leads to the two peaks in the profile of $\langle u^2 \rangle$ (4.19a). Similarly to the stations A and B, upstream of the curved ramp, $\partial \langle U \rangle_0^+ / \partial y$ is the main source of $\mathscr{P}_{11}$ (Figs. 4.33b, 4.37a and 4.37b) and Π_{11} is a sink of $\langle u^2 \rangle$, while Π_{22} and Π_{33} are sources of $\langle v^2 \rangle$ and $\langle w^2 \rangle$, respectively. In the case of $\langle w^2 \rangle$, Π_{33} is its main source since its production $\mathscr{P}_{33}$ is zero. The production of $\langle v^2 \rangle$, non-negligible at station G (Figs. 4.35c and 4.37c), gradually reduces to zero at station H (Figs. 4.35d and

4.37d) as the mean velocity derivative eventually decays to zero at station H (4.23d). The budgets of $\langle v^2 \rangle$ and $-\langle uv \rangle$ at station G (Figs. 4.35c and 4.36a) are similar to those reported for a turbulent mixing layer in Figs. 21b and 21d by Rogers & Moser (1994). Even if the budgets of $\langle v^2 \rangle$ and $-\langle uv \rangle$ tend towards their shapes characteristic of a ZPG SDTBL, this happens more slowly than for those of $\langle u^2 \rangle$ and $\langle w^2 \rangle$. This is consistent with the observation of Song & Eaton (2004) that the recovery rate of the Reynolds stresses to their characteristic ZPG behavior, ordered from fastest to slowest, is $\langle u^2 \rangle$, $\langle uv \rangle$, and $\langle v^2 \rangle$. The pathways of production and dissipation of Reynolds stresses in this reattachment and recovery region is represented by a transition from the behavior of Fig. 4.46b to that of Fig. 4.46a as the flow recovers downstream of the reattachment location.

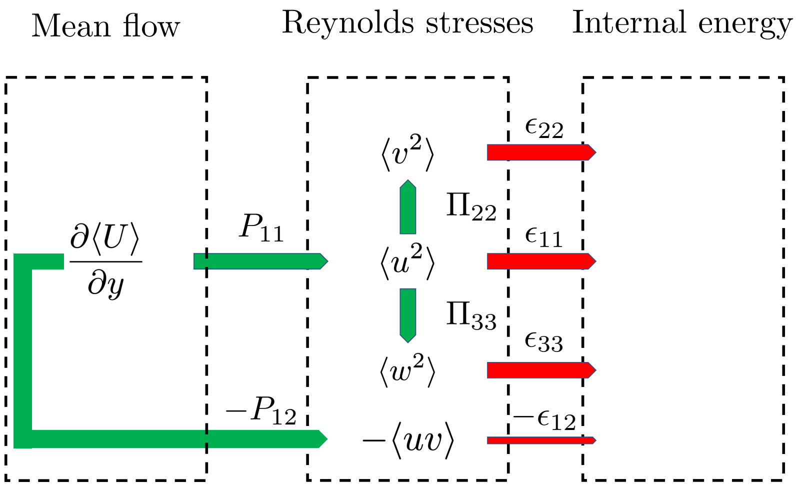

(a) Flat plate region region upstream of the ramp

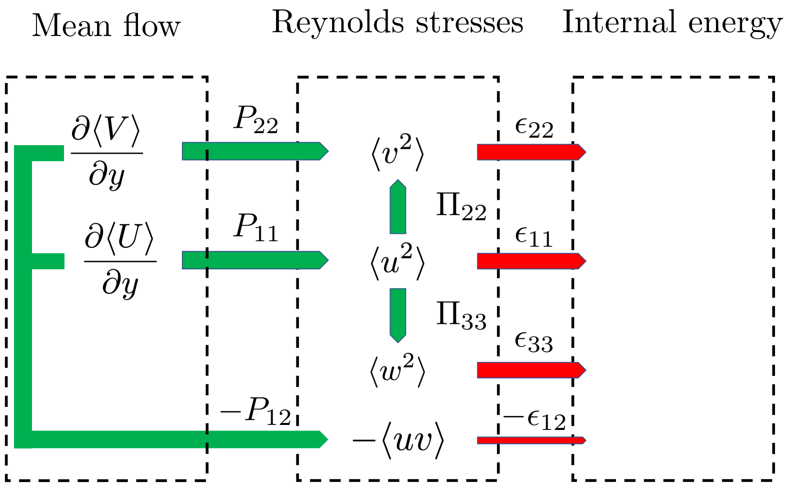

(b) Curved ramp region

Figure 4.46: Schematic of pathways of production, velocity-pressure-gradient transfer and dissipation of Reynolds stresses in (a) attached flow over the flat-plate region upstream of the ramp (e.g., stations A and B) and (b) curved ramp region (stations C, D and E) of a SDTBL separating over a curved ramp (Fig. 4.2).

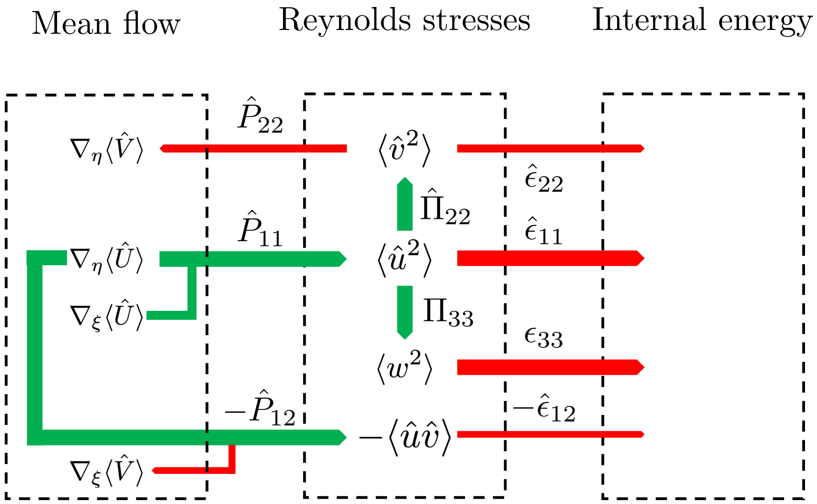

Figure 4.47: Schematic of pathways of production, velocity-pressure-gradient transfer and dissipation of Reynolds stresses in curvilinear coordinates over the curved ramp region of the flow (Fig. 4.2), e.g., stations C, D and E (Fig. 4.9a).

4.3 Summary

We have performed direct numerical simulation (DNS) of a spatially developing turbulent boundary layer (SDTBL) separating over a curved ramp (Figs. 4.1 and 4.2) with the goal to study the dynamics of turbulence of the separated flow. Since most Reynolds averaged Navier-Stokes (RANS) models fail to model accurately fully separated flows, understanding the key mechanisms of turbulence in SDTBL over curved ramps is crucial to improving these models, as well, for training neural networks for machine learning tools for separated turbulent boundary layers. We have studied via DNS the SDTBL over the curved ramp (Fig. 4.1) experimentally studied by Song & Eaton (2004) with the Reynolds number based on momentum thickness at $x = -2L$ (inflow plane) from the beginning of the curved ramp, $\mathrm{Re}_\theta = 1100$. We have performed these simulations using FastRK3, that has been developed by Aithal & Ferrante (2020) and has been presented in Chapter 2. The temporal accuracy of

FastRK3 has been analyzed by Aithal, Tipirneni & Ferrante (2022) and has been presented in Chapters 2 and 3. Once we performed the DNS, we have identified eight streamwise stations (A-H, Table 4.3) to analyze the turbulence characteristics of the separated flow. The findings of this study are summarized as follows:

1. The convex shape of the ramp leads to the adverse pressure gradient or APG (Fig. 4.8a) in the turbulent flow.
    (a) The streamwise velocity $\langle U \rangle$ in the boundary layer decreases in the x-direction over the ramp slows down (Fig. 4.7a) and separates ($\partial\langle \hat{U} \rangle/\partial\eta = 0$ for $\eta = 0$) at station C, $x_{\text{sep}} = 0.37L$ (Fig. 4.10).
    (b) Because of the separation bubble over the curved (Fig. 4.7b), the flow moves upwards in the section of the bubble closer to the wall where the flow is reversed, thus, the y-component of the mean velocity, $\langle V \rangle_0^+ > 0$ for $y_0^+ < 5$ at station D and $y_0^+ < 100$ at station E (Fig. 4.13b).
    (c) Above this region in the upper section of the bubble, the flow turns downwards, thus $\langle V \rangle < 0$ (Fig. 4.13b).
    (d) Therefore, in addition to the mean shear $\partial\langle U \rangle_0^+/\partial y$, the mean velocity derivative $-\partial\langle V \rangle_0^+/\partial y$ is significant in this curved ramp region.

2. The Reynolds stress budgets at stations A and B (Figs. 4.24 and 4.25) exhibit similar characteristics as that of a flat-plate turbulent boundary layer discussed by Pope (2000) in their Chapter 7, Sec. 7.3.5, Figs. 7.34-7.38.
    (a) In this region, $\partial\langle U \rangle/\partial y$ is the only significant component of the mean velocity gradient in this region as shown in Fig. 4.23.
    (b) Therefore, $\mathscr{P}_{11}$ is the main source of production of Reynolds stress while $\mathscr{P}_{22}$ and $\mathscr{P}_{33}$ are negligible (Figs. 4.24 and 4.25).

   (c) Therefore, most of the TKE production in this region occurs through the production of $\langle u^2 \rangle$.

   (d) Over most of the boundary layer, the velocity-pressure-gradient term, $\mathit{\Pi}_{11}$, is a sink of $\langle u^2 \rangle$ while $\mathit{\Pi}_{22}$ and $\mathit{\Pi}_{33}$ are the main sources of $\langle v^2 \rangle$ and $\langle w^2 \rangle$, respectively.

   (e) Therefore, the primary role of the velocity-pressure-gradient tensor is as a sink of $\langle u^2 \rangle$ while being a source of $\langle v^2 \rangle$ and $\langle w^2 \rangle$.

   (f) The dissipation of $\langle v^2 \rangle$ and $\langle w^2 \rangle$, i.e., ϵ_{22} and ϵ_{33}, respectively, are approximately balanced by $\mathit{\Pi}_{22}$ and $\mathit{\Pi}_{33}$.

   (g) Finally, in the shear-stress budget, the production $\mathscr{P}_{12}$, whose main source is the mean shear $\partial\langle U \rangle/\partial y$, is approximately balanced by $\mathit{\Pi}_{12}$ while the dissipation ϵ_{12} is negligible, except near the wall.

   (h) These pathways of production and dissipation of the Reynolds stresses in this region are shown in Fig. 4.46a.

3. The characteristics of the Reynolds stresses budgets in Cartesian coordinates in the separated region of the flow, at stations C, D and E, are as follows (Figs. 4.27 - 4.32):

   (a) In addition to the mean shear $\partial\langle U \rangle_0^+/\partial y$, the mean velocity derivative $\partial\langle V \rangle_0^+/\partial y$ is significant in this curved ramp region.

   (b) As a result, the production of $\langle v^2 \rangle$, $\mathscr{P}_{22}$, is non-negligible (Figs. 4.29c, 4.29d and 4.33c) when $\partial\langle V \rangle/\partial y < 0$ (Fig. 4.23d).

   (c) Therefore, the TKE production in this curved ramp region occurs through the production of both $\langle u^2 \rangle$ and $\langle v^2 \rangle$.

   (d) Further, the viscous diffusion and dissipation of $\langle v^2 \rangle$ and $-\langle uv \rangle$, in this curved ramp region, are not equal to zero at the wall, since $\partial v/\partial y \neq 0$ for $\eta = 0$ (Fig. 4.26).

   (e) The profiles of the mean flow convection and turbulent convection in the shear layer region of the flow ($y_0^+ < 100$ for stations C and D and $y_0^+ < 500$ for station E) are similar to those reported for a turbulent mixing layer in Fig. 21 by Rogers & Moser (1994).

   (f) Hence, this curved ramp region of the flow is characterized by enhanced transport of the Reynolds stresses compared to that at station A, due to the mixing layer created in the flow by the flow separation.

   (g) Finally, in the budget of $-\langle uv \rangle$, the main sources of production $-\mathscr{P}_{12}$ are the mean shear $\partial \langle U \rangle / \partial y$ as well as the mean velocity derivative $\partial \langle V \rangle_0^+ / \partial y$ (Figs. 4.30a, 4.30b and 4.34a).

   (h) The pathways of production and dissipation of the Reynolds stresses for the separated flow over the curved ramp are summarized in Fig. 4.46b.

4. The Reynolds stresses budgets in orthogonal curvilinear coordinates over the curved ramp, at stations C, D and E, exhibit similar behavior to those in the APG region of a pressure-gradient-induced turbulent flow separation over a flat plate (Figs. 4.40-4.45):

   (a) The budget of $\langle \hat{u}^2 \rangle$ (Fig. 4.40) is similar to its Cartesian counterpart of $\langle u^2 \rangle$ (Figs. 4.27a, 4.27b and 4.31a), but with increased production of $\langle \hat{u}^2 \rangle$ compared to that of $\langle u^2 \rangle$.

   (b) This is due to the contribution to $\hat{\mathscr{P}}^{11}$ of the velocity derivative $\nabla_\xi \langle \hat{U} \rangle$ (Figs. 4.41), in addition to the mean shear $\nabla_\eta \langle \hat{U} \rangle$, which is not the case for the counterparts terms of the production of $\langle u^2 \rangle$ (Figs. 4.29a,4.29b and 4.33a).

   (c) The viscous diffusion and dissipation of $\langle \hat{v}^2 \rangle$ (Fig. 4.42) and $-\langle \hat{u}\hat{v} \rangle$ (Fig. 4.44) are zero at the wall, analogously to the Cartesian profiles in a turbulent flat-plate boundary layer, since $\partial \hat{v} / \partial \xi = \partial \hat{v} / \partial \eta = \partial \hat{v} / \partial \zeta = 0$ at $\eta = 0$ (Fig. 4.26, Eqs. (F.3) and (F.6)).

   (d) The production $\hat{\mathscr{P}}^{22}$ is negative (Fig. 4.43) indicating that it is a sink of $\langle \hat{v}^2 \rangle$.

   (e) The main source of negative $\hat{\mathscr{P}}^{22}$ is the velocity derivative $\nabla_\eta\langle\hat{V}\rangle > 0$. The negative production of $\langle\hat{v}^2\rangle$ was also reported in Figs. 14b and 14d of Abe (2017) in the APG region of a pressure-gradient-induced flow separation in a flat plate boundary layer. Hence, the profile of $\langle\hat{v}^2\rangle_0^+$ at stations C, D and E have smaller magnitudes than their respective Cartesian counterparts.

   (f) In the budget of $-\langle\hat{u}\hat{v}\rangle$, the mean shear $\nabla_\eta\langle\hat{U}\rangle > 0$ is the main contributor to $-\hat{\mathscr{P}}^{12}$ (Fig. 4.45). This term was also identified as the primary source of $-\hat{\mathscr{P}}^{12}$ in Sec. 3.3, pp 582 of Abe (2017) in the APG region of a pressure-gradient-induced flow separation in a flat plate boundary layer.

   (g) However, the mean shear $\nabla_\xi\langle\hat{V}\rangle < 0$ for most of the boundary layer at stations C, D and E (Fig. 4.39c), and decreases $-\hat{\mathscr{P}}^{12}$.

   (h) The pathways of production and dissipation of the Reynolds stresses in the region over the curved ramp are summarized in Fig. 4.47.

5. The characteristics of the Reynolds stresses budgets in Cartesian coordinates in the reattachment and recovery region of the flow, stations F, G and H, are as follows (Figs. 4.35 and 4.36):

   (a) The Reynolds stress budgets of at the reattachment location, station F, are similar to those at stations in the curved ramp region of the flow, with the exception that the viscous diffusion and dissipation of $\langle v^2\rangle$ and $-\langle uv\rangle$ are equal to zero at the wall ($\eta = 0$) (Figs. 4.31 and 4.32). This is because station F is located in the flat-plate region downstream of the ramp (Figs. 4.8b and 4.26).

   (b) Downstream of the reattachment location, at stations G and H, the budgets of $\langle u^2\rangle$ and $\langle w^2\rangle$ at $y_0^+ < 60$ tend towards their shapes characteristic of ZPG SDTBL. The budgets of $\langle u^2\rangle$ and $\langle w^2\rangle$ at $y_0^+ > 60$ for station G are similar to those reported for a turbulent mixing layer in Figs. 21a and 21c by Rogers & Moser (1994).

(c) The production of $\langle v^2 \rangle$, non-negligible at station G (Figs. 4.35c and 4.37c), gradually reduces to zero at station H (Figs. 4.35d and 4.37d) as the mean velocity derivative eventually decays to zero at station H (4.23d).

(d) The budgets of $\langle v^2 \rangle$ and $-\langle uv \rangle$ at station G (Figs. 4.35c and 4.36a) are similar to those reported for a turbulent mixing layer in Figs. 21b and 21d by Rogers & Moser (1994).

(e) Even if the budgets of $\langle v^2 \rangle$ and $-\langle uv \rangle$ tend towards their shapes characteristic of a ZPG SDTBL, this happens more slowly than for those of $\langle u^2 \rangle$ and $\langle w^2 \rangle$. This is consistent with the observation of Song & Eaton (2004) that the recovery rate of the Reynolds stresses to their characteristic ZPG behavior, ordered from fastest to slowest, is $\langle u^2 \rangle$, $\langle uv \rangle$, and $\langle v^2 \rangle$.

(f) As the flow recovers downstream of the reattachment location from the separated turbulent flow towards a ZPG flat-plate behavior, pathways of production and dissipation of Reynolds stresses in this reattachment and recovery region are represented by a gradually transitional from the behavior of Fig. 4.46b to that of Fig. 4.46a.

Chapter 5

CONCLUSIONS

In the present work, we have made advances in direct numerical simulation (DNS) of spatially-developing turbulent boundary layers separating over curved wall. Specifically, we have: (i) developed an efficient numerical methodology to perform DNS of spatially-developing turbulent boundary layers (SDTBLs) over curved walls, and (ii) improved our understanding of the dynamics of turbulence in SDTBLs separating over curved walls. Herein, we summarize such advancements.

(i) In Chapter 2, we have described the new explicit pressure-correction method called FastRK3, that we have developed to simulate incompressible flows over curved walls (Aithal & Ferrante, 2020). FastRK3 solves the incompressible Navier-Stokes (NS) equations in the orthogonal curvilinear coordinates. The orthogonal formulation of the NS equations substantially reduces the computational cost of the flow solver and the numerical stencils of its second-order finite difference discretization mirror that of the Cartesian formulation. This property of the orthogonal formulation allowed us to develop an FFT-based Poisson solver for pressure, called FastPoc, for those cases where the components of the metric tensor are independent of one spatial direction: surfaces of linear translation (e.g., curved ramps and bumps) and surfaces of revolution (e.g., axisymmetric shapes). Our results showed that FastPoc, is thirty to sixty times faster than the multigrid-based linear solver, and FastRK3 is four to seven times faster when using FastPoc rather than multigrid. FastRK3 is an explicit, three-stage, third-order Runge-Kutta based projection-method which requires solving the Poisson equation for pressure only once per time step. To that regard, we have shown theoretically that FastRK3 has the same temporal order of accuracy for pressure and velocity as the standard RK3 method for both free-shear and wall-bounded flows when the RK3 coefficients and the pressure extrapolation scheme satisfy specific conditions herein theoretically derived (Aithal, Tipirneni & Ferrante, 2022).

In Chapter 3, we have verified and validated FastRK3 for wall-bounded flows. We have also showed numerically that FastRK3 is third-order accurate in time for velocity and second-order accurate in time for pressure for free-shear flows, and second-order accurate in time for velocity and pressure for 'stiff' wall-bounded flows, as the standard RK3 methodology (Sanderse, 2013) while requiring only one Poisson solver per time-step vs three of standard RK3. In summary, given that the computational mesh satisfies the property of orthogonality, FastRK3 simulates flows over curved walls with second-order accuracy in both space and time.

(ii) In Chapter 4, we have reported the results of our DNS of a SDTBL separating over a curved wall using FastRK3. We adopted the experimental test-case developed by Song & Eaton (2004) and have compared our DNS results with theirs for an upstream $\mathrm{Re}_\theta = 1100$ at $x = -2L$ from the curved wall. We have also derived, for the first time, the budget equations of the turbulence kinetic energy and of the Reynolds stresses in orthogonal coordinates. Then, we have studied the dynamics of turbulence of the separated flow by analyzing these budget equations in both Cartesian and orthogonal curvilinear coordinates. This has allowed us to explain some of the physical mechanisms of turbulence of SDTBL separating over a curved ramp. Our analysis shows that, in the separated region over the curved ramp, the TKE production occurs through the production of $\langle u^2 \rangle$ as well as $\langle v^2 \rangle$, in contrast to a ZPG SDTBL where the TKE production is mostly through the production of $\langle u^2 \rangle$. In the curved ramp region, the viscous diffusion and dissipation of $\langle v^2 \rangle$ are not zero at the wall, unlike that for both a ZPG SDTBL over a flat-plate as well as a pressure-gradient induced turbulent flow separation over a flat plate. And, the curved ramp region of the flow is characterized by enhanced transport of the Reynolds stresses compared to those of the upstream ZPG SDTBL due to the mixing layer created in the flow by the flow separation. Finally, our results have shown, for the first time, that the Reynolds stress profiles and budgets in the orthogonal curvilinear coordinates are very similar to those in the APG region of the 'pressure-gradient induced flow separation' in a flat-plate turbulent boundary layer. Such a comparison is only possible because (i) we employ a structured orthogonal grid (Appendix D) over the curved ramp in our simulations, and (ii) FastRK3 solves the governing equations written in orthogonal curvilinear coordinates.

While we have advanced the state-of-the-art for DNS of SDTBLs separating over curved walls, these findings open up new avenues for further research. We suggest a few here:

- Based on our DNS results, Reynolds stress models for SDTBL separating over curved walls could be designed in orthogonal curvilinear coordinates, where the computational domain after coordinate transformation is equivalent to the Cartesian domain over a flat plate. Further, the DNS data generated herein could be used for the development and validation of predictive wall-models for LES and RANS modeling of such flows. The DNS data could also be used to launch an AI campaign to facilitate training of neural networks for machine learning tools on SDTBL separating over curved walls (Wu *et al.*, 2018; Duraisamy *et al.*, 2019).

- Recently, Lu, Aithal & Ferrante (2021) discovered a law that predicts the incipience of flow separation over curved ramps by knowing only a few geometrical parameters of the ramp and the Reynolds number of the flow. They discovered the law of incipient separation over curved ramps by solving the Reynolds averaged Navier-Stokes (RANS) equations. FastRK3 can be used to perform DNS of turbulent flow over the set of smooth, curved ramps studied by them and provide more accurate coefficients for such law.

- The unsteadiness of pressure-gradient induced flow separation in a flat-plate turbulent boundary layer have been extensively studied (Wu *et al.*, 2005; Mohammed-Taifour & Weiss, 2016; Wu *et al.*, 2020). However, such a study for geometry induced flow separation over curved walls has not yet been performed. Such a a study can be performed using FastRK3.

- FastRK3 can be extended to simulate multiphase flows over curved walls. In order to study the modulation of separated turbulent boundary layers over curved walls by solid particles, the Lagrangian tracking algorithm of Ferrante & Elghobashi (2003); Dodd & Ferrante (2013) could be added. The effects of droplets and bubbles could also be studied using the volume-of-fluid method of Baraldi *et al.* (2014) along with the FastP* method of Dodd & Ferrante (2014). For example, Trefftz-Posada & Ferrante (2022) have recently developed an explicit and direct pressure-correction method (FastRK3P*) to solve the incompressible Navier Stokes equations for two-fluid flows under shear-periodic boundary conditions by combining FastRK3 with FastP* of Dodd & Ferrante (2014).

BIBLIOGRAPHY

Abe, H. 2017 Reynolds-number dependence of wall-pressure fluctuations in a pressure-induced turbulent separation bubble. *Journal of Fluid Mechanics* **833**, 563–598.

Abe, H. 2019 Direct numerical simulation of a turbulent boundary layer with separation and reattachment over a range of Reynolds numbers. *Fluid Dynamics Research* **51** (1), 011409.

Abe, H., Mizobuchi, Y., Matsuo, Y. & Spalart, P. 2012 DNS and modeling of a turbulent boundary layer with separation and reattachment over a range of Reynolds numbers. *Annual Research Briefs* **143**, 311–322.

Aithal, A. B. & Ferrante, A. 2018 A fast pressure-correction method for incompressible flows over curved surfaces. *Bulletin of the American Physical Society* **63**.

Aithal, A. B. & Ferrante, A. 2019 Direct numerical simulation of turbulent flows over curved walls with adverse pressure gradient. *Bulletin of the American Physical Society* **64**.

Aithal, A. B. & Ferrante, A. 2020 A fast pressure-correction method for incompressible flows over curved walls. *J. Comput. Phys.* **421**, 109693.

Aithal, A. B., Tipirneni, M. & Ferrante, A. 2022 Temporal accuracy of FastRK3. *J. Comput. Phys., Under review* .

Aris, R. 1962 *Vectors, Tensors and the Basic Equations of Fluid Dynamics*. Prentice-Hall.

Ascher, U. M. & Petzold, L. R. 1998 *Computer methods for ordinary differential equations and differential-algebraic equations*, , vol. 61. SIAM.

Baker, A. H., Falgout, R. D., Kolev, T. V. & Yang, U. M. 2012 Scaling hypre's multigrid solvers to 100,000 cores. In *High-Performance Scientific Computing*, pp. 261–279. Springer.

Balakumar, P., Park, G. & Pierce, B. 2014 Dns, les, and wall-modeled les of separating flow over periodic hills. In *Proceedings of the Summer Program*, pp. 407–415.

Balaras, E. & Benocci, C. 1994 Subgrid-scale models in finite-difference simulations of complex wall bounded flows. *AGARD, Neuilly-Sur-Seine, France* .

Balaras, E., Benocci, C. & Piomelli, U. 1996 Two-layer approximate boundary conditions for large-eddy simulations. *AIAA journal* **34** (6), 1111–1119.

Balin, R. & Jansen, K. E. 2021 Direct numerical simulation of a turbulent boundary layer over a bump with strong pressure gradients. *J. Fluid Mech.* **918**.

Baraldi, A., Dodd, M. S. & Ferrante, A. 2014 A mass-conserving volume-of-fluid method: Volume tracking and droplet surface-tension in incompressible isotropic turbulence. *Comput. Fluids* **96**, 322–337.

Blasius, H. 1908 Grenzschichten in flüssigkeiten mit kleiner reibung. *Z Math Physik* **56** (1), 1–37, English translation in NACA TM 1256.

Butcher, J. C. 2016 *Numerical methods for ordinary differential equations*. John Wiley & Sons.

Capuano, F., Coppola, G., Chiatto, M. & de Luca, L. 2016 Approximate projection method for the incompressible Navier–Stokes equations. *AIAA Journal* **54** (7), 2179–2182.

Choi, H., Moin, P. & Kim, J. 1993 Direct numerical simulation of turbulent flow over riblets. *J. Fluid Mech.* **255**, 503 – 539.

Chorin, A. J. 1967 A numerical method for solving incompressible viscous flow problems. *J. Comput. Phys.* **2** (1), 12–26.

Coleman, G., Rumsey, C. & Spalart, P. 2018 Numerical study of turbulent separation bubbles with varying pressure gradient and reynolds number. *Journal of Fluid Mechanics* **847**, 28–70.

Coles, D. 1956 The law of the wake in the turbulent boundary layer. *J. Fluid Mech.* **1**, 191–226.

De Michele, C., Capuano, F. & Coppola, G. 2020 Fast-projection methods for the incompressible Navier–Stokes equations. *Fluids* **5** (4), 222.

DeGraaff, D. B. & Eaton, J. K. 2000 Reynolds-number scaling of the flat-plate turbulent boundary layer. *J. Fluid Mech.* **422**, 319–346.

Disotell, K. J. & Rumsey, C. L. 2017 Design of an axisymmetric afterbody test case for cfd validation. In *23rd AIAA Computational Fluid Dynamics Conference*, p. 3792.

Dodd, M. S. & Ferrante, A. 2013 Direct numerical simulation of particle dispersion in a spatially developing turbulent boundary layer. *8th International Conf. on Multiphase Flow, Jeju, South Korea* (ICMF2013-484), 1–14.

Dodd, M. S. & Ferrante, A. 2014 A fast pressure-correction method for incompressible two-fluid flows. *J. Comput. Phys.* **273**, 416–434.

Duraisamy, K., Iaccarino, G. & Xiao, H. 2019 Turbulence modeling in the age of data. *Annu. Rev. Fluid Mech.* **51**, 357–377.

Eça, L. 1996 2D Orthogonal grid generation with boundary point distribution control. *J. Comput. Phys.* **125**, 440 – 453.

Falgout, R. D., Jones, J. E. & Yang, U. M. 2006 The design and implementation of hypre, a library of parallel high performance preconditioners. In *Numerical solution of partial differential equations on parallel computers*, pp. 267–294. Springer.

Ferrante, A. & Elghobashi, S. 2003 On the physical mechanism of two-way coupling in particle-laden isotropic turbulence. *Phys. Fluids* **15** (2), 315–329.

Ferrante, A. & Elghobashi, S. E. 2004 A robust method for generating inflow conditions for direct simulations of spatially-developing turbulent boundary layers. *J. Comput. Phys.* **198** (1), 372–387.

Fischer, P. F., Lottes, J. W. & Kerkemeier, S. G. 2008 nek5000 web page. *Web page: http://nek5000. mcs. anl. gov* .

Fletcher, C. A. 1988 *Computational techniques for fluid dynamics 2: Specific techniques for different flow categories*. Springer Science & Business Media.

Frigo, M. & Johnson, S. G. 2005 The design and implementation of FFTW3. *Proceedings of the IEEE* **93** (2), 216–231.

Fröhlich, J., Mellen, C. P., Rodi, W., Temmerman, L. & Leschziner, M. A. 2005 Highly resolved large-eddy simulation of separated flow in a channel with streamwise periodic constrictions. *J. Fluid Mech.* **526**, 19–66.

Fuchs, L. & Tillmark, N. 1985 Numerical and experimental study of driven flow in a polar cavity. *International journal for numerical methods in fluids* **5** (4), 311–329.

Ge, L. & Sotiropoulos, F. 2007 A numerical method for solving the 3D unsteady incompressible Navier-Stokes equations in curvilinear domains with complex immersed boundaries. *J. Comput. Phys.* **225**, 1782 – 1809.

George, A. 1973 Nested dissection of a regular finite element mesh. *SIAM Journal on Numerical Analysis* **10** (2), 345–363.

Griffiths, D. F. & Higham, D. J. 2010 *Numerical methods for ordinary differential equations: initial value problems*, , vol. 5. Springer.

GROVES, N. C., HUANG, T. T. & CHANG, M. S. 1989 Geometric characteristics of DARPA (defense advanced research projects agency) SUBOFF models (DTRC model numbers 5470 and 5471). *Tech. Rep.*. David Taylor Research Center Bethesda, MD Ship Hydromechanics Dept.

HAIRER, E. & WANNER, G. 1996 *Solving ordinary differential equations II*, , vol. 375. Springer Berlin Heidelberg.

HAMEL, G. 1917 Spiralförmige bewegungen zäher flüssigkeiten. *Jahresbericht der deutschen mathematiker-vereinigung* **25**, 34–60.

HARLOW, F. H. & WELCH, J. E. 1965 Numerical calculation of time-dependent viscous incompressible flow of fluid with free surface. *Phys. Fluids* **8**, 2182–2189.

HIRSCH, C. 1990 *Numerical Computation of Internal and External Flows*, , vol. 2. John Wiley & Sons.

HOEFLER, T. & GOTTLIEB, S. 2010 Parallel zero-copy algorithms for fast Fourier transform and conjugate gradient using MPI datatypes. In *European MPI Users' Group Meeting*, pp. 132–141. Springer.

HSL 2013 HSL: A collection of Fortran codes for large scale scientific computation. `http://www.hsl.rl.ac.uk`.

HUNG, C. 2002 Definition of Contravariant Velocity Components. *Tech. Rep.*. NASA Ames ResearchCenter, Moffett Field, CA.

JANG, S. J., HYUNG, J. S. & KROGSTAD, P. 2011 Effects of an axisymmetric contraction on a turbulent pipe flow. *J. Fluid Mech.* **687**, 376 – 403.

JEFFERY, G. 1915 L. The two-dimensional steady motion of a viscous fluid. *The London, Edinburgh, and Dublin Philosophical Magazine and Journal of Science* **29** (172), 455–465.

KARAM, M., SUTHERLAND, J. C. & SAAD, T. 2021 Low-cost runge-kutta integrators for incompressible flow simulations. *J. Comput. Phys.* **443**, 110518.

VON KÁRMÁN, T. 1930 Mechanische ähnlichkeit und turbulenz. In *3rd Int. Congr. Applied Mechanics*, pp. 85–105.

KARYPIS, G. & KUMAR, V. 2009 MeTis: Unstructured graph partitioning and sparse matrix ordering system, version 4.0. `http://www.cs.umn.edu/~metis`.

KITSIOS, V., SEKIMOTO, A., ATKINSON, C., SILLERO, J. A., BORRELL, G., GUNGOR, A. G., JIMÉNEZ, J. & SORIA, J. 2017 Direct numerical simulation of a self-similar adverse pressure gradient turbulent boundary layer at the verge of separation. *Journal of Fluid Mechanics* **829**, 392–419.

KOOIJ, G. L., BOTCHEV, M. A., FREDERIX, E. M., GEURTS, B. J., HORN, S., LOHSE, D., VAN DER POEL, E. P., SHISHKINA, O., STEVENS, R. J. & VERZICCO, R. 2018 Comparison of computational codes for direct numerical simulations of turbulent Rayleigh–Bénard convection. *Computers & Fluids* **166**, 1–8.

LE, H. & MOIN, P. 1991 An improvement of fractional step methods for the incompressible Navier-Stokes equations. *J. Comput. Phys.* **92** (2), 369–379.

LEE, J.-H. & SUNG, H. J. 2008 Effects of an adverse pressure gradient on a turbulent boundary layer. *International Journal of Heat and Fluid Flow* **29** (3), 568–578.

LEVEQUE, R. J. 2007 *Finite difference methods for ordinary and partial differential equations: steady-state and time-dependent problems*, , vol. 98. SIAM.

LORANG, T. & CARR, J. 2017 C-17A Globemaster III aft fuselage drag reduction flight demonstrations. In *AIAA Aviation Forum*.

LOWERY, P. S. & REYNOLDS, W. C. 1986 Numerical simulation of a spatially-developing, forces, plane mixing layer. Rep. TF-26. Stanford University.

Lu, D., Aithal, A. B. & Ferrante, A. 2021 Law of incipient separation over curved ramps as inferred by reynolds-averaged navierstokes. *AIAA Journal* **59** (1), 196–214.

Marquillie, M., Ehrenstein, U. & Laval, J.-P. 2011 Instability of streaks in wall turbulence with adverse pressure gradient. *J. Fluid Mech.* **681**, 205–240.

Mohammed-Taifour, A. & Weiss, J. 2016 Unsteadiness in a large turbulent separation bubble. *Journal of Fluid Mechanics* **799**, 383–412.

Mollicone, J.-P., Battista, F., Gualtieri, P. & Casciola, C. 2017 Effect of geometry and Reynolds number on the turbulent separated flow behind a bulge in a channel. *J. Fluid Mech.* **823**, 100–133.

Na, Y. & Moin, P. 1998 Direct numerical simulation of a separated turbulent boundary layer. *Journal of Fluid Mechanics* **374**, 379–405.

Nicholls, S. C., Phillips, D. J., Primozich, J. F., Lawrence, R. L., Kohler, T. R., Rudd, T. & Strandness Jr, D. 1989 Diagnostic significance of flow separation in the carotid bulb. *Stroke* **20** (2), 175–182.

Nikitin, N. 2006*a* Finite-difference method for incompressible Navier-Stokes equations in arbitrary orthogonal curvilinear coordinates. *J. Comput. Phys.* **217**, 759– 781.

Nikitin, N. 2006*b* Third-order-accurate semi-implicit Runge–Kutta scheme for incompressible Navier–Stokes equations. *International journal for numerical methods in fluids* **51** (2), 221–233.

Oberkampf, W. L. & Roy, C. J. 2010 *Verification and validation in scientific computing*. Cambridge Univ. Press.

Ohlsson, J., Schlatter, P., Fischer, P. F. & Henningson, D. S. 2010 Direct numerical simulation of separated flow in a three-dimensional diffuser. *J. Fluid Mech.* **650**, 307–318.

Omidyeganeh, M. & Piomelli, U. 2013 Large-eddy simulation of three-dimensional dunes in a steady, unidirectional flow. part 1. turbulence statistics. *J. Fluid Mech.* **721**, 454 – 483.

Piomelli, U., Ferziger, J., Moin, P. & Kim, J. 1989 New approximate boundary conditions for large eddy simulations of wall-bounded flows. *Physics of Fluids A: Fluid Dynamics* **1** (6), 1061–1068.

Pope, S. B. 2000 *Turbulent Flows*. Cambridge Univ. Press.

Prandtl, L. 1925 Bericht über die Entstehung der Turbulenz. *Z. Angew. Math. Mech.* **5**, 136–139.

Rogers, M. M. & Moser, R. D. 1994 Direct simulation of a self-similar turbulent mixing layer. *Physics of Fluids* **6** (2), 903–923.

Rosenfeld, M., Kwak, D. & Vinokur, M. 1991 A fractional step solution method for the unsteady incompressible Navier-Stokes equations in generalized coordinate systems. *J. Comput. Phys.* **94**, 102 – 137.

Sanderse, B. 2013 Energy-conserving Runge–Kutta methods for the incompressible Navier–Stokes equations. *J. Comput. Phys.* **233**, 100–131.

Sanderse, B. & Koren, B. 2012 Accuracy analysis of explicit Runge-Kutta methods applied to the incompressible Navier-Stokes equations. *J. Comput. Phys.* **231** (8), 3041–3063.

Sanz-Serna, J. M., Verwer, J. G. & Hundsdorfer, W. 1986 Convergence and order reduction of Runge-Kutta schemes applied to evolutionary problems in partial differential equations. *Numerische Mathematik* **50** (4), 405–418.

Song, S. & Eaton, J. K. 2004 Reynolds number effects on a turbulent boundary layer with separation, reattachment, and recovery. *Experiments in fluids* **36** (2), 246–258.

Spalart, P. R. 1988 Direct simulation of a turbulent boundary layer up to R_θ=1410. *J. Fluid Mech.* **187**, 61–98.

Spalart, P. R. & Coleman, G. N. 1997 Numerical study of a separation bubble with heat transfer. *European Journal of Mechanics-B/Fluids* **16** (2), 169–189.

Spalart, P. R., Jou, W.-H., Strelets, M. & Allmaras, S. R. 1997 Comments on the feasibility of LES for wings and on a hybrid RANS/LES approach. In *Advances in DNS/LES* (ed. C. Liu & Z. Liu), pp. 137–148.

Taylor, G. I. 1923 On the decay of vortices in a viscous fluid. *Philos. Mag.* **XLVI**, 671–674.

Terrenoire, E., Hauglustaine, D., Gasser, T. & Penanhoat, O. 2019 The contribution of carbon dioxide emissions from the aviation sector to future climate change. *Environmental Research Letters* **14** (8), 084019.

Trefftz-Posada, P. & Ferrante, A. 2022 Direct numerical simulation of droplet laden homogeneous shear turbulence: numerical method and flow physics. *11th International Conference on Computational Fluid Dynamics, ICCFD, Maui (HI), July 11-15* .

Wang, C., Jang, Y. & Leschziner, M. 2004 Modelling two-and three-dimensional separation from curved surfaces with anisotropy-resolving turbulence closures. *International Journal of Heat and Fluid Flow* **25** (3), 499–512.

Warsi, Z. U. A. 1993 *Fluid dynamics: Theoretical and Computational Approaches*. CRC Press.

Wasistho, B. & Squires, K. 2005 Prediction of turbulent separation over a backward-facing smooth ramp. *Journal of Turbulence* (6), N1.

White, F. M. & Corfield, I. 2006 *Viscous fluid flow*, , vol. 3. McGraw-Hill New York.

Wilcox, D. C. 2006 *Turbulence modeling for CFD*, 3rd edn. D C W Industries.

Wu, J.-L., Xiao, H. & Paterson, E. 2018 Physics-informed machine learning approach for augmenting turbulence models: A comprehensive framework. *Physical Review Fluids* **3** (7), 074602.

Wu, S., MIAU, J.-J., Hu, C. & Chou, J. 2005 On low-frequency modulations and three-dimensionality in vortex shedding behind a normal plate. *Journal of Fluid Mechanics* **526**, 117–146.

Wu, W., Meneveau, C. & Mittal, R. 2020 Spatio-temporal dynamics of turbulent separation bubbles. *Journal of Fluid Mechanics* **883**.

Wu, X. & Squires, K. D. 1998 Numerical investigation of the turbulent boundary layer over a bump. *Journal of Fluid Mechanics* **362**, 229–271.

Appendix A

FORMULATION OF THE VISCOUS TERMS IN THE NAVIER-STOKES EQUATIONS

The Laplacian of **U** in curvilinear coordinates takes the following form

$$\nabla^2 \mathbf{U} = g^{mn} \nabla_n \nabla_m \hat{U}^i = g^{mn} \left[\frac{\partial A^i_m}{\partial \xi^n} + \mathit{\Gamma}^i_{jn} A^j_m - \mathit{\Gamma}^j_{mn} A^i_j \right], \tag{A.1}$$

where A^i_m is given by

$$A^i_m = \frac{\partial \hat{U}^i}{\partial \xi^m} + \mathit{\Gamma}^i_{mk} \hat{U}^k. \tag{A.2}$$

Because of the numerical complexity of discretizing and then computing all the terms of (A.1) using (A.2), we rewrite the Laplacian of the velocity field **U** as

$$\nabla^2 \mathbf{U} = \nabla \left(\nabla \cdot \mathbf{U} \right) - \nabla \times \left(\nabla \times \mathbf{U} \right) = -\nabla \times \left(\nabla \times \mathbf{U} \right), \tag{A.3}$$

where we have used the incompressibility condition, $\nabla \cdot \mathbf{U} = 0$. The components in the three curvilinear directions ξ, η and ζ of (A.3) are given in Eq.(2.20) and discretized with the centered second-order finite-difference scheme in FastRK3.

Appendix B

NUMERICAL COMPARISON OF FASTRK3 WITH THE LM METHOD

Herein, we list the differences between the Le & Moin (1991) (LM) method and FastRK3 of Aithal & Ferrante (2020):

1. The RK3 schemes used by the two algorithms are different. This difference is highlighted in Figs. 2.4a and 2.4c, and by comparing Eqs. (2.30)-(2.36) and Eqs. (3.7)-(3.9) of Le & Moin (1991).

2. We observed that the numerically stiff viscous term in the incompressible Navier-Stokes equations causes loss of accuracy in the second-order Adams Bashforth method. We performed numerical tests of the viscous Berger's equation using the various three-stage methods described in Sanderse & Koren (2012) and chose the RK3 coefficients that did not exhibit loss of accuracy. In contrast, the RK3 coefficients of the LM method were selected on the basis of private communications (see Ref 3 of Le & Moin (1991)). We have tried to test the Le & Moin (1991) method, however, the numerical solution obtained with the LM method does not match the experimental solution as FastRK3 does (see Sec. 3.2.1). Figures B.1 and B.2 show the steady-state results of lid-driven square cavity flow at Re=280 for FastRK3 and LM method.

3. The LM method requires computing the divergence of velocity, $\delta \hat{u}_j^{k-1}/\delta xj$ in Eq. (3.6) of Le & Moin (1991) at every substep, which is not required for FastRK3.

4. The linear terms $L\left(\hat{u}_i^{k-1}\right)$ and the non-linear term $N\left(u_i^{*k-1}\right)$ in Eq. (3.6) of Le & Moin (1991) are computed using two different arrays $\hat{u}_i^{k-1}$ and u_i^{*k-1} whereas for FastRK3

the fluxes in Eq. (2.32) are computed using $F\left(U^*_{j-1} - \check{c}_{j-1} \Delta t G \phi_{j-1}\right)$ which greatly simplifies the computations.

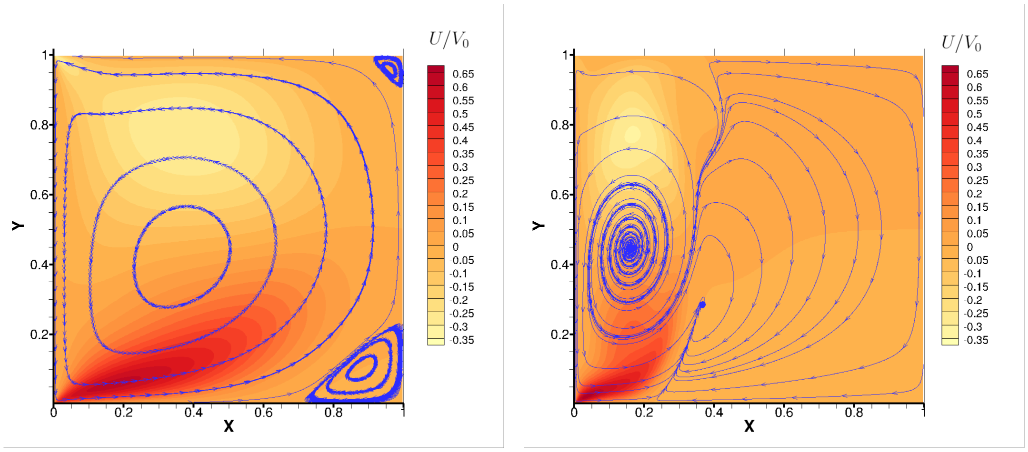

(a) FastRK3

(b) LM

Figure B.1: U/V_0 velocity contour with streamlines

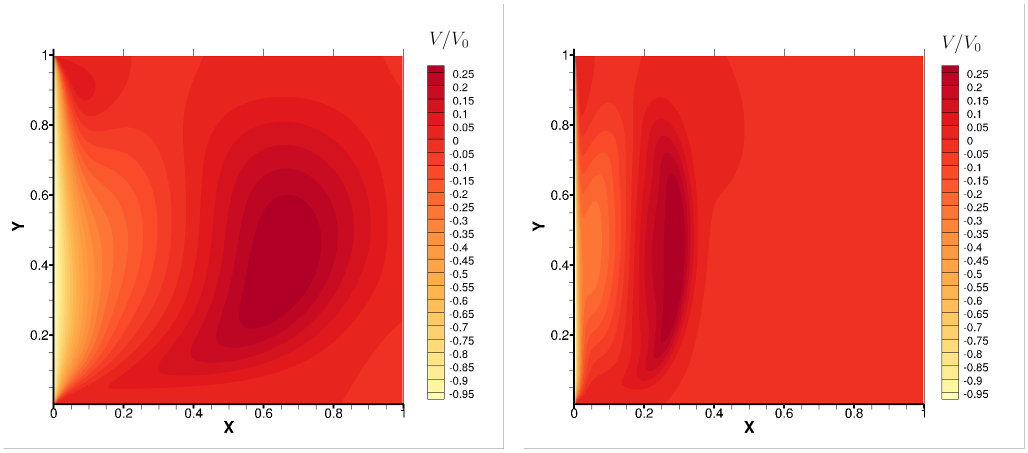

(a) FastRK3

(b) LM

Figure B.2: V/V_0 velocity contour

Appendix C

PROOF OF THE INDEPENDENCE OF THE VECTOR COEFFICIENTS C_{ϕ_I} ON $\varDelta T$

We begin the proof by noticing that the linear extrapolation of $\tilde{\phi}$ in time can be written as a second-order approximation of the standard RK3 solution with $\tilde{\alpha}$ and $\tilde{\beta}$ coefficients, analogously to Fig. 2.3, as follows:

$$\tilde{\phi}_1 = \underbrace{(1+\tilde{\beta}+\tilde{\alpha}\check{c}_1)\tilde{\phi}_{n-\frac{1}{2}} - (\tilde{\beta}+\tilde{\alpha}\check{c}_1)\tilde{\phi}_{n-\frac{3}{2}}}_{\text{linear extrapolation of } \tilde{\phi}} + \mathcal{O}(\varDelta t^2). \tag{C.1}$$

For a general linear extrapolation of ϕ_1 of FastRK3 (Fig. 2.3), Eq. (2.103) gives ϕ_1 as

$$\phi_1 = (1+\beta+\alpha\check{c}_1)\tilde{\phi}_{n-\frac{1}{2}} - (\beta+\alpha\check{c}_1)\tilde{\phi}_{n-\frac{3}{2}}. \tag{C.2}$$

Subtracting Eq. (C.2) from Eq. (C.1) gives:

$$\tilde{\phi}_1 - \phi_1 = \left[\tilde{\beta} - \beta + \check{c}_1\left(\tilde{\alpha}-\alpha\right)\right]\left(\tilde{\phi}_{n-\frac{1}{2}} - \tilde{\phi}_{n-\frac{3}{2}}\right) + \mathcal{O}(\varDelta t^2). \tag{C.3}$$

From the r.h.s. of (C.3), we define the constant c_1 as

$$c_1 = \tilde{\beta} - \beta + \check{c}_1\left(\tilde{\alpha}-\alpha\right). \tag{C.4}$$

In (C.3) the difference $\tilde{\phi}_{n-\frac{1}{2}} - \tilde{\phi}_{n-\frac{3}{2}}$ is at worst first-order accurate in time, and can be written as:

$$\tilde{\phi}_{n-\frac{1}{2}} - \tilde{\phi}_{n-\frac{3}{2}} = \bar{c}\varDelta t + \mathcal{O}(\varDelta t^2) \tag{C.5}$$

where $\bar{c}$ may have spatial dependence, but is independent of $\varDelta t$. Thus, using Eqs. (C.4) and (C.5), Eq. (C.3) can be simplified to:

$$\tilde{\phi}_1 - \phi_1 = c_1\bar{c}\varDelta t + \mathcal{O}(\varDelta t^2). \tag{C.6}$$

We then take the gradient of Eq. (C.6), and noting that only $\bar{c}$ has spatial dependence, this gives:

$$G\tilde{\phi}_1 - G\phi_1 = c_1 \mathit{\Delta} t G\bar{c} + \mathcal{O}(\mathit{\Delta} t^2). \tag{C.7}$$

By defining,

$$c_{\phi_1} = c_1 G\bar{c}, \tag{C.8}$$

Eq. (C.7) can be written as

$$G\tilde{\phi}_1 - G\phi_1 = c_{\phi_1} \mathit{\Delta} t + \mathcal{O}(\mathit{\Delta} t^2), \tag{C.9}$$

which is the proof of Eq. (2.59) which is numerically proved in Fig. 3.12. A similar derivation can be done for c_{ϕ_2} as well. Thus, c_{ϕ_i} are vectors which have spatial dependence via $\bar{c}$ but have no dependence on $\mathit{\Delta} t$. We have updated the text in the current revised manuscript to reflect the fact that c_{ϕ_i} are vectors of coefficients which do not depend on $\mathit{\Delta} t$. That said, we should also note that there is a specific case in which $c_{\phi_1} = c_{\phi_2} = 0$ (Case C of Eq. (2.90)), in which the vector coefficients are constant with respect to space and $\mathit{\Delta} t$, and are equal to zero.

Appendix D

GENERATION OF ORTHOGONAL GRIDS

Since the FastRK3 flow solver, described in Sec. 2.3, is designed to solve the NS equations (2.15) and (2.16) written in the orthogonal curvilinear formulation, we need to generate orthogonal grids for the computational domain. For simplicity, we describe the method in two dimensions, allowing uniformity in the third (azimuthal, ζ) direction of the grid, but the following method can also be easily extended to three dimensions. An orthogonal grid in two dimensions has to satisfy the condition of the vanishing off-diagonal term of the metric tensor g_{12}:

$$g_{12} = \frac{\delta x}{\delta \xi}\frac{\delta x}{\delta \eta} + \frac{\delta y}{\delta \xi}\frac{\delta y}{\delta \eta} = 0. \tag{D.1}$$

In order to generate an orthogonal mesh over a curved surface, we started with the method described by Eça (1996) which was developed to generate two-dimensional orthogonal grids over arbitrary geometries. The method involves solving numerically the following coupled system of non-linear Poisson equations:

$$\begin{aligned} \frac{\delta}{\delta \xi}\left(\frac{h_\eta}{h_\xi}\frac{\delta x}{\delta \xi}\right) + \frac{\delta}{\delta \eta}\left(\frac{h_\xi}{h_\eta}\frac{\delta x}{\delta \eta}\right) &= 0, \\ \frac{\delta}{\delta \xi}\left(\frac{h_\eta}{h_\xi}\frac{\delta z}{\delta \xi}\right) + \frac{\delta}{\delta \eta}\left(\frac{h_\xi}{h_\eta}\frac{\delta z}{\delta \eta}\right) &= 0, \end{aligned} \tag{D.2}$$

with the appropriate boundary conditions prescribed as:

- Dirichlet boundary conditions at the bottom boundary ($\eta = 0$) by specifying the profile of the curved wall, denoted as $x_0(\xi)$ and $y_0(\xi)$:

$$\begin{aligned} x(\xi, \eta = 0) &= x_0(\xi), \\ y(\xi, \eta = 0) &= y_0(\xi), \end{aligned} \tag{D.3}$$

- Dirichlet boundary conditions at the inflow plane ($\xi = 0$) by fixing the distribution of grid points along the wall normal (η) direction, denoted as $y_1(\eta)$, where $y_1(\eta)$ is a prescribed function, e.g. a hyperbolic tangent function as in (Ferrante & Elghobashi, 2004):

$$\begin{aligned} x(\xi = 0, \eta) &= x_0(0), \\ y(\xi = 0, \eta) &= y_1(\eta), \end{aligned} \tag{D.4}$$

- Neumann-Dirichlet boundary conditions at the outflow plane ($\xi = L_\xi$):

$$\begin{aligned} x(\xi = L_\xi, \eta) &= x_0(L_\xi), \\ \left.\frac{\delta y}{\delta \xi}\right|_{\xi = L_\xi} &= 0, \end{aligned} \tag{D.5}$$

- Neumann-Dirichlet boundary conditions at the free-stream plane ($\eta = L_\eta$):

$$\begin{aligned} \left.\frac{\delta x}{\delta \eta}\right|_{\eta = L_\eta} &= 0, \\ y(\xi, \eta = L_\eta) &= y_1(L_\eta). \end{aligned} \tag{D.6}$$

We write Eq. (D.2) in discretized form using the second-order central difference scheme and we solve the resulting discretized system by successive overrelaxation (SOR) and the convergence criterion of reaching $||g_{12}||_2 < 10^{-7}$ for the grid solution. We extend the method described by Eça (1996) to incorporate grid stretching in the wall-normal (η) and stream-wise (ξ) directions according to the analytical stretching function defined by Ferrante & Elghobashi (2004). Also, the stream-wise (ξ) discretization of the bottom boundary is carried out on the basis of constant arc length as opposed to constant grid spacing, Δx. This allows us to generate orthogonal grids over ramp geometries with different degrees of slopes. In order to demonstrate the usefulness of our orthogonal grid generator, we generate grids over the three ramp profiles shown in Fig. D.1a and a Gaussian bump shown in Fig. D.1b. The two-dimensional grid can then be used to generate three-dimensional grids over surfaces of linear translation (e.g., curved ramps, Fig. D.2a and bumps, Fig. D.2b) and surfaces of revolution (e.g., axisymmetric ramps, Fig. D.2c).

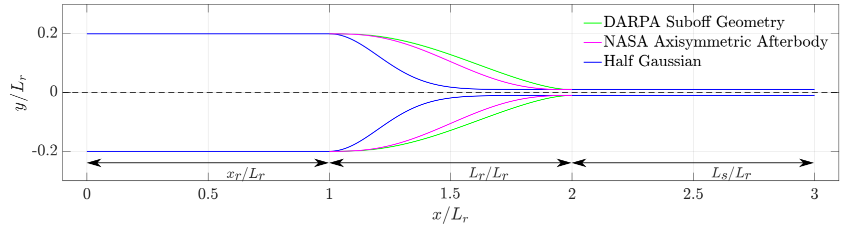

(a) Ramp profiles: DARPA Suboff geometry by the square-root of a sixth order polynomial (Groves *et al.*, 1989), NASA axisymmetric afterbody is defined by a fifth-order polynomial function (Disotell & Rumsey, 2017) and the, half-Gaussian profile. These profiles have been stretched and include a "sting" at the end of the ramp. The half-Gaussian profile is described by $y = h_s + (h_r - h_s)\exp(-[x - x_r]^2/[2L_r^2/25])$, where h_s is the height of the sting, h_r is the height of the ramp, L_r is the length of the ramp, and x_r denotes the x-location of the beginning of the ramp.

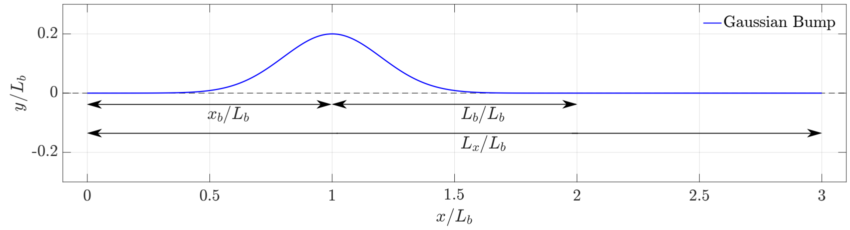

(b) Bump profile: the Gaussian bump is described by $y = h_b \exp(-[x - x_b]^2/[2L_b^2/25])$, where h_b is the height of the bump, L_b is the length of the bump, and x_b denotes the x-location of the peak of the Gaussian bump.

Figure D.1: Profiles of curved walls

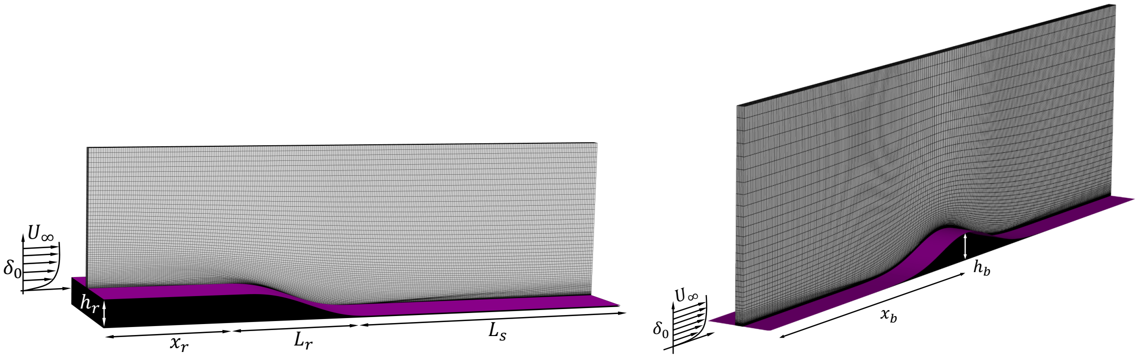

(a) 3D grid over the NASA curved ramp.

(b) 3D grid over the Gaussian bump.

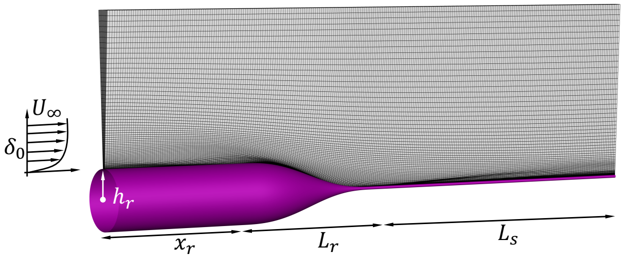

(c) 3D grid over NASA axisymmetric ramp.

Figure D.2: Schematic of flow over 3D curved walls

Appendix E

ORTHOGONAL FORMULATION OF THE TURBULENCE KINETIC ENERGY EQUATION

The terms of the budget equation (4.11) of the turbulence kinetic energy, k, expressed in orthogonal curvilinear coordinates (Sec. 2.1), are herein summarized:

1. Mean flow convection

$$-\langle\mathbf{U}\rangle\cdot\nabla k \equiv -\langle\hat{U}^i\rangle\nabla_i k = -\left\langle \hat{U}^i \right\rangle \frac{\partial k}{\partial \xi^i}, \tag{E.1}$$

2. Turbulent convection

$$\frac{1}{2}\nabla\cdot\langle\mathbf{u}(\mathbf{u}\cdot\mathbf{u})\rangle \equiv -\frac{1}{2}\nabla_i\langle\hat{u}^i\hat{u}^j\hat{u}^m g_{jm}\rangle = -\frac{1}{2}\frac{1}{\sqrt{g}}\frac{\partial}{\partial\xi^i}\left(\sqrt{g}\langle\hat{u}^i\hat{u}^j\hat{u}^m g_{jm}\rangle\right), \tag{E.2}$$

3. Viscous diffusion

$$2\nu\nabla\cdot\langle\mathbf{u}\cdot\mathbf{s}\rangle \equiv 2\nu\frac{1}{\sqrt{g}}\frac{\partial}{\partial\xi^i}\left(\sqrt{g}\langle s_{mn}\hat{u}^n g^{im}\rangle\right), \tag{E.3}$$

   where s_{ij} are the covariant components of the fluctuating rate of strain

$$s_{ij} = \frac{1}{2}\left(\frac{\partial\check{u}_i}{\partial\xi_j} + \frac{\partial\check{u}_j}{\partial\xi_i} - 2\mathit{\Gamma}^m_{ij}\check{u}_m\right), \tag{E.4}$$

   and the covariant components of the fluctuating velocity $\check{u}_i$ are

$$\check{u}_i = \hat{u}^j g_{ij}, \tag{E.5}$$

4. Production

$$\mathscr{P} = -\langle\mathbf{uu}\rangle : \overline{\mathbf{S}} \equiv -\langle\hat{u}^i\hat{u}^j\rangle\nabla_j\langle\check{U}_i\rangle = -\left\langle\hat{u}^i\hat{u}^j\right\rangle\left[\frac{\partial\left\langle\check{U}_i\right\rangle}{\partial\xi^j} - \mathit{\Gamma}^m_{ij}\left\langle\check{U}_m\right\rangle\right], \tag{E.6}$$

   and the covariant components of the mean velocity $\langle\check{U}_i\rangle$ are

$$\langle\check{U}_i\rangle = \langle\hat{U}^j\rangle g_{ij}, \tag{E.7}$$

5. Velocity-pressure-gradient

$$\mathit{\Pi} = \frac{1}{\rho}\nabla \cdot \langle \mathbf{u} p' \rangle \equiv -\frac{1}{\rho}\nabla_i \langle p' \hat{u}^i \rangle = -\frac{1}{\rho}\left\langle \hat{u}^i \frac{\partial p'}{\partial \xi^i} \right\rangle, \tag{E.8}$$

6. Dissipation

$$\epsilon = 2\nu \langle \mathbf{s} : \mathbf{s} \rangle \equiv 2\nu \langle s_{ij} s_{mn} g^{im} g^{jn} \rangle. \tag{E.9}$$

Appendix F

ORTHOGONAL FORMULATION OF THE REYNOLDS STRESS EQUATION

The contravariant tensor components of the Reynolds stress transport equation (4.18) expressed in orthogonal curvilinear coordinates (Sec. 2.1), are herein summarized:

1. Mean flow convection tensor

$$\begin{aligned}\langle \mathbf{U}\rangle \cdot \nabla \langle \mathbf{uu}\rangle &\equiv -\frac{\partial}{\partial t}\langle \hat{u}^i \hat{u}^j\rangle - \langle \hat{U}^k\rangle \nabla_k \langle \hat{u}^i \hat{u}^j\rangle \\ &= -\frac{\partial}{\partial t}\langle \hat{u}^i \hat{u}^j\rangle - \langle \hat{U}^k\rangle \frac{\partial}{\partial \xi^k}\langle \hat{u}^i \hat{u}^j\rangle - \langle \hat{U}^k\rangle \langle \hat{u}^m \hat{u}^j\rangle \varGamma^i_{mk} - \langle \hat{U}^k\rangle \langle \hat{u}^i \hat{u}^m\rangle \varGamma^j_{mk},\end{aligned} \tag{F.1}$$

2. Turbulent convection tensor

$$\begin{aligned}\nabla \cdot \langle \mathbf{uuu}\rangle &\equiv \nabla_k \left\langle \hat{u}^i \hat{u}^j \hat{u}^k \right\rangle \\ &= -\frac{\partial}{\partial \xi^k}\left\langle \hat{u}^i \hat{u}^j \hat{u}^k \right\rangle - \left\langle \hat{u}^m \hat{u}^j \hat{u}^k \right\rangle \varGamma^i_{mk} - \left\langle \hat{u}^i \hat{u}^m \hat{u}^k \right\rangle \varGamma^j_{mk} - \frac{\langle \hat{u}^i \hat{u}^j \hat{u}^m\rangle}{\sqrt{g}} \frac{\partial \sqrt{g}}{\partial \xi^m},\end{aligned} \tag{F.2}$$

3. Viscous diffusion tensor

$$\begin{aligned}\nu \nabla^2 \langle \mathbf{uu}\rangle &\equiv \nu \nabla^2 \left\langle \hat{u}^i \hat{u}^j \right\rangle \\ &= \frac{1}{\sqrt{g}}\frac{\partial}{\partial \xi^m}\left(g^{mk}\nabla_k \left\langle \hat{u}^i \hat{u}^j \right\rangle \sqrt{g}\right) + g^{mk}\nabla_k \left\langle \hat{u}^n \hat{u}^j \right\rangle \varGamma^i_{mn} + g^{mk}\nabla_k \left\langle \hat{u}^i \hat{u}^n \right\rangle \varGamma^j_{mn},\end{aligned} \tag{F.3}$$

4. Production tensor

$$\mathscr{P}^{ij} = -\langle \hat{u}^i \hat{u}^k\rangle \left[\frac{\partial \langle \hat{U}^j\rangle}{\partial \xi^k} + \varGamma^j_{km}\langle \hat{U}^m\rangle\right] - \langle \hat{u}^j \hat{u}^k\rangle \left[\frac{\partial \langle \hat{U}^i\rangle}{\partial \xi^k} + \varGamma^i_{km}\langle \hat{U}^m\rangle\right], \tag{F.4}$$

5. Velocity-pressure-gradient tensor

$$\mathit{\Pi}^{ij} = -\frac{1}{\rho}\left\langle \hat{u}^i \frac{\partial p'}{\partial \xi^k} g^{kj} + \hat{u}^j \frac{\partial p'}{\partial \xi^k} g^{ik} \right\rangle, \tag{F.5}$$

6. Dissipation tensor

$$\epsilon^{ij} = 2\nu \left\langle \left(\frac{\partial \hat{u}^i}{\partial \xi^m} + \mathit{\Gamma}^i_{mk} \hat{u}^k \right) \left(\frac{\partial \hat{u}^j}{\partial \xi^n} + \mathit{\Gamma}^j_{nk} \hat{u}^k \right) g^{mn} \right\rangle. \tag{F.6}$$

VITA

List of publications

1. AITHAL, A. & FERRANTE A. 2022 Direct numerical simulation of a spatially developing turbulent boundary layer separating over a curved wall. In Preparation.
2. AITHAL, A. TIPIRNENI, M. & FERRANTE A. 2022 Temporal accuracy of FastRK3 *Journal of Computational Physics*, Rev 2, Under Review.
3. HUANG, SC. AITHAL, A. & FERRANTE A. 2022 Law of incipient separation for turbulent flows over airfoils as inferred by Reynolds averaged Navier-Stokes. *Physics of Fluids* **34**, 085117. DOI: `https://doi.org/10.1063/5.0099523`
4. LU, D. AITHAL, A. & FERRANTE A. 2021 Law of Incipient Separation over Curved Ramps as Inferred by Reynolds-Averaged Navier-Stokes. *AIAA Journal* **59**, 196-214. DOI: `https://doi.org/10.2514/1.J059611`
5. AITHAL, A. & FERRANTE A. 2020 A fast pressure-correction method for incompressible flows over curved walls *Journal of Computational Physics* **421**, 1-28. DOI: `https://doi.org/10.1016/j.jcp.2020.109693`